NIST GCR 01-809

EVALUATION OF THE HDR FIRE TEST DATA AND ACCOMPANYING COMPUTATIONAL ACTIVITIES WITH CONCLUSIONS FROM PRESENT CODE CAPABILITIES. VOLUME 4: TEST SERIES DESCRIPTION AND CFAST VALIDATION FOR HDR T52 OIL POOL FIRE TEST SERIES

Jason Floyd
Lothar Wolf
Brian Rauch
Kevin Mun
Department of Materials and Nuclear Engineering
University of Maryland
College Park, MD 20742

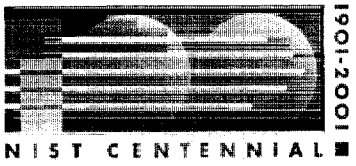

NIST
National Institute of Standards and Technology
Technology Administration, U.S. Department of Commerce

NIST GCR 01-809

EVALUATION OF THE HDR FIRE TEST DATA AND ACCOMPANYING COMPUTATIONAL ACTIVITIES WITH CONCLUSIONS FROM PRESENT CODE CAPABILITIES. VOLUME 4: TEST SERIES DESCRIPTION AND CFAST VALIDATION FOR HDR T52 OIL POOL FIRE TEST SERIES

Prepared for
U.S. Department of Commerce
Building and Fire Research Laboratory
National Institute of Standards and Technology
Gaithersburg, MD 20899-8640

December 2000

U.S. Department of Commerce
Norman Y. Mineta, Secretary

Technology Administration
Dr. Cheryl L. Shavers, Under Secretary of Commerce for Technology

National Institute of Standards and Technology
Karen H. Brown, Acting Director

Notice

This report was prepared for the Building and Fire Research Laboratory of the National Institute of Standards and Technology under Contract number 60NANB6D0127. The statement and conclusions contained in this report are those of the authors and do not necessarily reflect the views of the National Institute of Standards and Technology or the Building and Fire Research Laboratory.

Evaluation of the HDR Fire Test Data and Accompanying Computational Activities with Conclusions from Present Code Capabilities

NIST CONTRACT 60NANB6D0127

Volume 4:
Test Series Description and CFAST Validation for HDR T52 Oil Pool Fire Test Series

June 2000

Jason Floyd
Lothar Wolf
Brian Rauch
Kevin Mun

Nuclear Engineering Program
Department of Materials and Nuclear Engineering
University of Maryland at College Park

EXECUTIVE SUMMARY

Between 1984 and 1992 four major test series were performed in the HDR containment encompassing various fuels and three different axial positions in the high-rise, multilevel, multi-compartment facility. At that time, each HDR fire test series was accompanied by extensive efforts to evaluate the predictive capabilities of a variety of fire models and codes developed in different countries by both blind pretest and open posttest computations. A large number of open issues remained in the area of fire computer code predictive qualities upon completion of the HDR program.

In the meantime, large progress has been made in improving and consolidating fire models and computer codes of all levels of simulations. This progress merits revisiting both experimental results and fire computer code capabilities. The results of the research efforts for this grant during FY 1998/99 are documented in this volume:

Volume 4: Test Series Description and CFAST Validation for HDR T52 Oil Pool Fire Test Series.

Volume 4 by focusing on the HDR T52 oil pool fire experiments covers the following aspects:

- Section 1 provides an overall introduction to the HDR test facility and especially the containment building layout. It provides an overview of all four major HDR fire test groups utilizing a range of fire sources including: propane gas burners, wood cribs, liquid fuel pools, and prototypical electrical cables. These fires have been set at three different axial elevations within the containment building under natural, forced, and combined ventilation conditions. This section is identical for all reports published thus far.
- Section 2 gives a detailed account for the compartment layouts for the oil pool fire experiments. It also lists all fuel amounts, pool sizes, and thermophysical material properties involved in the individual experimental setups.
- Section 3 describes the objectives, requirements, and functional principles of the instrumentation applied during the test series and documents the positions of all sensors used in both tabular and graphical forms and summarizes sensor failures during individual tests.
- Section 4 briefly summarizes the common test procedure used for executing every experiment and lists test-induced damages.
- Section 5 provides an overview of major experimental results of the oil pool fire tests in two subsections. First, selected transient histories are shown for temperatures, gas concentrations, and velocities in the different connected compartments, including the dome, for the four experiments spanning the range of fire powers examined. The second set of experimental results involves the maximum values of the same quantities as a function of the applied fire power. This section also documents velocity, temperature and gas concentration results from multidimensional sensor arrays.
- Section 6 addresses numerous aspects of potential contributions of the oil pool fire experiments towards the validation of zone model codes such as CFAST, containment system codes such as GOTHIC, and field models such as FDS.

- Section 7 describes the CFAST models developed for simulating selected experiments of the T52 test series.
- Section 8 discusses the results of computations using the CFAST models described in section 7 for two of the four oil pool fire tests.
- Section 9 addresses the accomplishments achieved with CFAST while modeling the oil pool fire tests and pits these in perspective to previous results of similar codes.
- Appendix A contains the CFAST input files for the models discussed in Section 7.

A follow-up standalone report from UMCP [38], will document:

- additional assessments and insights from test data evaluations
- three dimensional models for tests T52.14 and T51.23 using the FDS computer code
- computational results of multidimensional, steady-state and transient simulations using different model options
- comparisons between HDR data and FDS computed results
- the re-analysis of HDR gas fire test T51.23 with CFAST using an expanded model based on the learning effects from CFAST simulations of the HDR oil pool fire tests reported in Section 8
- additional information about CFAST results for T52.14 and respective comparisons with data
- performance-based judgments on predictive qualities of different computational tools including hand computations, CFAST, and FDS

ACKNOWLEDGMENTS

The work reported under this grant was performed under the auspices of the Building and Fire Research Laboratory at the National Institute of Standards and Technology. It was funded by the Department of Commerce.

The program was monitored at NIST by Dr. Glenn Forney whose continued interest in and support of this work is greatly appreciated.

We thank Dr. Kevin McGrattan for his continued interest and support in our efforts related to containment fire experiments.

Also, we would like to thank Dr. Richard Peacock and Dr. Glenn Forney for supporting the validation efforts documented in this Volume 4 of this report.

TABLE OF CONTENTS

TABLE OF CONTENTS (CONT.)

TABLE OF CONTENTS (CONT.)

LIST OF FIGURES

LIST OF FIGURES (CONT.)

LIST OF FIGURES (CONT.)

LIST OF TABLES

1 INTRODUCTION

1.1 HDR Test Facility and Containment Building

The HDR (Heiss-Dampf Reaktor) facility, shown in Figure 1.1, was the containment building for a decommissioned, experimental reactor in Germany. The building, while smaller in volume than a typical US containment building, contained many features which made it valuable for use in a containment research program. Many of these features also make it extremely valuable as a generic source of test data for industrial facilities. The building was a cylinder approximately 20 m in diameter by 50 m in height topped by a 10 m radius hemispherical dome for a total facility height of 60 m. Internally the building was divided into eight levels with each level further subdivided into smaller compartments. For a typical HDR test approximately 60-70 compartments were available. Compartments were connected by a variety of flow paths which included doorways, pipe runs, cable trays, hatches, and staircases. Three fixed and two adjustable vertical channels were provided for in the form of an elevator shaft, two staircases, and two sets of equipment hatches running the axial length of the building which could be opened or closed to change the available vertical flow path at each level. Much of the original equipment from the nuclear steam supply system was still present in the facility including the reactor vessel, primary and secondary piping, pumps, electrical connections, and ventilation and exhaust systems. The total free volume of the facility was 11,000 m^3 of which the dome contained 4,800 m^3 above the operating deck. The HDR containment, its compartments, and internal structural materials, vent flow openings and other pertinent data are documented in [1].

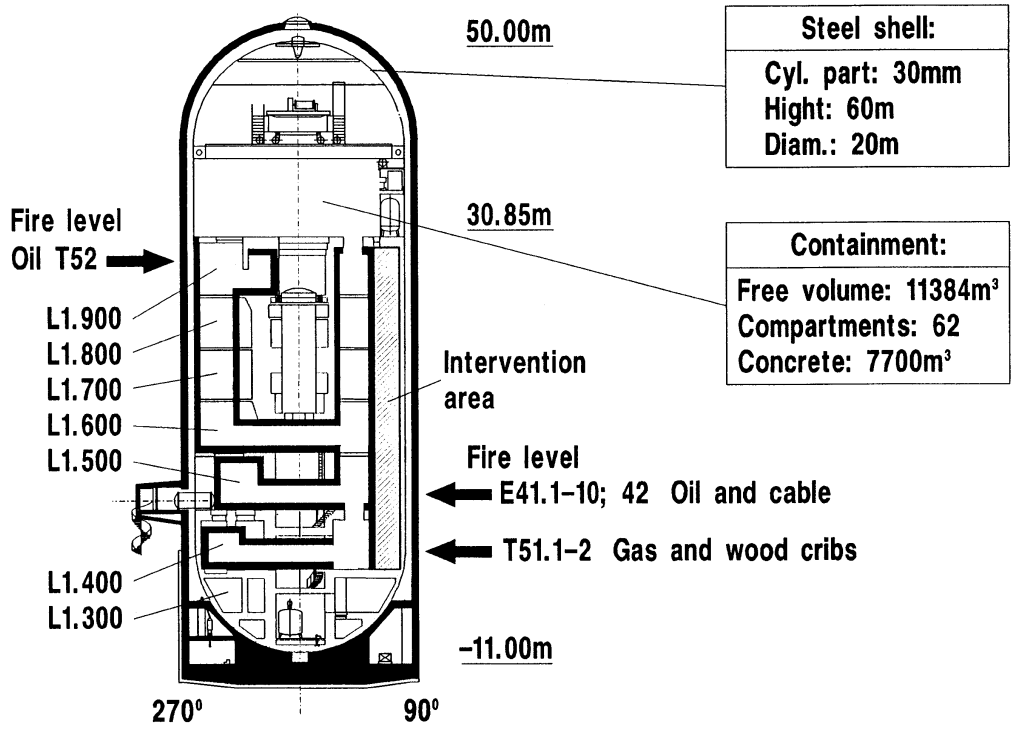

Figure 1.1: HDR Facility and Fire Test Group Locations

1.2 Summary of Fire Test Matrix

From 1984 to 1991 a total of four test series divided into seven fire test groups were performed inside the HDR facility. The fire tests consisted of the T51 series, six propane gas tests, three wood crib tests, and five more propane gas tests; the T52 series, four hydrocarbon oil pool tests; the E41 series, ten hydrocarbon oil pool tests; and the E42 series, three cable fire tests. Figure 1.2 shows the overall test matrix and range of fires powers tested and Figure 1.1 shows the locations of the various test series inside the HDR facility. Each test series was performed at a different location inside the containment building as indicated.

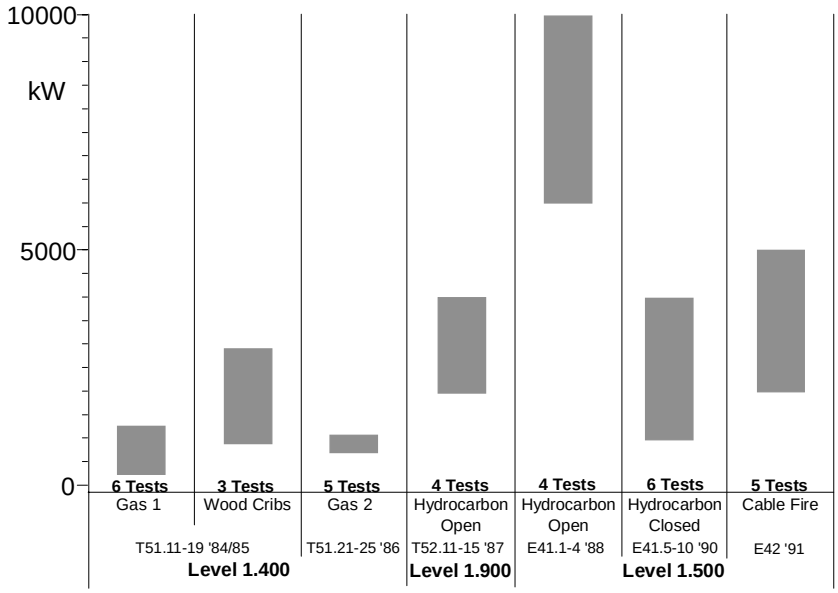

Figure 1.2: Fire Test Group Summary

The fire tests were performed with the following general objectives:

- An improvement in the general understanding of fire phenomena including smoke and aerosol production, distribution, and removal; temperature and pressure changes; and transient combustion in a large-scale building.
- A better understanding of the effects of boundary conditions on fire phenomena.
- The creation of a large database for fire model and fire computer code validation.
- An increase in the ability to plan for successful fire fighting and rescue operations inside a burning high-rise structure.

The multi-level, multi-compartment structure of the HDR facility with its vertical shafts, large dome, and concrete and steel construction means that subsets of the fire test database have applications outside the nuclear industry. In general the fire test data can be used to gain insight on many industrial and commercial facilities as most share basic HDR features such as being a multilevel, steel and concrete structure with ventilation systems. More specifically, data from the large dome can be applied to hangars and atrium spaces. Data from the vertical shafts can be applied to any facility containing elevators, large vertical pipe channels, etc.

Each individual test series had its own specific objectives, which have been specified in the respective test series Design Report containing all pertinent geometric data, initial and boundary conditions, instrumentation plan, test procedures, and summary descriptions of the computer codes that participated in the pre-test and post-test computations. Data Reports were issued right after the experiments were performed and contained corrections/modifications of test procedures, qualification of the sensor operability and quality as well as all measured data in plots. All documented data have been stored on the PHDR data bank with the same format and sensor descriptions as used in all other HDR safety research experiments. Quick Look reports present and interpret the data according to the test series objectives and the associated physical phenomena. In addition to the presentation of the data of the individual experiments, results across the test series are documented. Moreover, Quick Look reports contain the comparisons between data and blind pre-test computational results by different models and codes used by the respective group of national and international participants. The Final Evaluation report documents all data assessments from the test series together with final conclusions and open issues. In addition, it contains the comparisons between data and open post-test predictions and identifies the learning effect, model and code improvements observed, lists remaining discrepancies, and open modeling issues. It is the final document for the test series. Section 10 lists all relevant documentation cited above for the respective HDR fire test series. The respective reports will be referenced where applicable in Section 1.3, which summarizes the fire tests.

The T51 test series, performed at the 1.400 level in the lower portion of the containment, was designed to be a relatively low power, exploratory test series in order to determine basic parameters of fire phenomena inside the facility [2-10]. The temperature changes inside of the fire room and the spread of smoke through the building and building ventilation systems was examined to determine safety margins for future, higher powered tests.

The T52 test series, performed just below the operating deck, was designed to simulate a large cable fire through an equivalent oil fire [11-13]. The effects of ventilation systems on smoke movement was examined to assess rescue and fire fighting techniques. One major objective was to measure the plume behavior from the fire into the dome.

The E41 test series, performed in the level above the one for the T51 test series, incorporated experiments that spanned the total range of fire powers examined in the HDR facility [14-20]. Additional parameters examined during this fire test series were the effects of opening and closing doors to the fire room, filter loading rates, and the effects of fire suppression systems.

The final test series, E42, was performed at the same level as the E41 tests. The tests, consisting of cable fires, were to collect data on the burning of prototypical cables in cable trays under natural convection conditions [21-25]. The fires took place in a completely isolated set of subcompartments to prevent the spread of toxic combustion products, namely dioxin, resulting from the burning of the PVC insulation. A primary objective of these tests was to monitor the propagation of the fire through racks of cable trays in various orientations and to closely examine the spread and impact of combustion products.
Initially, the HDR fire tests were designed, performed, and evaluated solely by the Project HDR at the Nuclear Center Kalrsruhe, German universities, industry, and research labs. However, the

international nuclear community quickly realized the value of these tests [10], which resulted in international support, cooperation, and participation throughout much of the fire testing program at the HDR. Reflecting this is the fact that one of the E42 tests was selected to be a Commission of European Community (CEC) Standard Problem for the evaluation of computer fire models [24,25].

1.3 Overview of Individual Fire Test Series

With the large variety of fire experiments performed in the HDR over many years, it is important to see where any one particular set of tests fits into the overall database of information. To this end a brief description of each of the fire test groups follows.

1.3.1 Gas Fire Tests (T51.11-T51.15, T51.19, and T51.21-T51.25)

The gas fire tests, the T51 test series [2-10], were the first set of fire experiments performed in the HDR facility, and they are the subject of Volume 1 [33] as well as Volume 2 [34] of the report series under this grant. A total of 14 tests were executed between 1984 and 1985. These tests consisted of three subgroups of five gas fires, a single gas fire performed at the end of the wood crib test series [5], and five additional gas fires [6-8,10]. The tests all took place in a specially constructed fire room on the 1.400 level, shown in Figure 1.3, of the HDR facility. This fire room was connected to a hallway which terminated under a vertical shaft formed by open maintenance hatches. Each experiment followed a similar test plan of a short period of pre-fire data collection to record initial conditions, followed by an hour long fire, and ending with approximately half an hour of cool down data collection. The fuel for each of the test was propane gas intended to be premixed with 10% excess air drawn from a vent in room 1.603. For the first group of gas fire tests no ventilation systems other than the air supply for the gas burners was employed. For the second group of gas fire tests a vent was constructed which connected the fire room to the 1.600 level. The vent had an adjustable damper which could be controlled during an experiment to change the size of the vent opening.

This first test series had a number of primary objectives. The foremost objective was to demonstrate that fire tests could be performed safely inside the HDR containment building as the integrity of the structure was still regulated as a nuclear facility. Another objective was to determine the extent to which the fire would involve the building in its entirety. A further objective was to examine the ability of the ventilation systems to remove smoke and other fire products. Lastly, data collected during the tests would serve as a initial data for computer code evaluation.

The gas fire tests contain a number of characteristics which pose different challenges for fire code models. These are:

- The fire room is not a rectangular parallelepiped. The floor cross-section is L-shaped as can be seen in Figure 2.1 of Section 2. This geometric irregularity acts to impede some of the mixing that would otherwise occur in a symmetric compartment.
- The fire source is not a single location on the floor in the center of the room. Rather, there are six gas burners mounted on the wall 0.375 m off the floor along the L-side of the rooms length. Therefor the fire cannot be truly considered a point or local area source for the purpose of

evaluating mixing and entrainment using common zone model approaches. Also the presence of the wall that the burners are mounted on prevents the formation of a typical, axi-symmetric plume that is assumed in many fire models.

- The number and selection of burners used varied depending on fire power.
- The doorway of the fire room is located at a corner, rather than at the center of one of the room's walls. As with the shape of the room and the location of the fire source this affects the mixing that takes place inside the fire compartment.
- The hallway from the fire room terminates in a subcompartment with a narrow vent, 0.5 m high, along the floor and a ceiling vent to a shaft leading to the hemispherical dome. Therefore, a fire model must be capable of handling a large ground level airflow as well as a separate, large buoyant plume in the same compartment.
- The hallway from the fire room is not a rectangular parallelepiped. It is a volume of revolution, a rectangle slowly increasing in width rotated at a fixed distance about an axis.

Table 1.1 on the next page contains a brief summary of the major characteristics of the gas fire tests. Figure 1.3 shows a top view of the fire floor.

Table 1.1: Gas Fire Test Series Summary

Test	Fire Power (kW)	Gas Consumption (m^3)	Ventilation and Other Test Execution Comments	Burners Used
T51.11	229	8.82	All run with the same configuration with only fire power changing	Burner 3
T51.12	380	14.63		Burners 2,3
T51.13	692	26.62		Burners 2,3,4,5
T51.14	1,025	39.44		Burners 1,2,3,4,5
T51.15	380	14.62	T51.12 with closed vent between 1.600 and 1.700	Burners 2,3
T51.19	1,255	48.30	Increased number of sensors Uses Wood Crib sensor map	Burners 1,2,3,4,5
T51.21	716	27.55	Changes in sensor map Repeat of test T51.13 with vent to 1.600 closed	Burners 1,2,5,6
T51.22	715	27.55	30 minutes with vent 100% open 15 minutes with vent 75% open 15 minutes with vent 25% open	Burners 2,3,4,5
T51.23	1,011	38.98	Repeat of test T51.14 with vent to 1.600 closed	Burners 1,2,3,4,5
T51.24	951	36.58	30 minutes with vent 100% open 15 minutes with vent 75% open 15 minutes with vent 25% open	Burners 1,2,3,4,5
T51.25	985	37.91	30 minutes with vent 100% open 30 minutes with vent closed	Burners 1,2,3,4,5

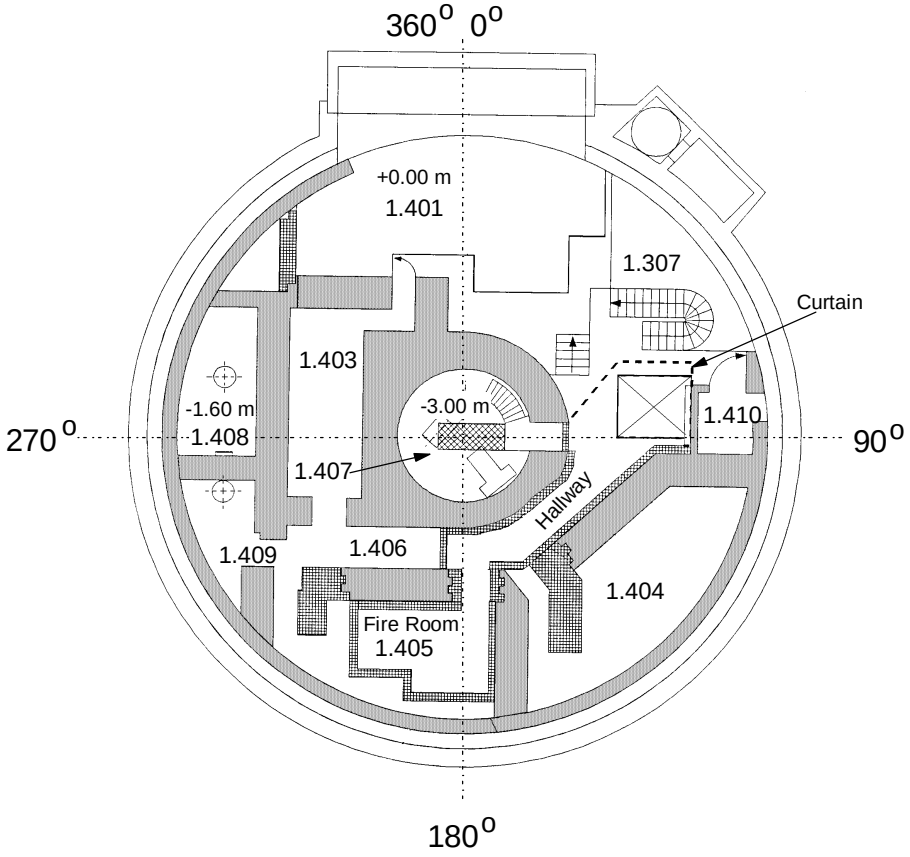

Figure 1.3: Level 1.400, Fire Floor for the T51 Tests

1.3.2 Wood Crib Fire Tests (T51.16-T51.18)

The wood crib tests were part of the T51 series of experiments [5,8,9]. The wood crib tests, while not a fuel typically available in a nuclear power plant, were added for the benefit of the fire community which does use wood cribs as a standard fire load. Three separate tests of increasing fire power were executed. The tests took place in the same fire room as the gas fire tests. Each test consisted of burning one or more cribs made up of 30 cm x 4 cm x 4 cm beams of pine containing 8% humidity. The beams were nailed together into 15 layers of 4 beams each with adjacent layers having a 90° rotation of the beams, Figure 1.4 shows the construction of a wood crib. A 300 ml reservoir of mineral spirits was used to start the ignition of the wood cribs which were allowed to burn uncontrolled. Electronic scales underneath the wood cribs were used to determine the time-dependent burning rate for use as input functions for the computer code simulations. As compared to propane gas which burns relatively smokeless, these wood crib tests were performed with the main purpose of evaluating the response of the HDR facility and ventilation systems to heavy loadings of smoke in an effort to determine safety margins for future oil fires. The wood crib fires lasted on the order of 30 minutes. Table 1.2 gives some additional details on the wood crib tests.

The wood crib tests produced large quantities of smoke which were quickly distributed throughout the whole containment. This smoke overloaded the building ventilation system's HEPA filters and

resulted in adjusting the testing schedule to accommodate the longer time required to clean the containment atmosphere between tests. The smoke was corrosive to the test equipment of other experiments, and some instrumentation was damaged. The smoke deposits of the HDR surfaces also proved difficult to remove, with success only occurring in cleaning of metal surfaces.

The wood crib fire test results and CFAST computations have been reported in Volume 3 [37] of the report series under this grant.

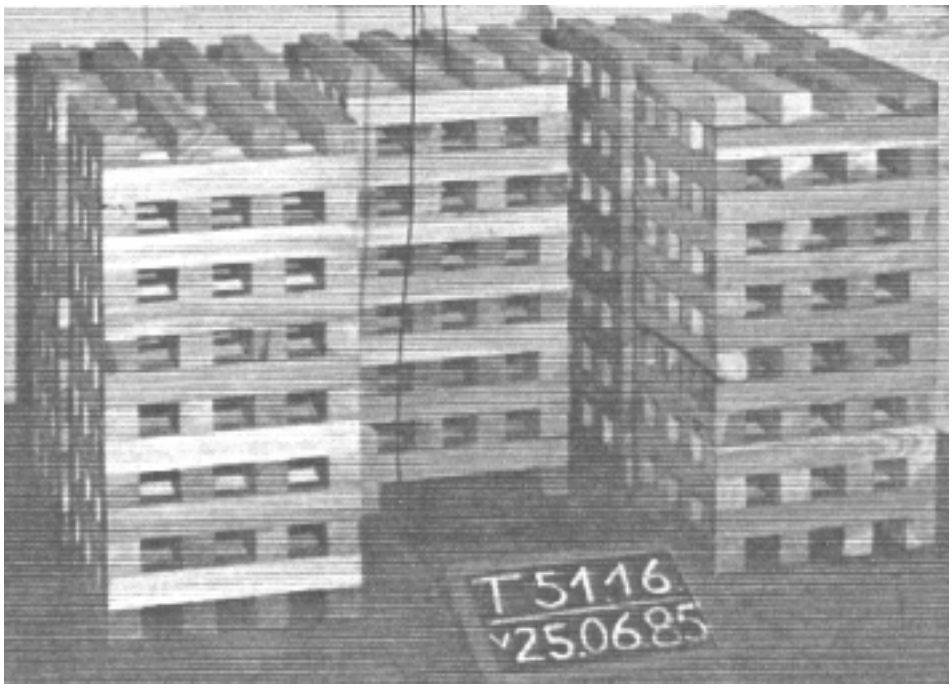

Figure 1.4: Wood Crib Construction

Table 1.2: Wood Crib Fire Test Series Summary

Test	Fire Power (kW)	Wood Consumption (kg)	Ventilation and Other Test Execution Comments
T51.16	1,000	79 (5 cribs)	Start of Wood Crib sensor map. Fires were naturally ventilated and natural convection conditions existed in the containment.
T51.17	1,500	109.8 (7 cribs)	Increase in fire load.
T51.18	2,300	169.1 (11 cribs)	Further increase in fire load.

1.3.3 Oil Fire Test Summary (T52)

The second test series of fire experiments was the T52 oil fire test series which consisted of four oil pool fire tests performed in 1986 [10-14]. The tests ranged in power from two to four megawatts with the fire lasting approximately 30 minutes. Whereas the previous test series, the gas and wood fires, were performed at a level low in the containment building it was decided to position this test series high up in the containment building as shown in Figure 1.1. Thus, the fires were positioned in a special fire compartment constructed on the 1.900 level, the level just below the operating deck. It was anticipated that this would confine smoke and soot to the dome region. The fire compartment, shown in Figure 1.5, was located such that it vented directly into the dome through the maintenance hatch next to the spiral staircase. Fuel for the fires consisted of an initial volume of oil in a pool with a surface area ranging from 1 m^2 to 3 m^2 in size.

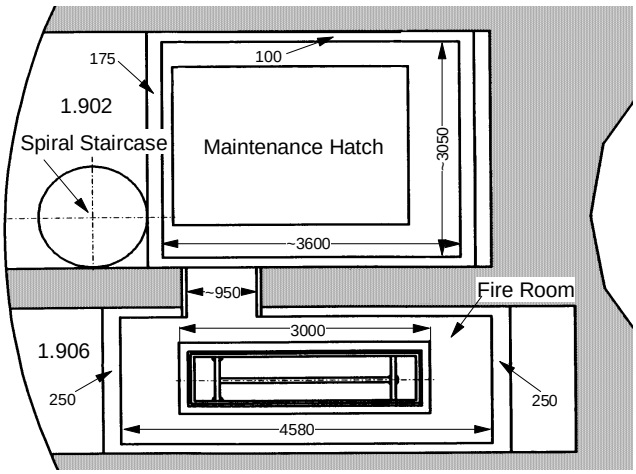

Figure 1.5: T52 Oil Fire Compartment

The initial amount of fuel was augmented by a nozzle feeding a continuous supply of oil once the initial pool was consumed. Each fire lasted approximately 30 minutes. Oxygen for the fires was supplied by natural convection alone.

For this test series special attention was paid to the buoyant fire plume entering the upper dome. Two-dimensional grids of thermocouples and other sensors were placed at two axial levels within the plume to aid in determining the plume's evolution in the dome.

In addition to the generic purposes of improvements in knowledge about fire dynamics in a complex structure this test series introduced the concept of selective pressurization of test compartments for the prevention of smoke entry in rescue/intervetion areas. For this test series the elevator shaft next to the main staircase, see Figure 1.1, was pressurized and monitored to determine if selective pressurization was indeed capable of maintaining the entire shaft as a relatively smoke free area for the purpose of evacuation or for the staging of emergency personnel.
Some of the significant results are noted below:

- The fires quickly reached flashover conditions, turning the fire room into a large fire ball with heavy soot production.
- As the fire vented directly into the upper dome a large buoyant plume formed whose basic characteristics were measured.
- The large buoyancy forces of the plume rising through the maintenance hatch behaved like a jet pump; that is large quantities of air were entrained into the plume which resulted in a large global circulation inside of the entire facility which widely spread the soot throughout the whole building.
- Provided a sufficient air flow rate was used, the selective pressurization strategy was successful in keeping the elevator shaft free of smoke.
- Due to the high entrainment, fire plume temperatures directly impinging on the containment steel shell at higher elevations were rather low.

Table 1.3 below summarizes some details on the T52 tests.

Table 1.3: T52 Oil Fire Test Series Summary

Test	Peak Fire Power (kW)	Pool Size (m^2)	Initial Fuel Volume (liters)	Fuel Delivery Rate (liter/min)
T52.11	2,000	1	25	3.72
T52.12	3,000	2	50	5.57
T52.13	4,000	3	75	7.43
T52.14	3,500	2	50	5.57

The description and evaluation of the T52 series test data and the development of pertinent CFAST models and their comparisons with the data are the subjects of this report, Volume 4, in the report series under the grant. The main author's Ph.D. Dissertation ideally supplements and expands upon the contents of this present report.

1.3.4 Oil Fire Test Summary (E41)

The T52 test group indicated that both higher power and longer duration tests could be withstood by the HDR facility. A further set of oil fires, the E41 test group [14-20], was performed to take advantage of this. This test group, which consisted of ten tests ranging in power from six to ten megawatts, took place on the 1.500 level of the containment building. As with the other test groups a specially prepared fire compartment was used for this series. This compartment, shown in Figure 1.6, was significantly larger than compartments for the other tests and included sprinkler systems, ventilation systems, and a remotely operated doorway. For this test series the building ventilation systems were equipped with different types of filter setups. Furthermore, autonomous, aerosol measurement devices were added to the sensor equipment.

The addition of extra features to the fire room and ventilation system allowed the examination of some additional fire phenomena. Filter loading and clogging was examined through the use of the different filter systems. The effects of steam release into the fire room was examined. The

interrelationships of doorway openings and mechanical ventilation were explored. The selective pressurization strategy was examined further. Tables 1.4 and 1.5 provide details on this test group. Note that each test in the latter portion of this test series actually consists of a series of individual subtests.

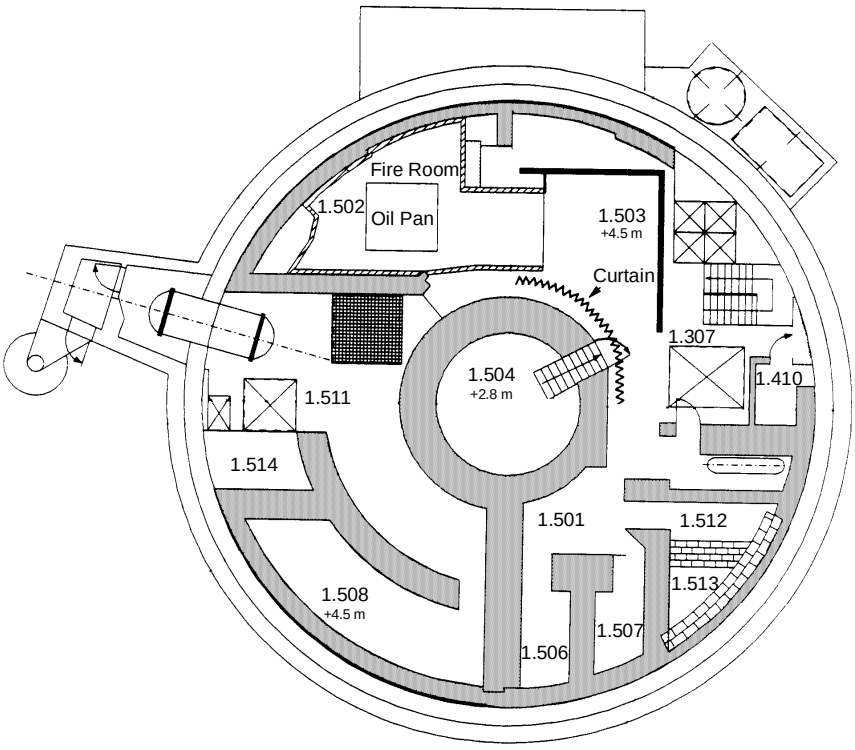

Figure 1.6: E41 Oil Fire Compartment

Some of the significant results of this test group are given below:

- Fire extinguishing systems were tested under extreme conditions of fire power and temperature due to the high fire powers, as high as 10 MW, in the fire compartment.
- Spatial and temporal distributions of aerosols were measured at different locations.
- Depending on the ventilation system settings a variety of flow circulation modes were observed inside the containment building.
- Selective pressurization of the elevator shaft was again successful in preventing smoke from entering this rescue shaft.
- Filters continued to become overloaded with soot even when a prefiltered bank consisting of coarse filters was added to the filtration system.

Table 1.4: E41.1-10 Oil Fire Test Series Summary

Test	Pool Size (m^2) and Pool Wall Material	Fuel Volume* (l)	Max Power (kW)	Fire Duration (min)
E41.1	3 (steel)	224	7,055	17
E41.2	2 (steel)	150	4,016	20
E41.3	2 (steel)	224	4,798	25
E41.4	2 (steel)	224	5,452	22
E41.5	2 (steel)	20	850	78
E41.6	2 (steel)	60	4,250	68
E41.7	2 (steel)	40	5,100	65
E41.8	2 (steel)	40	3,400	74
E41.9	1.7 (concrete)	48	4,250	43
E41.10	1.7 (concrete)	40	2,550	50

*For tests E41.5-10 the fuel volume represents the initial pool volume.

Table 1.5: E41.5-10 Oil Fire Test Subsection Summary

Test	Subsection	End Time (min)	Fuel Addition (kg/s)	Door
E41.5	E41.51a	5	Initial Volume	Closed
	E41.51b	20	0.01	Closed
	E41.52	35	0.01	Closed
	E41.53	50	0.02	Closed
	E41.54	65	0.05-0.07	Closed
	E41.55	90	0.07	Door 1,45°
E41.6	E41.61	15	Initial Volume	Closed
	E41.62	30	0.01	Door 1,45°
	E41.63	45	0.02	Door 1,45°
	E41.64	60	0.02	Door 1 Open
	E41.65	75	0.01	Both Open
	E41.66	80	None	Both Open
E41.7	E41.71	15	Initial Volume	Closed
	E41.72	30	0.1	Door 1 Open
	E41.73	45	0.02	Closed
	E41.74	60	0.1	Both Open
	E41.75	75	.03-.05	Door 1 Open
	E41.76	90	.03-.05	Door 1, 45°
E41.8	E41.81	15	Initial Volume	Both Open
	E41.82	30	0.1	Both Open
	E41.84	45	0.1	Door 1 Open
	E41.84	60	0.03-0.05	Door 1 Open
	E41.85	75	0.03-0.05	Door 1 Open
	E41.86	90	None	Closed
E41.9	E41.91	15	Initial Volume	Both Open
	E41.92	30	0.1	Both Open
	E41.93	45	0.1	Door 1 Open
	E41.94	60	0.05-0.07	Closed
	E41.95	75	0.01	Closed
	E41.96	90	None	Closed
E41.10	E41.101	15	Initial Volume	Closed
	E41.102	30	0.05	Door 1 Open
	E41.103	45	0.03	Closed
	E41.104	60	0.05	Door 1, 90°
	E41.105	75	0.05	Closed

1.3.5 Cable Fire Test Summary (E42)

The cable fire test group was the last set of fire experiments performed in the HDR and had the primary purpose of evaluating the effects of a prototypical fire using real fuel sources, e.g. the electric power and instrumentation cables used in power plants [21-25]. Due to concerns of dioxin production from the PVC cable insulation, this test group was performed in an isolated subset of compartments on the 1.500 level which is shown in Figure 1.7. Additional partitions and ventilation and fire extinguishing systems were constructed on this level to prevent the spread of toxic combustion products through the rest of the facility and into the local environment. Three tests involving different amounts and types of cables were performed. It is important to note that the fire compartments were completely sealed for the duration of this test series which created problems in determining the exact fuel source available or consumed during any given test. As shown in Figure 1.8, before the first test, E42.1, many of the cable trays were wrapped in Alsiflex mats in an attempt to prevent the combustion of those cables during the first test. Attempts were made to isolate specific cable trays from burning by covering some of the cable trays in Alsiflex blankets which could be removed for other tests. The blankets did not completely prevent combustion of the protected cables; that plus a lack of information on the fraction of exposed cables which completely burned results in an uncertainty in specifying the exact fuel source available and consumed during each test.

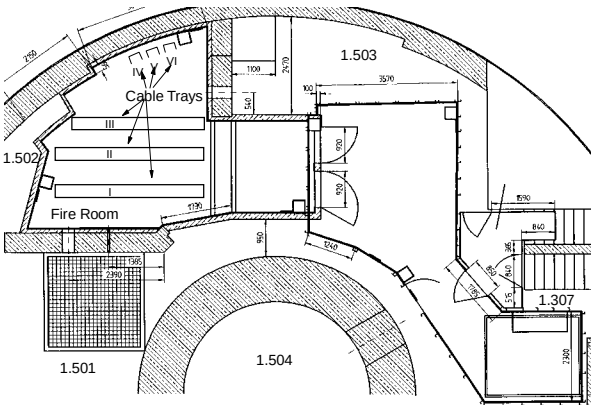

Figure 1.7: E42 Cable Fire Room

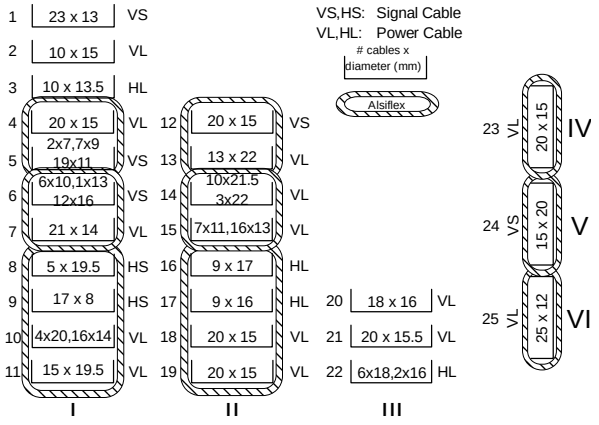

Figure 1.8: Cable Tray Layout

Some of the important results from the E42 test series are given below:

- Depending on the particular configuration of available cables the cables fires were either self sustaining to the point of flashover or burned out after a short period of time.
- Dioxin production from the PVC insulation was not detectable/measureable.
- The fires were capable of becoming intense enough to burn the cables underneath the Alsiflex blankets.
- The presence of the blankets actually acted to prolong fires as they prevented water from the sprinklers from reaching the cables under the blankets.

2 FACILITY DESCRIPTION

2.1 Compartment Layouts for the T52 Oil Fire Tests

2.1.1 Fire Floor (Level 1.900)

The T52 test series was performed with the fire room, R1.906, located at the 1.900 level (see Figure 1.1 for the location), immediately below the dome floor (+ 25.0 m), to simulate a postulated cable fire in the area above the RPV. The fire room was relatively small and was located adjacent to the spiral staircase and the maintenance hatch. The maintenance hatch (1.902) located directly outside of the fire room exit provided connections between each containment levels from the 1.600 level to the reactor dome as shown in Figure 1.1. The maintenance hatch had a cross-section of 1.85 m x 2.60 m at both its inlet and its outlet. Figures 2.1 shows a cross-section view of the 1.900 level and indicates the location of the fire room in that level. Figures 2.3 and 2.4 show respectively a vertical cross-section and a horizontal cross-section of the fire compartments in the 1.900 level and gives details on the compartments' dimensions. Table 2.1 below summarizes the geometric data of the fire room and the neighboring compartments.

Table 2.1: Fire Compartment Dimensions

Compartment	Height (m)	Floor Surf. Area (m^2)	Volume (m^3)	Hatch Openings (m^2)
Fire Room	2.800	4.5x1.75=7.88	23.63	n/a
Doorway	3.000	0.95x0.78=0.74	2.22	n/a
Maintenance Hatch	n/a	n/a	51.54	1.85x2.6=4.81

As with the T51 test group, there was concern about damaging the HDR structure in the fire compartments from the intense heat expected during the fires. To avoid damaging the building structures, Ytong fire bricks were used to shield the walls of the fire room in a similar manner as for all previously performed HDR fire experiments. The floor, back and front walls, and ceiling of the fire room were lined with a 25 cm-thick layer of Ytong bricks, whereas the side walls were lined with a 10 cm-thick layer of Ytong bricks. The ceiling and the walls, which would be exposed directly to the fire plume, had additional protection in the form of a 3 cm-thick layer of Alsiflex, a ceramic fabric, fire resistant matting. The walls of the doorway region were covered only with 3 cm-thick Alsiflex since a thick brick layer would have reduced the available flow area too much.

The steel shell of the HDR containment can maintain its structural integrity up to a maximum temperature of 155 $^{\circ}$C. In order to preserve the structural integrity of the steel shell against the direct impact of the fire load, a 17.5 cm-thick Ytong brick wall was installed to separate the maintenance hatch from the spiral staircase. Also, the side walls of the hatch area were protected with a 10 cm-thick layer of Ytong bricks, and the ceiling of the hatch area was covered with a 2 cm-thick layer of Promatec plates. Furthermore, the temperatures in the vicinity of the steel shell from the 1.900 level to the dome region were continuously monitored especially in the region of the direct contact with the hot gas plume. As an additional safety measure for protection of the

steel shell, a video camera which continuously monitored the fire room and the maintenance shaft was installed.

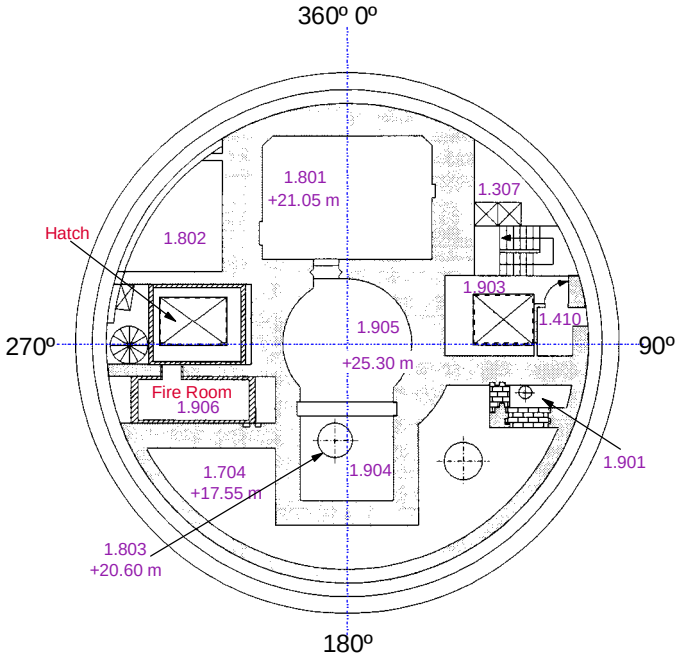

Figure 2.1: Fire Floor at Level 1.900 for T52 Oil Pool Tests

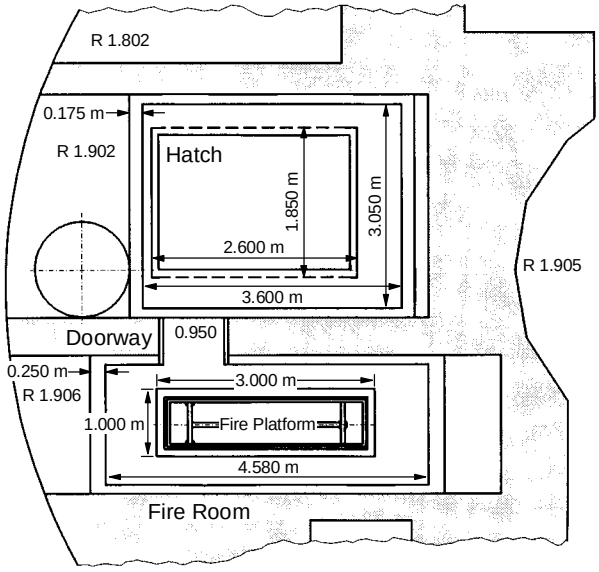

Figure 2.2: Fire Compartments Top View

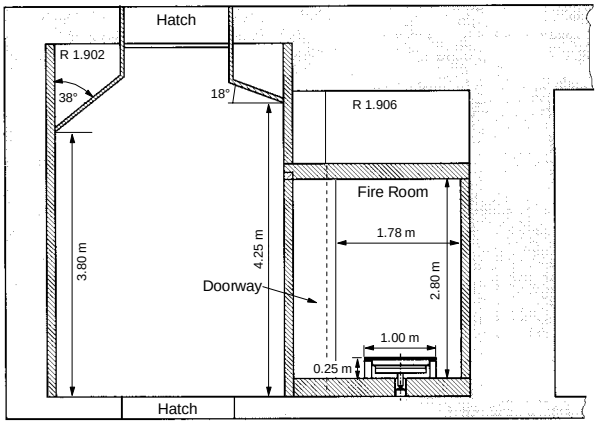

Figure 2.3: Fire Compartments Side View

The oil pool platform was located in the center of the fire room, equipped with a weighing scale to determine the oil's burning rate. A total of three force measurement sensors were used underneath a weighing plate for the weighing scale. The scale plate was insulated with three layers of insulating materials to protect the measurement sensors from the high temperatures of the fire. Two layers of Promalan HT 400 with an intermediate layer of Promasil 1060 where used

to protect the surface of the scale plate, see Figure 2.4. The sides of the platform were protected by a wall of 10 cm-thick Ytong firebrick. On the fire room floor beneath the scale, two flat water cooled heat sinks (0.800 m x 0.826 m) were installed for further protection of the scales from the energy transport by radiation from the oil pool pan, see Figure 2.5.

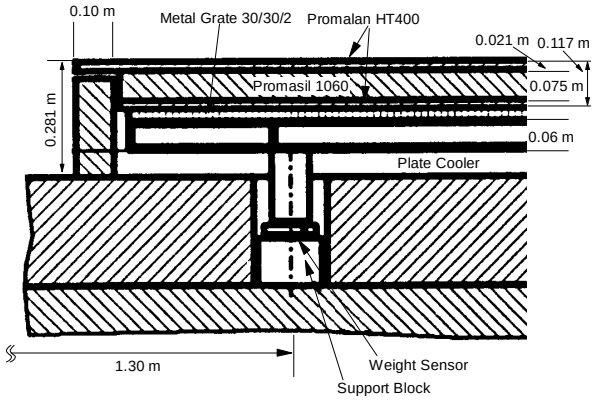

Figure 2.4: Oil Pool Platform Side View

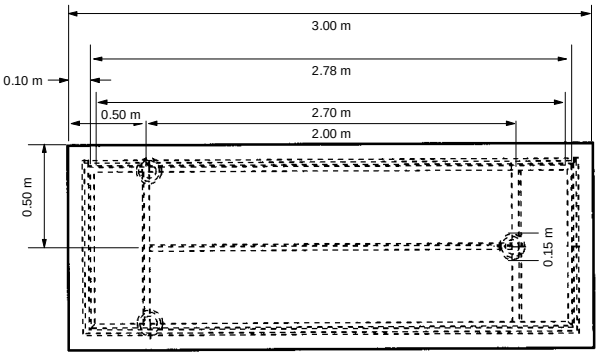

Figure 2.5: Oil Pool Platform Top View

In order to allow for different fire loads for the different subtests, T52.11 through T51.14, three different oil pans were constructed for placement on the oil pool platform as shown in Figure 2.5. The pan surface area utilized for each test can be found in Table 2.2. The oil pool pans were made of steel and positioned in the center of the oil pool platform.

Table 2.2: Measurements of the Oil Pans for T52 Test Series

Test	Length (m)	Width (m)	Surface Area (m^2)	Height (m)
T52.11	1	1	1	0.2
T52.12	2	1	2	0.2
T52.13	3	1	3	0.2
T52.14	3	1	3	0.2

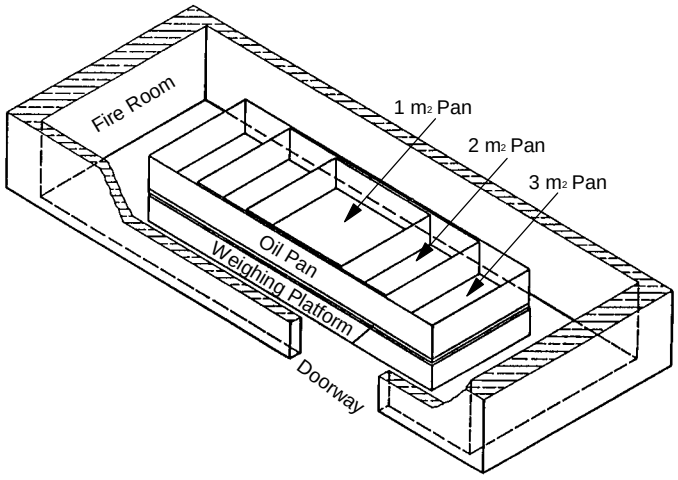

Figure 2.6: Oil Pan Configurations for T52 Test Series

2.1.2 Facility Remainder

The following two tables, Tables 2.3 [1,26-27] and 2.4 [1,26-28], document the volumes of the different compartments in the HDR facility as well as the sizes of the major room interconnections available during the gas fire tests. Details of the layout of the HDR compartments can be located on the instrumentation maps shown in Section 3.

Table 2.3: HDR Compartment Volumes

Compartment Number	Volume (m^3)	Elevation (m)	Height (m)	Comments
1.201	152	-8.50	1.80	
1.202	4	-9.20	0.50	
1.203	4	-9.20	0.50	
1.303	70	-8.50	5.30	
1.301	206	-5.80	5.30	
1.302	93	-5.80	3.60	
1.304	39	-5.80	3.60	
1.305	43	-4.80	4.60	
1.311	20	-4.80	4.60	
1.307	58	-5.80	4.10	Main staircase level 1.300
1.308	102	-5.80	3.60	
1.317	63	-1.10	5.45	Main staircase level 1.400
1.327	61	4.50	5.25	Main staircase level 1.500
1.337	40	10.00	4.80	Main staircase level 1.600
1.347	83	15.05	4.70	Main staircase level 1.700
1.357	40	20.60	4.65	Main staircase level 1.800
1.367	82	25.30	5.30	Main staircase level 1.900
1.401	296	0.00	4.10	Not open for T52 test series.
1.403	76	-1.10	4.60	
1.404	116	-1.10	4.60	
1.405	95	-1.10	4.60	
1.406	266	-1.10	4.60	
1.407	84	-3.00	5.00	
1.408	59	-1.60	4.60	
1.409	37	-1.10	4.60	
1.410	113	-2.60	39.90	Elevator shaft. Not open for T52 test series.
1.501	60	4.50	4.50	
1.506	24	4.50	4.50	
1.507	19	4.50	4.50	
1.512	28	4.50	4.50	
1.502	107	4.50	4.50	
1.503	304	4.50	5.25	

Compartment Number	Volume (m^3)	Elevation (m)	Height (m)	Comments
1.504	57	2.80	3.40	
1.505	10	4.50	4.50	
1.508	57	4.50	4.50	
1.511	222	4.50	5.00	
1.513	8	3.50	8.80	Not open for T52 test series.
1.514	13	4.50	5.00	
1.602	61	10.00	4.75	Not open for T52 test series.
1.603	280	8.70	7.70	
1.604	25	10.00	3.25	
1.605	78	7.40	4.70	
1.606	183	10.00	4.60	
1.607	42	10.00	3.40	
1.608	45	10.00	3.40	
1.609	59	10.00	4.75	Not open for T52 test series.
1.611	192	10.00	4.75	
1.701u	64	13.85	3.90	
1.701o	44	20.60	2.50	
1.702	54	15.05	4.20	Not open for T52 test series.
1.703	83	15.05	4.20	
1.704	793	14.25	15.60	
1.901	12	25.00		
1.706	19	15.05	4.20	Not open for T52 test series.
1.707	119	15.05	4.20	
1.708	90	15.05	5.35	
1.801	343	21.05	9.80	
1.802	125	20.60	7.10	
1.804	79	20.60	5.00	
1.805	58	20.60	5.00	
1.902	90	25.30	4.50	
1.903	71	25.30	4.50	
1.904	78	25.30	4.60	
1.905	79	25.30	4.60	
1.803	7	20.60	4.70	
1.906	62	25.30	4.50	
Lower Dome	2,153	30.85	9.15	Cylindrical portion of dome
Upper Dome	2,660	40.00	10.00	Hemispherical portion of dome

Table 2.4: HDR Room Interconnections for the T52 Oil Pool Fire Tests

Connects		Type	Width (m)	Height (m)	Depth (m)	Comment	Connects		Type	Width (m)	Height (m)	Depth (m)	Comment
Room 1	Room 2						Room 1	Room 2					
1.201	1.202	C	0.2	0.2	1		1.201	1.203	C	0.2	0.2	1	
1.201	1.308	P	1	0.5	0.82	2 of these	1.201	1.301	P	0.45		0.7	Width is diam.
1.201	1.301	P	0.35		0.8	Width is diam.	1.201	1.301	W	0.1	0.9	0.1	
1.202	1.302	P	0.28	0.51	4	Min. opening	1.203	1.305	P	0.28	0.56	4	Min. opening
1.301	1.302	W	0.1	0.15	0.5		1.301	1.302	P	0.3	1	11.9	Min. opening
1.301	1.302	P	0.1	0.4	5.2		1.301	1.303	P	0.5	0.5	1.2	2 of these
1.301	1.308	W	1.27	1.77	1.15		1.301	1.408	W	1.2	1	0.35	
1.302	1.308	B	0.1		0.5	Width is diam. 22 of these	1.302	1.308	D	0.66	1.97	0.6	Min. opening
1.302	1.408	P	1.1	0.6	0.54	2 of these	1.302	1.408	P	0.7	0.6	0.54	
1.302	1.408	P	1.3	0.6	0.54		1.302	1.409	B	0.13		0.6	Width is diam. 2 of these
1.302	1.502	P	0.93		5	Width is area (m^2)	1.303	1.308	B	0.1		1.29	Width is diam. 22 of these
1.303	1.308	D	1.9	0.96	1.02	Min. opening	1.303	1.407	P	0.9	0.55	0.81	Min. opening
1.303	1.407	P	0.3	1.45	0.8		1.304	1.305	P	0.32	0.54	0.4	
1.304	1.305	W	2.5	3.73	0.43		1.304	1.308	D	0.56	1.9	1	Min. opening
1.304	1.308	O	1.2	2	0.4	Min. opening	1.305	1.308	W	1.52	2	0.4	Min. opening
1.305	1.308	D	0.55	1.98	0.48	Min. opening	1.308	1.404	P	2.1	0.7	1.05	
1.307	1.317	S	1.8			Width is area (m^2)	1.402	1.403	D	0.54	1.82	2.8	Min. opening
1.403	1.406	W	0.5	1.21	1.05	1.4	1.403	1.406	P	1	1.2	2.18	
1.403	1.511	W	2.3	2.3	1	1.4	1.403	1.406	C	0.4	0.25	0.8	
1.404	1.507	0.07			1.05	Width is area (m^2)	1.405	1.406	W	2.72	1.9	1.05	
1.406	1.409	D	0.56	1.9	1		1.406	1.501	P	3.35			Width is area (m^2)
1.407	1.504	C	0.19		1.89	Width is diam. 6 of these	1.408	1.502	P	0.4	0.84	1	
1.317	1.327	S	3.61			Width is area (m^2)	1.501	1.511	B	0.06		1.2	Width is diam.
1.502	1.503	B	0.08		0.5	Width is diam. 4 of these	1.501	1.606	P	2.55			Width is area (m^2)

Connects		Type	Width (m)	Height (m)	Depth (m)	Comment	Connects		Type	Width (m)	Height (m)	Depth (m)	Comment
Room 1	Room 2						Room 1	Room 2					
1.502	1.511	B	0.08		0.5	Width is diam. 7 of these	1.502	1.503	D	0.5	1.95	1.58	Min. opening
1.502	1.511	C	0.66	0.15	0.5		1.502	1.511	C	0.47	0.42	0.5	
1.502	1.611	P	0.7	2.2	0.5		1.502	1.603	P	0.8	0.7	5	Min. opening
1.503	1.511	W	1.08	3.67			1.503	1.504	D	0.96	2	1.15	Min. opening
1.503	1.605	C	0.27		2.9	Width is diam.	1.503	1.603	C	0.27		2.9	Width is diam.
1.504	1.605	W	0.08		1.2	Width is area (m^2)	1.503	1.605	C	0.16			Width is area (m^2)
1.506	1.508	W	0.95	1.5	1.22		1.505	1.607	W	0.12		1.06	Width is area (m^2)
1.508	1.511	D	0.55	1.92	0.1		1.507	1.608	P	0.41	1	1.05	
1.511	1.611	C	0.14		0.57	Width is area (m^2) 2 of these	1.501	1.606	M	4.54		0.57	Width is area (m^2)
1.327	1.337	S	3.2				1.603	1.605	W	0.3	0.67	1.3	
1.603	1.606	W	5.5		1.2	Width is area (m^2)	1.603	1.606	D/S	1.6	0.69	2.8	Min. opening
1.603	1.608	W	1	1	1.2		1.603	1.608	W	0.6	0.47	1.2	
1.603	1.704	C	1.7	0.5	1.4		1.603	1.704	W	1.64		0.15	Width is area (m^2)
1.603	1.704	W	1.8	2	4		1.603	1.704	C	0.39	0.4	1.9	Min. opening 3 of these
1.603	1.708	O	2	1.64	1.2	Min. opening	1.605	1.606	C	0.3		2.3	Width is diam. 5 of these
1.606	1.704	P	0.5	0.5	3	Width is diam. 5 of these	1.605	1.701u	B	1.37		2	Width is area (m^2) 2 of these
1.606	1.707	M	4.54		0.5	Width is area (m^2)	1.606	1.707	P	3.58			Width is area (m^2)
1.606	1.708	S	0.74		0.42	Width is area (m^2) Spiral stair	1.606	1.708	M	4.81		0.6	Width is area (m^2) Spiral stair
0.000	1.704	W	0.3	0.14	1.3		1.607	1.704	P	0.5	0.5	1.06	
1.611	1.703	C	0.25	1.74	0.56		1.608	1.704	C	0.4	0.4	1.9	

Connects		Type	Width (m)	Height (m)	Depth (m)	Comment	Connects		Type	Width (m)	Height (m)	Depth (m)	Comment
Room 1	Room 2						Room 1	Room 2					
1.701u	1.701o	W	1.7		3	Width is area (m^2)	1.337	1.347	S	3.39			Width is area (m^2)
1.701o	1.704	W	1.3	1.8	1.6	Min. opening	1.701o	1.704	P	0.7	0.48	1.75	Min. opening 2 of these
1.701o	1.704	C	0.6	0.6	1.6	2 of these	1.701o	1.704	B	0.52		1.75	Width is diam.
1.701o	1.804	C	0.4	0.6		Min. opening	1.701o	1.707	B	0.3		3	Width is diam.
1.703	1.707	D	0.84	2.01	0.28	Min. opening	1.701o	1.805	B	0.08		2	Width is area (m^2) 3 of these
1.704	1.804	P	0.79	0.6	2.27		1.704	1.707	D	2.09	0.62	2.37	Min. opening
1.704	1.901	W	0.8	0.6	0.8		1.704	1.805	B	0.25		1.24	Width is diam. 2 of these
1.704	1.904	B	0.55		1.25	Width is diam.	1.704	1.903	W	1.64		0.15	Width is area (m^2)
1.707	1.805	P	2.32			Width is area (m^2)	1.704	1.906	W	1.6		1.3	Width is area (m^2)
1.708	1.804	M	4.81		0.6	Width is area (m^2) Spiral stair	1.707	1.805	M	4.54		0.5	Width is area (m^2)
1.347	1.357	S	3.24			Width is area (m^2)	1.708	1.804	S	0.74		0.42	Width is area (m^2) Spiral stair
1.802	1.804	D	0.63	0.2	0.4		1.801	1.905	W	4.5			Width is area (m^2)
1.802	1.902	W	0.4	0.23	0.4		1.802	1.902	D	0.94	1.87	0.4	
1.804	1.902	M	4.81		0.6	Width is area (m^2) Spiral stair	1.805	1.903	P	2.32			Width is area (m^2)
1.802	Dome	W	0.4	1.2	1.52		1.804	1.902	S	6.73		0.42	Width is area (m^2)
0.000	1.367	S	3.24			Width is area (m^2)	1.805	1.903	M	4.54		0.5	Width is area (m^2)
1.902	Dome	W	0.4	0.2	0.4	2 of these	1.902	1.906	P	0.3	0.5	0.5	2 of these

Connects		Type	Width (m)	Height (m)	Depth (m)	Comment	Connects		Type	Width (m)	Height (m)	Depth (m)	Comment
Room 1	Room 2						Room 1	Room 2					
1.902	Dome	M	4.81		0.6	Width is area (m^2) Spiral stair	1.902	Dome	W	0.45	2.65	0.4	
1.903	Dome	P	2.32			Width is area (m^2)	1.902	Dome	S	6.73		0.42	Width is area (m^2) Spiral stair
1.906	1.902	D	0.95	3	0.78		1.903	Dome	M	4.54		0.5	Width is area (m^2)
1.906	Dome	C	0.2	1.3		Width is diam.	1.367	Dome	S	3.25			Width is area (m^2)

2.2 Auxiliary Systems

2.2.1 Protective Measures

The steel shell of the HDR containment has been designed for a maximum structural temperature of 155 °C. The following safety measures were undertaken in order to assure that the steel shell temperature would not reach its maximum:

- All walls of the fire room and the maintenance shaft adjacent to the steel shell have been protected by fire resistant bricks
- The atmospheric temperature in the vicinity of the steel shell is continuously monitored, especially in the region of the ascending hot gas plume.
- The initial amount of oil in the pan suffices for a fire of only 10 minutes duration, which increases the upper dome steel shell temperature only up to about 80 ^{o}C. After this initial phase, the oil supply to the pan is controlled such as to reach the anticipated power level specified. If the steel shell temperature approaches its limit value, the fire can be abruptly terminated by interrupting the oil supply.
- Video cameras, installed opposite to the fire room door, continuously monitor the fire room and the maintenance shaft to observe any possible damages to the HDR containment.

2.2.2 HDR Exhaust System

The HDR exhaust system consists of three filter units, each with 16 pre-filters and 16 fine filters. The first unit takes suction from the reactor building and passes through a filter housing and a ventilator. The second unit similarly operates to serve the waste treatment building. The third filter unit is at standby for either serving the reactor building or the waste treatment building. Thus, two filter units (first and third) have been available for the HDR containment, of which only one has been operated.

The filter system was designed for a volumetric flow of 35,500 m^3/hr per unit. The volumetric exhaust flow was controlled such as to keep a flow rate of 22,500 m^3/hr. The filters applied had the following characteristics:

Table 2.5: Characteristics of the Filters in the HDR Exhaust System

	Prefilter	Main Filter
Classification	type G	HEPA, class S
Dimensions	610 x 610 x 46 mm	610 x 610 x 292 mm
Volumetric Flow Rate	2200 m^3/hr	1700 m^3/hr
Initial ΔP	32 Pa	32 Pa
Final ΔP	120 Pa	120 Pa

2.2.3 Containment Recirculation System

This autonomous system was designed by the Laboratory of Aerosol Research at KfK. As shown in Figure 2.7, the recirculation system consists of a suction channel, filter unit and ventilator. The system was operated at a volumetric flow rate of 3,000 m^3/hr and was positioned at the operating deck at an axial elevation of +30.85 m. As the suction channel extends another 9 m in height, smoke gases from the upper region (≈40 m) in the dome are sucked and passed through the filter unit. The purified air is then released into the vicinity of the dome floor.

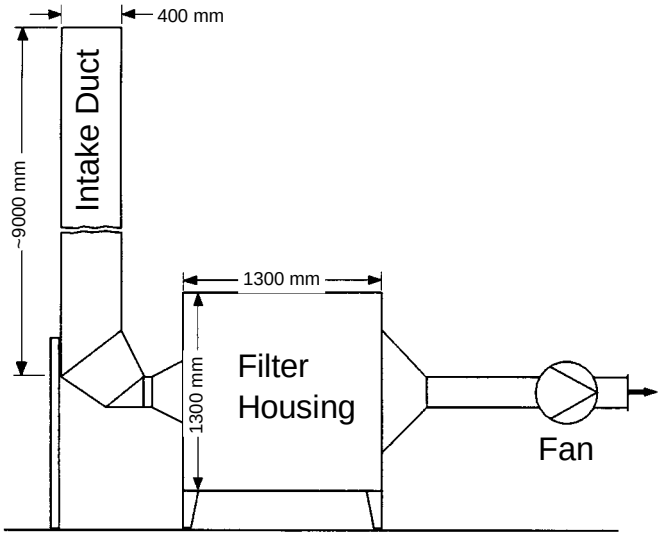

Figure 2.7: HDR Containment Recirculation System Developed by LAR/KfK

The total filter surface made from stainless steel fibers was about 2.5 m^2. As depicted in Figure 2.8, the filter unit consisted of the following multiple layers:

- metallic fabric
- layer 1: 20 mm, fiber diameter = 30 μm
- layer 2: 20 mm, fiber diameter = 22 μm
- layer 3: 20 mm, fiber diameter = 8 μm
- supporting steel plate with holes

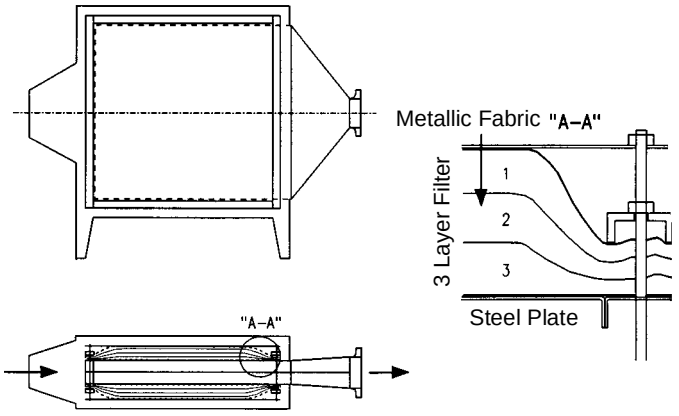

Figure 2.8: Multi-Layer Filters in the HDR Recirculation System

2.3 Thermophysical Material Properties

2.3.1 Thermophysical Wall Surfaces Properties

There were five different materials which were used as compartment surfaces within the HDR facility. Alsiflex mats and Ytong firebrick were used to protect the fire room and neighboring compartments from fire damages. In general, rooms in the HDR facility had painted concrete for the room surfaces with a different paint used for the floor than was used on the other room surfaces. Tables 2.5 and 2.6 provides the thermophysical properties for these materials [16,20,35]

Table 2.6 :Material Properties for Room Surfaces

Material	Density (kg/m^3)	Specific Heat (J/kg K)	Thermal Conductivity (W/m K)
Alsiflex Mats	130	1,000	See Table 2.5
HDR Concrete	2,225	879	2.10
HDR Floor Paint	1,540	1,280	0.29
HDR Wall Paint	1,250	1,550	0.20
Ytong Fire Brick	600	950	See Table 2.5

Table 2.7 :Thermal Conductivities for Room Surfaces

Material	Thermal Conductivity (W/m K)				
	100 °C	300 °C	500 °C	800 °C	1000 °C
Alsiflex Mats	0.05	0.05	0.10	0.18	0.25
Ytong Fire Brick	0.09	0.15	0.19	0.23	0.24

2.3.2 Thermophysical Fuel Properties

Hydrocarbon liquid, SHELLSOL T, was selected as the fuel for the T52 fire test series. The SHELLSOL T generates less soot compared to common light heating oil. The material properties of the oil are listed in Table 2.8

Table 2.8: Material Properties* of the Hydrocarbon Liquid Fuel, SHELLSOL T

Density (kg/m^3)	Boiling Temp. (°C)	Ignition Temperature (°C)	Heat of Combustion (kJ/kg)
756.0	184 ~ 217	54	42,500

*Note : the material properties provided in this table are given at STP condition (T = 20 °C, P = 1 bar)

The fuel tank was positioned outside of the containment with a special safety installation to protect the tank against any flame propagation from the inside of the containment. The fire is started by igniting the oil pool using a small volume of methyl alcohol. The instantaneous propagation and continuation of the fire throughout the whole fuel pool surface is assured by the low ignition temperature of 54 °C.

3 INSTRUMENTATION LAYOUT

3.1 Introduction

Because the fire research experiments were added to the HDR Safety Program about midway in the course of numerous safety experiments, the development of an instrumentation plan and the selection of the sensor types rested upon tested and proven measurement technologies. Most of these technologies were successfully applied during the previous HDR containment experiments. This proved to hold for the majority of typical pressure and temperature sensors. However, it was apparent from the outset that the fire experiments had somewhat different instrumentation criteria owing to the high temperature, low flow, and corrosive environment that the sensors would be exposed to.

The primary objective of the instrumentation for the test series T52 was to obtain data for a simulated cable fire in the dome region of the HDR-facility. Therefore, the instrumentation map was developed to give high priority to collecting data on the temperature and flow characteristics in the large-volume dome along with the associated entrainment and mixing behavior. In addition to the primary objective, the following elements were taken into consideration for the instrumentation layout:

- measurement of smoke gas temperatures, velocities, concentrations and density along the flow path from the fire room into the dome
- measurement of connective flow circulation through the containment
- examination of the characteristics of fresh air supply to the fire room
- examination of the impact of operating the containment exhaust system and its filter behavior during a fire
- determination of the duration to keep rescue paths free of smoke gases and toxic aerosols resulting from a partial pressurization
- protection of the integrity of the containment dome steel shell by continuous monitoring

Whereas the instrumentation in the fire room needs to satisfy the special fire requirements, the rest of the containment instrumentation relied upon the available, proven containment experiment measurement sensors. All data acquisition needs were accomplished by the central HDR computer and data acquisition storage system.

3.2 Instrumentation Descriptions

3.2.1 Temperature Measurement

For the test series T52, sheathed, NiCrSi-NiSi (Type N) and PtRh-Ph 10% (Type S) thermocouples were used for temperature measurements in the fire compartment in accordance with German DIN 43710. The NiCrSi-NiSi thermocouples had a 2 mm diameter Inconel sheath of and a 0.5 mm Teflon coated, compensation line and were insulated at their tips. The PtRh10%-Pt thermocouple had a sheath diameter of 1.5 mm. The total lengths of the signal wires of NiCrSi-NiSi and PtRh10%-Pt thermocouples were 20 m and 10 m, respectively. The

PtRh10%-Pt thermocouples had a 3 m of Pt and 7 m of Inconel, with a Teflon coated, compensation line. There are a total of 24 NiCrSi-NiSi thermocouples and 3 PtRh10%-Pt thermocouples installed in the fire room and the doorway to the maintenance hatch.

For all other temperature measurements, NiCr-Ni, sheathed, thermocouples were used. The thermocouple sheath had a 3 mm diameter and an insulated tip. The signal wires did not require special treatment as long as they remained outside of the hot flue gasses. Depending on the thermocouples' physical location in the facility, the signal wires were up to 20 m in length. As high frequency temperature changes were not anticipated outside the fire room, thermocouples with standard response characteristics were chosen; e.g. for temperature an error of ±1% of the measured value and for strong thermal radiation conditions an error of ±5%.

3.2.2 Pressure Measurement

Figure 3.1 shows schematically the major elements of determining the pressure difference with the TELEPERM measurement converter. The difference between containment inside and outside pressures acts on the bellow and is transmitted through a lever to the flexible beam tube which in turn transmits to a differential capacitor providing an analog signal. The TELEPERM converter works for a pressure difference of up to 5 mbar with a response time of 0.3 s and a measurement accuracy of ±1%. This device had to be protected from high temperatures; hence, its placement on the 1.600 level of the facility.

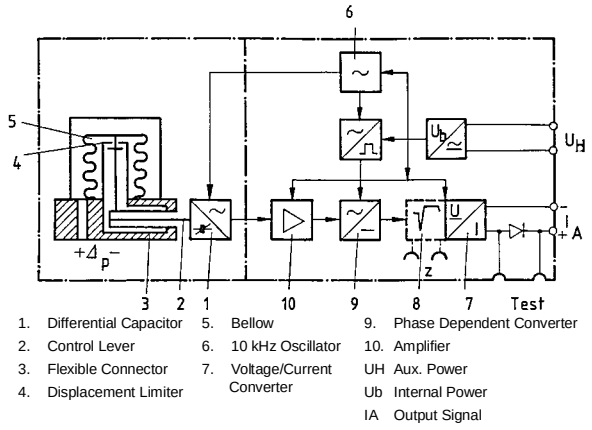

Figure 3.1: TELEPERM Transmitter

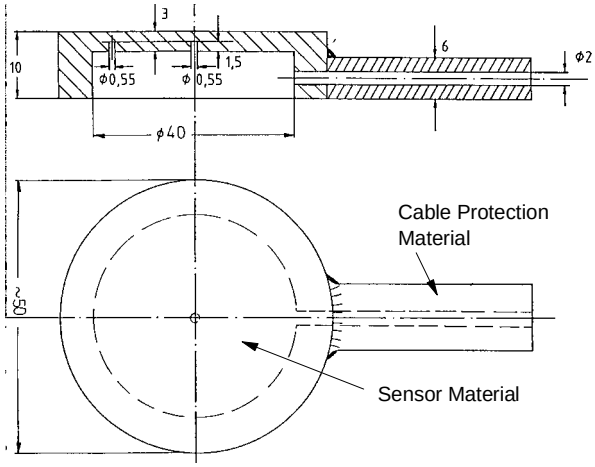

Figure 3.2: Local Heat Transfer Measurement

For the measurement of the pressure difference in the fire room doorway, Pitot tubes were installed at the cross-sectional area of the doorway.

3.2.3 Heat Transfer Measurement

The local heat transfer at the containment steel shell was determined using the sensor depicted in Figure 3.2. The sensor used a 40 mm diameter annular control volume with a thin disk bottom of

known material properties. Two NiCr-Ni sheathed thermocouples with a 0.5 diameter measured the disk temperature.

Additionally, large concrete blocks were devised and equipped with thermocouples as schematically shown in Figure 3.3. The type of concrete chosen was the same as used for the construction of the HDR containment Except for the front surface of the block all other surfaces were insulated. These massive concrete blocks were positioned at location where high convective flows, such as in the staircases, could be anticipated.

As the determination of the heat flux and subsequently the heat transfer coefficient at the measurement block's front surface rests on the solution of the inverse heat conduction problem, errors in these quantities became larger when temperature differences between thermocouples became smaller. Therefore, the expected accuracy of these blocks was only ±20%.

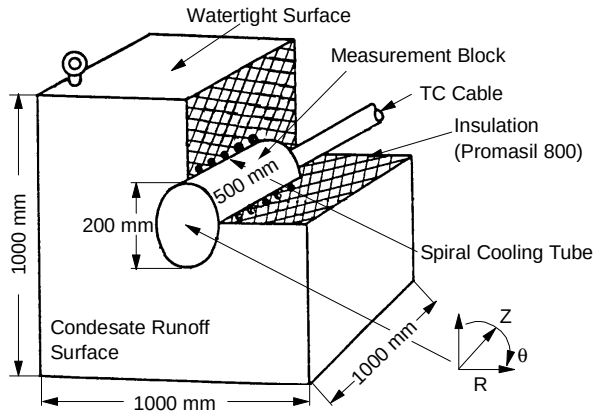

Figure 3.3: Heat Transfer Block

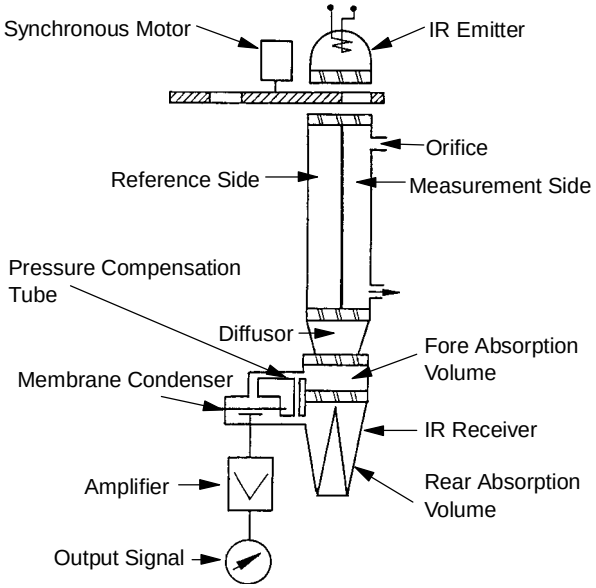

Figure 3.4: Gas Volume Analyzer

3.2.4 Smoke/Flue Gas Analysis

One of the major overall objectives of the HDR fire test series was the evaluation of the hazard potential to personnel, fire fighting, and rescue teams dependent on the type of burning substance, ventilating conditions, and fire location within the high-rise, containment building. Aside from direct exposure to heat, it is the smoke and flue gas mixture (O_2, CO, CO_2, C_nH_m, NO_x, SO_x) as well as the production of HCl and potentially dioxin in the case of burning PVC cables which determines the hazard level. Therefore, instrumentation measuring the concentrations of these individual components had to be in place. The requirements for smoke and gas analysis for the oil fire tests consisted of measuring O_2, CO, CO_2, and C_nH_m concentrations.

Figure 3.4 shows a schematic of the non-dispersive infrared photometer which worked with a modulated, single beam. This instrument allowed for continuous operation using a suction pump

in the range of 10-100 l/h volumetric flow. The device outputs a 0-10 VDC signal proportional to the volumetric concentration in terms of vol. % or ppm.

Prior to the start of each experiment, these sensors were calibrated with a calibration gas. The measurement accuracy of these sensors was expected to be ±2%.

3.2.5 Optical Smoke Density (Extinction Coefficient)

In order to follow the distribution and propagation of the flue gases inside the containment, an optical smoke densitometer, type ME82 made by Maurer, was positioned throughout the containment. A schematic of this sensor is shown in Figure 3.5, This sensor was used to determine the optical gas density in the rescue paths as well as the smoke density according to German Standard DIN 4102 Pt. 1. The output from this device was converted to an extinction coefficient prior to data recording.

As shown in Figure 3.5, a standardized light source in accordance with DIN 5033 emits a beam of light which passes through a control volume containing the gas to be analyzed. The control volume size can be modified. The amount of light passing through the volume is converted to an analog signal from 0-10 VDC corresponding to 100-0% transmittance. The measured values had an accuracy of ±2%.

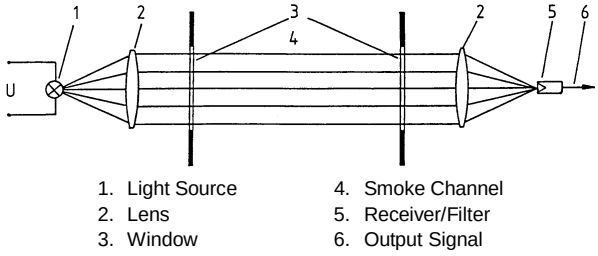

Figure 3.5: Smoke/Gas Density Sensor

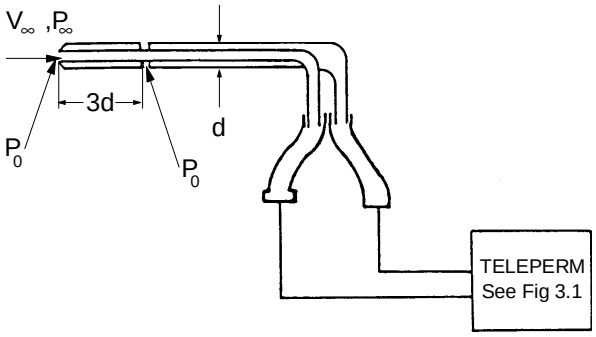

Figure 3.6: Pitot Tube Velocity Sensor

3.2.6 Velocity Measurement

Flow velocities within the HDR containment during the T52 tests were measured by one of four methods which are describe in this subsection. The methods used in the T52 series are listed below:

- Pitot Tube
- Anemometer
- Temperature Correlation Method
- ΔT Method

3.2.6.1 Pitot Tubes

Pitot tubes, shown in Figure 3.7, were used in the fire room doorway (CV9601-7) and in sensor grid 1 at the +39 m elevation of the dome (CV 410-424) to measure pressure and velocities. Pitot tubes measure velocity by comparing the ambient pressure to the stagnation pressure of the flow. Velocity is determined by the equation

$$V = \sqrt{\frac{2\Delta P}{\rho}}$$

Density was determined by using the Ideal Gas Law and the thermocouple closest to the Pitot tube. The pressure difference measurement made use of the TELEPERM transmitter discussed in Section 3.2.2.

3.2.6.2 Anemometer

Two types of anemometers were used in the T52 test series. Both types of anemometers consisted of ten, equally spaced, rotating arms. The component of the flow parallel to the rotational axis imparts angular momentum to the anemometer arms, causing it to rotate. Velocity was determined from the rotational frequency of the anemometer. The types differed in their ability to measure the direction of the flow.

The first type of anemometer that was used could not determine the direction of the flow. This device would only measure flow occurring within 10° of the axis rotational direction. Flow reversal could not be recognized. It can only be inferred if the measured velocity drops to zero and then increases again which indicates that a change in direction may have occurred. This type of anemometer was used in measurement grid 3 at the +25.5 m (CF9201-9209) as only upward flow was anticipated for those sensor locations. These anemometers could measure velocities from 0.2 m/s to 20 m/s for a temperature range of -3 °C to 150 °C. The measurement error of these sensors is 2% of the upper velocity limit.

The second type of anemometer, used for all other sensors outside of the fire room and measurement grids, could detect flow reversal. As with the aforementioned anemometers, these could only measure flow occurring within 10° of the axis rotational direction. These anemometers could measure velocities from 0.1 m/s to 20 m/s for a temperature range of -25 °C to 100 °C.

3.2.6.3 Temperature Correlation Method

This sensor, shown in Figure 3.7, consisted of two thermocouples placed in a flow guide at a known separation. Velocity is determined by cross-correlating the temperature measurements of the thermocouples to determine the flow transport time between the thermocouples. This velocity measurement method assumes that the flow is parallel to the line determined by the two thermocouples. If there is a cross-flow component to the flow, this method will not work as the cross correlation will not yield meaningful results. Since the small volume of gas whose temperature was measured at the first thermocouple and the volume of gas measured by the

second will not be the same volume as a result of the cross flow, there is nothing to correlate. This method is described in detail in [12]

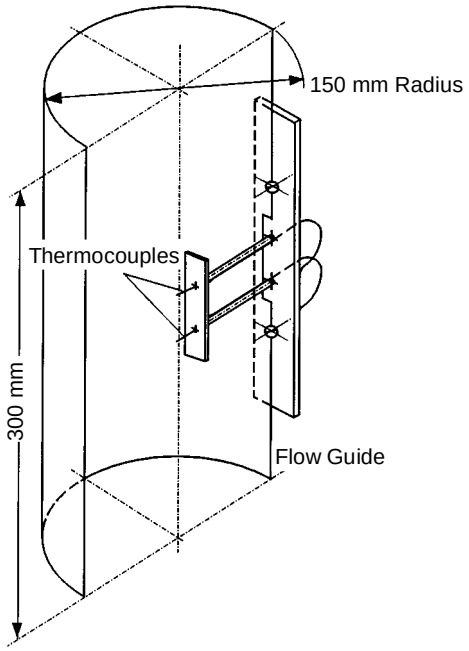

Figure 3.7: Temperature Correlation Velocity Sensor

These sensors were used for sensor grid 2 (CV 480-497). The measured signals were identified with a three digit sensor ID (CV 480), and the correlated results were identified with the measured sensor ID with an added 1 infront of the three digit sensor ID(CV 1480).

3.2.6.4 ΔT Method

The ΔT method uses the temperature fluctuation of a single thermocouple at a defined position [12]. This method is calibrated using the results from the cross-correlation at the same location. The results of this method were identified by the measured sensor ID with an added 3 infront of the three digit sensor ID (CV 3480).

3.2.7 Video System

3.2.7.1 Introduction

The HDR facility was equipped with a color video system consisting of cameras, monitors, and tape machines. This system was used for monitoring the fire behavior in the fire compartments. The camera position for the T51 test series is shown in Figure 2.5.

In addition, a black and white video network consisting of 20 cameras with a switching board was installed. This system was developed by the Technical University of Karlsruhe, Germany, for use in monitoring the evacuation of personnel from high-rise buildings during fire exercises.

3.2.7.2 Black & White Video System Network

Figure 3.8 shows the black and white video network which was used to monitor smoke movement at up to 20 locations under low lighting conditions, 20 lux. The cameras are connected with 50 m long cables to a video switching board. This device switches to the next camera after three half pictures are taken. With a camera frequency of 50 frames per second, the switching board could rotate through the cameras in 1.2 s. This results in a nearly simultaneous observation of the smoke throughout the building. The other elements shown in the Figure are self-explanatory.

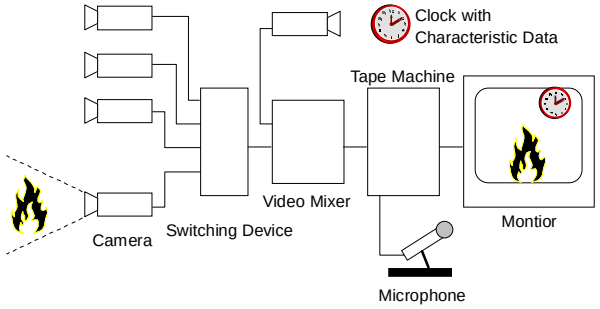

Figure 3.8: B&W Video System

3.2.8 Digital Scales

The oil platform was supported by three digital scales, see Figures 2.4 and 2.5 in Section 2.1. The scales were tared with the weight of the platform. Each of the three scales measured the force in Newtons exterted by the oil on the platform. To generate the burning rate the total of the three scales was taken and converted to kilograms of mass.

3.2.9 Safety Measures

In addition to the thermal insulations listed in Section 3.1, the measures described below were implemented for safety purposes:

- The color video system monitoring the fire compartment was continuously operated.
- A number of gas detectors were positioned at Levels 1.4 and 1.6 for safety reasons.
- All other containment regions including the steel shell were monitored with thermocouples.
- A fire suppression system was installed along the ceiling of the fire compartment.

3.3 Comments on Sensor Performance

For the most part, the various sensors and the data acquisition system performed as expected during the T52 test series. However, a few deviations from expected performance were observed. Some general comments on sensor performance are noted below.

3.3.1 Temperature Measurement

Due to the unexpected fire development during the T52.13 experiment, flames propagated through the fire room doorway into the maintenance shaft. This resulted in a number of sensor failures during the test. The heat caused the direct failure of some of the NiCr-Ni thermocouples. Also, thermocouples positioned in the lower region of the door saturated as the selected measurement range was too low for the temperatures experienced during the T52.13 experiment. Further thermocouple failures occurred in the maintenance shaft were again the high temperatures experienced during T52.13 exceeded the selected measurement range. Altogether, this resulted in the failure of a number of thermocouples causing a loss of valuable test data. Thermocouples elsewhere did not see any performance deviations.

3.3.2 Velocity Measurement

All four different methods resulted in the collection of physically meaningful data. The following observations were made during the tests:

- The Pitot tubes in the fire room doorway did not become clogged with soot during the experiments as the temperatures and velocities were sufficiently high to preclude local soot formation and deposition.
- Both types of velocity anemometers worked as expected. Soot formation on the blades was acceptable and did not cause measurement errors outside the accepted range. However, it was observed that the bearings had to be completely encapsulated.
- Comparisons made between the cross-correlation and the ΔT methods at the same position indicated that the former has large oscillations and that the fast increase in velocity due to the rapid development of the fire in the first few minutes was not picked up. The magnitude of the average velocity in the latter portion of each test was the same for both methods.
- Unanticipated cross-flow at the operating deck of the dome near sensor grid 2 resulted in the inability to utilize most of the velocity sensors in that grid.

3.3.3 Heat Transfer Measurement

The determination of the heat transfer coefficients using the heat transfer blocks described in Section 3.2.3 [6] was questionable in the regimes far away from the fire room. This was especially the case for the lead heat transfer block positioned in the far-field of the fire. Reliable heat transfer measurements were not generated because the measurement errors associated with the thermocouples imbedded in the block were simply too large to produce meaningful results.

Also, the large steel heat transfer block positioned at the operating deck in the dome did not generate reliable heat transfer coefficients for the same reason given for the lead block. Therefore, the evaluation of heat transfer coefficients from the temperature signals was only partially performed and successful.

The heat transfer coefficients determined at the +38 m elevation of the dome steel shell at 0°, 203°, and 270° resulted in high values. For example, for experiment T52.14 the deduced heat transfer coefficient ranged between 80 and 270 $W/m^2 \cdot K$. This is higher than the commonly reported values for fire in the literature.

Heat transfer coefficients deduced from the concrete heat transfer block ranged from 10 to 30 $W/m^2 \cdot K$ which is the same order as what has been obtained during the T51.18 and T51.19 HDR fire experiments. This range also agrees with data reported in the literature.

3.3.4 Smoke Density Measurement

The smoke density could not be directly measured because the levels of soot and smoke formed during the T52 test series were simply too high. However, the measured local CO_2 concentrations allow one to estimate when soot and smoke reach certain containment regions. Those time spans are of the same order as what has been determined for experiments T51.16-18 on the 1.400 level.

3.3.5 Mass Flows

Mass flows through defined cross sections can be determined if temperature and velocity profiles are known. Therefore, the availability of sensors plays a major role, especially at important cross-sections such as the fire room doorway, maintenance hatch, and plume cross-sections in the dome.

3.4 Instrumentation Layout for T52 Oil Pool Fire Tests

This subsection describes the instrumentation mapping for the T52 oil pool fire test series. A complete listing of all instruments as well as diagrams showing their locations within the facility are documented in the tables following. To aid in reading the tables and diagrams the following nomenclature, standard for all HDR tests, is used for the instrumentation:

Table 3.1: Sensor Nomenclature

Sensor Name Header	Description	Unit
Direct Quantities		
CA	Force Sensor	N
CF	Velocity Sensor	m/s
CG	Gas Concentration Sensor	Vol. %
CP	Pressure Sensor	bar
CQ	Heat Transfer Measurement Block Sensor	W/m^2K
CS	Temperature Sensor	^oC
CT	Temperature Sensor	^oC
CV	Velocity Sensor	m/s
OA	Steel Shell Expansion Measurement Sensor	Exp. Coeff.
Indirect Quantities		
CD	Calculated Density	kg/m^3
CM	Calculated Mass Flow Rate	kg/s
CQ	Calculated Heat Flux or Heat Transfer Coefficient	W/m^2 or W/m^2K

In addition to the directly measured quantities, post processing was performed for some of the data to yield indirectly measured parameters such as density and mass flow rate. These indirect measurements were not performed consistently throughout the test series. These measurements used the nomenclature as depicted in Table 3.1 under the heading "indirect quantities".

In the table that follows sensor location refers to one of two HDR coordinate systems. For heat transfer measurement blocks the location uses the front, center of the measurement block for the reference location with the position given in Cartesian coordinates [9]. All other sensors use the HDR center line at the +0.0 m elevation, see Figure 1.1, for the reference location with the position given in cylindrical coordinates [1].

Table 3.2 lists all sensors in place for tests T52.11-T52.14. The table shows the quantity/parameter measured, and the location for each sensor relative to the appropriate coordinate system. Any special comments about the sensor's performance is also given. Figures 3.9 through 3.27 schematically depict the sensors' locations level by level in the HDR facility for Table 3.2.

Table 3.2: T52.11-14 Instrument Network

Sensor	Location			Comments			
	R (cm)	θ (deg)	Z (cm)	T52.11	T52.12	T52.13	T52.14
CA9600	778	250	2540				
CA9601	758	255	2540				
CA9602	580	246	2540				
CA9610	0	0	0				
CF 434	652	81	3100				
CF3701	900	51	2500				
CF3721	825	43	100				
CF3723	925	52	1200				
CF4602	652	81	0				
CF6602	652	81	1200				
CF6606	495	328	1100				
CF6607	495	328	1300				
CF7703	652	81	1700				
CF7802	657	278	1900				
CF7803	990	267	1700				
CF9201	583	290	2550		Not Plausible	Not Plausible	Not Plausible
CF9202	558	280	2550				
CF9203	550	269	2550			Not Plausible	Not Plausible
CF9204	678	287	2550			Not Plausible	Not Plausible
CF9205	657	278	2550				
CF9206	651	269	2550				
CF9207	774	284	2550				
CF9208	755	277	2550				
CF9209	750	269	2550				
CF9210	990	268	2500				

Sensor	Location			Comments			
	R (cm)	θ (deg)	Z (cm)	T52.11	T52.12	T52.13	T52.14
CF9301	652	81	2500				
CG 411	899	289	3900				
CG 412	714	294	3900				
CG 413	537	303	3900				
CG 414	856	276	3900				
CG 415	657	278	3900				
CG 416	460	282	3900				
CG 417	856	263	3900				
CG 418	659	261	3900				
CG 419	462	256	3900				
CG 420	750	269	3100				
CG 421	755	277	3100				
CG 422	774	284	3100				
CG 423	651	269	3100				
CG 424	657	278	3100				
CG 425	678	287	3100				
CG 426	550	269	3100				
CG 427	558	280	3100				
CG 428	583	290	3100				
CG 429	652	81	3100				
CG1104	500	270	600				
CG2166	495	328	1450				
CG2266	495	328	1360				
CG2366	495	328	1270				
CG2466	495	328	1180				
CG2566	495	328	1090				
CG3707	740	44	-435				

Sensor	Location			Comments			
	R (cm)	θ (deg)	Z (cm)	T52.11	T52.12	T52.13	T52.14
CG4602	652	81	0				
CG5306	652	81	600				
CG6601	652	81	1200				
CG6606	495	328	1100				
CG6607	495	328	1300				
CG6631	495	328	1450				
CG6632	495	328	1360				
CG6633	495	328	1270				
CG6634	495	328	1180				
CG6635	495	328	1090				
CG9210	657	278	255				
CG9310	495	81	2500				
CG9601	760	262	2825				Out of Range (3-9 min.)
CG9602	760	262	2825				
CG9603	760	262	2825				
CG9604	760	262	2825				
CP 403	707	292	3100				
CP 498	405	300	3178				
CP 499	405	300	3178				
CP6201	1005	0	1100				
CP9601	760	262	2825			Not Plausible	
CQ 421	0	0	100				
CQ 422	0	0	200				
CQ 423	0	0	300				
CQ 424	0	0	400				
CQ 425	0	0	500				
CQ 426	0	0	2000				

Sensor	Location			Comments			
	R (cm)	θ (deg)	Z (cm)	T52.11	T52.12	T52.13	T52.14
CQ3701	75	120	0			Defected at 41 min.	
CQ3702	75	0	40				
CQ3703	75	30	200				
CQ3704	75	60	500				
CQ3705	75	90	950				
CS6602	535	0	1300			Defected before test	
CS7801	500	281	1700				
CS9201	680	286	2850				
CS9601	708	243	2800				
CT 403	0	0	5000				
CT 419	652	81	3100				
CT 430	899	289	3900				
CT 431	806	291	3900				
CT 432	714	294	3900				
CT 433	624	298	3900				
CT 434	537	303	3900				
CT 435	872	283	3900				
CT 436	774	284	3900				
CT 437	678	287	3900				
CT 438	583	290	3900				
CT 439	490	293	3900				
CT 440	856	276	3900				
CT 441	755	277	3900				
CT 442	657	278	3900				
CT 443	558	280	3900				
CT 444	460	282	3900				

Sensor	Location			Comments			
	R (cm)	θ (deg)	Z (cm)	T52.11	T52.12	T52.13	T52.14
CT 445	850	269	3900				
CT 446	750	269	3900				
CT 447	651	269	3900				
CT 448	550	269	3900				
CT 449	450	269	3900				
CT 450	856	263	3900				
CT 451	756	262	3900				
CT 452	659	261	3900				
CT 453	560	259	3900				
CT 454	462	256	3900				
CT 455	750	269	3100			Out of Range (2-7 min.)	
CT 456	751	273	3100				
CT 457	755	277	3100			Out of Range (4-6 min.)	
CT 458	764	281	3100				
CT 459	774	284	3100				
CT 460	699	269	3100				
CT 461	701	273	3100				
CT 462	706	277	3100				
CT 463	714	281	3100				
CT 464	726	285	3100				
CT 465	651	269	3100				
CT 466	652	274	3100				
CT 467	657	278	3100				
CT 468	666	282	3100				
CT 469	678	287	3100				
CT 470	600	269	3100				

Sensor	Location			Comments			
	R (cm)	θ (deg)	Z (cm)	T52.11	T52.12	T52.13	T52.14
CT 471	602	274	3100				
CT 472	608	279	3100				
CT 473	617	283	3100				
CT 474	631	288	3100				
CT 475	550	269	3100				
CT 476	552	274	3100				
CT 477	558	280	3100				
CT 478	569	285	3100				
CT 479	583	290	3100				
CT 480	657	278	3300				
CT 481	657	278	3500				
CT 482	657	278	3700				
CT 483	657	278	4100				
CT 484	657	278	4300				
CT 485	657	278	4500				
CT 486	657	278	4755				
CT 487	995	66	3100				
CT 488	995	66	3700				
CT 489	995	0	3100				
CT 490	995	0	3800				
CT 491	995	270	3100				
CT 492	995	270	3800				
CT 493	995	203	3100				
CT 494	995	203	3800				
CT 495	0	0	3400				
CT 496	482	0	3872				
CT 497	0	0	4500				

Sensor	Location			Comments			
	R (cm)	θ (deg)	Z (cm)	T52.11	T52.12	T52.13	T52.14
CT 498	405	300	3100				
CT 499	240	13	3178				
CT1104	500	270	600				
CT3701	970	72	2511				
CT3705	900	51	2500				
CT3707	740	44	435				
CT3709	825	43	100				
CT3723	925	52	1200				
CT4602	652	81	0				
CT5302	980	55	600				
CT5306	652	81	600				
CT6601	652	81	1200				
CT6607	657	278	1200				
CT6612	657	278	1300				
CT6613	495	328	1020				
CT6614	495	328	1050				
CT6615	495	328	1100				
CT6616	495	328	1200				
CT6617	495	328	1250				
CT6618	495	328	1300				
CT6619	495	328	1400				
CT6620	495	328	1450				
CT7702	970	56	1700				
CT7703	652	81	1700				
CT7802	657	278	1900				
CT7803	990	267	1700				
CT8402	657	278	2257				

Sensor	Location			Comments			
	R (cm)	θ (deg)	Z (cm)	T52.11	T52.12	T52.13	T52.14
CT8403	947	280	2140				
CT8502	652	81	2300				
CT9210	990	268	2500				
CT9211	750	269	2550				
CT9212	774	284	2550				
CT9213	701	273	2550				
CT9214	714	281	2550				
CT9215	657	278	2550				
CT9216	602	274	2550				
CT9217	617	283	2550				
CT9218	550	269	2550				
CT9219	583	290	2550				
CT9220	565	295	3065				
CT9301	652	81	2500				
CT9601	871	251	2800			Defected at 32 min.	Defected before test
CT9602	794	248	2800				
CT9603	699	245	2800				
CT9604	607	241	2800				
CT9605	518	235	2800			Defected at 32 min.	Defected before test
CT9606	482	242	2800				
CT9607	502	251	2800		Defected at 35 min.	Defected before test	Defected before test
CT9608	652	256	2800			Out of Range (2-4 min.)	
CT9609	870	255	2800				
CT9610	811	249	2700				
CT9611	777	257	2700				
CT9612	765	248	2700				

Sensor	Location			Comments			
	R (cm)	θ (deg)	Z (cm)	T52.11	T52.12	T52.13	T52.14
CT9613	729	256	2700				
CT9614	718	246	2700			Defected during test	Defected before test
CT9615	680	255	2700				
CT9616	672	250	2700				
CT9617	674	244	2700				
CT9618	632	254	2700				
CT9619	628	243	2700				
CT9620	595	253	2700				
CT9621	584	240	2700				
CT9622	536	251	2700				
CT9631	737	261	2845				
CT9632	737	261	2835				
CT9633	737	261	2825				
CT9634	737	261	2815			Defected at 32 min.	Defected before test
CT9635	737	261	2805			Defected at 32 min.	Defected before test
CT9636	737	261	2795			Defected at 32 min.	Defected before test
CT9637	737	261	2785				Defected at 33 min.
CT9638	737	261	2775			Defected at 32 min.	Defected before test
CT9639	737	261	2765				
CT9640	737	261	2755				
CT9641	737	261	2745				
CT9642	737	261	2735				
CT9643	737	261	2725			Defected at 34 min.	Defected before test
CT9651	737	261	2560			Out of Range (2-6 min.)	Out of Range (2-8 min.)
CT9652	737	261	2565			Out of Range (2-35 min.)	Out of Range (2-35 min.)
CT9653	737	261	2590			Out of Range (2-9 min.)	Out of Range (2-9 min.)

Sensor	Location			Comments			
	R (cm)	θ (deg)	Z (cm)	T52.11	T52.12	T52.13	T52.14
CT9654	737	261	2615			Defected during test	Defected before test
CT9655	737	261	2640			Defected during test	Defected before test
CT9656	737	261	2665			Defected during test	Defected before test
CT9657	737	261	2690		Out of Range (2-12 min.)	Out of Range (2-6 min.)	
CV 411	899	289	3900	Out of Range (3-33 min.)	Out of Range	Out of Range (2-32 min.)	Out of Range (3-9 min.)
CV 412	714	294	3900				
CV 413	537	303	3900				
CV 414	774	284	3900				
CV 415	583	290	3900				
CV 416	856	276	3900				
CV 417	657	278	3900				
CV 418	460	282	3900				
CV 419	750	269	3900				
CV 420	550	269	3900				
CV 421	856	263	3900				
CV 422	659	261	3900				
CV 423	462	256	3900				
CV 424	657	278	4500				
CV 480	748	269	3100				
CV 481	748	269	3110				
CV 482	772	284	3100	Not Plausible	Not Plausible	Not Plausible	Not Plausible
CV 483	772	284	3110	Not Plausible	Not Plausible	Not Plausible	Not Plausible
CV 484	699	273	3100	Not Plausible	Not Plausible	Not Plausible	Not Plausible
CV 485	699	273	3110	Not Plausible	Not Plausible	Not Plausible	Not Plausible
CV 486	712	281	3100				
CV 487	712	281	3110				

Sensor	Location			Comments			
	R (cm)	θ (deg)	Z (cm)	T52.11	T52.12	T52.13	T52.14
CV 488	658	278	3100				
CV 489	658	278	3110				
CV 490	604	274	3100				
CV 491	604	274	3110				
CV 492	618	283	3100	Not Plausible	Not Plausible	Not Plausible	Not Plausible
CV 493	618	283	3110	Not Plausible	Not Plausible	Not Plausible	Not Plausible
CV 494	553	269	3100	Not Plausible	Not Plausible	Not Plausible	Not Plausible
CV 495	553	269	3110	Not Plausible	Not Plausible	Not Plausible	Not Plausible
CV 496	585	290	3100	Not Plausible	Not Plausible	Not Plausible	Not Plausible
CV 497	585	290	3110	Not Plausible	Not Plausible	Not Plausible	Not Plausible
CV9600	737	261	2825				
CV9601	737	261	2795				
HF 1	2620	1260	-1975				
HG 1	1106	1532	-1650				
HL 1	2540	1265	-1995				
HP 1	2845	866	-2690				
HP 2	2845	818	-2690				
HP 3	3033	866	-2690				
HP 4	3033	818	-2690				
HT 1	2540	1250	-1965				
MK 2	0	0	0				
MK 3	0	0	0				Not Plausible
MK 4	0	0	0				Not Plausible
MK 5	0	0	0				
MK 6	0	0	0				
MK 7	0	0	0				
OA 11	1003	66	3100				

Sensor	Location			Comments			
	R (cm)	θ (deg)	Z (cm)	T52.11	T52.12	T52.13	T52.14
OA 12	1003	66	3700				
OA 13	1003	0	3100				
OA 14	1003	0	3800				
OA 15	1003	270	3100				
OA 16	1003	270	3800				
OA 17	1003	203	3100				
OA 18	1003	203	3800				
OF 1	1033	270	4000				
OI 11	1000	66	3100				
OI 12		66	3700				
OI 13	1000	0	3100				
OI 14	1000	0	3800				
OI 15	1000	0	3800				
OI 16	1000	270	3800				
OI 17	1000	203	3100				
OI 18	0	203	3800				
OI 410	657	278	4760				
OT 50	1033	66	3400				
OT 51	1033	0	3400				
OT 52	1033	270	3100				
OT 53	1033	270	3800				
OT 54	1033	203	3400				
RF7004	672	250	2540				

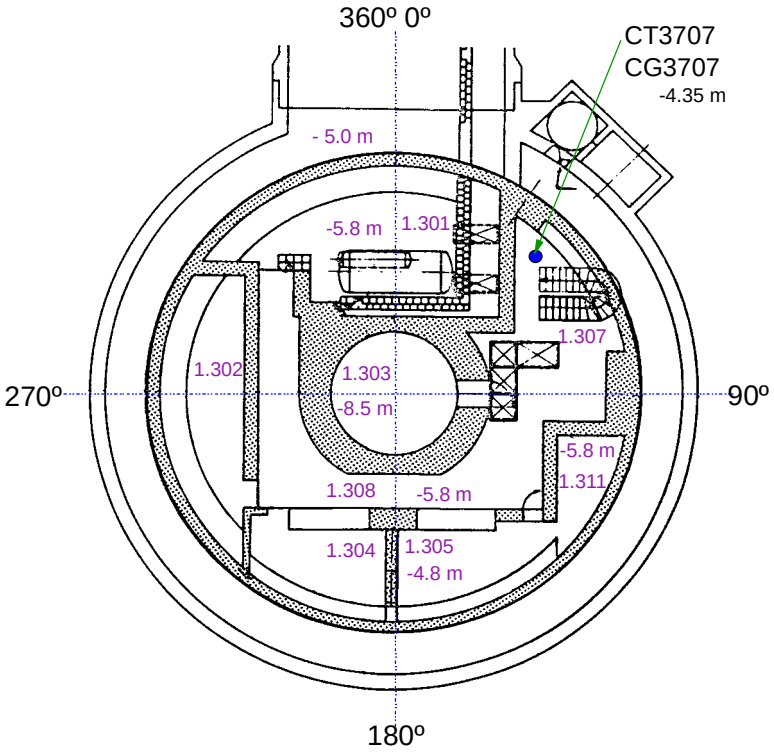

Figure 3.9: T52 Level 1.300

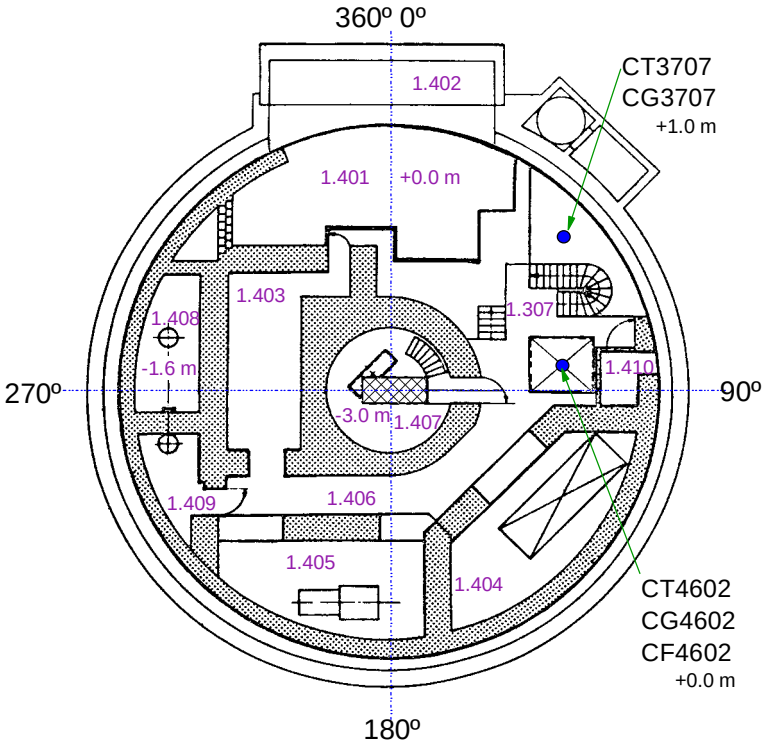

Figure 3.10: T52 Level 1.400

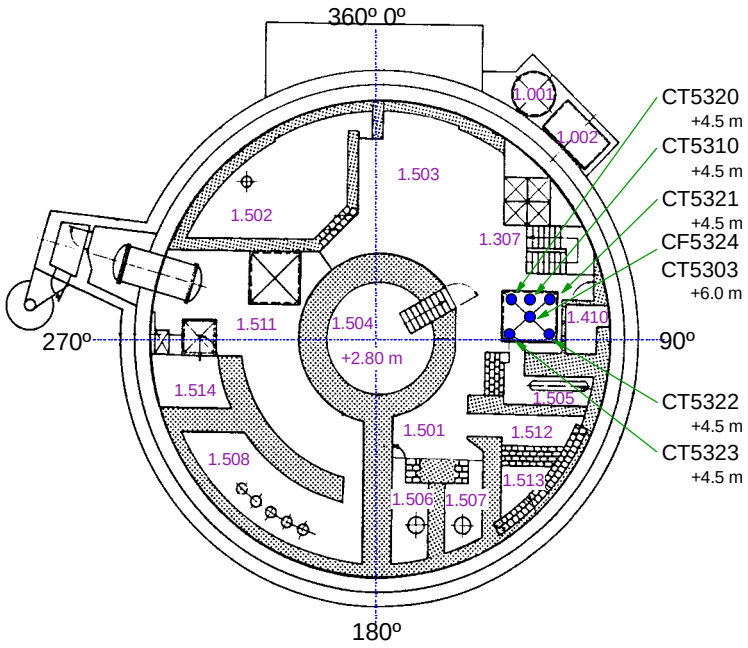

Figure 3.11: T52 Level 1.500

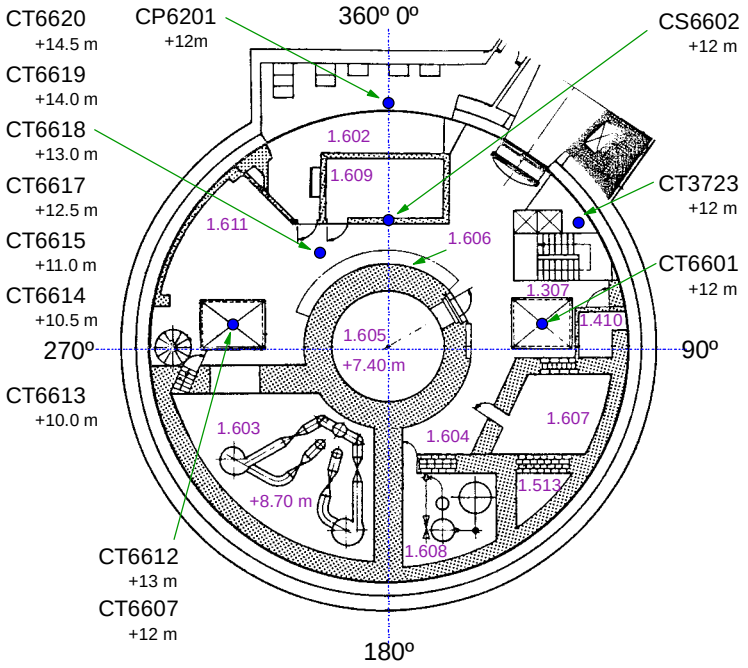

Figure 3.12: T52 Level 1.600 Temperature + Pressure Sensors

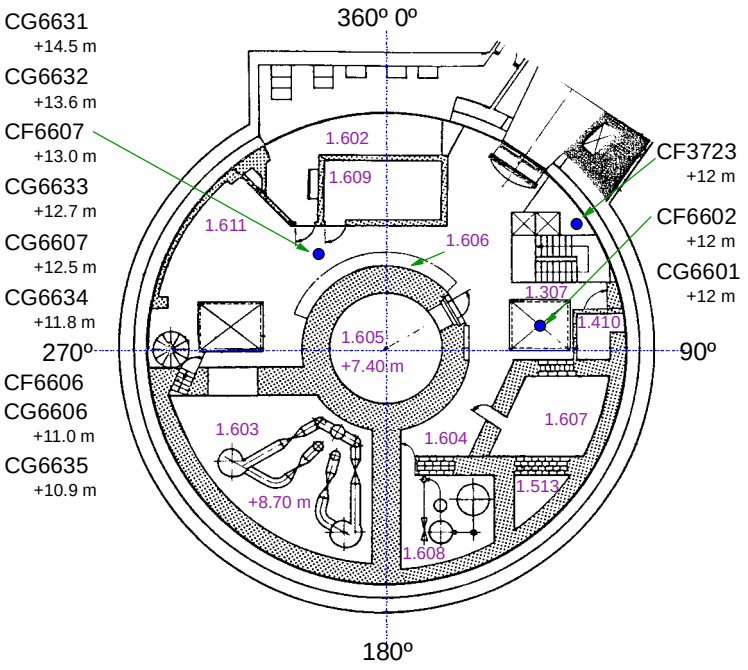

Figure 3.13: T52 Level 1.600 Gas + Velocity Sensors

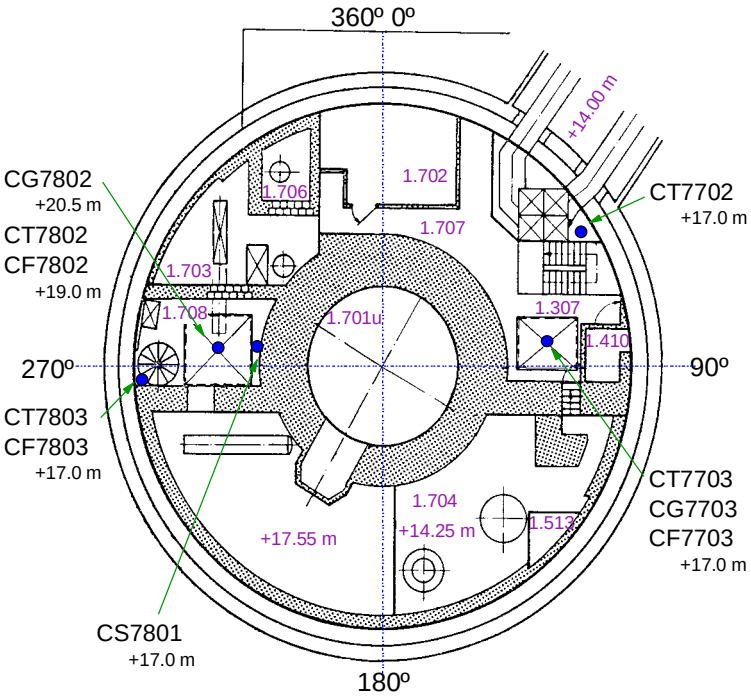

Figure 3.14: T52 Level 1.700

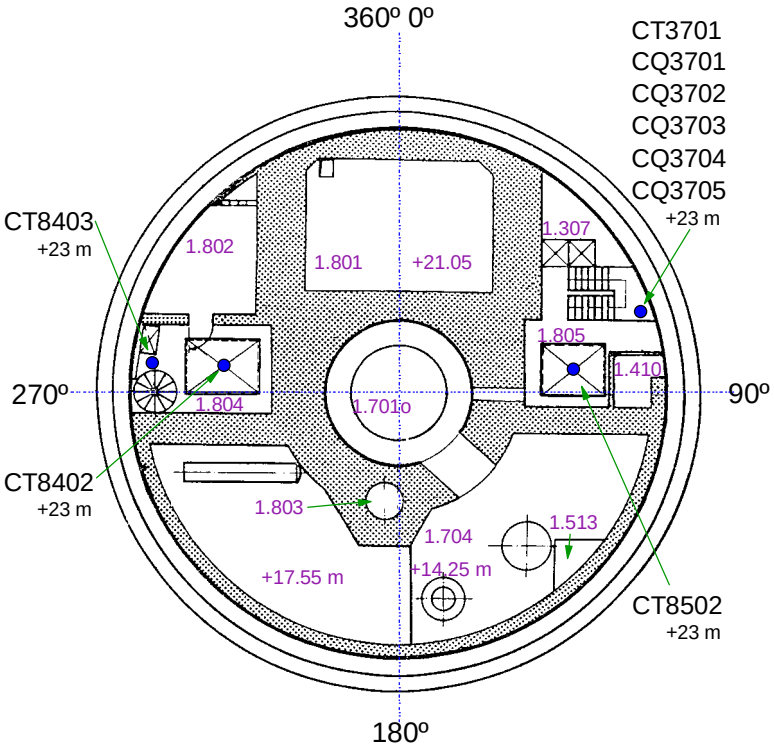

Figure 3.15: T52 Level 1.800

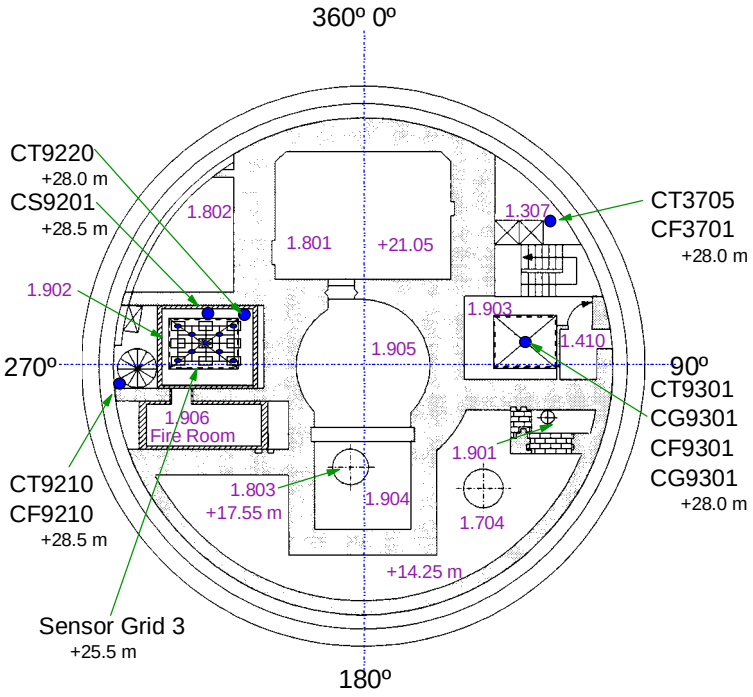

Figure 3.16: T52 Level 1.900

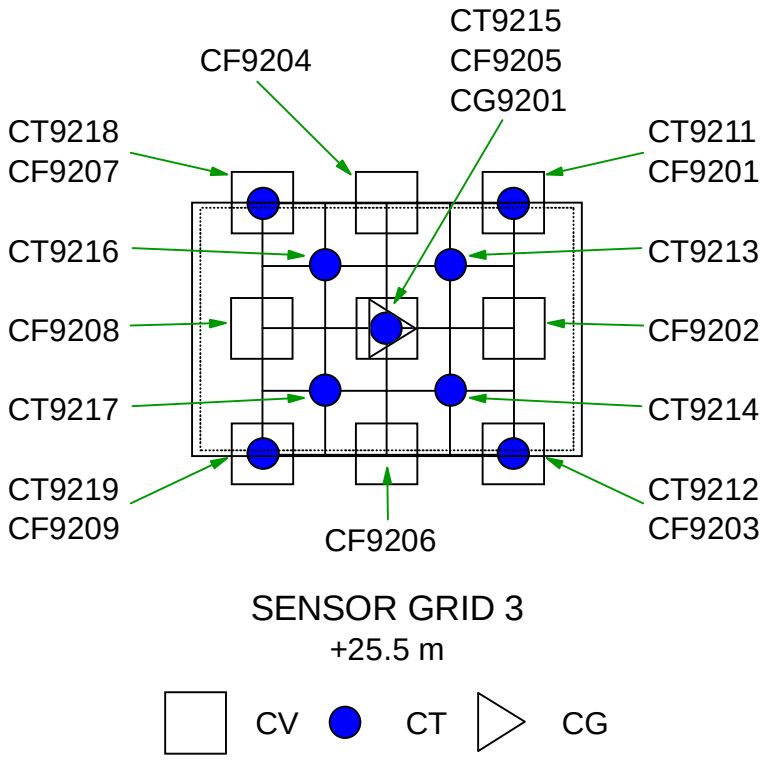

Figure 3.17: T52 Sensor Grid 3

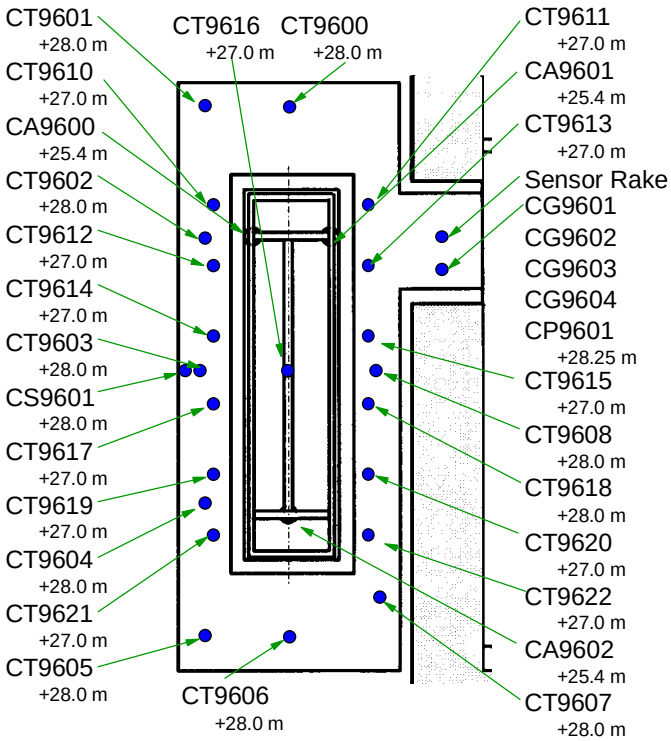

Figure 3.18: T52 Fire Room

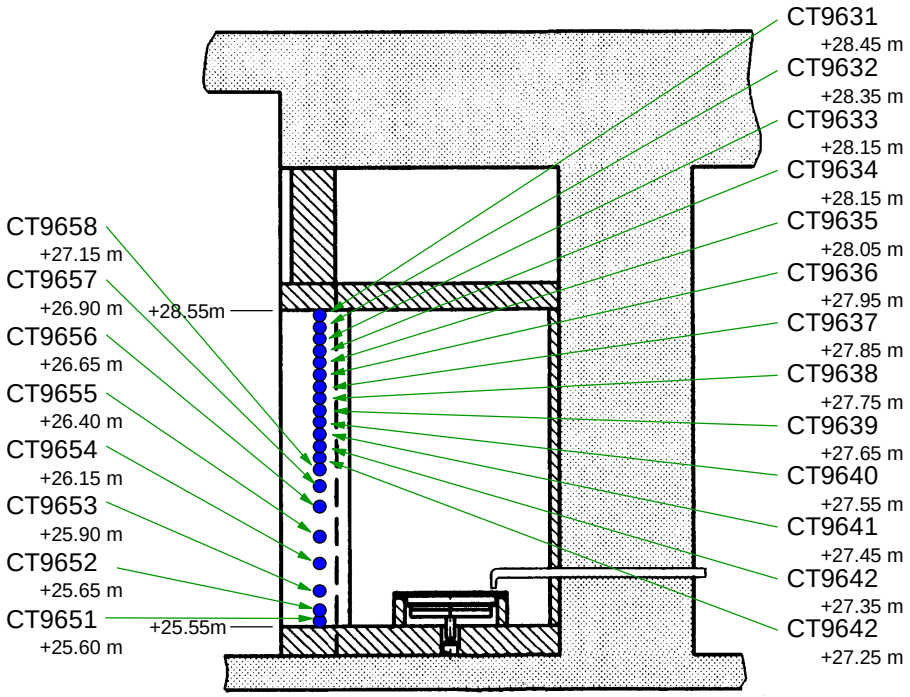

Figure 3.19: T52 Doorway Temperature Sensors

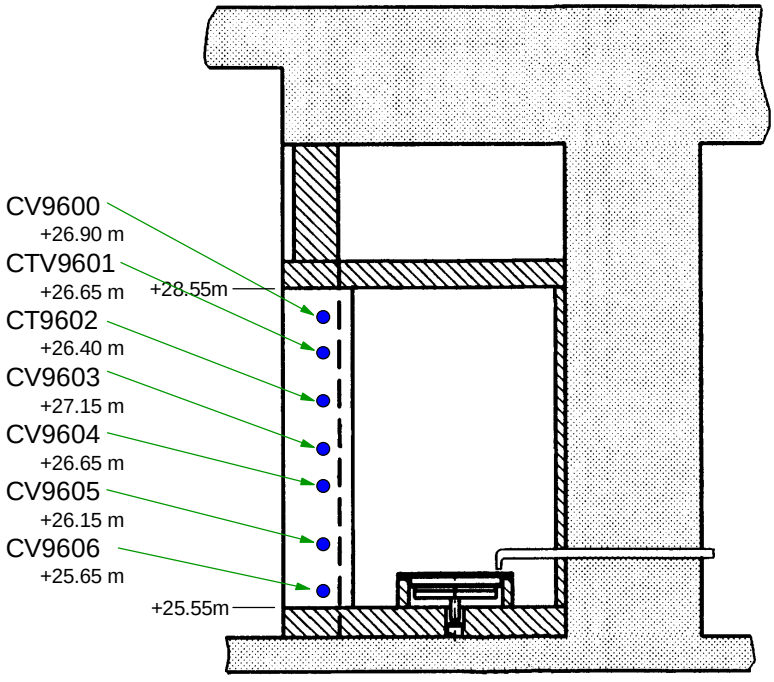

Figure 3.20: T52 Doorway Velocity Sensors

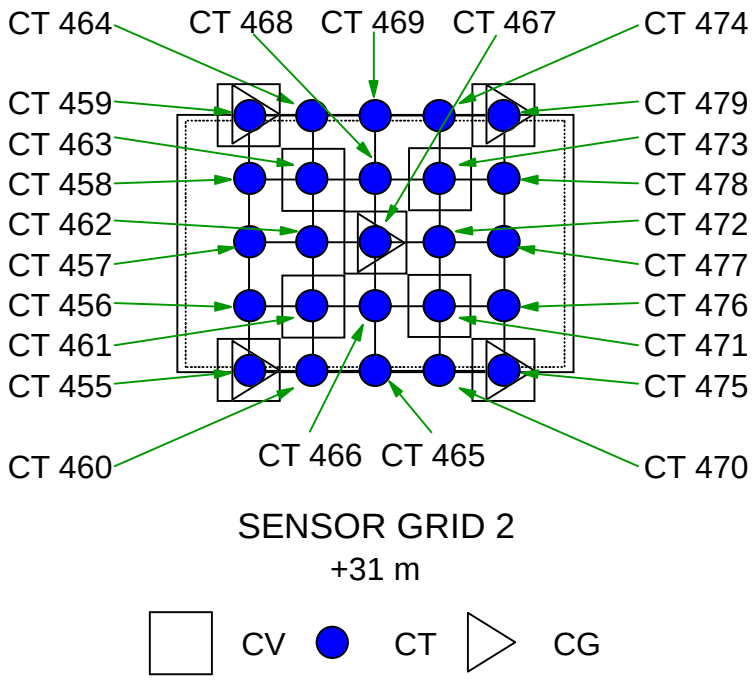

Figure 3.21: T52 Sensor Grid 2 Temperature Sensors

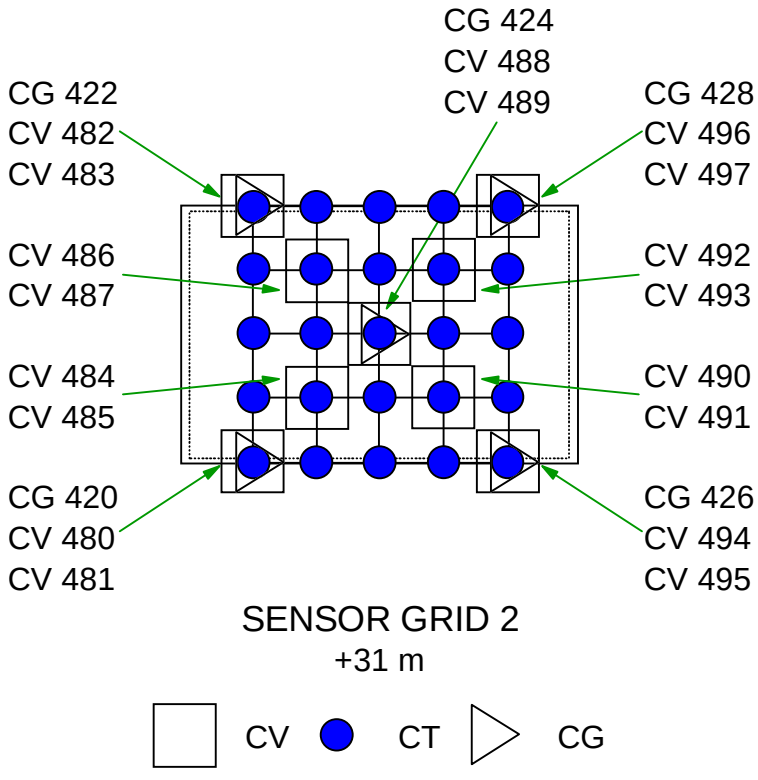

Figure 3.22: T52 Sensor Grid 2 Velocity + Gas Sensors

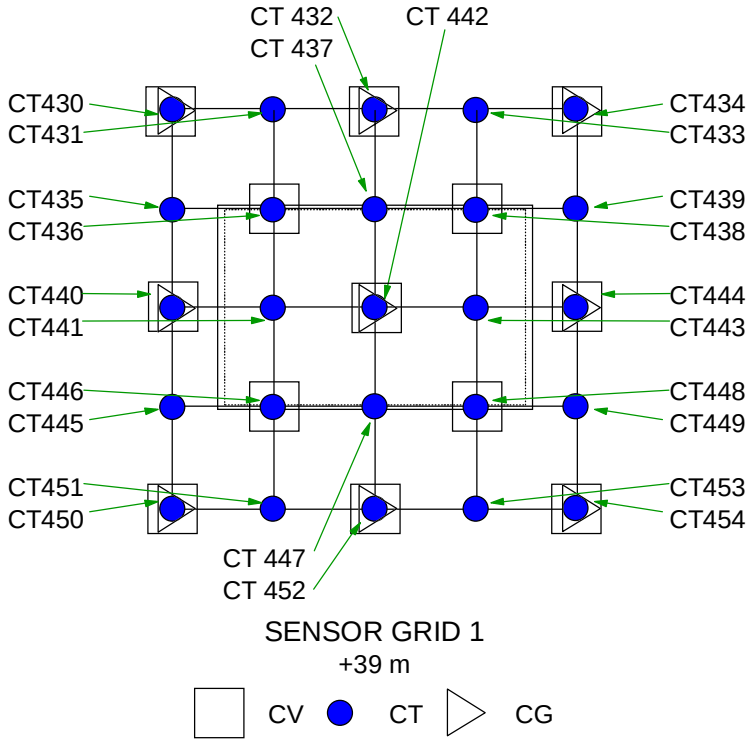

Figure 3.23: T52 Sensor Grid 1 Temperature Sensors

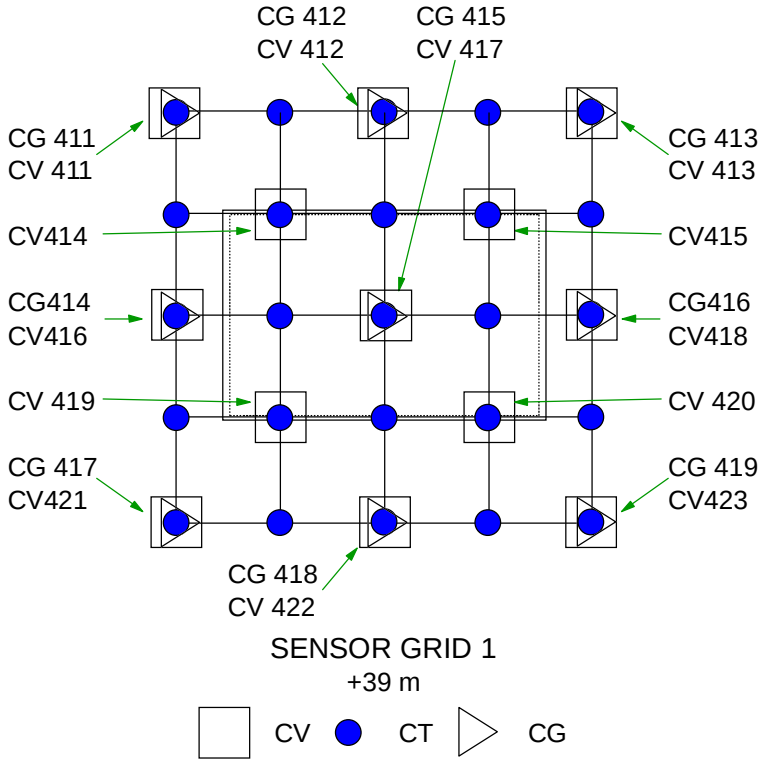

Figure 3.24: T52 Sensor Grid 1 Velocity + Gas Sensors

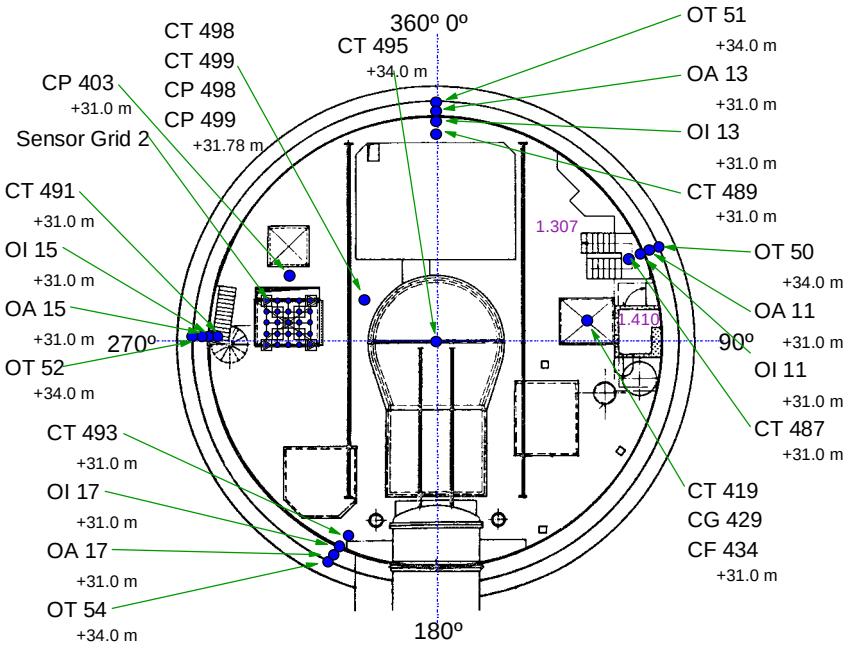

Figure 3.25: T52 Lower Dome

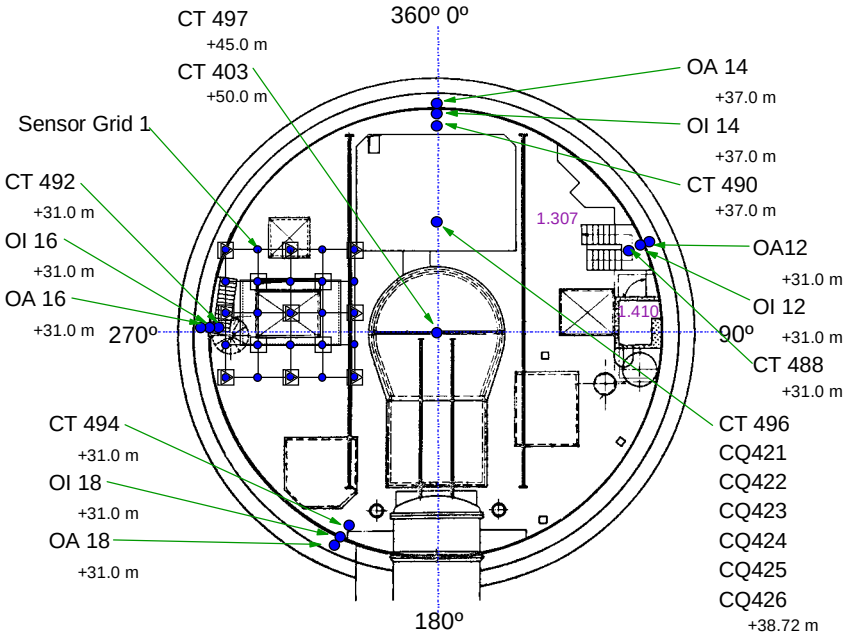

Figure 3.26: T52 Upper Dome

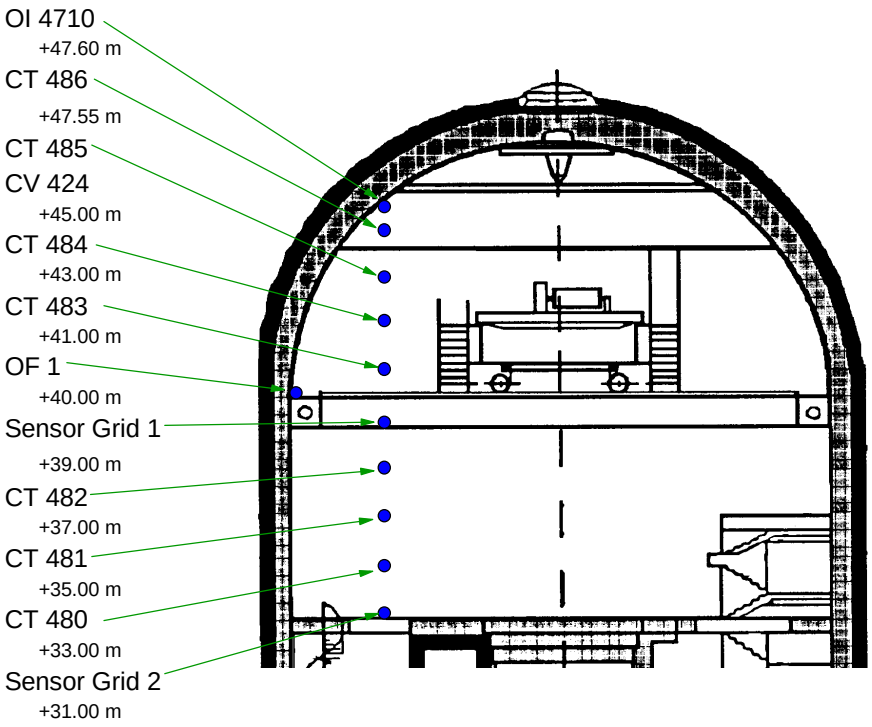

Figure 3.27: T52 Dome Plume Sensor Rake

4 TEST EXECUTION

4.1 Test Procedure

This section describes the test procedures for the oil pool fire test series T52. The test series was comprised of four individual tests designated T52.11-14. The test series varied the following parameters of interest:

- size of the initial pool
- rate of fuel supply after the initial fuel load
- rate of forced air supply

In order to simulate the different fire loads while minimizing the test setup efforts, fire load was controlled by changing the surface area of the fuel pool. The oil was burned in one of three different oil pans with surface areas of 1, 2, and 3 m^2 as shown in Figure 2.6. The smaller pans were placed into larger pans to comply with the test specification. Table 4.1 lists the oil pan arrangement for each test.

Table 4.1: Oil Pan Arrangement for T52 Oil Fire Test Series

Test	*Surface Area (m^2)*	*Pan Arrangement*
T52.11	1	Pan 1 into Pan 3
T52.12	2	Pan 2 into Pan 3
T52.13	3	only Pan 3
T52.14	2	only Pan 2

Prior to any given test, the pan was filled with fuel oil, SHELLSOL T, to a level of 25 mm, which yielded 25 liter per 1 m^2 of fuel pool surface area. Additional oil was supplied into the pan about 6 to 8 minutes after the ignition by an oil supply line. The HDR main control room could predose desired amounts of oil supplied such that the specified power level is reached; however the actual volumetric flow had to be manually adjusted by a fine regulation valve at the tank facility located outside the containment.

The oil pool was ignited remotely from the main control room using a special ignition device, installed into each oil pan. The device contained a small metallic can, that had three-side recesses covered with wax plates and contained 0.5 liter of methanol which was ignited with electrodes. One electrode was positioned at the alcohol surface and the other was located 0.5 cm above the surface. Switching on the ignition transformer produced an arc that immediately ignited the methanol. The resulting heat melted the wax plate covering the recesses and the flame propagated to the fleece by which the oil in the pan was ignited over a short time span. The complete burning of the oil surface was achieved within 2 minutes.

Total duration of each test was approximately 30 minutes. Table 4.2 provides an overview of all major operational data for each test of T52 oil pool fire test series.

The measured volumetric flow rates of the additional oil supplied to the pans for the specific experiments are shown in Figure 4.1.

Table 4.2: Major Operational Data for T52 Oil Pool Fire Test Series

Test ID		**T52.11**	**T52.12**	**T52.13**	**T52.14**
Oil Pan Size		1 m x 1 m	2 m x 1 m	3 m x 1 m	2 m x 1 m
Maximum Fire Power		2000 kW	3000 kW	4000 kW	3000 kW
Initial Amount of Oil		25 liter	50 liter	75 liter	50 liter
Ignition Time		11:10	10:53	9:20	11:40
Oil Feed Start Time		11:17	10:59	9:28	11:47
Oil Feed Finish Time		11:40	11:23	9:50	12:11
Total Oil Feed Time		22.42 min	23.97 min	22.33 min	23.37 min
Volumetric Flow rate	Planned	3.72 l/min	5.57 l/min	7.43 l/min	5.57 l/min
	Actual	3.77 l/min	5.59 l/min	7.38 l/min	5.54 l/min
Total Oil Supplied		84.6 liter	130.0 liter	164.75 liter	129.5 liter
Total Amount of Oil		109.6 liter	180.0 liter	239.75 liter	189.5 liter
End of Fire		11:44	11:27	9:55	12:15
Fire Duration		34 min	34 min	35 min	35 min

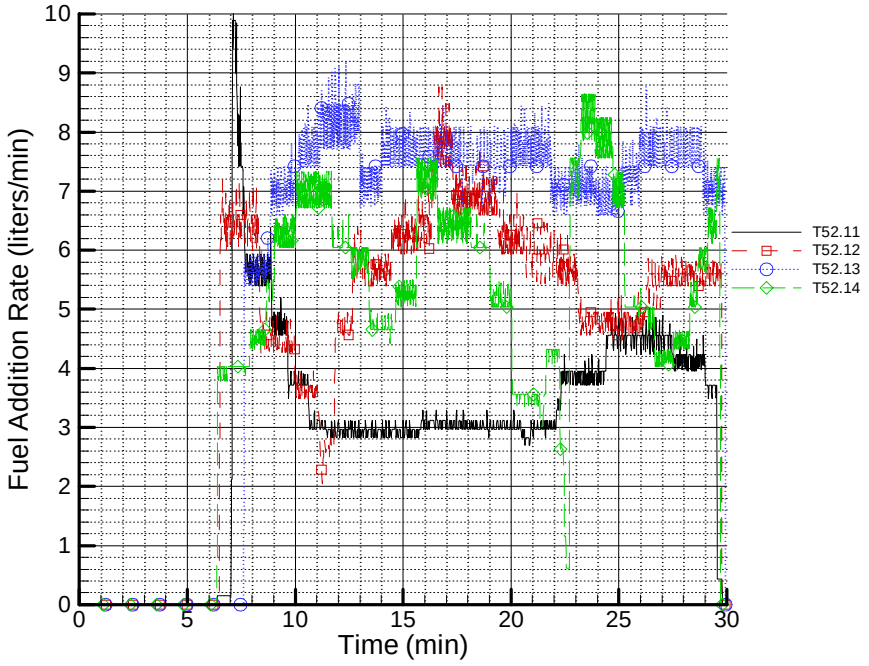

Figure 4.1: Fuel Addition Rate (RF7004)

4.2 Deviations From the Original Test Planning

The experiments T52.11 through T52.14 were performed during the planned time as anticipated and without major perturbations. A few noteworthy deviations are listed below:

- Contrary to the original planning, experiment T5.14 had to be used to replicate experiment T52.12 (3000 kW) because the burning rate was judged to be unreliable. This was thought to result from the relative movement of the pan-in-pan arrangement resulting from high thermal gradients in the oil pans. For single pan experiments like T52.13 (only pan 3) and T52.14 (only pan 2) the data were plausible.
- Minor deviations from the specified oil feeds listed in Table 4.2 and the transient flows are shown in Figure 4.1.
- The reactor building exhaust filter was not operational after experiment T52.14, see Section 5.3 for a discussion of the filter experiments.
- The replicated experiment T52.14 resulted in much higher fire room temperatures and higher temperatures in all other locations compared with T52.12, the test being replicated. Video observation also showed a quite different fire behavior. A possible explanation for these remarkable differences may be that the smaller oil pan resulted in an improved circulation around the oil pan by fresh, cool air sucked in from lower regions of the HDR facility through the maintenance hatch.

4.3 Measurement Quality

Although the majority of the measurement sensors worked properly throughout the Test Series T52.11-14 as anticipated, a number of sensors failed due to the specific characteristics of each experiment. The failure occurred specifically in the door region during T52.13 where the fire load was the highest among the four tests. The extremely hot flames exiting out to the maintenance hatch led to the failure of the NiCr-Ni thermocouples in this region. Furthermore, the temperatures in the lower door region as well as in the maintenance hatch were actually higher than anticipated and therefore the selected measurement ranges were too narrow for some of the thermocouples. Details on instrument failures are given in Section 3.

4.4 Test-Induced Damages

The T52 experiments did not result in any major damages to the facility or its equipment. However, a number of minor damages, sensor failures, and inconveniences did occur:

- T52.11 - The first color video camera in the fire room failed because of electronics degradation caused by soot formation. The camera was replaced by a new one which was better encapsulated.
- T52.13 and 14 - During both tests, the first protection glass of the pre-positioned infrared camera filter burst; however, the camera continued to operate.
- Sensor failures in the fire room doorway as discussed in Section 3.

- Totally unexpected by fire specialists and the HDR staff, a tremendous amount of soot and smoke formation developed throughout the whole building. This coated all vertical and horizontal surfaces with soot layers with thicknesses ranging from 1 to 9 mm. Soot retention and layers were also found in closed rooms as well as inside electronic cabinets, which were prepositioned to be specially protected against just such an occurrence.
- As all containment surfaces, including the dome's large steel shell surface, were involved, it took the HDR staff three weeks and 100 tons of special cleaning water to clean the facility. During that time span all other experiments were ceased. It was impossible to separate the soot from the wastewater on site.
- 44 thermocouples of different types were positioned in the fire room, all of them were not radiation shielded. NiCr-Ni and NiCrSi-NiSi thermocouples are designed for temperatures up to 1300 °C. For temperatures higher than that as observed during the T52 fire experiments, larger error bands apply. PtRh10%-Pt thermocouple systems are applicable up to 1600 °C, but only three of this type were used in the fire room. Temperatures in the fire room were so high during T52.13, that three thermocouples partially melted. 13 out of 44 thermocouples were electronically defective after this test. Outside the fire room, the failure rate was very low.
- Due to the high soot formation on the blades, the initial startup of the anemometers is expected to shift to progressively higher velocities during the testing program.

5 OVERVIEW OF EXPERIMENTAL RESULTS

This section contains selected results from the T52 oil fire tests performed in the HDR facility. Data from selected instruments for the four tests are shown in the first subsection to give a general overview of the transient histories and their similarities and differences. The second subsection shows contour plots of the measurement grid data averaged over 5 minutes starting at 20 minutes from the start of the oil fires.

5.1 Selected Results

This section shows selected results from each of the four T52 oil tests, T52.11 through T52.14. The first figure, Figure 5.1, shows the pyrolysis rate for each of the four tests. This rate is results from taking the sum of the three weight sensors, CA9601 through CA9603, beneath the oil pool platform. The quality of the measurements are such that it is likely the weight sensors were affected by the intense heat of the fire; however, the data are useful to indicate the basic evolution of the individual fires.

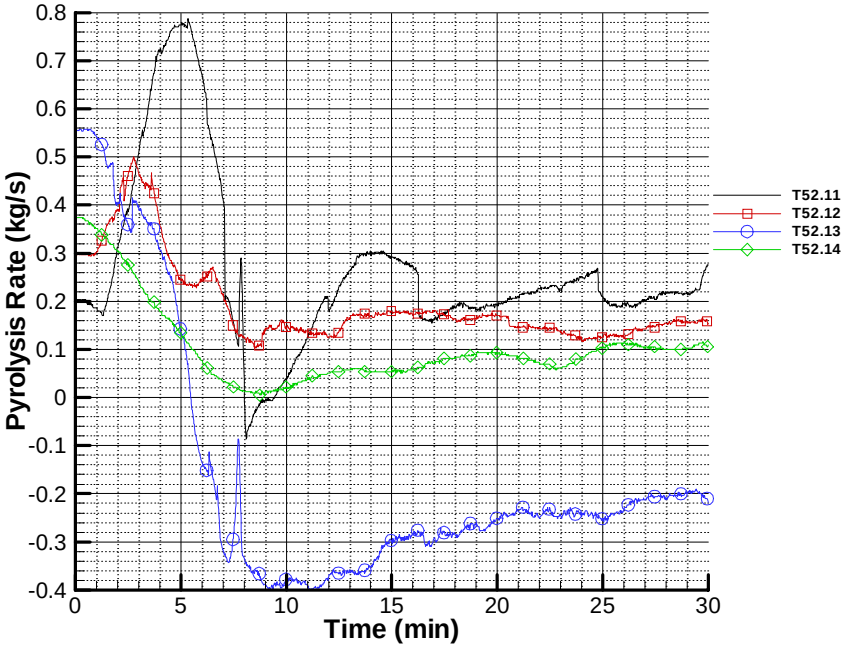

Figure 5.1: Pyrolysis Rate (CA9610)

The next figure, Figure 5.2, shows CT9616 which was located above the center of the oil platform. From this figure we can see that all four tests have the same evolution of the fire. However, it is interesting to note that T52.12 had a significantly narrower peak during the early phase of the fire and a lower temperature during the constant oil addition compared to T52.14 even though both tests had nearly identical initial oil volumes and oil delivery rates. The only difference between the tests was that T52.12 used the 2 m^2 oil pan inside the 3 m^2 oil pan whereas

T52.14 used just the 2 m^2 oil pan. It appears the added entrainment resulted in significantly higher temperatures.

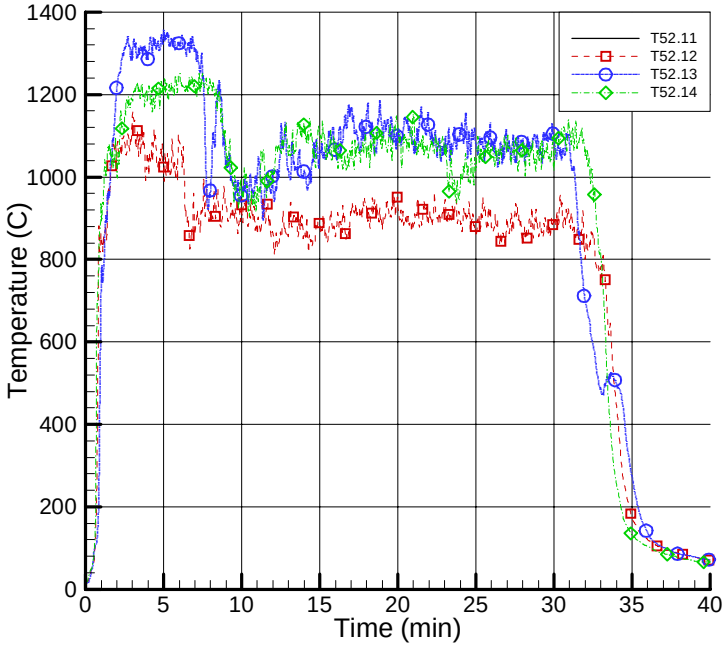

Figure 5.2: Fire Room Temperature Above Oil Platform (CT9616)

Figure 5.2 also shows the 4 phases that each of the fire tests underwent during the evolution of the fire. The first phase is the early growth phase in which the fire rapidly develops. For each of the tests the peak temperature is seen near three minutes after ignition. The second phase is a cooldown that occurs as the initial volume of oil is depleted. The third phase is a steady-state phase which occurs during the constant-rate oil addition. For all four tests this phase extended from approximately 12 minutes after ignition until the end of oil addition near 30 minutes after ignition. The final phase is the post-fire cooldown. During this phase the oil addition has stopped, the remaining amount of fuel in the oil pan is consumed, and the facility begins its cooldown.

Figure 5.3 below displays fire room temperatures above the corner of the oil platform closest to the fire room doorway. The same observations regarding profile and T52.12 and T52.14 that were made for Figure 5.2 apply to Figure 5.3. It is also observed that the temperatures for all tests are almost 200 °C lower near the doorway than over the middle of the fuel pool. This is at a separation distance of approximately two meters.

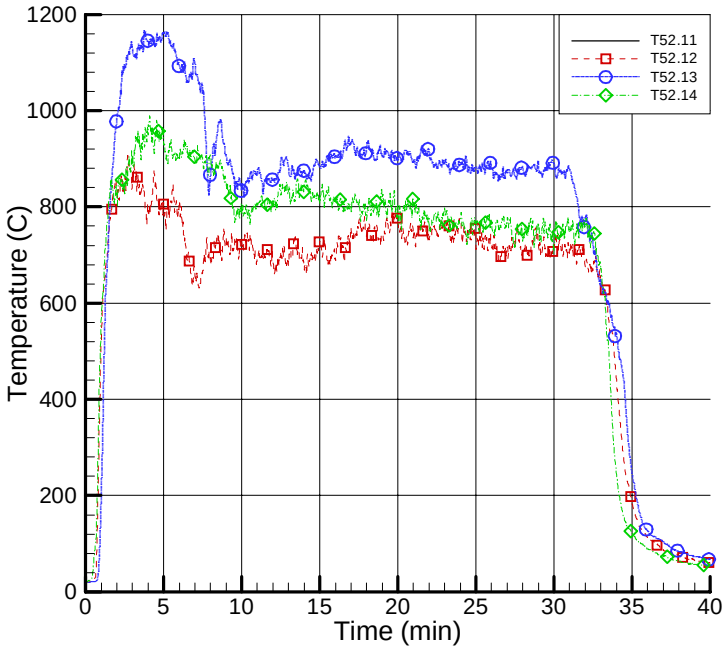

Figure 5.3: Fire Room Temperature Near Doorway (CT9611)

Temperatures in the diagonally opposite corner of the fire room are shown in Figure 5.4. A number of interesting observations can be made about this figure. First is that T52.13 has a peak temperature almost 500 °C above the other tests whereas the difference in Figures 5.2 and 5.3 is only 200 °C. Second, T52.12 and T52.14 have reversed their relative values. In Figures 5.2 and 5.3 T52.14 had higher temperatures by 200 °C. In this figure, T52.12 is higher by 200 °C. Third, in general, temperatures at this location are quite close to those measured in the doorway indicating the strong mixing occurring inside the fire room do to mass exchange at the doorway.

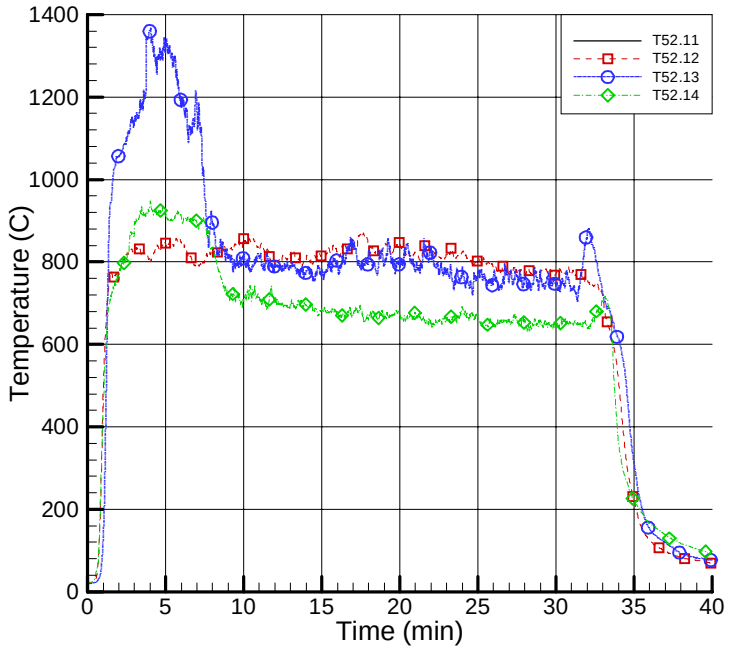

Figure 5.4: Fire Room Temperature Diagonal Corner From Doorway (CT9621)

The next two figures, Figures 5.5 and 5.6, plot the measured temperatures at the top and the bottom of the fire room doorway. Figure 5.5 shows that the steady state temperatures in the upper doorway do not vary much with the fuel delivery for tests T52.12 - T52.14. Similarly, for all but the highest power test, T52.13, the lower doorway temperatures do not vary with delivery rate. For both doorway locations there is a variance during the initial peak. Note that the flattened peaks for T52.13 and T52.14 for the lower doorway result from a range selection error in the data acquisition system. It is also observed that temperatures in the upper doorway match those seen in the fire room above the fuel pool indicating that little cooling of the combustion gasses is occurring before exiting the fire room.

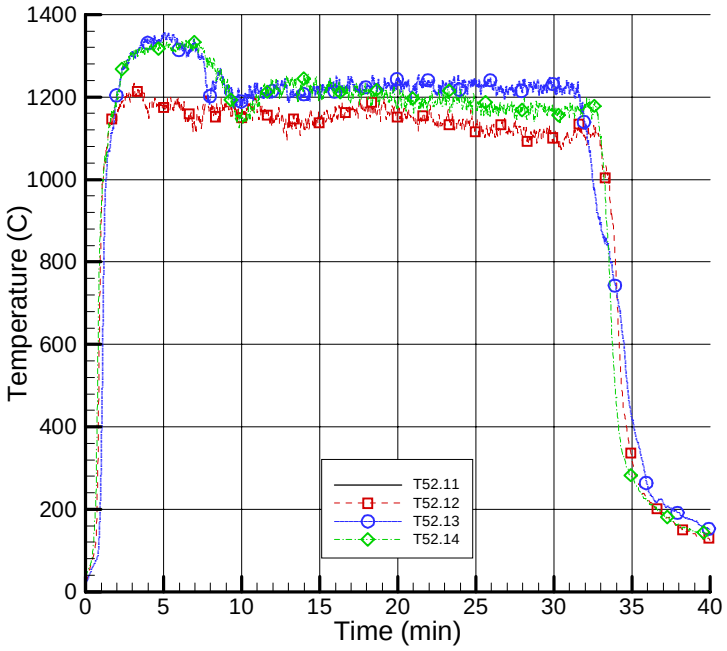

Figure 5.5: Temperature at Top of Doorway (CT9631)

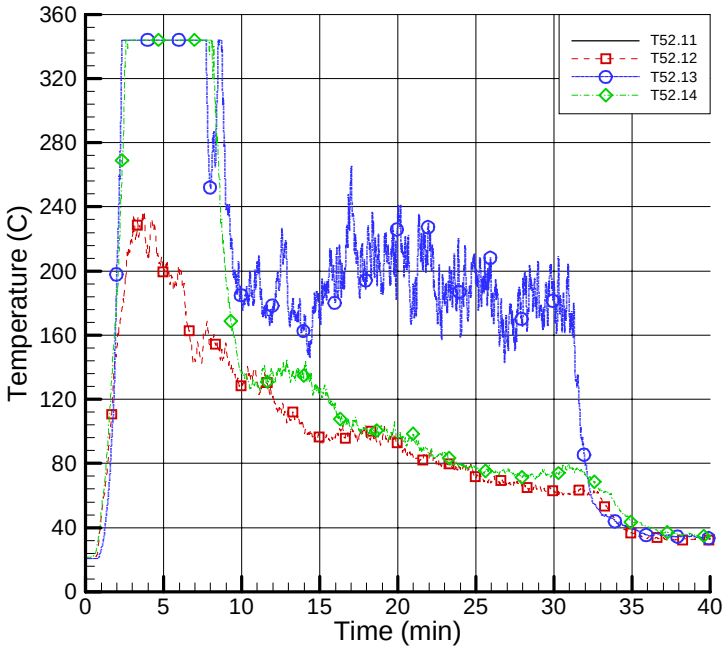

Figure 5.6: Temperature at Bottom of Doorway (CT9651)

Figures 5.7 through 5.9 display the measured O_2, CO_2, and CO concentrations in the upper doorway. Also note that as with the temperature sensors in the lower doorway, there was a range selection error in the data acquisition system for the CO sensor. The O_2 and CO data indicate that T52.11 remained well ventilated throughout the entire test. From all three charts it can be deduced that T52.12 was fairly underventilated during the early phase of the fire but became more ventilated during the constant oil addition phase. The large drop in CO_2 concentration with the accompanying spike of the CO concentration for T52.14 indicates that T52.14 had large quantities of unburned hydrocarbons leaving the fire room. This is bolstered by Figure 5.5 which shows flame temperatures for T52.14 in the upper doorway, indicating burning material leaving the fire room. Similar observations can be made for T52.13 as were made for T52.14.

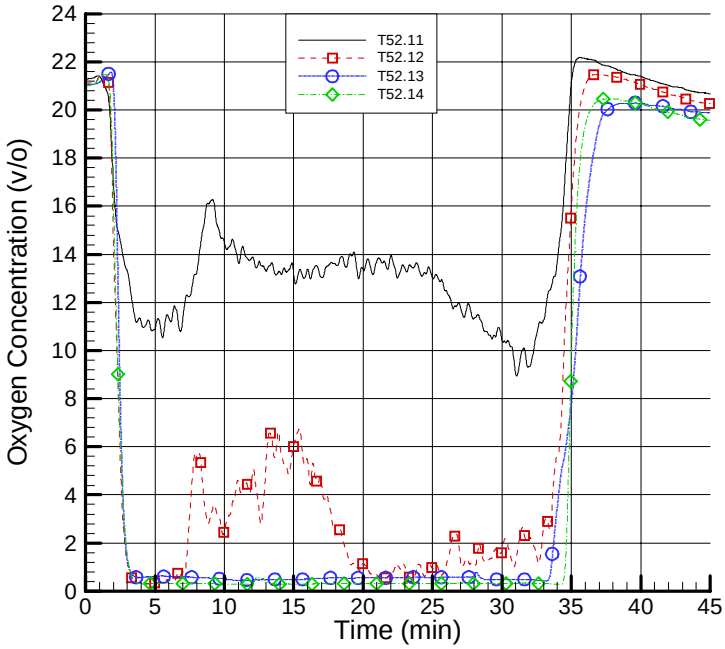

Figure 5.7: O_2 Concentration in Top of Doorway (CG9602)

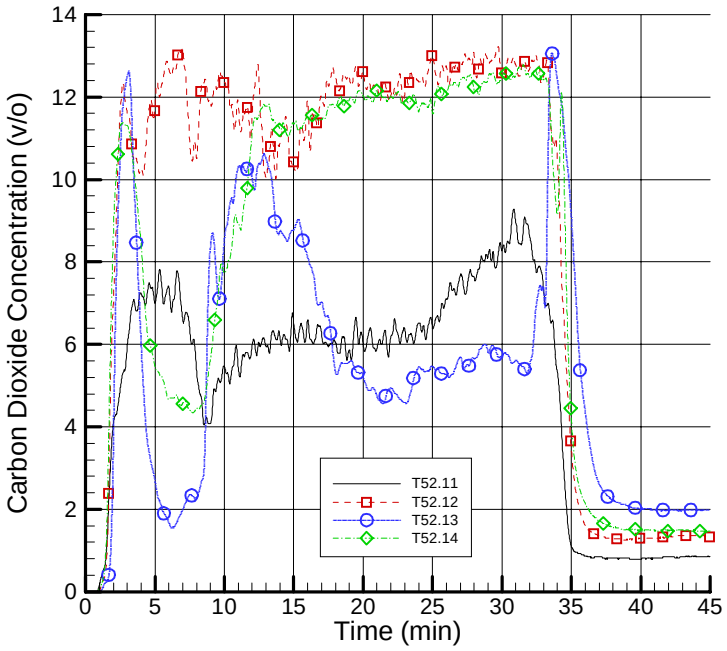

Figure 5.8: CO_2 Concentration in Top of Doorway (CG9603)

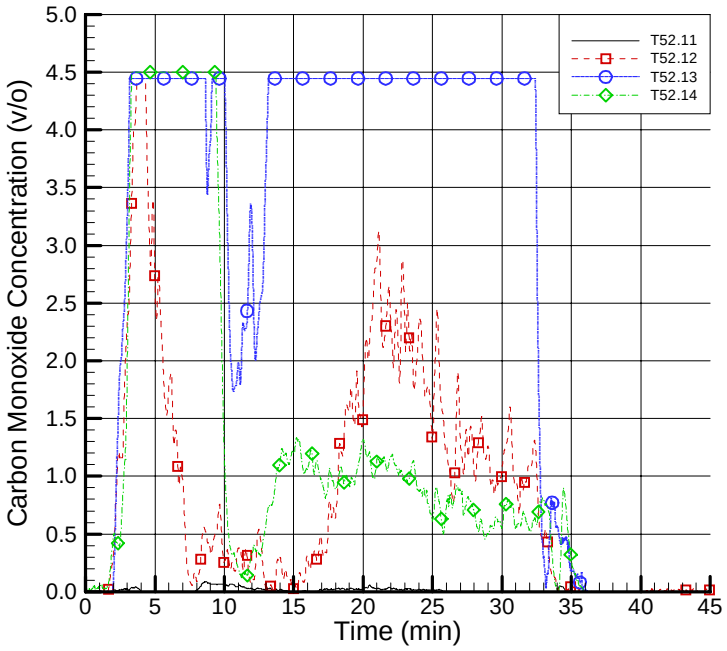

Figure 5.9: CO Concentration in Top of Doorway (CG9601)

The next figure, Figure 5.10, shows upper and lower-positioned velocities in the fire room doorway. All four tests show the same lower velocity profile. As this velocity is the oxygen rich air feeding the fire, one can see how the oxygen limited combustion arose in the later tests as the low power test, T52.11, shows the same basic inflow into the fire room as the higher power tests. Again the large difference between T52.12 and T52.14 is seen in the upper velocity leaving the fire room. Even though both tests had the same amount of fuel, T52.14 has velocities over twice those of experiment T5.12. Strangely, T52.13 velocities are slightly larger than T52.12 but much less than T52.14. This is unexpected as T52.13 was a higher powered fire than T52.14 and one would expect the higher power to be accompanied by higher velocities.

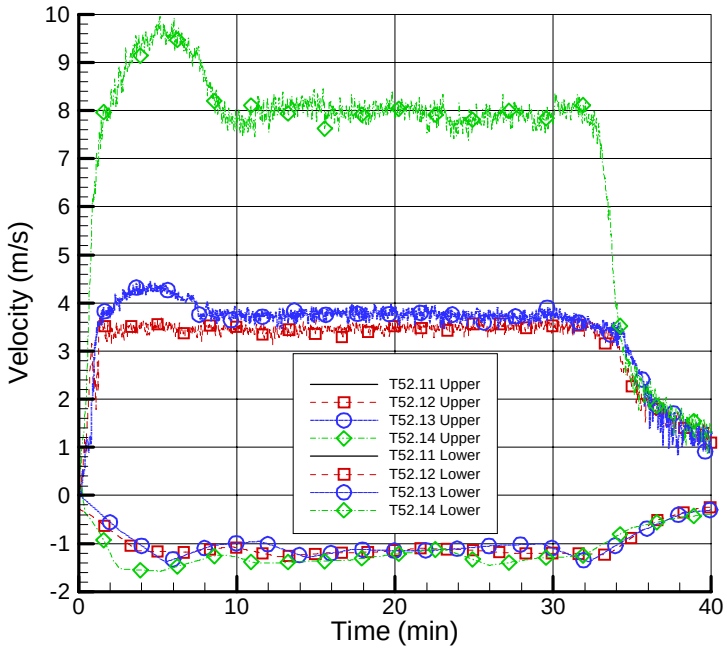

Figure 5.10: Doorway Upper (CV9600) and Lower (CV9606) Velocities

Figures 5.11 through 5.14 show temperatures in the center of the lowest sensor grid, the center of the middle sensor grid, in the center of the upper sensor grid, and just below the top of the dome. These figures show the basic development of the global circulation loop from its start below the fire room up into the dome. Substantial cooling of the plume is seen in the 8 m separation between Figures 5.12 and 5.13. It is interesting to note that T52.13 shows lower temperature than T52.14 in Figure 5.13. This most likely results in a shift of the plume centerline in one or both of the tests resulting in the sensor seeing a different region of the plume. Temperatures in Figure 5.14 show a slight temperature increase over T52.13 even though they are vertically separated by 10 m. As later contour plots will show, the plume centerline was closer to the outer edge of the grid. Thus this increase is due to the hotter plume center following the steel shell and thus shifting to be over the upper sensor. Figure 5.11 shows a temperature increase at the lower grid during the first phase of the fire which then drops back to a few degrees above the original

ambient temperature during the oil addition phase. This initial increase is due to radiative heat transfer from the hot, still burning, gas leaving the fire room doorway and rising into the dome.

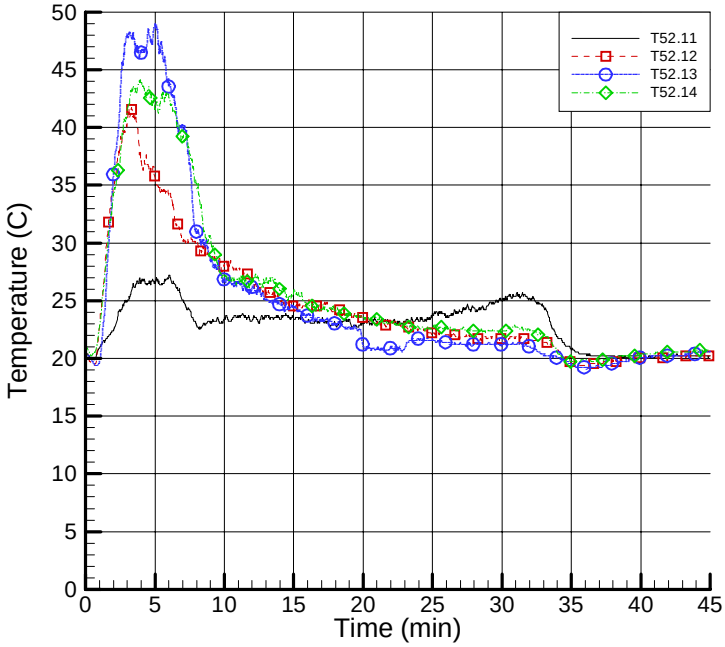

Figure 5.11: Temperature in Center of Lower Measurement Grid (CT9215)

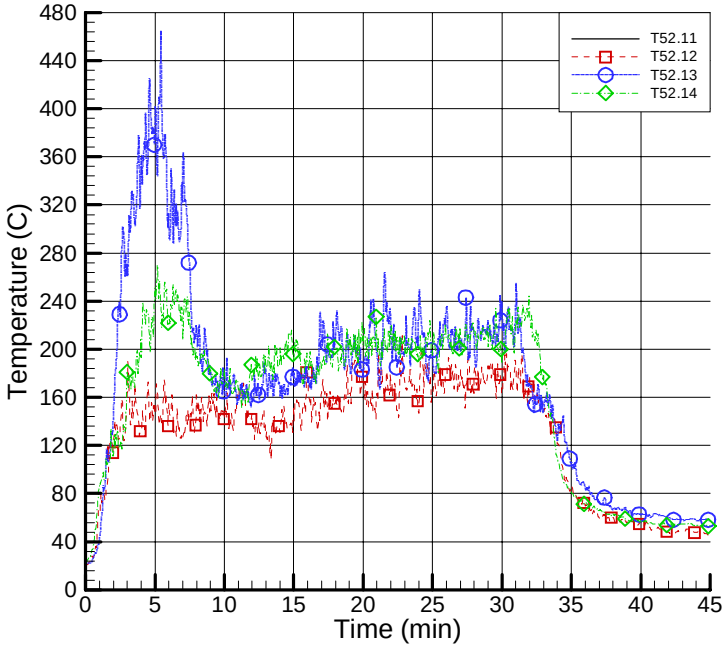

Figure 5.12: Temperature in Center of Middle Measurement Grid (CT 467)

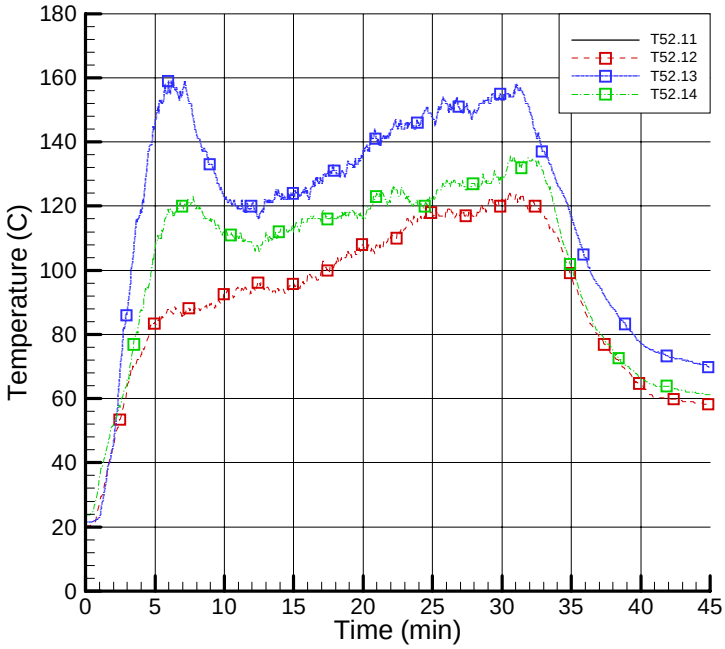

Figure 5.13: Temperature in Center of Upper Measurement Grid (CT 442)

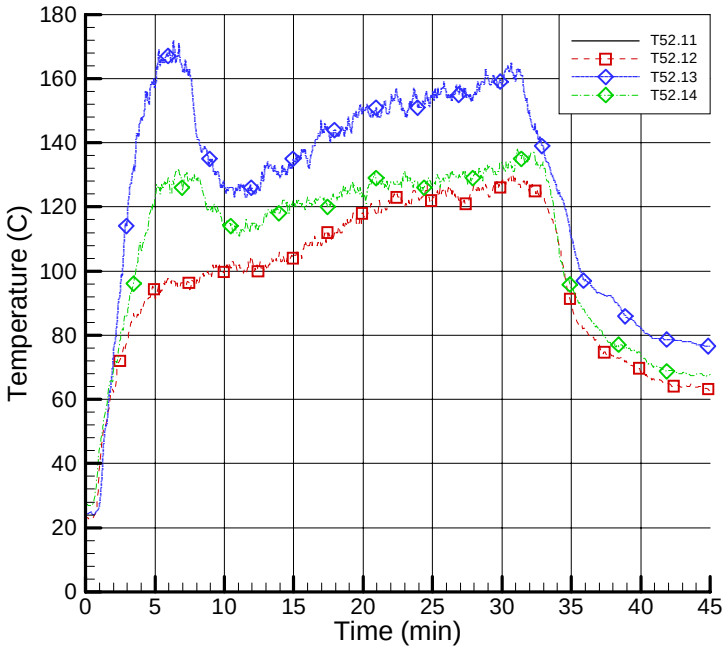

Figure 5.14: Temperature at the Steel Shell Above the Measurement Grids (CT 486)

Figures 5.15 through 5.17 show velocity measurements in the centers of each of the three measurement grids. Since plumes are multidimensional structures, these plots do not truly reveal the plume behavior for each of the tests. However, some observations can be made. Figure 5.15 shows similar behavior both in trend and magnitude for each of the tests indicating physical limitations on the ability of the fire to entrain air from lower regions of the containment. Figure 5.16 shows that a substantial flow is emanating from the fire level into the dome. This flow continues even after the end of the fire indicating that large stores of thermal energy absorbed by the walls of the fire room are still capable of inducing a global flow in the containment. Figure 5.17 clearly indicates that the fire plume is not passing through the center of the measurement grid at this location as the velocities are low, highly oscillatory, and drop below zero during the fire. At the end of the fire a flow reversal is seen as velocities become consistently negative at that location.

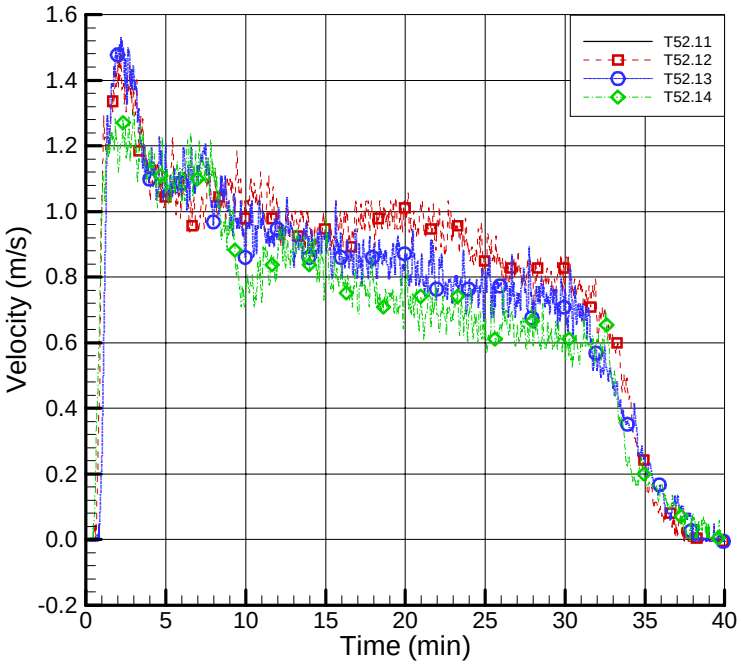

Figure 5.15 Vertical Velocity at the Center of the Lower Measurement Grid (CF9205)

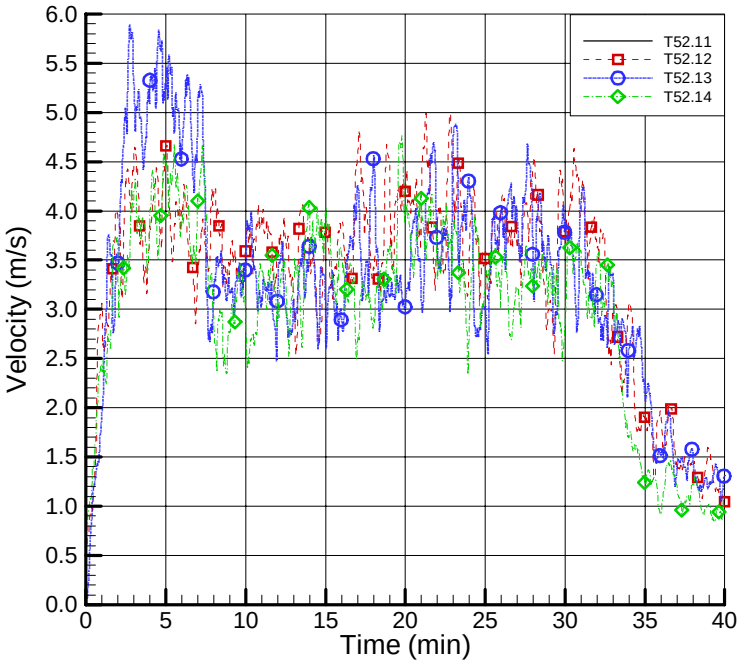

Figure 5.16 Vertical Velocity at the Center of the Middle Measurement Grid (CV 488)

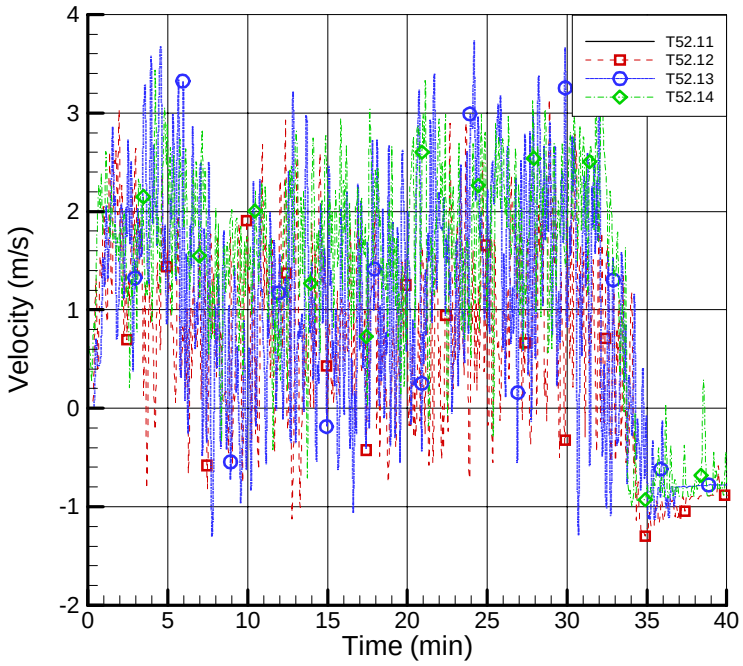

Figure 5.17 Vertical Velocity at the Center of the Upper Measurement Grid (CV 417)

Figures 5.18 through 5.20 plot CO_2 concentrations at the center of each of the measurement grids. These three figures show the transient evolutions of the CO_2 concentrations for all four T52 experiments and reveal the following characteristics:

1. CO_2 generation is a function of power and it continuously increases during the fire.

2. For positions high in the containment, the maximum values is reached at the end of the fire and for positions low in the containment, the maximum value is reached during the cooldown period. This results from the continued transport of CO_2-rich atmosphere from higher elevation as a result of continued global circulation and diffusion.

3. For T52 the maximum measured values range between 2 and 4.2 v/o for T52.11 and T52.13, respectively, at the position of the uppermost measurement grid, sensor grid 1.

4. For positions below the fire room, e.g. downstream of the dome in the direction of the global circulation, CO_2 concentrations are much lower as demonstrated in Figure 5.18. At this location, the lowest sensor grid, the measured CO_2 concentrations range between 0.9 and 1.7 v/o for T52.11 and T52.13, respectively.

5. Substantial transport times are visible along the circulation loop as can be seen by comparing the start of concentration increase from the start of the loop in Figure 5.19 to the end of the

loop in Figure 5.18. These times are 8 minutes for T52.11 and T52.12 and 5 minutes for T52.13 and T52.14.

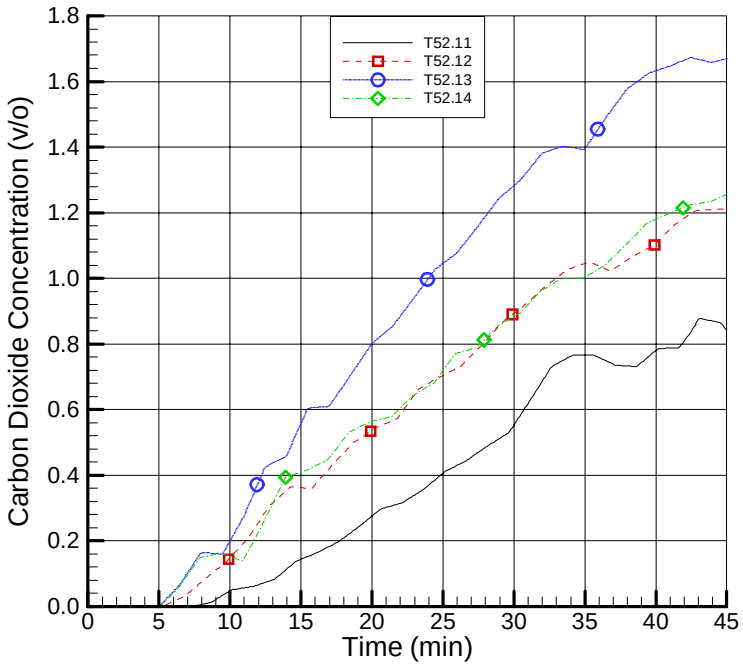

Figure 5.18 CO_2 Concentration at the Center of the Lower Measurement Grid (CG9201)

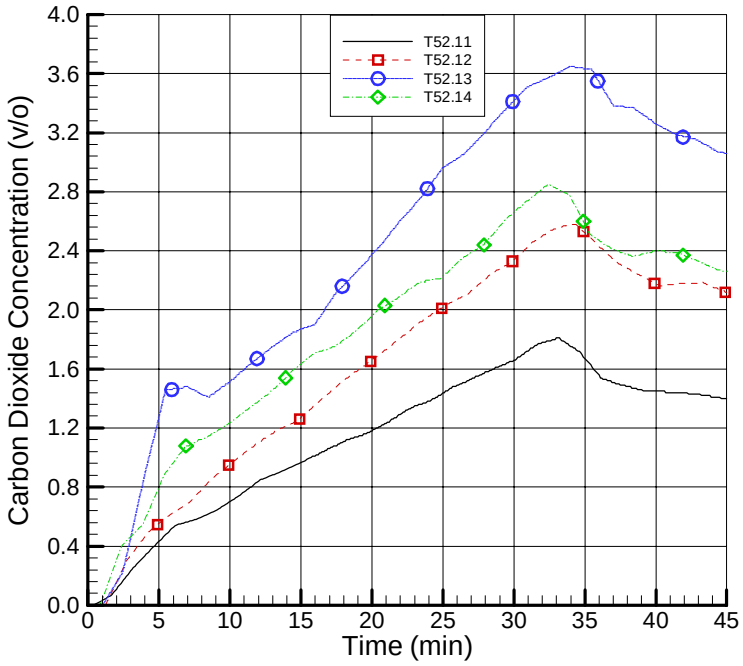

Figure 5.19 CO_2 Concentration at the Center of the Middle Measurement Grid (CG 424)

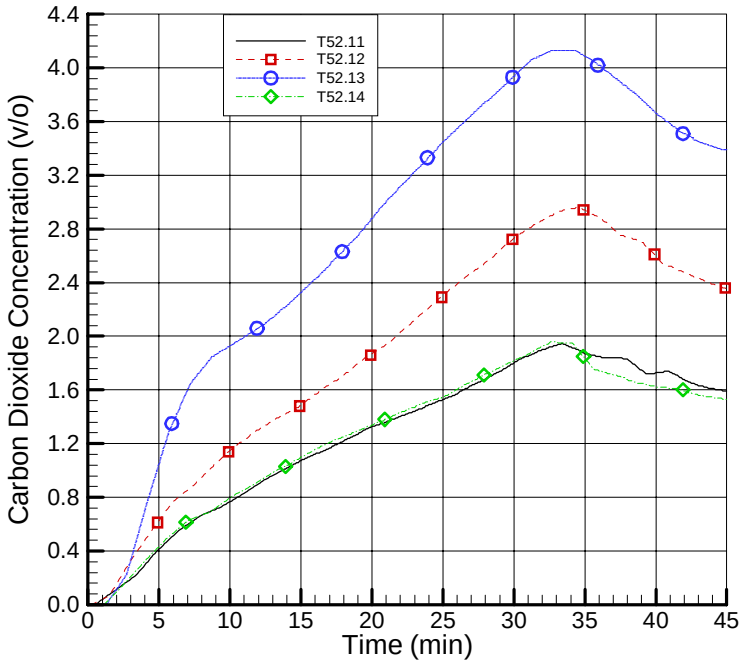

Figure 5.20 CO_2 Concentration at the Center of the Upper Measurement Grid (CG 415)

The next four figures, Figures 5.21 through 5.24, show temperatures at different locations around the global circulation loop: the main staircase maintenance shaft on the 1.900 level (CT9301), same side of the facility on the 1.600 level (CT6601), the 1.600 level on the spiral staircase side (CT6607) and below the fire room (CT8402) for each of the four T52 experiments. The following conclusions can be drawn from the experimental evidence regarding atmospheric temperatures:

1. Due to the tremendously efficient entrainment and mixing processes that act upon the fire plume as it rises through the maintenance hatch and propagates through the dome, temperatures have essentially decreased to the ambient background temperatures. This can be seen in Figure 5.21 where temperatures range from 27 °C for T52.11 to 37 °C for T52.13.

2. The respective temperature histories clearly depict the dependence upon the respective, experiment specific, fire powers with T52.11 and T52.13 setting the lower and upper bounds, respectively.

3. Dependent upon the experiment, transport delays range from 1 to 2 minutes.

4. Due to heat transfer and cooldown, temperatures of all four experiments completely equalize over all fire and cooldown phases at the lowest position in the main staircase shaft, except for the brief period of the initial transient fire phase when maximum temperatures are higher by 2 to 4 °C to the quasi steady-state fire period, see Figure 5.22.

5. As shown in Figure 5.23 for the spiral staircase side, further cooling occurs along the horizontal flow path at the 1.600 level. Surprisingly, the temperature for T52.14 drops below those measured for the other experiments.

6. As depicted in Figure 5.24, higher up in the spiral staircase at the 1.800 level, e.g. just below the fire room, temperatures increase due to thermal radiation from the proximity of the fire room doorway. This is clearly evident during the initial fire growth phase when the maximum of 34 °C is reached for T52.13. Also, the temperature level during the quasi steady-state phase increases slightly by 2 to 3 °C for all experiments.

In summary the following statements hold from the observations cited above:

1. No thermal hazards ensue at positions below a high-elevation fire source whose energy exits into a large dome (atrium) and follows a global circulation pattern through two long shafts interconnected at the bottom.

2. Rescue and interventions are certainly not hampered by temperature hazards.

3. All major equipment in a nuclear power plant is not subject to any thermal loads for conditions similar as those examined in the T52 test series.

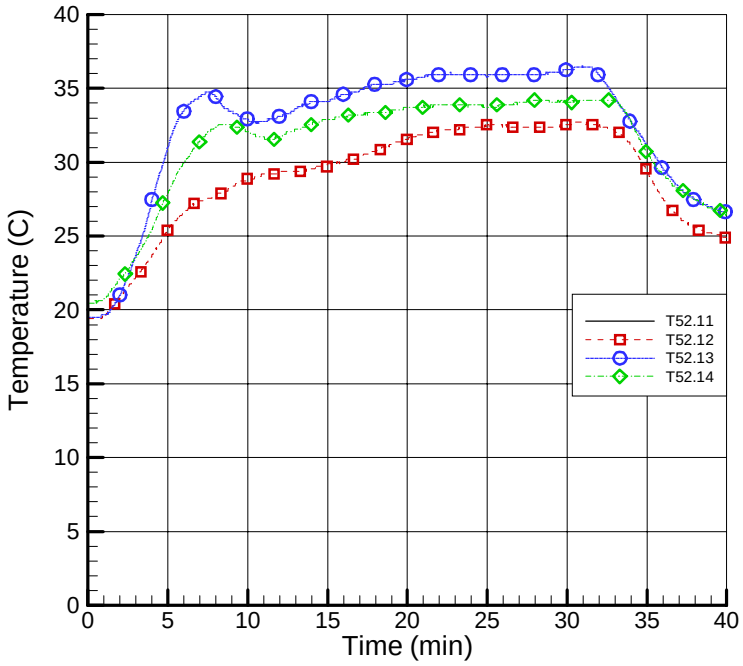

Figure 5.21 1.900 Level Temperature Main Staircase Side (CT9301)

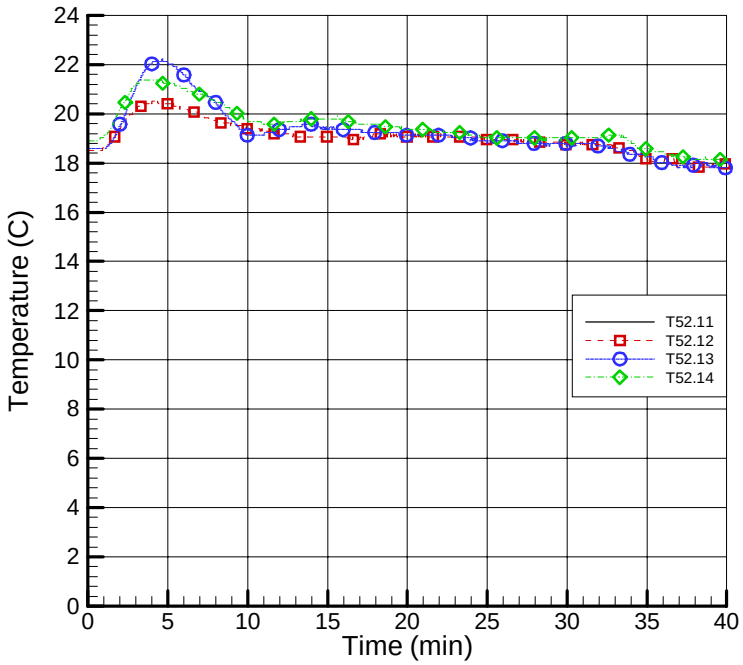

Figure 5.22 1.600 Level Temperature Main Staircase Side (CT6601)

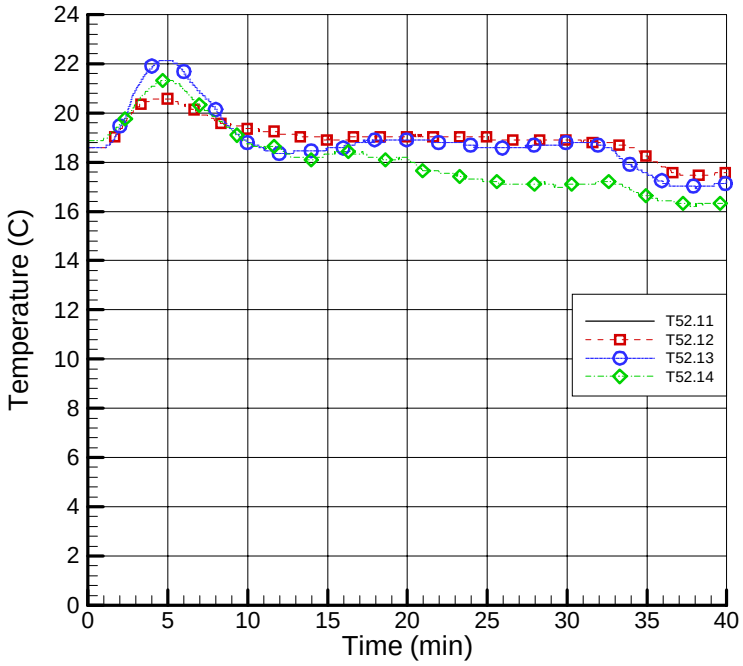

Figure 5.23 1.600 Level Temperature Spiral Staircase Side (CT6607)

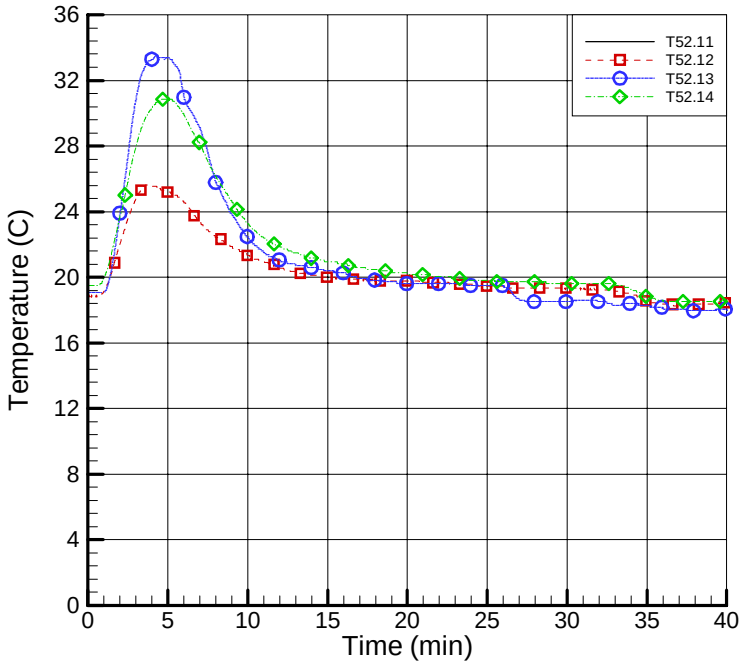

Figure 5.24 1.800 Level Temperature Spiral Staircase Side (CT8402)

The next two figures, Figures 5.25 and 5.26, display the CO_2 concentrations on the main staircase side on the 1.900 and 1.600 levels. These two figures continue the presentation of the evolution of CO_2 concentrations throughout the dome and into the maintenance shaft on the main staircase side. These figures complement Figures 5.18 through 5.20 which focussed on the fire plume characteristics on the spiral staircase side.

Figure 5.25 reveals the following behavior at the top of the main staircase maintenance hatch:

1. Transport delays of 2.5 up to 4 minutes have been measured for T52.13 and T52.11, respectively.

2. As already discussed for Figure 5.18 through 5.20, the upper and lower bounds are given by the data of T52.13 and T52.11, respectively.

3. CO_2 concentrations have been slightly decreased by entrainment and mixing as the plume wraps around the upper dome toward the maintenance hatch at the main staircase side.

4. Maximum values of 1.7 and 3.6 v/o are reached for T52.11 and T52.13, respectively, somewhat after the end of the fire, i.e. a time delay exists, and stay at that level.

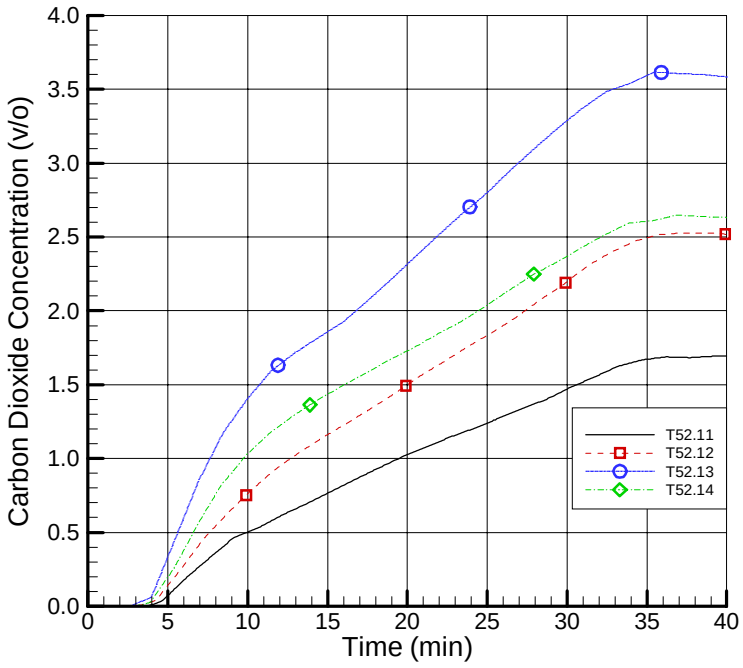

Figure 5.25 CO_2 Concentration on the 1.900 Level Main Staircase Side (CG9301)

Figure 5.26 shows the CO_2 concentrations at the bottom of the maintenance shaft on the main staircase side. The following conclusions can be drawn:

1. Transport times of about 8 minutes hold for each of the four experiments, e.g. it takes 4 minutes to transport CO_2 from the top to the bottom of the maintenance shaft over 16 m, which translates into an average velocity of 0.067 m/s (compare with later figures and comments about measured velocities).

2. The measured CO_2 concentrations are lower by a factor of two compared to those measured at the top of the shaft.

3. The characteristic order of increasing CO_2 concentrations with fire power increase only holds for the first 20 minutes and during the post-fire cooldown phase, while between 20 minutes and 35 minutes, the order is nearly reversed.

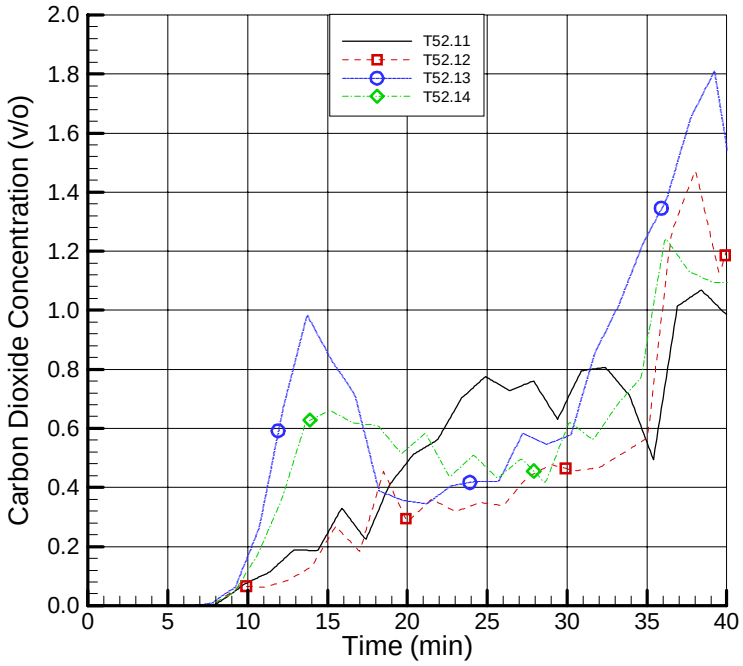

Figure 5.26 CO_2 Concentration on the 1.600 Level Main Staircase Side (CG6601)

Finally, Figures 5.27 through 5.29 show measured velocities around the flow loop at the 1.900 level (CF9301), the 1.700 level (CF7703), and the 1.700 level on the spiral staircase side (CF7802). These three figures display measured velocities at those positions for all of the four T52 experiments. The following conclusions can be drawn fron the information depicted:

1. Velocities on the opposite side of the fire room are only fractions of the velocities measured in the plume (compare to Figures 5.15 through 5.17).

2. Velocities scale with fire power.

3. The velocities in the maintenance hatch reach their maximum values at around 2 to 3 minutes after the fire started during the rapid, initial, fire growth phase with a peak velocity of 0.54 m/s reached for the T52.13 experiment.

4. Velocities during the quasi steady-state fire phase are much lower, by a factor of 5, reaching maximum values of only 0.1 m/s.

5. The data depict high frequency, large fluctuations during the quasi steady-state fire phase. The frequency contains certain periodicities.

6. As shown in Figure 5.28, two levels downward, at the 1.700 level, measured peak velocities are already reduced by a factor of two during the initial growth phase. No reliable measurement signal can be picked up during the quasi steady-state fire phase as the creeping flow is below the detection threshold of the sensor.

7. The situation is quite different at the same elevation at the opposite side in the spiral staircase as shown in Figure 5.29. Strong fluctuating velocities between 0.06 m/s and 0.15 m/s occur for the three high-powered experiments T52.12, T52.13, and T52.14 while a different pattern of fluctuating and periodic velocity changes are observed for T52.11, the lowest fire power experiment along with a much lower velocity.

8. While fluctuations completely ceased and the velocities reduce to zero for the three tests cited above at the end of the fire, for T52.11 the velocity increases abruptly up to peak values of close to 0.3 m/s and fluctuates with low frequency with decreasing amplitude during the cooldown phase.

In summary, the observations cited above clearly indicate different flow characteristics during different phases of the fires and in different positions in the global circulation loop. Some of these phenomena are locally confined and highly dependent upon the respective sensor position.

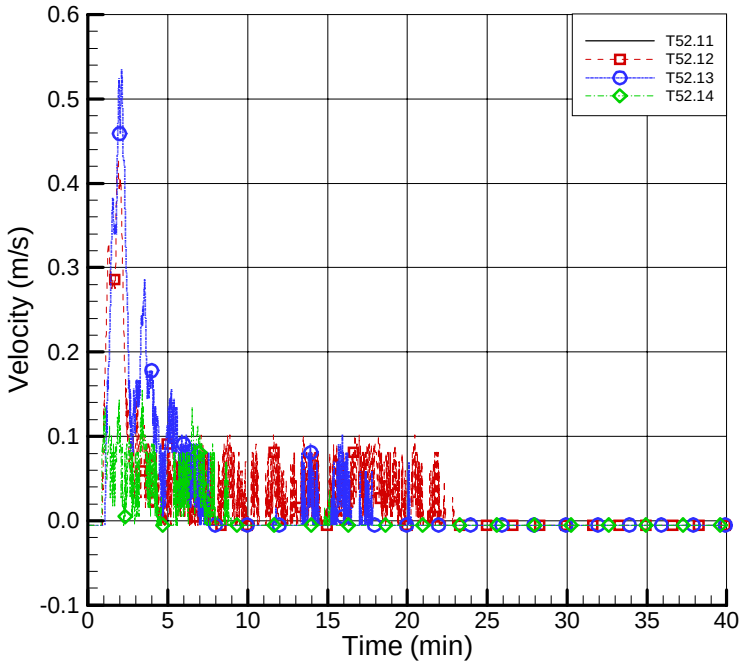

Figure 5.27 Velocity on the 1.900 Level Main Staircase Side (CF9301)

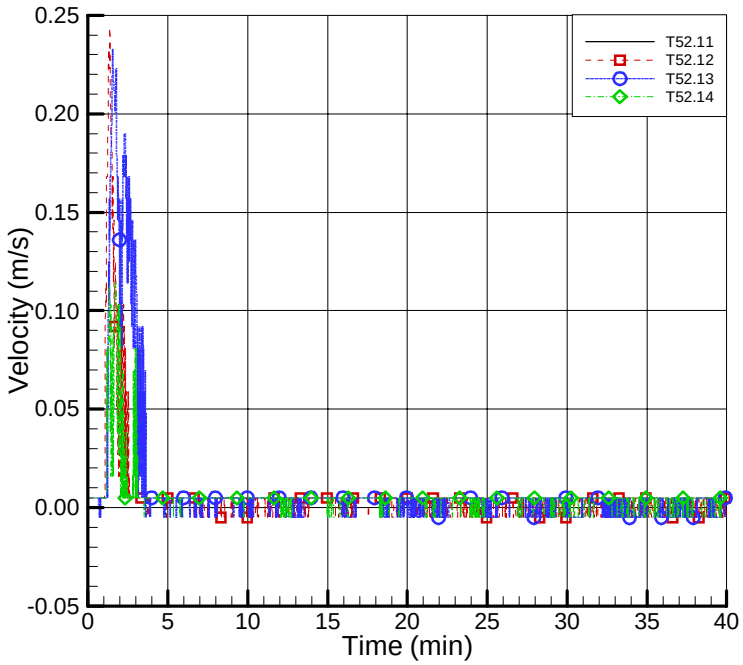

Figure 5.28 Velocity on the 1.700 Level Main Staircase Side (CF7703)

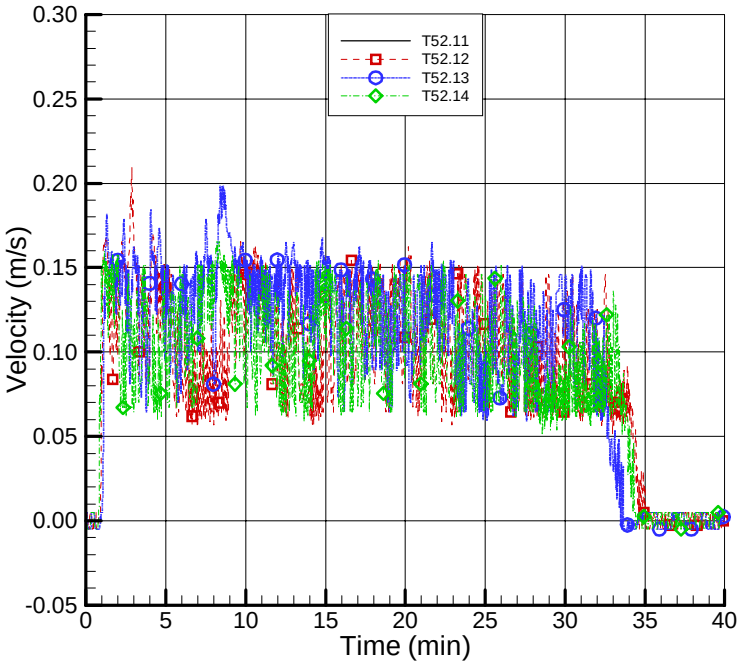

Figure 5.29 Velocity on the 1.700 Level Spiral Staircase Side (CF7802)

5.2 Representative Experimental Results from Sensor Arrays

This subsection shows contour and profile plots of the various arrays of sensors in the HDR for the all four of the experiments of T52 test series. Measured data were averaged over five minutes starting at 20 minutes past the start of the fire before rendering the plots. This time represents a time phase in the tests where sufficient time has passed since the start of continuous oil addition to establish quasi-steady state conditions.

The first set of contour plots, Figure 5.30, shows temperatures in the fire room above the oil pool platform at +27 m in elevation. For the purpose of orientation it is worth mentioning that the fire room doorway is located at the left of the top boundary of the region shown. Furthermore, the two-dimensional sections assembled in Figure 5.30 span the area provided by the two-dimensional array of thermocouples located at +27 m elevation and enclosing the oil pan as displayed in Figure 3.18. In other words, the cross-sections do not show the whole cross section of the fire room.

The contours were constructed from the discrete thermocouple locations by performing a Kriging interpolation. Since only one thermocouple (CT9616 at the pool center) was located over the pool, the interpolated temperature field may introduce a certain level of ambiguity. Therefore, the results shown in Figure 5.30 for the individual T52 experiments should be interpreted with care and not taken as face values. Furthermore, the results are best viewed in conjunction with the temperature, Figure 5.31, and velocity profile, Figure 5.32, plots over the door height. From the

latter two figures it is apparent that the 27 m plane is located in the region of the lower, inflowing gas layer, but close to the neutral plane of zero velocity.

With this background information in mind, the following conclusions can be drawn from Figure 5.30 for the temperature field at the +27 m elevation plane.

1. The temperature field in the fire room is highly asymmetric due to both the asymmetric location of the doorway and the horizontal circulation pattern of the incoming "colder" lower gas layer as it flows around the oil pan.

2. The peak temperature occurs on the right of the doorway side and not in the center of the oil pan.

3. Peak temperature and asymmetry increase with fire power.

4. The horizontal circulation patter in controlled by the oil pan size used during the individual experiments.

5. With reference to the temperature profiles shown in Figure 5.31 it is apparent that with increasing fire power, underventilation increases and combustion outside the fire room becomes more important. As a consequence, the temperature in the "colder" lower gas layer at +27 m increases from a low 200 C for T52.11 up to 600 C for T52.13. This increase occurs due to both radiation heat transfer and energy transfer across the stratified interface.

6. As the incoming gas layer temperature increases, the temperature inside the fire room increases and the region of maximum temperature expands in size.

In summary of the aforementioned observations it must be stated that the T52 experiments show:

1. High thermal asymmetries in the fire room

2. Distinct circulation patterns in the fire room

3. Preheating of the incoming low gas layer by combustion occurring in the upper gas layer outside the fire room

In total, the above three conditions provide stringent challenges for all types of computational fire simulation, foremost zone models but also multidimensional CFD codes.

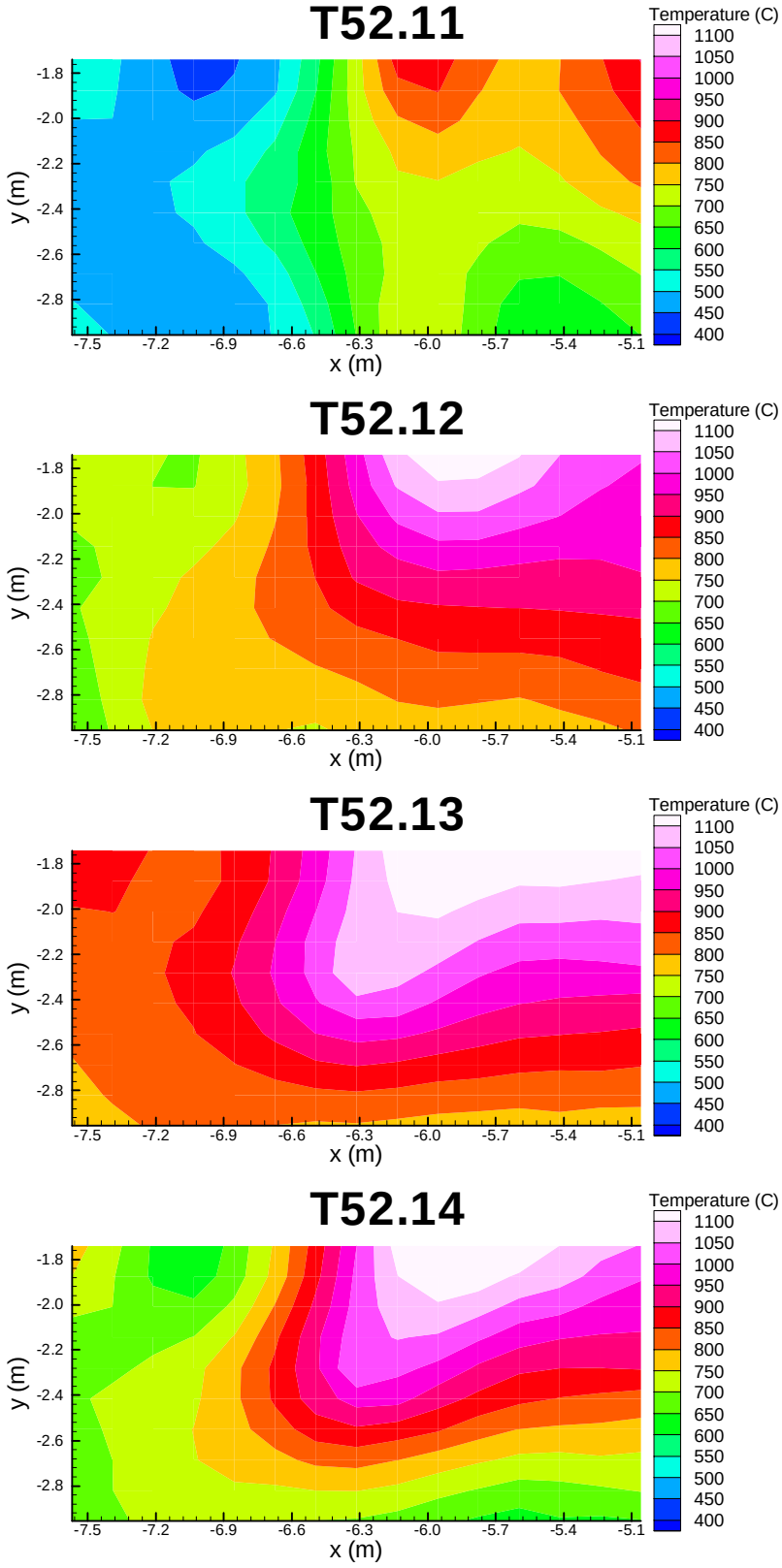

Figure 5.30: Fire Room Temperatures at +27 m at 20-25 Minutes

The second set, Figure 5.31, show the temperature profiles in the doorway, and the third set, Figure 5.32, shows velocity profiles in the doorway. The axial profiles shown in Figures 5.31 and 5.32 have been obtained by time-averaging the signals between 20 to 25 minutes of all of the sensors positioned in rakes as documented in Figures 3.19 and 3.20 respectively. The following conclusions can be drawn from Figures 5.31:

1. Extremely large axial temperature gradients exist over the height of the doorway and the gradients increase with fire power.

2. The largest axial temperature occurs over a rather thin gas layer between +27 m and +27.4 m for each experiment.

3. As seen in Figure 5.32, this layer encompass this layer encompasses regions below and above the neutral plane.

4. For the high-powered, underventilated fire tests T52.13 and T52.14 the temperature profiles across the upper layer are essentially uniform with temperatures of 1200 °C and 1150 °C, respectively which indicates that combustion is occurring outside the fire room.

5. Consequently, the upper portion of the lower layer is substantially heated up be thermal radiation and energy transfer across the stratified interface for both experiments to temperatures as high as 600 °C and 450 °C, respectively.

6. Contrary to T52.13 and T52.14, the other two tests show more or less steep axial temperature gradients across the upper layer; in the case of T52.12 the gradient amounts to 350 °C, while for T52.11 it is about 200 °C.

7. For all experiments, the peak temperatures in the upper layer occur close to the doorway top at the highest positioned thermocouple.

8. As indicated by the temperature profiles across the upper layer for experiments T52.11 and T52.12, the upper layer itself obviously consists of numerous sublayers itself, leading to obvious and distinct discontinuities in the temperature profiles in cases of well-ventilated fires.

9. The lower layer is characterized by much lower averaged temperatures in all experiments.

10. For the well-ventilated experiments, T52.11 and T52.12, the axial temperature profiles over the lower layer height are pretty much uniform and of about the same shape. However, the increase in the temperature in the upper portion of the lower layer from 200 °C for T52.11 to 350 °C for T52.12 is very noticeable.

11. These increases are much more pronounced for the underventilated experiments, T52.13 and T52.14, for which temperatures are as high s 600 °C and 450 °C, respectively, for the reasons already mentioned above.

12. For T52.13 and T52.14 the details of the axial temperature profiles are not traceable over most of the lower layer height because of three thermocouples that failed at the respective positions.

In summary, due to the many thermocouples placed in the fire room doorway rake, a tremendous amount of temporal and spatial information is available to such a detail which would merit further investigation with CFD codes along the line of the FDS applications as documented in [38].

Naturally, these details are beyond the scope and outside the realm of zone models such as CFAST. Nevertheless, plenty of data are available to derive representative averages for the two zones for comparison purposes.

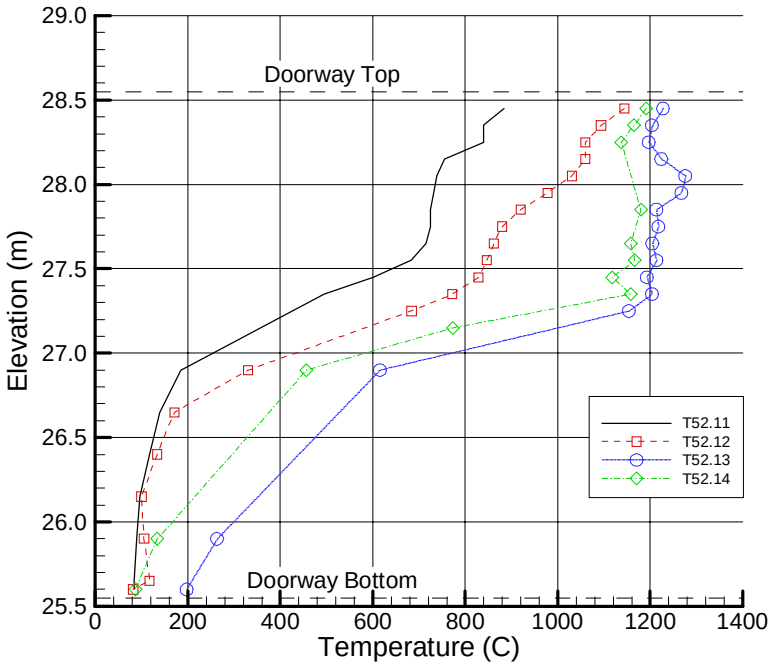

Figure 5.31: Doorway Temperature Profile at 20-25 Minutes

The velocity profiles shown in Figure 5.32 are less detailed than the temperature profiles shown above. This is because a much lower number of velocity sensors were used in the velocity rake. Naturally the temperature and velocity profiles are tightly coupled, e.g. the data given in both Figures 5.31 and 5.32 should actually be assessed simultaneously.

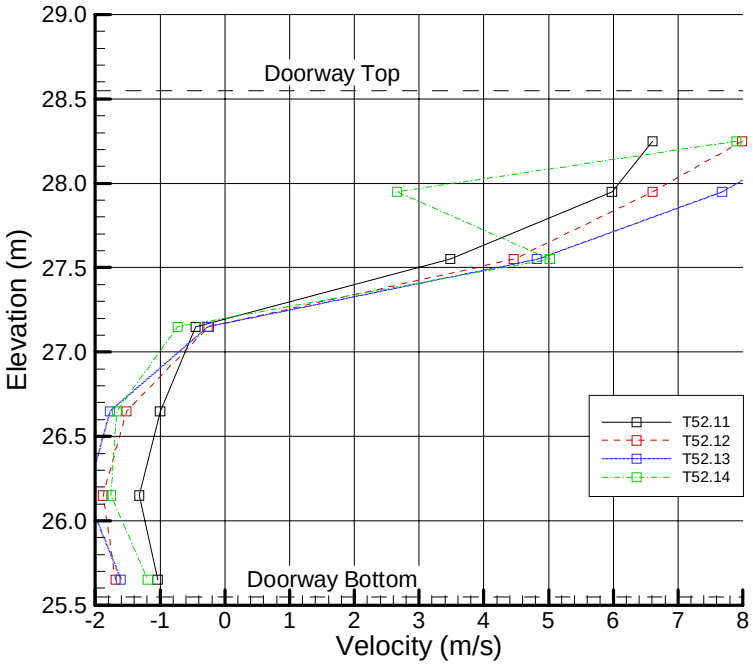

Figure 5.32: Doorway Velocity Profile at 20-25 Minutes

The following conclusions can be drawn from Figure 5.32:

1. The axial velocity profiles show the typical characteristic of a stratified, counter current, flow situation; e.g. high velocity gasses exiting the fire room in the upper layer and opposing, lower velocity flow entering the fire room over the lower layer.

2. A steep axial, velocity gradient of 5.5 m/s occurs over a thin region of 0.25 m for the fire experiments. The gradient increases with increasing fire power going from 4 m/s for T51.11 to 5.5 m/s for T52.13.

3. Peak outward velocities in the upper layer reach values of 8 to 9 m/s for the higher powered tests while being somewhat lower, 6.5 m/s, for T52.11. These may not be real maximum velocities as the somewhat sparse sensor array may not have captured the highest velocity.

4. Peak inward velocities in the lower layer are much lower, ranging from 1.4 m/s for T52.11 to 2 m/s for T52.13.

5. The velocity profiles are highly asymmetric over the upper layer with the peak velocity shifted toward the top of the doorway. Velocity profiles in the lower layer are more symmetric with the peak velocity near almost halfway between the neutral plane and the floor.

6. The erratic profile for T52.14 in the upper layer is a result sensor CV9601 failing.

In summary, while the axial velocity profiles in the doorway do not show as much detail as the temperature profiles discussed before, the information is sufficient for further assessment of CFD codes' predictive qualities as already initiated in [38] for the FDS software. This is especially true when done in combination with the temperature profiles. For zone models, the velocity profiles may have just sufficient information to derive layer-averaged values for comparison purposes. For the conditions tested during the T52 test series, the average velocities in the lower layer range between 1.3 m/s up to 1.6 m/s, while they range from about 4.5 m/s up to 6.5 m/s for the upper layer.

The next two sets, Figures 5.33 and 5.34, show contour plots of the temperature and gas concentrations in the middle sensor grid, see Figures 3.21 and 3.22, at the dome operating deck. The contours were generated in the same manner as described for Figure 5.30 and the same limitations apply to the plots. The plot boundary is given by the outermost sensors in measurement grid 2. For the purposes of orienting the reader, the fire room doorway is located on the left side of the bottom boundary.

From the temperature fields depicted in Figure 5.33, the following conclusions can be made:

1. The plume center is asymmetrically offset from the center of the measurement grid with peak temperatures occurring on the lower left side of the grid for all four experiments.

2. The right side corner regions show extremely low temperatures indicating the possibility of counter current flow from the operating deck downward into the maintenance hatch, thereby providing a cold source for entrainment and mixing purposes with the ascending plume.

3. Peak temperatures at that elevation are reduced by as much as up to 600 °C when compared to the upper layer temperatures exiting the doorway a short distance below the operating deck.

4. The fire plumes all four experiments obviously occupy only a fraction of the cross section of the hatch to the dome.

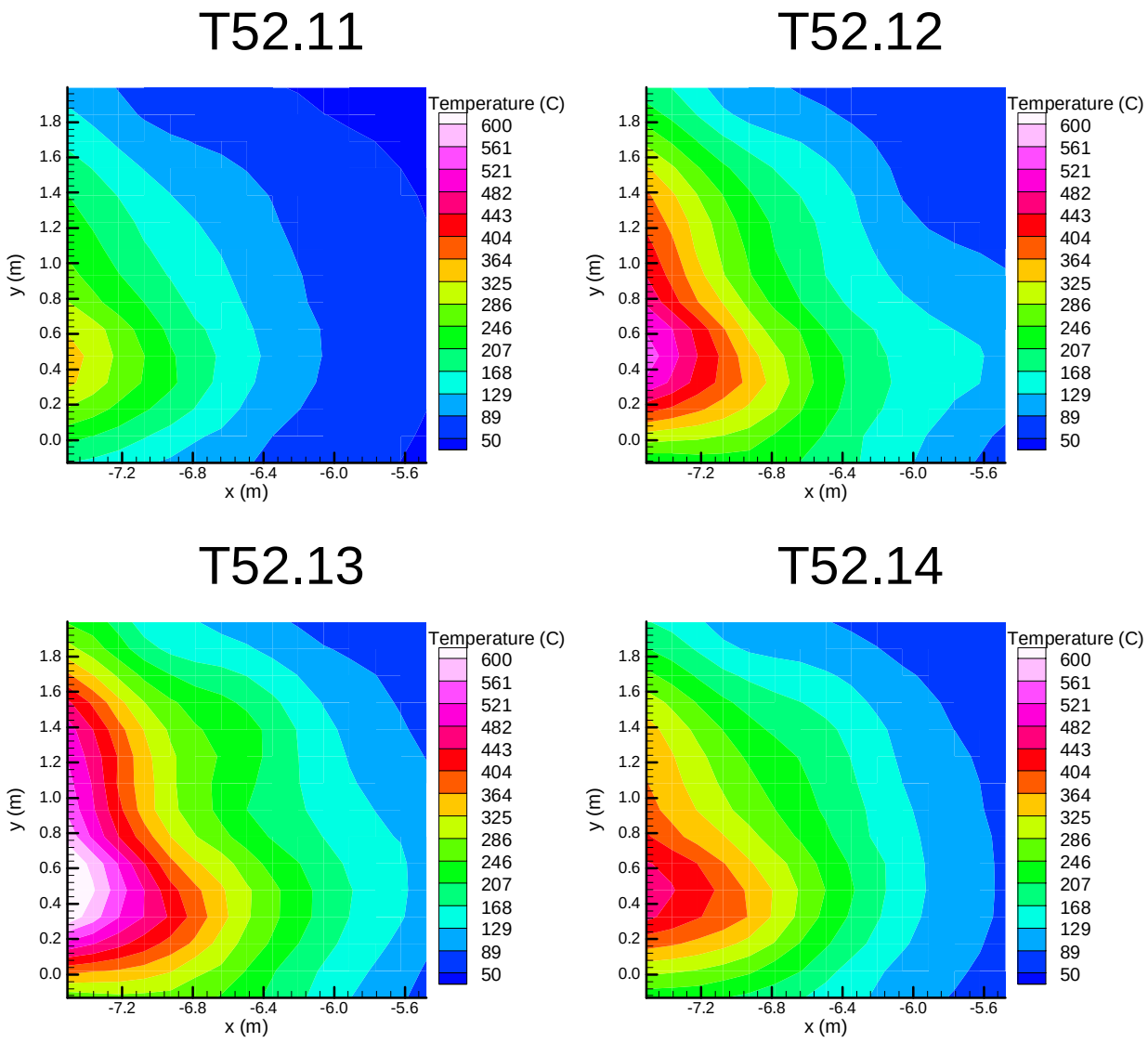

Figure 5.33: Middle Sensor Grid Temperatures at 20-25 Minutes

In summary, the observations cited above clearly indicate the introduction of additional asymmetries into the data actually by means of the geometrically asymmetric arrangement of the doorway exit into the maintenance hatch. Contrary to the expectations by the design team, the fire plume did not center itself; rather it attached to the left hand side wall remained attached to it up to the exit into the dome as far as can be inferred from available measurements. As a consequence, the plumes only occupy a part of the vent cross section allowing counter current downflow into the containment hatch thereby continuously supplying cold dome atmosphere for entrainment and mixing. As a final consequence, a dramatic drop in peak temperatures over a short distance occurs. This in turn results in much lower than expected plume temperatures in the dome. As much as this is of highly technical interest for mitigating fire hazards, it poses an unexpected deviation and additional complications for code validation efforts. These complications relate to the facts that:

1. Zone models are not prepared to analyze plumes taking up only fractions of the horizontal vent cross sections.
2. Zone models in fire analysis codes are not prepared to cope with vertical counter current flow situations in vents, at least CFAST is not.
3. The data measured in the two dimensional grid 2 cannot be used simply as transient prescribed boundary conditions for simulating clear cut few room models by CFD codes below the operating deck nor can it be used to drive a stand-alone dome model. This is due to the lack of sufficient velocity information due to sensor failures.

Figure 5.34 shows the two-dimensional CO_2 concentrations in the hatch leading to the dome for all for T52 experiments. These contour plots tell about the same story as discussed before for the temperature contour plots. The following observations hold here:

1. The CO_2 concentrations are asymmetrically distributed over the vent cross section with the peak concentrations measured at the left side of the vent in line with the peak temperature locations observed in Figure 5.33.
2. Peak CO_2 concentrations are slightly more centered than the peak temperatures.
3. Maximum CO_2 concentrations increase with increasing fire power. The highest concentration measured was 4.25 v/o for T52.13.
4. Rather similar contour patterns evolve for each experiment.
5. The right side regions and corners have much lower CO_2 concentrations, e.g. the profile is highly skewed; concentrations there are in the range of 1.35 v/o up to 2.8 v/o for T52.11 and T52.13, respectively. In other words, CO_2 occupies the whole cross section, albeit with highly varying concentrations. This essentially means that the colder, downward flowing dome atmosphere, see discussion above, is being premixed with CO_2 higher up over the 20 minutes the fire already lasted.

For measurement grid 2, no two-dimensional velocity contours can be derived because of the lack of data. On the one hand, velocity sensors placed into the grid were not able to cope with the crossflows that resulted from air entrainment into the plume rising asymmetrically through the hatch. The original planning assumed the plume would cover the whole hatch. One the other hand, valuable data were unknowingly declared implausible and eliminated from the data sets because they showed negative velocities due to the unanticipated counter current flow which was not realized at the time of the original data assessment immediately following the test series. This is unfortunate and irreversible but at the same time symptomatic for the mindset and limitations set forth by the zone models as the methods of choice at that time as 3D CFD fire analyses were still in their infancy.

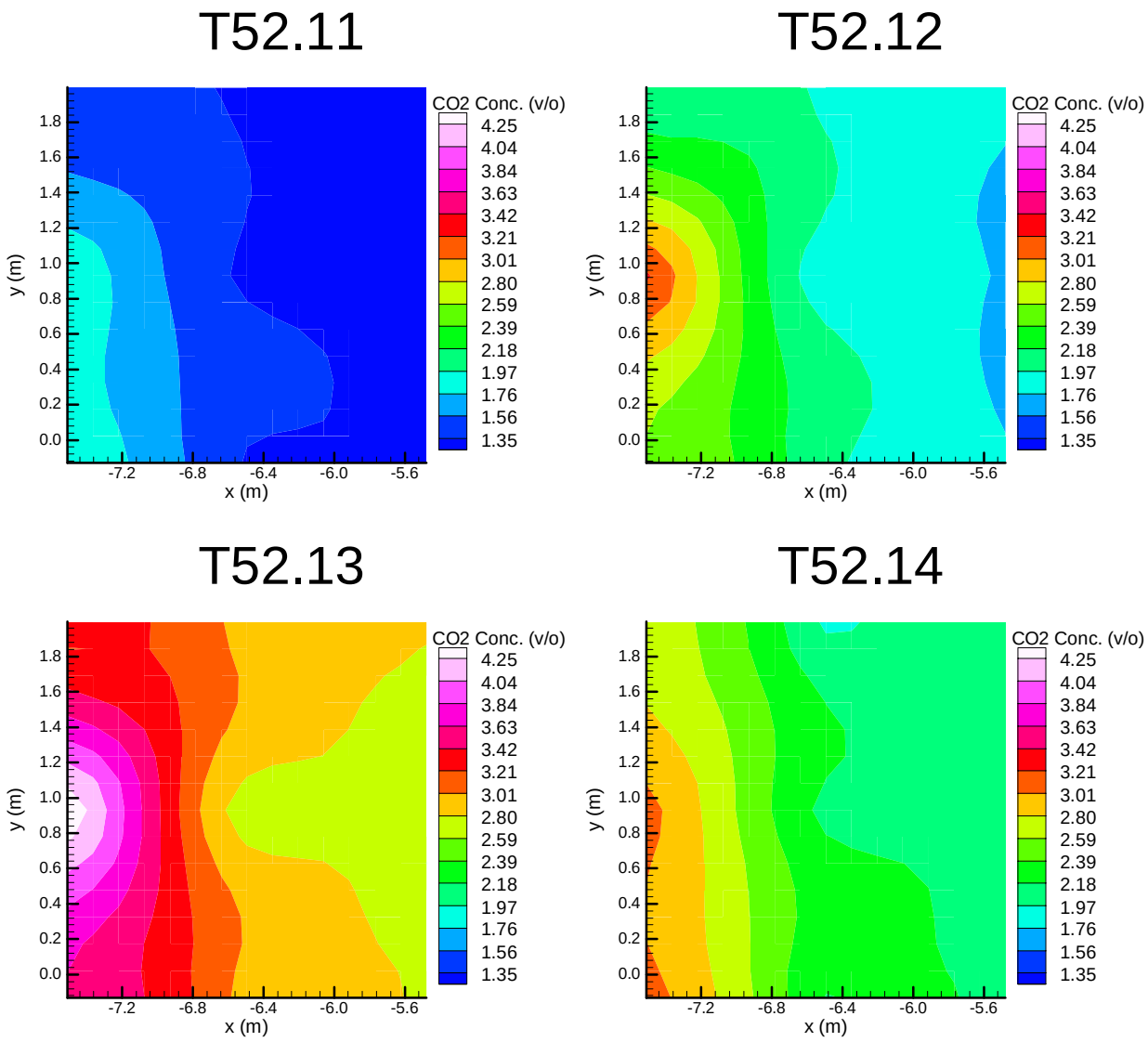

Figure 5.34: Middle Sensor Grid CO_2 Concentrations at 20-25 Minutes

The final three sets, Figures 5.35 through 5.37, show temperature, velocity, and gas concentration contour plots at the upper sensor grid, grid 1, below the polar crane for all four of the T52 experiments. The sensors used to create these figures are shown in Figures 5.23, temperature, and 5.24, velocity and gas concentration. As shown in the sensor map there were many more temperature sensors than velocity or gas concentration sensors. Thus it can be expected that the derived contour plots for temperature, Figure 5.35, will be more reliable than the other two sets of contour plots.

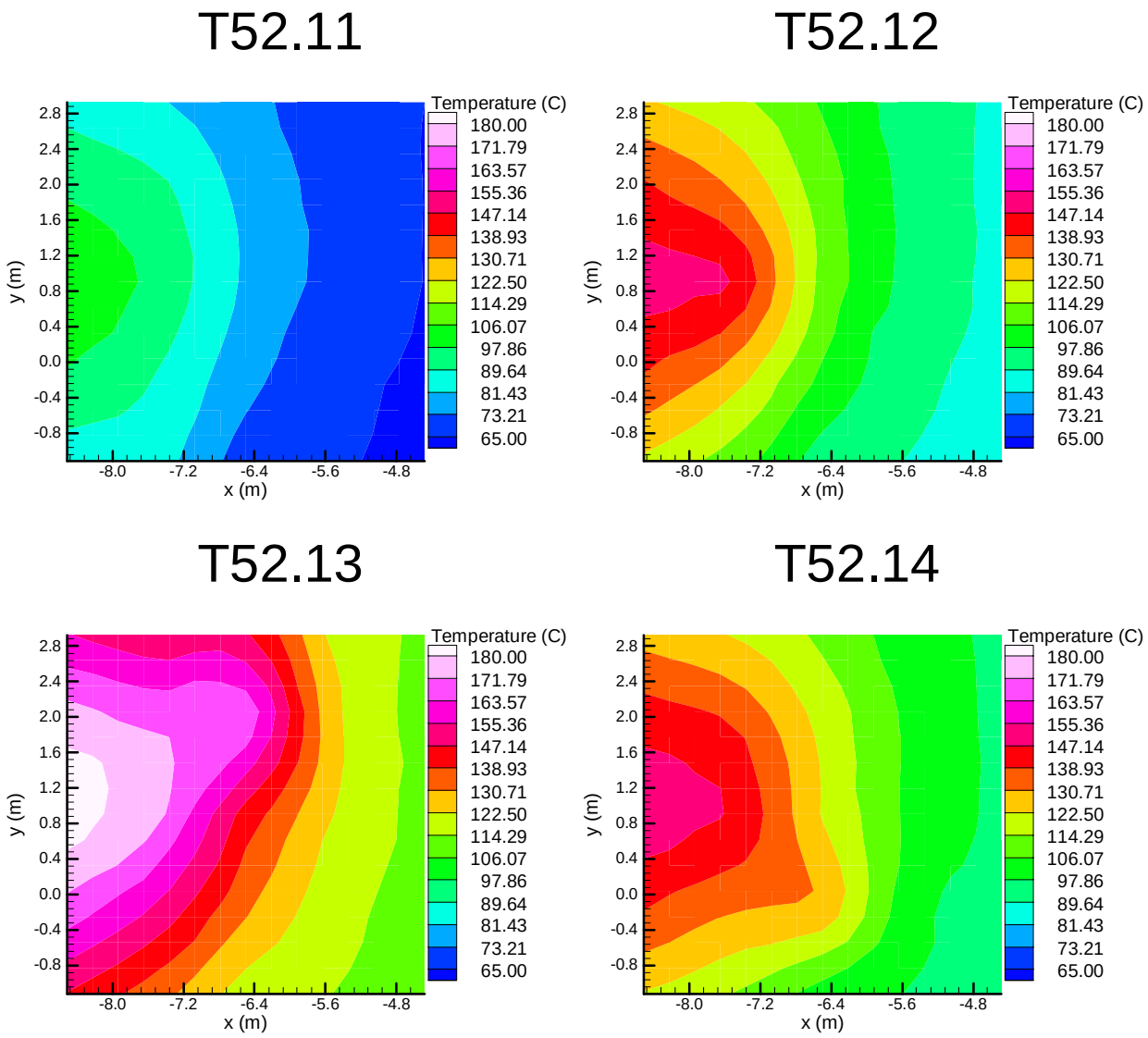

Figure 5.35: Upper Sensor Grid Temperatures at 20-25 Minutes

From the above plots the following conclusions can be drawn:

1. The positions of the plume centers moved slightly to the upper side, such that the hottest plume region is somewhat more centered on the left side boundary of sensor grid 1, while all other aspects of the fundamental asymmetry as compared to measurement grid 2 are preserved.

2. The highly efficient mixing inside the plume along with heat transfer to the steel shell further reduces peak temperatures to maximum values near 180 °C from the 600 °C maximum temperature at grid 2. This reduction occurs over the short distance of 10 m.

3. The transverse temperature gradient is about 100 °C for all four experiments at that position.

4. Peak temperatures increase with increase in fire power.

5. At the higher up position of grid 2, plume from all four tests feature rather symmetric characteristics.

6. For T52.11 the plume radius is seemingly smaller than the grid length. Therefore temperature shown in the right side region are certainly presenting temperatures of downflowing dome atmosphere (see velocities shown in Figure 5.37).

Figure 5.36 compares the two-dimensional CO_2 concentration fields derived from the respective sensor array for all T52 experiments. The contour plots shown for experiment T52.11, T52.12, and T52.13 are fully in line with the temperature contours shown in Figure 5.35 and discussed above. This observation does not hold for the derived T52.14 CO_2 concentration contours which shows a completely different pattern compared to the other three. In this experiment maximum concentrations occur at the lower left hand corner and partly along the lower side. This is not explainable as temperature and velocity contours (see Figure 5.37) do not show such anomalies. The only remaining explanation is that the data were unintentionally clockwise "rotated" from the original sensor positions during the data processing. Regions where countercurrent downflow of dome atmosphere is suspected show much lower CO_2 concentrations. These are not zero because the contour plots are shown 20 minutes into the fire and CO_2 has already propagated throughout the whole dome by then.

For the measurement grid 1, two-dimensional velocity contours were derived from the available sensors and they are depicted in Figure 5.37 for all four T52 experiments. Naturally, all three quantities, temperature, gas concentration, and velocity are coupled. Therefore, the velocity presentation completes the plume characterization at that grid about midway between the operating deck and the dome apex. In fact, the following interesting observations can be derived from the comparison:

1. The positions of peak velocities is moving away from the left side of the grid in the direction of the center of the upper grid side with increasing fire power. All four contour plots show this pattern, which may be the result of:

    a. The dome steel shell with its 10 m radius is hindering the transverse expansion of the plume expansion to left because it is closer to the left grid side (1.4 m distant) than the observed plume radius at that elevation.

    b. Simply the interpolation scheme which must interpolate between data of a very limited number of sensors (see Figure 3.24).

2. Peak velocities increase with increasing fire power. While velocities of up to 5 m/s are reached for T52.13 and T52.14, much lower values are obtained for T52.11 and T52.12, respectively.

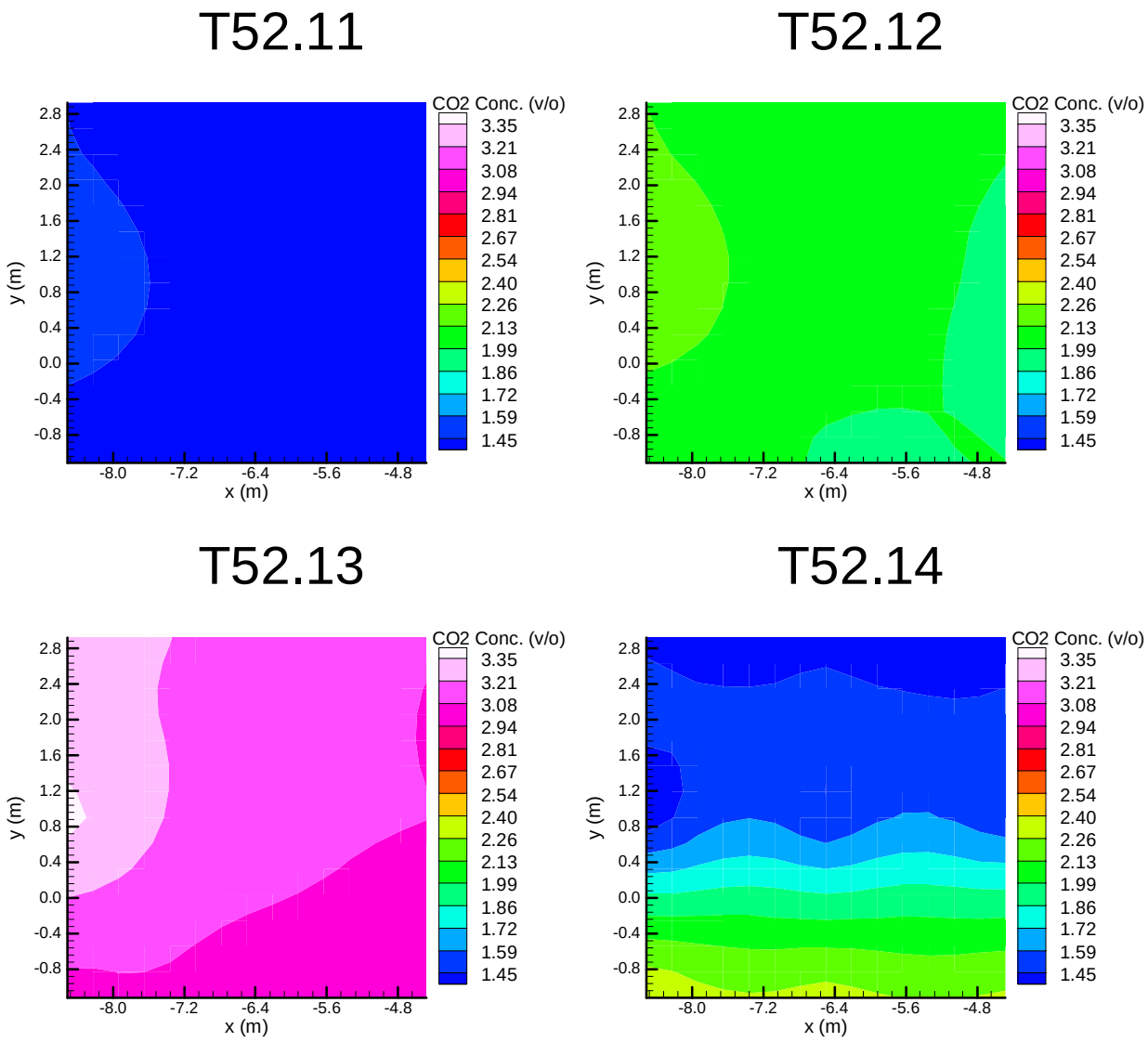

Figure 5.36: Upper Sensor Grid CO_2 Concentrations at 20-25 Minutes

3. Downward velocities prevail in the right side region of the grid over a range of about 1.6 m for all experiments. The size of the region changes somewhat with fire power, but the derived contours from the data are all similar between the experiments.

4. The proven fact of downward velocities clearly supports the notion that ascending plumes induce descending circulation patterns in large open spaces. These circulation patterns do not penetrate as low as the operating deck because there crossflows towards the plume prevail. However, the circulation pattern turns around somewhere in between grid 1 and the operating deck to flow countercurrently to the crossflow. This is inline with the low temperatures measured in the same region and shown in Figure 5.35.

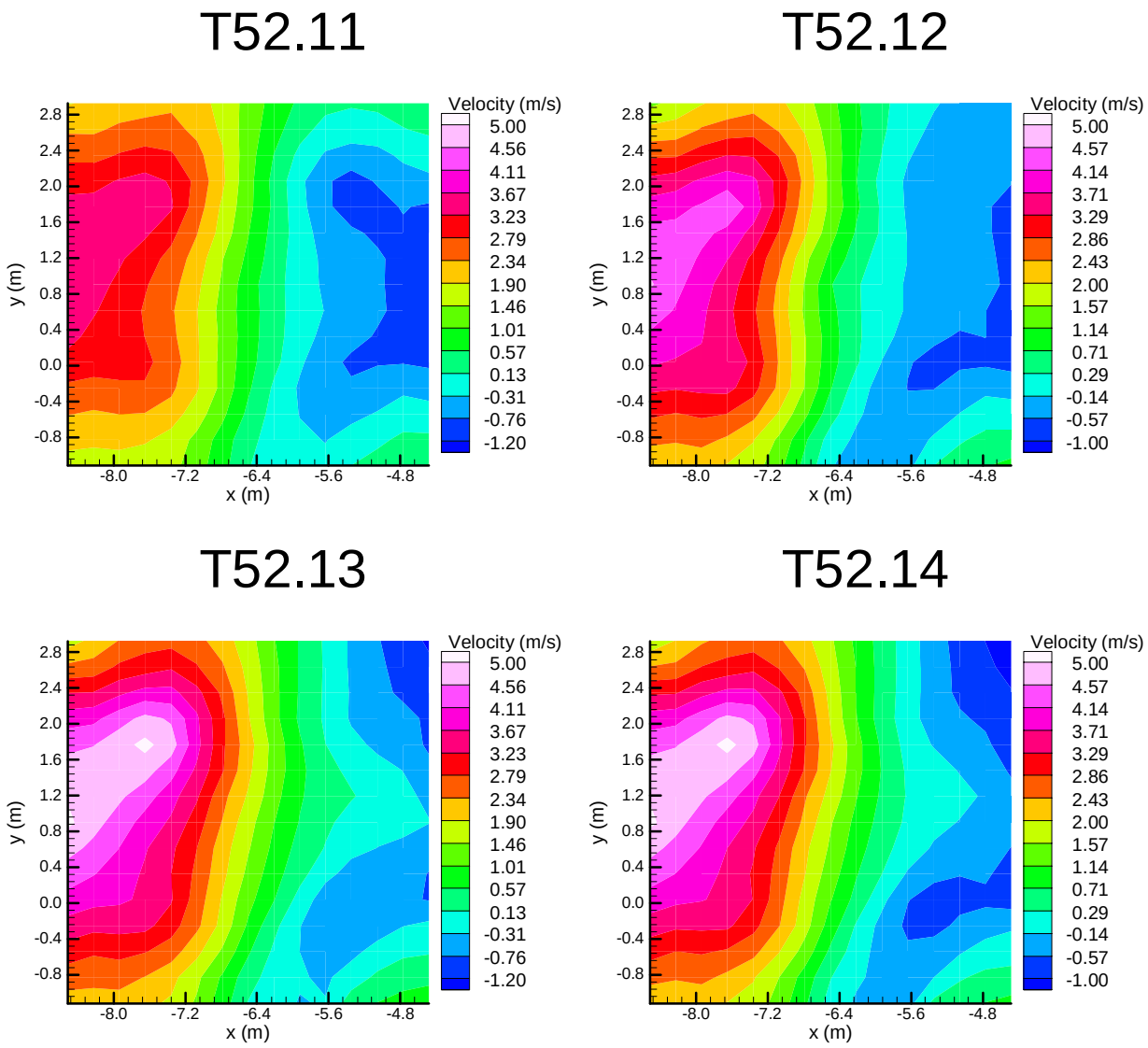

Figure 5.37: Upper Sensor Grid Velocities at 20-25 Minutes

In summary, sensor grid 1 provides a complete set of information about the transverse mass, momentum, and energy distribution inside one-half of the plume as well as outside the plume at that axial position. Together with the somewhat mode limited information from grid 2 10 m upstream and additional thermocouples at the steel shell surface and in front of it, a subset of data is available which would allow one ti study plume behavior in a large enclosure both analytically as well as numerically.

While the whole set of two-dimensional fields shown and discussed above were assembled only for a definite time window during the quasi steady-state fire phase, it should be emphasized that much more interesting information can be derived for the highly transient fire growth and cooldown phases from the available data.

5.3 Characteristic Quantities as a Function of Power and Position

In this subsection, selected quantities will be plotted as a function of fire power and position. All of the individual quantities will represent a single sensor time-averaged from 20 minutes to 25 minutes. This time period is during the steady-state oil addition phase of the four experiments and represents steady-state conditions. Furthermore, as the oil was burning essentially as fast as it was added, specification of the fire power during this time period is an easier task than it would be for the peak of the fire where the pyrolysis rate is not as well known. Where reasonable to do so, "best-fit" lines as a function of fire power will be drawn through the data shown to aid in visualization of trend resulting from a change in fire power.

The first figure in this section, Figure 5.38, plots four fire room temperatures as a function of fire power. The sensors are CT9611, near the doorway at +27 m in elevation; CT9616, over the center of the platform at +27 m in elevation; CT9604, kitty-corner to the doorway at +28 m in elevation; and CT9610, opposite the doorway at +27 m in elevation. Thus, the plotted temperatures present the variability of the fire room temperatures to the largest possible extent.

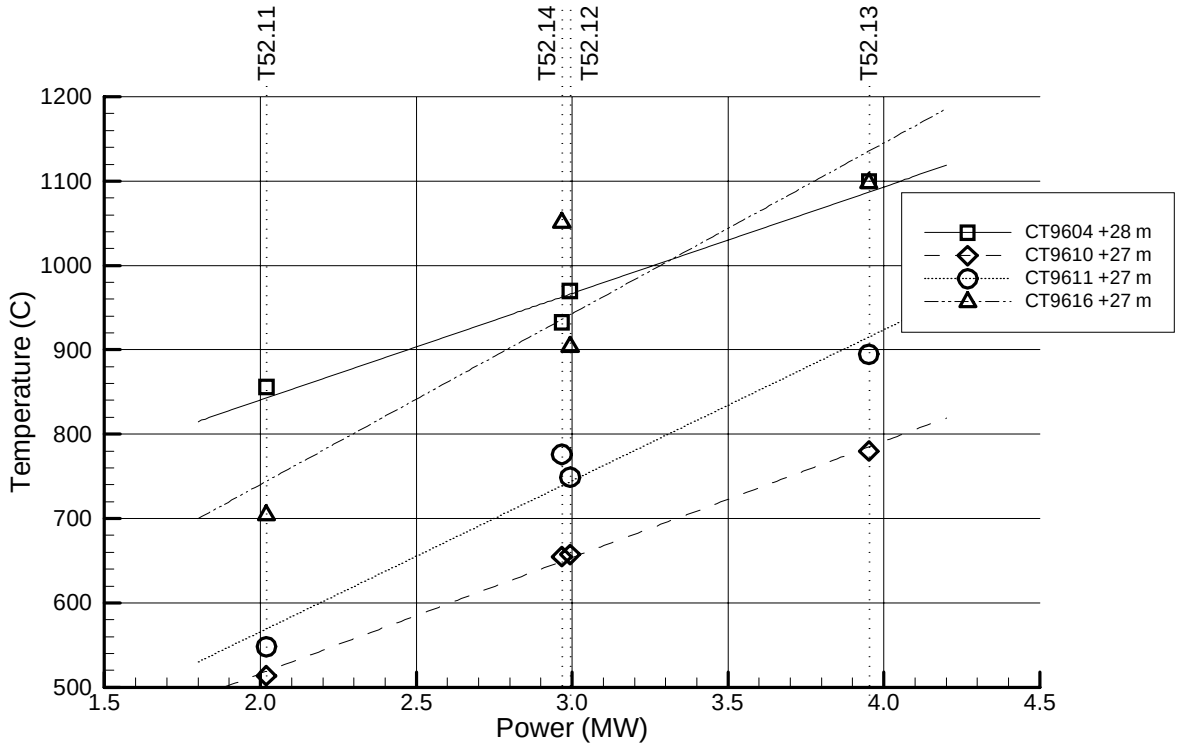

Figure 5.38: T52 Fire Room Temperatures as a Function of Power

The following conclusions can be drawn from this figure:

1. All fire room temperatures increase with increasing fire power.

2. With a few exceptions, the increase in fire power results in increases of all temperatures by about the same amount (straight lines have about the same gradient).

3. Maximum temperature differences of 300 °C to 350 °C exist in the fire room with CT9604 presenting the upper bound and CT9610 indicative of the lower bound.

4. While experiment T52.14 was supposed to duplicate T52.12, the relatively minor change in oil pan arrangement led to a distinctly higher center temperature above the oil surface (CT9616) for the former, while similar differences in the other sensor positions are noticeable but much less pronounced.

In summary, while all temperatures increase with as anticipated, asymmetric temperature fields are maintained at all fire power levels examined. These are the results of the asymmetric door position relative to the fire room at the fire source. Benign changes in oil pan arrangement results in an increase of the maximum temperature by 150 °C. None of these effects can be simulated by computer codes using zone models unless specially tuned correlations are implemented, which account for these variability's.

The O_2 and CO_2 concentrations in the upper doorway of the fire room are plotted as a function of power in Figure 5.39.

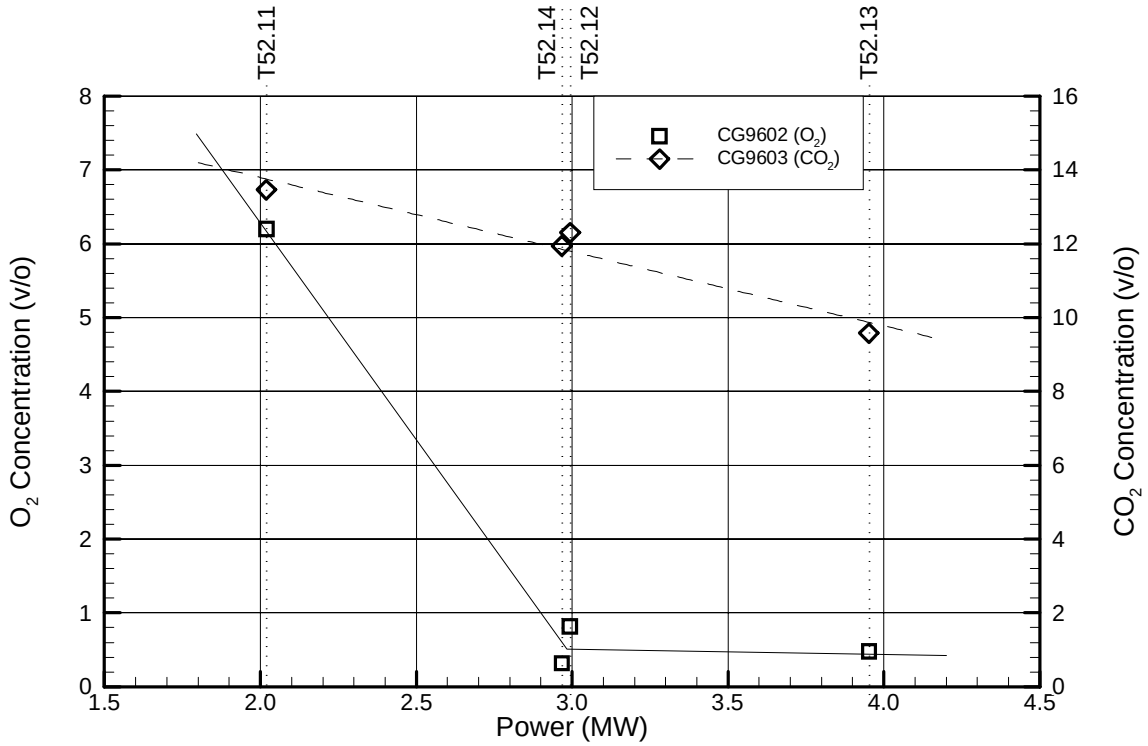

Figure 5.39: T52 Fire Room Doorway Gas Concentrations as a Function of Power

It is obvious from Figure 5.39 that only experiment T52.11 experienced sufficient air and thus oxygen supply such that the fire can be termed well-ventilated, while the other three experiments, due to the lack of oxygen were clearly underventilated. The transition from well to underventilated fire characteristics is a unique function of fire power as shown in Figure 5.39. The transition occurs somewhere between 2 and 3 MW of fire power for the conditions tested.

It is equally obvious from the information given in Figure 5.39 that notwithstanding differences experienced in the fire room for experiments T52.12 and T52.14 discussed before, both experiments result in the same amount of O_2 and CO_2 in the upper layer at the fire room doorway. Further increase in fire power reduces the amount of CO_2 (due to increased formation of CO) as in the case of the T52.13 test.

Figure 5.40 shows the temperatures measured at three locations in the hatch leading from the fire level to the dome. The locations shown are those for sensors CT456, the location of the highest hatch temperature for the tests; CT459, the corner opposite the doorway; CT467, the center of the hatch; and CT479, kitty-corner to the doorway.

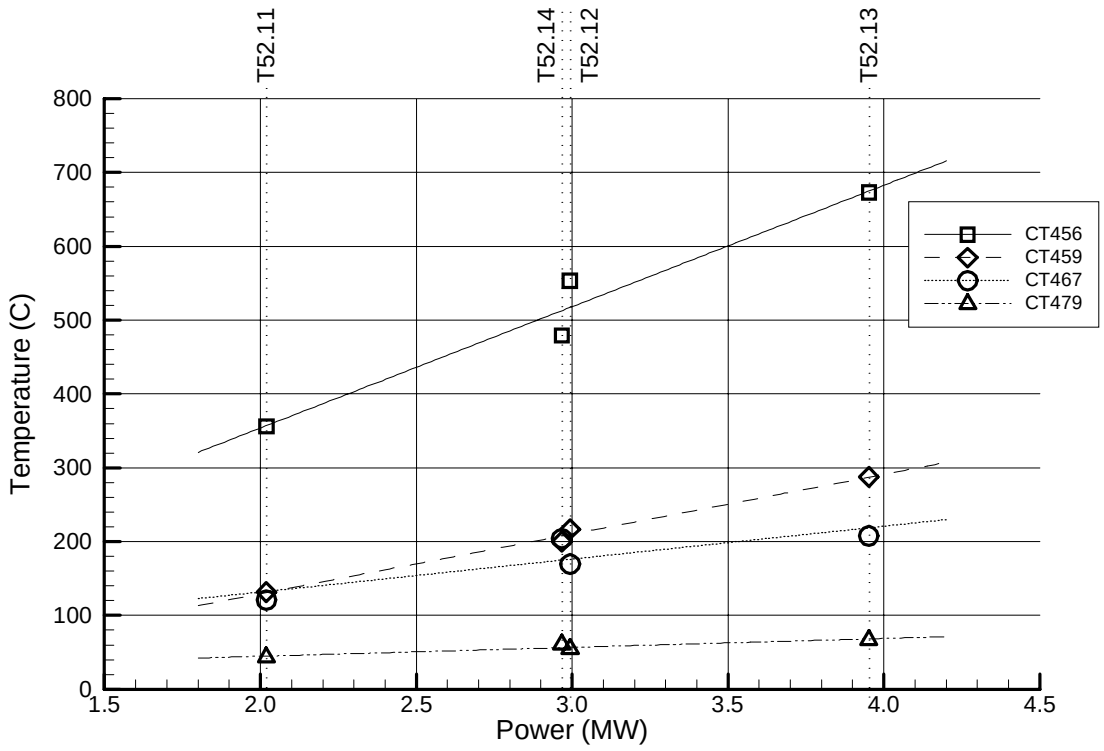

Figure 5.40: T52 Fire Level to Dome Hatch Temperatures as a Function of Power

The plotted temperatures show the total variation in the temperature fields over sensor grid 2 at four fire power of which two are very close. The following conclusions can be drawn from this information:

1. Except for CT 479 (and generally for the whole right side region as shown in subsection 5.2) all temperatures in the plume increase at various degrees as a function of fire power.

2. The steepest increase is noted for the peak temperature positioned asymmetrically at the left side of the grid close to the fire room door (CT 456) while the temperature increases at the

other grid positions are much less affected by the fire power increase and the temperature measured by CT 479 only shows a very small increase.

3. The independence from fire power as shown for the temperature CT 479 is a clear sign for the fact that this region is occupied by downflowing, cold, bulk dome atmosphere.

4. Doubling the fire power from 2 to 4 MW doubles the plume peak temperature from 350 °C to 680 °C. The same holds for the position opposite to the fire room door (CT 459) at a much lower temperature. A somewhat smaller increase is noted for the grid center position (CT 467)

5. The higher the fire power the larger is the temperature skew across grid 2. The maximum temperature difference of 700 °C has been measured for T52.13.

In summary, it is worthwhile to note that fire analysis codes using zone models cannot account for those asymmetries and must be simulated by means of three-dimensional CFD codes, such as for instance FDS.

The temperatures measured along the fire plume entering the dome at four different axial positions upstream of grid 2 are shown as a function of power in Figure 5.41. The sensors selected from the center of the upper grid in the dome and from a rake of instrumentation collinear with the centers of sensor grids 1 and 2.

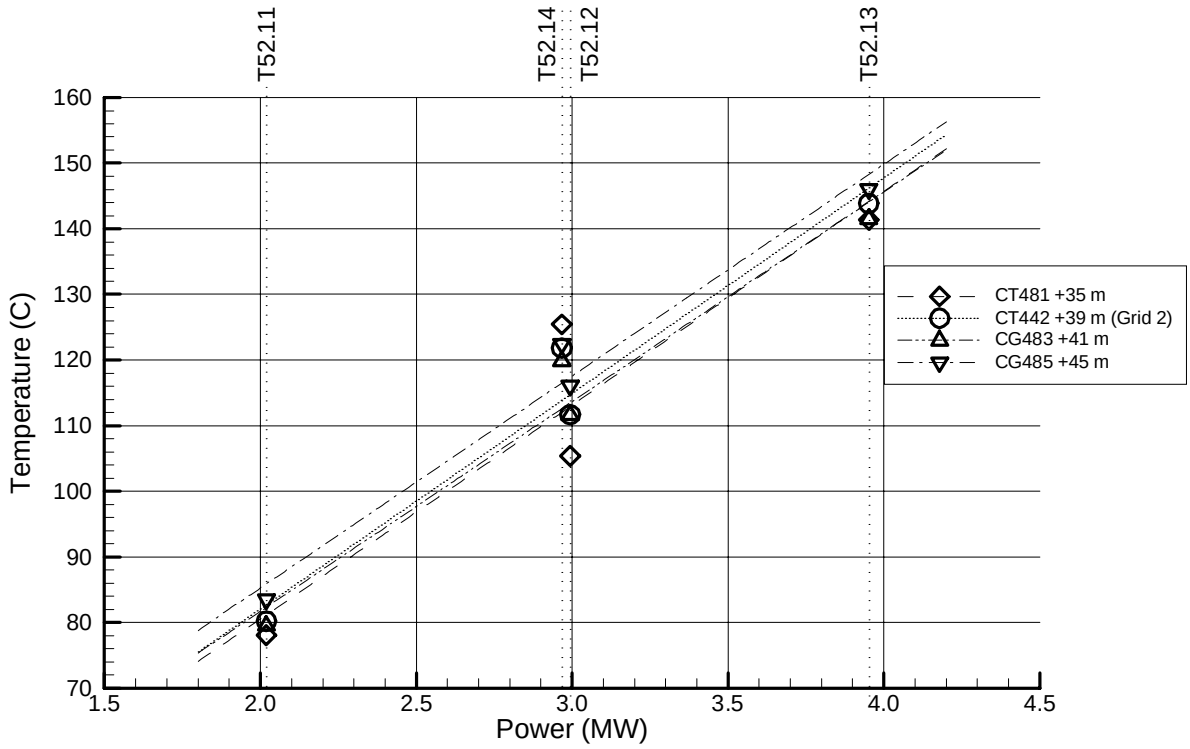

Figure 5.41: T52 Fire Plume Temperatures as a Function of Power

The following conclusions can be drawn from the temperature quadruples:

1. For each tested fire power the four temperatures recorded over an axial distance of 10 m are quite close to each other, except for T52.12.

2. For these, the maximum axial temperature is not more than 80 °C.

3. Doubling the fire power from 2 to 4 MW increases the temperature from around 80 °C up to about 145 °C, e.g. less than a factor 2, because of the additional entrainment and mixing over the height.

4. Unexpectedly, the highest positioned sensor, CT 485, measures the highest temperatures, while the lowest positioned sensor, CT 481, closet to the plume release vent, gives the lowest temperatures (except for T52.14), which is completely opposite to the known jet/plume release characteristics. The explanation for this extraordinary observation is:

    a. bending of the plume axis, such that the four axial thermocouples measured the plume temperatures at different radial distances inside the plume

    b. the plume bending is caused by

        1) asymmetric plume release

2) plume confinement effects by the constraining containment steel shell

5. Only for experiment T52.14, is the order of sensor readings kind of in line with expectations, e.g. higher temperatures upstream and lower temperatures downstream.

6. The closeness of the four temperatures for three of the experiments is indicative that entrainment and mixing in this region is much less significant compared to the others, jet pump effect, downflow, and crossflow, discussed before.

In summary, the temperatures in the dome region atop the center of grid 2 clearly provide experimental evidence that the fire plume is bent in its shape, because of the asymmetrical release as well as the proximity of the steel shell. In addition, the curvature effect of the hemispherical dome may play an important note.

None of the above effects can be accounted for by analytical or zone model approaches. Only the application of CFD codes may have a chance to simulate these types of effects, which are certainly challenging in all aspects.

From a hazards point of view, none of the plume temperatures shown in Figure 5.41 pose any threat to the containment steel shell integrity mainly because of the highly efficient exchange processes upstream of 35 m.

Figures 5.42 and 5.43 show temperatures and CO_2 concentrations, respectively, in the global recirculation loop starting at the 1.900 Level on the main staircase side of the HDR and ending at the 1.700 Level on the spiral staircase side.

The following observations can be drawn from the temperatures plotted in Figure 5.42:

1. With increasing distance from the fire room, the impact of fire power immediately decreases. In fact for positions lower than 28 m, representative temperatures in both downward and upward flow paths are independent of fire power.

2. The main staircase side clearly shows features of a stable situation, with higher temperatures at the top than at the bottom, where the maximum temperature difference is about 13 to 16 °C, weakly depending on fire power.

3. The spiral staircase side indicates features of an unstable situation with cold atmosphere overlaying warmer atmosphere, the related temperature differences are small, 2 °C, for T52.13; the conditions even seem to be isothermal.

4. Higher up, temperatures increase under the conditions listed in 2 and 3, it is counterintuitive that there is flow through the loop, as the main staircase is occupied by atmosphere with a stable temperature gradient, yet velocities have been measured. This is due to the convective driving force imparted by the fire room, even during the post-fire cooldown phase, which

results in a suction effect in the spiral staircase and is aided by the natural convection effects of the generated flue gasses and their cooldown.

In summary, experimental evidence shows that away from the fire room, thermal loads do not pose any technical hazard. Temperatures are very close to ambient and temperature differences are small. The suction effect by the exiting fire room upper layer and the resulting plume into the dome overcomes stabilizing effects by continuous heat sinks as the massive concrete structures are by no means thermally saturated. In addition, buoyancy and gravity effects of the participating flue gasses play a role in the complex combination of mass, energy, and momentum transfers which keeps the global circulation going. Many effects play an important role, including heat transfer to the confining structures.

Analytical models and zone models can only be expected to give estimates as the prevailing processes and their couplings are far beyond their scopes. Even for CFD codes, the simulation of the global circulation poses a major challenge, even by today's standards.

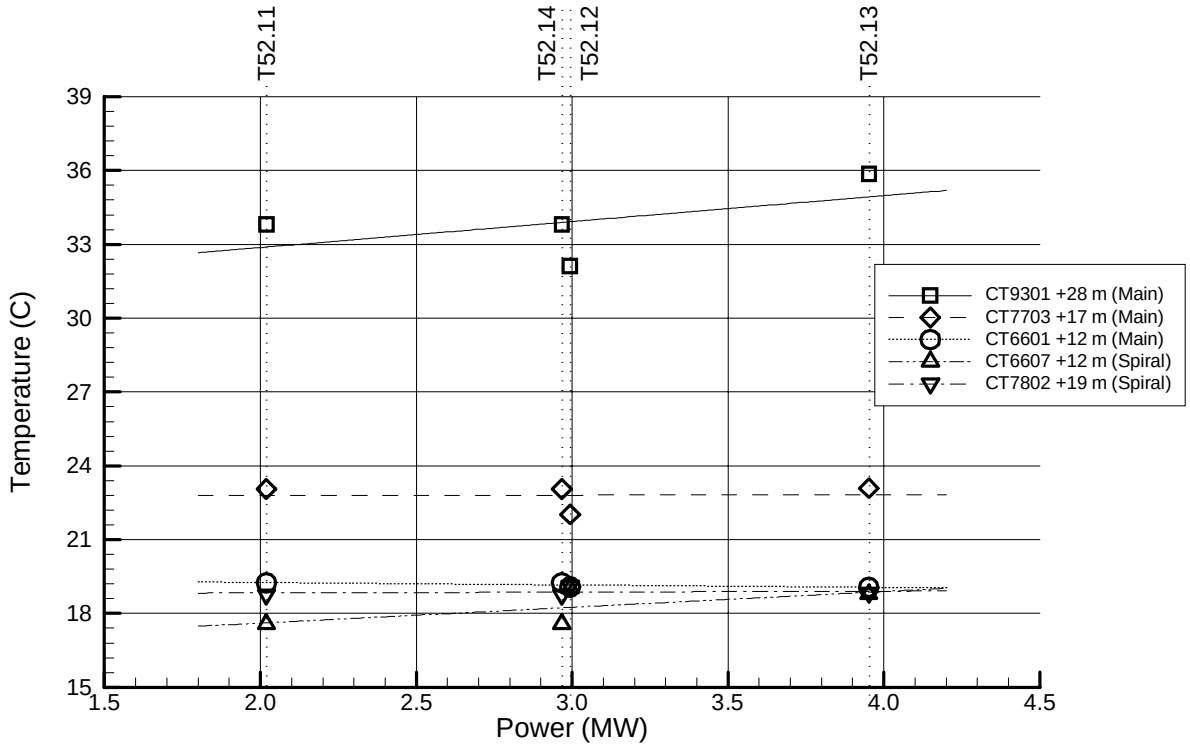

Figure 5.42: T52 Flow Loop Temperatures as a Function of Power

Figure 5.43 depicts the measured CO_2 concentrations at the same positions as the thermocouples whose temperatures are plotted in Figure 5.42. There is one exception to this, namely sensor CG7802, which is located some 4 m higher up, closer to the fire room doorway. From Figure 5.43, the following conclusions can be drawn:

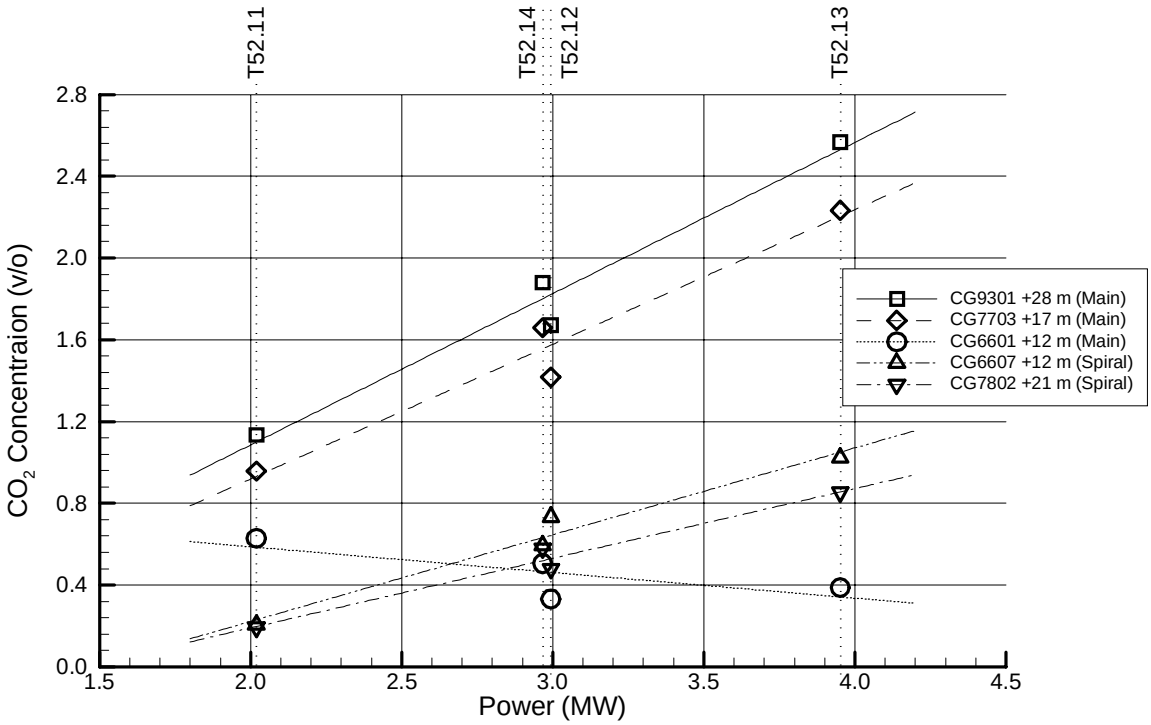

Figure 5.43: T52 Flow Loop CO_2 Concentrations as a Function of Power

1. With the exception of sensor CG6601 at the bottom of the main staircase shaft, CO_2 concentrations increase with fire power increases at all locations shown around the global circulation loop.

2. Steeper increases in CO_2 concentrations with fire power increase are noticeable at higher elevations in the main staircase side, while increases at the spiral staircase side are less.

3. The observations under 1 and 2 result in higher CO_2 concentration differences around the global circulation loop with fire power increase.

4. Also, CO_2 concentration differences slightly increase between the two positions of 28 m and 17 m on the main staircase side and 21 m and 12 m on the spiral staircase side.

5. In general, doubling the fire power from 2 MW to 4 MW slightly more than doubles the CO_2 concentrations at the difference positions in the downward and upward flow shafts.

6. From the CO_2 concentration data it is obvious that flue gasses are transported around the loop by a combination of transport processes, e.g. they reach all levels in both flow shafts.

7. While all sensor positions show increases in CO_2 concentrations, sensor CG6601 at 12 m (bottom of main staircase shaft), indicates just the opposite, namely a decrease with fire power

increase. This may be explained in terms of the sensor position as well as the fact that a transition occurs from vertical downflow to horizontal crossflow over to the spiral staircase side. The position under examination may be within this flow transition region and thus yield a different behavior than the other sensors as the exact location of the transition shifts with power.

In summary, the observations cited above clearly indicate that flue gasses penetrate and propagate throughout the containment. Thus, while Figure 5.42 showed that there are no thermal load hazards at any positions around the global circulation, the information given in Figure 5.43 clearly indicates that rescue and intervention may be hampered by gas propagation, and electrical gear, control sensors, etc. are subject to soot deposition and the possibility of malfunction. Both potential hazards occur with time delay, such that given the circumstances, a sufficiently long time window may be available for proper action and countermeasures.

It seems appropriate that fire analysis codes should give at least an order of magnitude accuracy for the effect discussed above in the far field of the fire room.

5.4 Filter Systems Tests

5.4.1 Overview of Filter Tests

The T52 test series was the first during which filters were tested as an integral part of a fire experiment at the HDR facility. The filter tests were performed at the end of each individual test in the T52 series. This allowed the filters to be loaded with the soot and other aerosols suspended in the containment's atmosphere. For this purpose, two independent filter systems were utilized. The first was the original HDR reactor building exhaust gas ventilation system. The second was a recirculation filter facility designed and constructed by LAF/KFK (Laboratory of Aerosol and Filter Techniques at KFK); see Sections 2.2.2 and 2.2.3 for a detailed description of these systems.

The filter tests had a dual purpose, to measure the flow reduction in the ventilation systems due to the filter loading and to evaluate the potential of the systems to withstand structural damage. The soot retention capabilities of the EU-4 pre-filter and the S-class main filters were determined by measuring temperature, relative humidity, soot concentration in the exhaust, pressure difference and the amount of soot loading in the filter stages. They were the first large scale filter tests with fire soot under realistic conditions in a containment. Tables 5.1 and 5.2 provide an overview of the filter experiments, their test procedures, and the filter designs. It should be understood that these experiments were primarily scoping experiments with additional more specific experiments planned. Nevertheless, some observations from the test are made in what follows.

Table 5.1: Overview of Filter Tests in Connection With T52 Test Series

Test	Power (kW)	Test Time/ DAS Time (min)	HDR Exhaust Ventilation	Recirculation Filter LAF at 30 m	Remarks	End of Fire	RGB 347 Exhaust Ventilation				LAF Recirculation Filter	
							Prefilter	Main Filter	Start Time	Shutoff Time	Start Time	Shutoff Time
T52.11	2,000	10/100	after test up to Δp max	after Δp max in HDR Exhaust	25 l in oil pan feed: 3.72 l/min	11:44	Vokes A1-A16	Atex A1-A16	12:13	12:31	12:41	14:40
T52.12	3,000	10/100	start 30 min after test up to Δp max	start 30 min after test	50 l in oil pan feed: 5.57 l/min	11:27	AAF B1-B16	Camfil B1-B16	12:06	13:00	11:27	11:58
T52.13	4,000	10/100	start 60 min after test up to Δp max	start 60 min after test	75 l in oil pan feed: 7.43 l/min	9:55	AAF C1-C16	Camfil C1-C16	11:00	12:00	9:55	10:55
T52.14	4,000	10/100	during test up to Δp max operational after test up to Δp max	after Δp max in HDR Exhaust up to test end	replication test for filter examination	12:15	N/A	Atex D1-D16	12:46	13:49	14:10	16:20

Table 5.2: Fire Soot Retention at the Reactor Building Exhaust Gas Filters

Test	Filter Bank Inlet		Prefilter EU-4		Main Filter			Average Soot Concentration in Exhaust Gas (mg/m^3)
	max Temp (°C)	max Rel. Humidity (% RH)	max ΔP (Pa)	Average Filter Loading (g/filter)	max ΔP (Pa)	Average Filter Loading (g/filter)	Degree of Retention	
T52.11	24	70	500*	N/A	180	N/A	none	N/A
T52.12	27	73	390	97	190	36	none	35
T52.13	N/A	N/A	210	73	180	N/A	6 to 10*	43
T52.14	28	77	No prefilter	No prefilter	320	166	4 to 12*	59

*The exhaust ventilation facility was shut down when the prespecified ΔP limit of 500 Pa was reached.

5.4.2 Observations of the HDR Recirculation System Performance

Only during experiment T52.11 had the HDR exhaust gas ventilation system to be shutoff because of reaching the design pressure at the pre-filter after 18 min. This limit pressure was not reached during any of the other experiments. Since T52.11 had the lowest fire power and was well ventilated, this result was unexpected. It can be explained, however, by the test procedure.

During experiments T52.12 and T52.13, the recirculation facility was operated for 30 minutes and 60 minutes, respectively, as documented in Table 5.1. This resulted in filtering a certain fraction of the soot content (about 1 to 1.4 kg). In addition, a larger soot fraction settled before the reactor building exhaust gas system started. Neither of these factors were present for the T52.11 test. Consequently, the pre-filter clogged early on. Filter loadings and pressure drops are given in Table 5.2.

With the exception of test T52.11, the other three fire tests clearly demonstrated that the filters were capable of operating in post-fire environments nearly as well as during normal operation. The few tests also showed that the pre-filters retained the fine soot with unexpectedly high efficiency. However, due to their smaller surfaces, their soot storage capability seems to be substantially lower than that for the S-class main filters. This may limit the operation time of ventilation among other criteria. Limit values were only reached during T52.11. As other fires may result in higher loadings, the application of newly developed high resistant filters seems appropriate for safety reasons.

5.4.3 Observations of the LAF/KFK Recirculation System Performance

In addition to the original reactor building exhaust gas ventilation system, the LAF designed and operated recirculation filter system was tested in the aftermath of the T52 test series. This filter system contained newly developed multi-layer, metal fiber fleece. The soot balance at these filters were determined by weighing the unloaded filters, the loaded filters, and the cleaned and dried (at 120 °C) filter packages. The results of this procedure are shown in Table 5.3 below.

Table 5.3: LAF Filter Loadings

Test	Filter Package	Soot Loading
T52.11/T52.12	1	1.002 kg
T52.13	2	1.336 kg
T52.14	3	0.050 kg

The LAF recirculation filter was operated with a volumetric flow of 3000 m^3/hr. The effective filter surface of the stainless steel fibers was about 2.5 m^2. As shown in Table 5.1, the recirculation filter system was operated for about one hour after the end of each T52 fire experiment, except for T52.11.

Soot surface loading values of 9.5 kg/m^2 were reached, much higher than achieved in previous laboratory scale tests. Consequently, the filter efficiency turned out to be higher at larger scales.

These scoping test results suggest further optimization regarding fiber distribution, package density, filter size, and volumetric flow. Subsequent filter tests were planned for test series E41 and E42.

6 POTENTIAL OF EXPERIMENTAL DATA FOR CODE VALIDATION

One of the primary purposes of the HDR fire experiments was to create a database of experimental data for use in code validation and model development. This section will discuss aspects of the T52 oil pool fire tests and the related data that can be used for code validation. The potential contributions of the tests will be discussed in terms of zone models, containment system codes and field models.

6.1 Zone Models

Zone model fire codes, such as CFAST (NIST) [29,30], MAGIC (Electricté de France), and COMPBRN (NRC), operate by assuming that in a fire situation every room in a building can be represented by two layers: a hot layer containing the combustion products from the fire and a cold layer which is oxygen rich. A number of elements of the instrumentation plan for the T52 oil pool fire tests were established for the purpose of collecting data for the evaluation of zone model codes. Some of these elements are discussed in this subsection.

6.1.1 Layer Height

Layer height is the key parameter calculated by zone model codes. Unfortunately, the instrumentation map for the T52 series only contained two vertical rakes in locations where a layer height could be determined. These locations were the fire room doorway, Figure 3.19, and near the spiral staircase maintenance hatch on the 1.600 level, Figure 3.12. There were two other rakes in the dome. One of the rakes was located in the plume exiting the maintenance hatch into the dome, Figure 3.27; therefore, it is not useful for determining the global conditions in the dome. The other rake consists of three thermocouples at the centerline of the HDR, Figure 3.25 and 3.26. This rake is too sparse to yield detailed information about the dome temperature profile.

6.1.2 Layer Temperatures

The T52 test series did not contain many rooms that were instrumented well enough to determine layer temperatures. There were essentially four locations for which some degree layer temperature determination could be made. The fire room had two arrays, one at 27 m and one at 28 m, which can be used to determine the upper layer temperature; however, there is no instrumentation lower in the fire for determining lower layer temperatures. The doorway thermocouple rake could be used to determine average conditions in the door, but this is sufficiently removed from the fire that those conditions could not be applied to the fire room. The maintenance shaft compartment near the fire room had two grids of sensors in the upper, sensor grid 2 at 31 m, and lower, sensor grid 3 at 25.5 m, maintenance hatches. These grids allow the calculation of the average temperatures at the hatches; however, those values would not necessarily be indicative of the layer temperatures inside the compartment. The final location is on the 1.600 level near the spiral staircase were a rake of thermocouples is present, Figure 3.12. Since large geometric temperature gradients would not be expected that far removed from the

fire, those instruments could be used to generate layer temperature for the 1.600 level near the spiral staircase.

The dome contained a large amount of instrumentation. However, almost all of that instrumentation was positioned to measure the conditions of the plume entering the dome from the fire room. Instrumentation throughout the remainder of the dome was sparse. Furthermore, the observed plume entrainment and velocities measured at the maintenance hatches indicate that a large recirculatory flow existed in the dome, Because of the instrumentation placement and the flow pattern in the dome, it is hard to draw conclusions regarding the average conditions in the dome outside of the plume.

6.1.3 Plume

The hot gas layer exiting the upper region of the doorway in all four of the T52 experiments propagates as a plume through the maintenance hatch at the operating deck of the dome and upward into the dome. This vertical flow path was extensively instrumented by a rake of 7 thermocouples, Figure 3.27; sensor grid 2, Figures 3.21 and 3.22; and sensor grid 1, Figures 3.23 and 3.24 The temperature, velocity, and CO_2 concentration data enable one to validate some features of vertical plume models imbedded in zone models. However, it should be observed from examination of the sensor grid data that the plume did not pass through the center of the grid. Therefore, the plume thermocouple rake does not represent the plume centerline. Additional velocity sensors and steel shell surface thermocouples at the position of the plume stagnation point supplement the rake and grid instrumentation.

The pronounced, vertical, hot gas plume is unique to the T52 test series. Therefore, the large volume dome region plays a prominent role for all experiments of this test group contrary to all other HDR fire experiments which occurred much lower in the containment where the dome was of minor overall importance.

6.1.4 Recirculation in the Dome

The dome connects both vertical flow shafts in the HDR containment. With a hot gas jet/plume asymmetrically entering into the dome on the spiral staircase side (270°), it is to be expected that a recirculation encompassing the majority of the dome may have developed during the test series. The instrumentation map in the dome, described in Section 3 with selected data shown in Section 5, was sparse outside of the plume. As such, it is insufficient to yield many details of the recirculation flow path, especially since the main staircase side of the dome has only instrumentation near the hatch. Therefore, the issue of recirculation and how to model it best in the realm of zone model codes must rely on the rake and sensor grids on the spiral staircase side, the center rake in the dome, and the instrumentation at the inlet of the main staircase maintenance shaft. As mentioned in the prior subsection, the high importance of the dome was unique to this test series.

6.1.5 Mass Flow Rates

In those locations where layer height and velocity information exist or where a velocity sensor is located in a maintenance hatch, mass flow rates between compartments or between levels can be determined. In the case of horizontal flow the doorway dimensions and layer height information is used to determine the flow area. This along with the ideal gas law and layer temperature then yields the mass flow rate. For vertical flow, assuming the plume occupies the whole hatch can also yield a rough estimate of the mass flow rate between axial levels.

In the T52 test series, horizontal mass flows can be determined in the doorway and on the 1.600 level for horizontal flow between the two maintenance shafts. Vertical mass flows using the whole hatch assumption can be made for the main staircase hatches between the dome and the 1.900 level, between the 1.900 level and the 1.800 level, between the 1.700 level and the 1.600 level, between the 1.600 level and the 1.500 level, and between the 1500 level and the 1.400 level. Vertical mass flows using the whole hatch assumption can be made for the spiral staircase hatches between the between the 1.700 level and the 1.600 level. Sensor grids 1,2, and 3 can be used to generate mass flows between the 1.900 level and the 1.800 level, between the 1.900 level and the dome, and from the lower dome into the upper dome by integrating the temperature and velocity information contained in the sensor grids.

6.1.6 Gas Concentrations

A rake with CO_2 concentration sensors was installed on the 1.600 level, Figure 3.13 The upper layer of the doorway was instrumented, Figure 3.18, with a collection of sensors: O_2, CO, CO_2, and C_mH_n. Each of the sensor grids contained a sparse array of CO_2 sensors that provide information about the CO_2 distribution in the plume from the fire room. Many of the hatches between levels contained a CO_2 sensor. These latter sensors can be used to obtain the arrival time of the combustion products as well as a dilution factor for the products along the propogation path.

6.1.7 Structural Temperatures

A selected number of thermocouples were placed at and into structures at various positions in the containment. One thermocouple, CS9603, was placed at the fire room wall near the same location and elevation as CT9603. A number of surface thermocouples were placed into the steel shell of the dome on both its inside and outside surfaces at different circumferential locations as shown in Figures 3.25 and 3.26. These instrumentation groups involved sets of four thermocouples measuring the temperatures of the containment atmosphere, the inside steel surface, the outside steel surface, and the air temperature in the gap between the steel shell and concrete outer shell. These allow one to determine the energy transfer across the containment steel shell. A few other thermocouples were mounted at containment surfaces positioned in lower containment regions (CS6602 in Figure 3.12) as well as embedded in heat transfer blocks. Comparisons with measured surface and structural temperatures allows one to validate heat transfer correlations and heat conduction solvers implemented in zone model codes.

6.1.8 Global Recirculation

With the fire room position high up in the containment and at an asymmetric position close to one of the vertical shafts, a global recirculation is induced throughout the containment. This is a unique feature of the T52 experiments and yields the distribution of the combustion products along its flow path in a closed loop. This global circulation is driven by the highly buoyant flow exiting from the fire room which for continuity preservation creates a countercurrent flow through the lower region of the doorway. This despite the entrainment of air into the plume is strong enough to lift containment atmosphere up through the spiral staircase maintenance shaft and overcome the buoyancy forces in the main staircase shaft as warm containment atmosphere is drawn from the dome downward with the net result of a complete global circulation loop. Clearly, this phenomena poses a stringent test for zone model codes, because it challenges the codes with regards to features in an enclosure fire, which are otherwise atypical of common fire scenarios and flow paths.

6.2 System Codes

Containment system codes, such as GOTHIC [31], GASFLOW [39], and RALOC, owe their origin to the nuclear power industry. The need to evaluate the effects of loss-of-coolant accident scenarios in a containment building requires thermal-hydraulic codes that accurately model the two-phase, thermal-hydraulic response of a large building to a source of energy, mass, and momentum, e.g. a break in a reactor coolant pipe. Containment system codes commonly use the lumped-parameter method, that is a compartment is considered to be a single point whose properties represent the volume-averaged properties of the compartments. By modifying the source to be combustion gases and radiant heat rather than steam and water, containment system codes can be applied to computing the effects of fires on large, enclosed structures. These codes usually model all vents between compartments, heat transfer to structures, sprays, ventilation systems, etc both by convection and condensation. In the case of GOTHIC, the discretization options also include a combination of lumped and distributed parameter nodalizations (1-D, 2-D, and 3-D).

For the purpose of fire modeling some adjustments to the typical lumped-parameter approach must be made. In order to appropriately generate the buoyant driving force for fire driven flow, the fire compartment and any immediately adjoining rooms cannot be modeled as lumped volumes. Rather each room must be subdivided into a network of lumped volumes to allow for thermal stratification in these compartments or must be nodalized in multidimensional control volumes as offered by GOTHIC and GASFLOW. Advanced containment codes account for complete sets of conservation equations for mass, momentum, and energy transport. Often they have droplet models and aerosol models, like GOTHIC and CONTAIN, which can be used to simulate coupled fluid-dynamic aerosol behavior. Those containment codes, which are used to simulate severe accidents also have sophisticated filter models which can be used to examine fire aerosol behavior in multi-compartment geometries together with complex ventilation systems.

6.2.1 Containment atmosphere temperatures

As many regions outside the fire compartments and adjoining compartments are modeled as lumped volumes, this results in more useable temperature information in the T52 data set than for the zone models. Regions where countercurrent flows and stratification is to be expected are nodalized by networks of lumped volumes or as multidimensional control volumes consistent with the coordinate system of choice. Only for rooms far away from the source may lumped-parameter nodes be chosen. For loop flow geometries, recommendations for nodalizations call for discretizations which horizontally cut through the whole facility, i.e. all axial elevations of node boundaries have the same axial positions on both sides of the loop. The T52 instrumentation map suits this recommendation well as instrumentation exists in both shafts at the same elevation for most levels of the building. This approach was followed in the development of a CFAST model for the T52 tests as documented in Section 7.

For all of the T52 tests, containment system codes, have comparison data for the fire room, doorway, maintenance hatches, dome, at each level in both maintenance shafts, and in the connecting hallway on the 1.600 level. The total of these regions represents the entire circulation loop induced by the fire. Commonly, containment models of fire scenarios using the aforementioned approach of a combination of lumped volumes and 3D volumes results in networks of over 100 nodes. This is typically an order of magnitude higher than commonly used for zone models, but at least two orders of magnitude less than what is required for field models.

6.2.2 Plume

Nowadays, containment system codes have at least two options to simulate vertical jets/plumes. One approach is to use correlations to describe jet/plume characteristics. Those correlations are normally for free jets/plumes. The other approach is to cope with this issue by using stacks of nodes or a network of nodes to subdivide important jet/plume regions. Both approaches try to predict major axial characteristics as a function of lateral entrainment as close as possible.

It is apparent that the containment system codes offer a better potential for jet/plume simulation than zone models, but mostly at the expense of additional nodalization.

The three 2D sensor grids as well as the many sensor rakes allow a much more consistent validation of the major features of containment system codes and respective models.

6.2.3 Recirculation in the Dome

Contrary to models developed in the past, present dome models utilize at least a network of lumped volumes for containment system codes even for standard LOCA analyses. This approach has been used for design basis accidents as well as for severe accident analyses and related H_2 distributions for many years now. Containment system code models for the dome in case of fire simulations take the same approach. Fire simulations are less complicated than severe accident scenarios as they tend not to involve complex surface and volume condensation effects.

Experience shows that containment system codes are capable of simulating dome recirculation with a minimum number of nodes. The information provided by the T52 instrumentation may just be sufficient to validate this coarse node approach. It is certainly insufficient for validation of finer details in the dome on the main staircase side.

6.2.4 Compartment Mass Flows

The T52 test series provides far greater wealth of information on mass flows than the T51 fire experiments. This information can be ideally used to validate containment system codes, which use the concept of flow stagnation in the nodes and flows in the network of junctions connecting the nodes.

6.2.5 Gas Concentrations

As with zone model codes, the T52 test data is ideally suited for evaluating the predictive capabilities of system codes with respect to the propagation of combustion products throughout the circulatory loop of the fire. Containment system codes have been originally developed to primarily cope with steam-air-water mixtures. Thus, most of them are ill prepared to handle combustion products. In some cases, special combustion modules have been developed for that purpose and integrated into the containment system codes. Other more advanced containment codes such as GOTHIC and CONTAIN provide a large spectrum of options for propagating numerous gas species and combinations thereof.

6.2.6 Structural Temperatures

Containment system codes commonly include conducting walls bounding the individual compartments. This approach allows for defining multi-layer walls and categorizes conductors in different classes of thickness and material properties to account for all potential heat sinks in a compartment. The information of the few thermocouples attached at different surfaces at different axial locations can be used to validate heat transfer correlations and heat conduction models implemented in current containment system codes.

The T52 tests featured a number of heat transfer blocks, all of them designed and constructed for the purpose of measuring transient condensation heat transfer. As a result of their design, they were not well suited to the non-condensing, single-phase environment of the fire tests. Therefore, with the exception of one heat transfer block, most of the stored data were not evaluated in terms of transient heat transfer coefficients because measurement uncertainties became to high, see Section 3.3.

6.2.7 Global Recirculation

The T52 instrumentation is well suited to validate predicted temperatures, velocities and gas concentrations by containment system codes in multi-compartment, muli-level enclosures. Although all of these containment analysis codes were originally developed for high momentum

driven flows, the majority now have been modified to cope with buoyancy driven flows as well as stratified conditions. Both phenomena are covered by the T52 data set.

6.2.8 Combustion Models

The nuclear containment codes were originally designed for the purpose of calculating a containment building's response to a loss-of-coolant accident in a nuclear power plant. Therefore, the energy, mass, and momentum sources that were originally coded were steam-water mixtures and hydrogen from metal-water reactions. For these codes to be used to model the effects of fires in containment buildings, additional models relating to the calculation of combustion physics were added. Unlike the models relating to energy and mass inputs from pipe breaks, these new combustion models have not been thoroughly tested. Therefore the pyrolysis and combustion product measurements made during these tests are invaluable to evaluating the effectiveness of these models.

6.3 Field Models

Field models, such as FLUENT [36], FLOW-3D, GASFLOW [39], and FDS [37], operate by solving a discretized form of the three-dimensional equations for mass, momentum, and energy conservation. For most real structures, accurate resolution of the velocity, temperature, and species fields for a fire require a large number of computational nodes. Therefore, use of field models is typically restricted to smaller subsets of a larger structure to reduce the computational resource requirements.

The oil pan fire experiments T52 are extensively instrumented at specific vital cross sections. These include the two axial levels of thermocouples over the oil pan platform, the rake in the fire doorway providing velocity and temperature profiles, the axial rake of thermocouples in the dome over the spiral staircase maintenance hatch, and the three sensor grids of velocity, temperature and CO_2 concentration. In this regard, the T52 test series provides the most detailed instrumentation pattern available for field model validation for all of the HDR fire tests.

A field model code should be able to capture the fire room temperature distribution resulting from the room's ventilation asymmetry. Also, the field model should be able to reproduce the doorway temperature and velocity distribution. Lastly, the field model should predict both the correct location of the fire plume entering the dome and correctly predict its growth and entrainment.

The adequacy of a field model approach is highly dependent on the accuracy of the boundary conditions to be applied to the model. In this regards the T52 test can provide excellent boundary conditions for the fire compartments as a result of the sensor grids above and below the fire compartments, grids 2 and 3. Such an examination of FDS has been performed and is presented and discussed in [38].

7 CFAST MODELS FOR THE T52 OIL POOL FIRE TESTS

This section will discuss the runtime and environmental parameters, the combustion properties for the fire, the room surface properties, and the geometric models developed for the CFAST computations [29,30] performed for T52.11 and T52.14. A description of the development path is also given for the CFAST models. Tables showing input cards for the CFAST model are shown for the T52.11 model only. A full listing of input decks can be found in Appendix A.

7.1 Environment and Runtime Control

The T52 oil pool fire tests had a fire duration of approximately 34 minutes. Data collection during the tests began 10 minutes prior to the fire's start and continued for a period of up to 60 minutes after the end of the fire. No preconditioning of the containment building was performed before the start of any tests, i.e. the containment was at ambient conditions at the start of each test in the series. The CFAST model encompassed the test time from the beginning of the fire to approximately 30 minutes after the end of the fuel addition. Table 7.1 below shows the CFAST input cards for environment and runtime control.

Table 7.1: Environment and Runtime Control Cards for T51.11 CFAST Model

Card	Variable	Value	Explanation
TIMES	Simulation Time (s)	3600	1800 s fire + 1800 s post fire
	Print Interval (s)	20	
	History Interval (s)	20	
	Display Interval (s)	0	No graphics during execution
	Copy Count	0	No graphics to copy
TAMB/ EAMB	Ambient Temperature (K)	293.15	20 °C
	Ambient Pressure (Pa)	101300	1 atmosphere
	Station Elevation (m)	0	Absolute ground level of HDR

7.2 Combustion Model

Each of the tests in the T52 test series used Shellsol T as a fuel. Shellsol T is a hydrocarbon solvent manufactured by Shell Chemicals of Norway. Shellsol T is a liquid isoparaffin consisting of 11 to 13 carbon atoms with 80% of the molecules having 12 atoms. It is a clear liquid that generates less soot than common fuel oils such as kerosene. The basic thermophysical properties of Shellsol T can be found in Table 2.8. This data yields the following CFAST input cards for the fuel properties:

Table 7.2: Combustion Related Input Cards

Card	Variable	Value	Explanation
CHEMI	Molar Weight (g/mol)	170	$C_{12}H_{26}$
	Relative Humidity (%)	20	Default
	Lower Oxygen Limit (%)	0	Based on O2 Sensor CG9602
	Heat of Combustion (J/kg)	4.25E+07	Table 2.8
	Initial Fuel Temperature (K)	293	Initial HDR Temperature
	Gaseous Ignition Temperature (K)	349	Table 2.8
	Radiative Fraction	0.2	
LBFO	Fire Compartment	1	Compartment 1
LBFT	Fire Type	2	Constrained Fire
CJET	Ceiling Jet	Off	Not needed
FPOS	Depth (m)	0.875	Locate fire in center of fuel pool in fire room.
	Breadth (m)	2.290	
	Height (m)	0.000	

During each test the oil pan was loaded with a prespecified volume of oil. Once the initial volume was nearly depleted, additional oil was added to the oil pan at a constant, prespecified rate through a small tube. The rate of combustion was determined by measuring the rate of change of the platform's weight via three force sensors (CA9600-2). Unfortunately, these sensors were affected by the intense heat of the fire resulting in their measurements being difficult to interpret. A number of assumptions were made to interpret the weight sensors in order to yield a pyrolysis curve.

1. CA9600 was least affected by the heat (i.e. this sensor was used to generate the input for CFAST).
2. The total volume of fuel burned equaled the sum of the initial oil volume plus the oil added during the fire (i.e. all the oil was combusted).
3. The pyrolysis rate during the oil addition phase of the fire equaled the rate of oil addition as measured by RF7004 (i.e. the oil burned as fast as it was fed in).

Using the assumptions above a pyrolysis curve was generated as follows. From 10 minutes till the end of the fire, CA9600 was renormalized to yield a total combusted mass equal to the amount of oil added. From the beginning of the fire to 10 minutes CA9600 was renormalized to preserve the total amount of oil. This renormalized curve was used to generate the CFAST input. This input curve accounts for 98.5% of the total oil mass. Figure 7.1 shows the measured data, the renormalized measured data, and the CFAST input for the pyrolysis rate. In addition to this curve, Table 7.3 shows the other input cards required for specifying the fire.

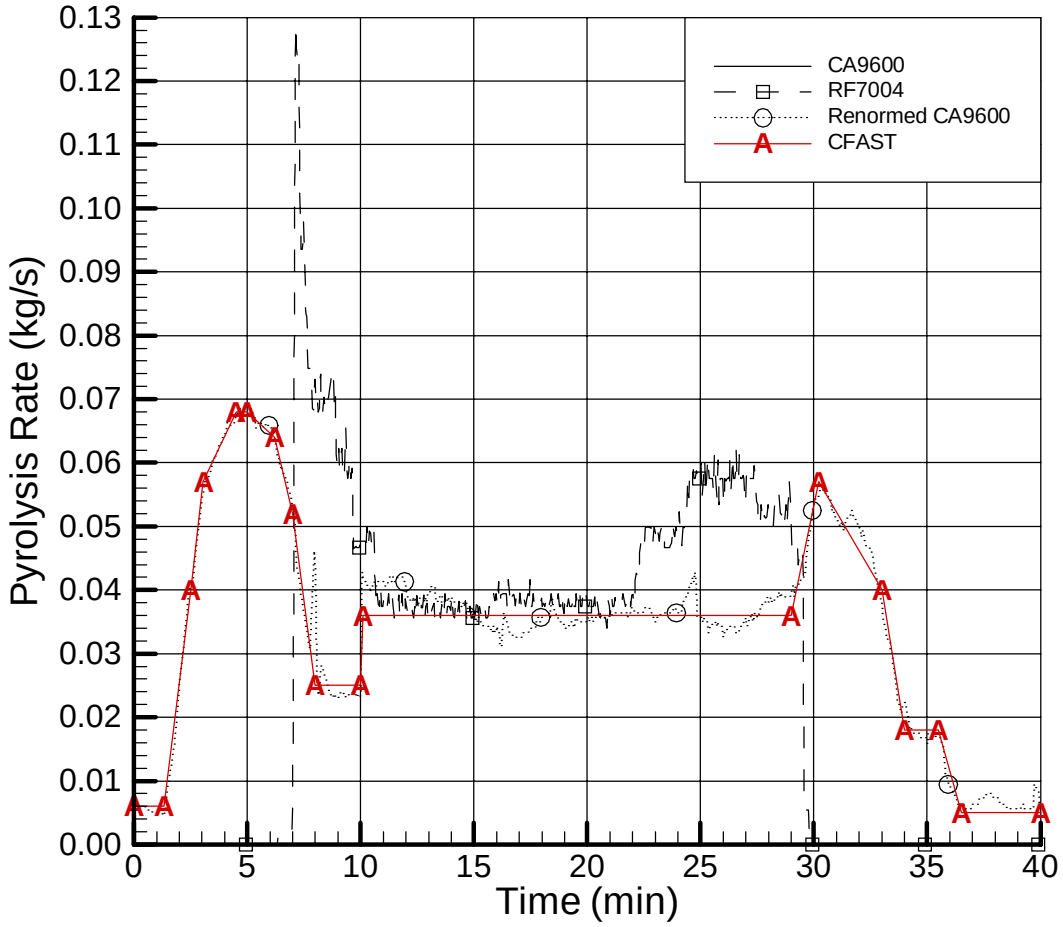

Figure 7.1: Generation of CFAST Pyrolysis Rate for T52.11

Table 7.3: Pyrolysis Cards for CFAST

Card	Variable	Value	Explanation
FTIME	Time Points (s)	30 70 103.6 190 220 292 340 400 520 526 1660 1732 1900 1960 2050 2110 2320 2392 3600	See Figure 7.1
FAREA	Fire Area (m^2)	0.0 0.0 1.0 1.0 1.0 1.0 1.0 1.0 1.0 1.0 1.0 1.0 1.0 1.0 1.0 1.0 1.0 1.0 1.0 1.0	Oil pan area for T52.11
FHIGH	Fire Height (m)	0.00 0.00 0.25 0.25 0.25 0.25 0.25 0.25 0.25 0.25 0.25 0.25 0.25 0.25 0.25 0.25 0.25 0.25 0.25 0.25	Elevation of oil platform top
FMASS	Pyrolysis Rate (kg/s)	0.000 0.000 0.040 0.057 0.068 0.068 0.064 0.052 0.025 0.025 0.036 0.036 0.057 0.040 0.018 0.005 0.005 0.000 0.000	See Figure 7.1
FQDOT	Heat Release Rate (W)	0 0 1700000 2422500 2890000 2890000 2720000 2210000 1062500 1062500 1530000 1530000 2422500 1700000 765000 765000 212500 212500 0 0	FMASS x Heat of Combustion
HCR	H to C Mass Ratio	0.00000 0.00000 0.15294 0.15294 0.15294 0.15294 0.15294 0.15294 0.15294 0.15294 0.15294 0.15294 0.15294 0.15294 0.15294 0.15294 0.15294 0.15294 0.15294 0.15294	$\frac{26}{170} = 0.15294$
O2	O_2 to C Mass Ratio	0.0 0.0 0.0 0.0 0.0 0.0 0.0 0.0 0.0 0.0 0.0 0.0 0.0 0.0 0.0 0.0 0.0 0.0 0.0 0.0	No oxygen in fuel
OD	C to CO_2 Mass Ratio	0.00 0.00 0.03 0.03 0.03 0.03 0.03 0.03 0.03 0.03 0.03 0.03 0.03 0.03 0.03 0.03 0.03 0.03 0.03 0.03	From CFAST object file
CO	CO to CO_2 Mass Ratio	0.00 0.00 0.03 0.03 0.03 0.03 0.03 0.03 0.03 0.03 0.03 0.03 0.03 0.03 0.03 0.03 0.03 0.03 0.03 0.03	From CFAST object file

7.3 Surface Properties

To model the HDR with CFAST requires generating material properties for the HDR's construction materials. For the T52 oil fire tests there are three materials which must be defined which are the HDR structural concrete, Ytong fire brick, steel, Promasil fire resistant wallboard, and Alsiflex fireproof, glass fiber matting. A CFAST material library was created for these materials and the surfaces which were constructed from them. Table 7.4 gives the thermophysical material properties which were obtained from [14] and [15].

Table 7.4: Thermophysical Properties of HDR Construction Materials

Material	Density (kg/m^3)	Conductivity (W/m·K)	Heat Capacity (J/kg·K)	Emissivity
Concrete	2,225	2.10	879	0.80[1]
Ytong Fire Brick	340	0.24	950	0.80[1]
Alsiflex	1,000	0.17	1,000	0.90[2]
Promasil	737	0.18	1,293	0.83[1]
Steel	7,854	59	559	0.90[1]

[1]Taken as fire brick (Concrete+Ytong), Marinite (Promatec) or steel from CFAST material library
[2]Taken from [15]

The above thermophysical properties were used to create a seven material library for use with CFAST. The seven materials included five single layer materials and two, two layer materials. The materials in the order listed below are 100 cm of concrete, the Alsiflex matting and Ytong firebrick ceiling for the fire room, the Ytong firebrick and concrete floor of the fire room, 3 cm thick Promasil wallboard, 1.2 cm thick steel, 10 cm of Ytong firebrick, and 25 cm of Ytong firebrick,. The material library is shown below. For single layer materials the format is material name, conductivity, density, heat capacity, thickness, emissivity, and seven parameters for HCl production. For multiple layer materials the format is the same with a '/' denoting values for each layer.

```
CONCR100  2.1 879 2225 1 0.8 0 0 0 0 0 0 0
FIRECEIL  0.17/0.24 1000/950 130/340 0.03/0.25 0.8 0 0 0 0 0 0 0
FIRE_FLR  0.24/2.1 950/879 340/2225 0.25/1 0.8 0 0 0 0 0 0 0
PROMASIL  0.18 1293 737 0.03 0.83 0 0 0 0 0 0 0
STEEL     59 559 7854 0.012 0.9 0 0 0 0 0 0 0
YTONG100  0.24 950 340 0.1 0.8 0 0 0 0 0 0 0  0
YTONG250  0.24 950 340 0.25 0.8 0 0 0 0 0 0 0  0
```

7.4 Compartments and Compartment Interconnections

The final portion of the CFAST model is of course the compartments and the compartment interconnections. As the HDR facility contains 9 levels and over 60 compartments with complex interconnections, it could not be modeled explicitly with CFAST. Therefore, simplifications were needed to model the HDR facility with CFAST. To this end, three different geometric models of the HDR facility were created with an increasing level of complexity. This was done,

in part, to see how different modeling assumptions affected the predictions made by CFAST. The following subsection will document the three geometric models in detail.

In general each model encompassed the fire room, fire room doorway, and the global circulation loop from the fire room to the dome, down to the 1.600 level, and back up to the fire room. Levels below the 1.600 level were not modeled as the maintenance hatches connecting the 1.500 and 1.600 levels were closed.

7.4.1 Inital Model

The Initial Model, schematically shown in Figure 7.2, was the simplest, although still complex for a zone model, model of the HDR facility. Since the doorway to the fire room was heavily instrumented, had a different height than the fire room, and was essentially a small room in and of itself (see Figure 2.2), it was decided to model the fire room as two compartments: one for the oil platform region and one for the doorway. The neighboring compartment, R1.902, was modified to protect the steel shell, so only that portion of R1.902 within the Ytong and Promasil walls was included. Thus three compartments were used to model the specially constructed fire compartments.

The remainder of the Initial Model encompassed the large flow loop through the HDR facility. The top of this loop is the dome which was modeled as a single compartment. The next set of compartments in the loop is the maintenance shaft on the main staircase side of the facility, see Figure 2.1. For the 1.900 through the 1.700 levels, a separate compartment was created for each level with flow connections to the levels above and below. The volumes of these compartments were set equal to the volume of the main staircase region on that level plus the volume of the region below the maintenance hatch. The flow area was set equal to the maintenance hatch as this represented the largest, free flowing connection between levels. On the 1.600 level a horizontal connection to the spiral staircase side of the building was created to form the bottom of the flow loop. The remainder of the model was one compartment each for the 1.700 level and the 1.800 level. The volumes of these compartments were set to the volume of the region containing the spiral staircase and maintenance hatch. The vertical flow connections on the spiral staircase side of the building were set equal to the maintenance hatch flow area.

Except for the fire room and doorway, all compartments were assumed to have a square floor area. Compartment heights were preserved according to the actual heights of each HDR floor level. Compartment volumes were also preserved as per the above discussion of the flow loop. Compartment floor areas were calculated based on volume and height. With the exception of the fire room, doorway, fire area hatch region, and the dome, all compartment surfaces were assumed to be concrete. For the fire rooms, the surfaces were set according to the facility description in Section 2. The dome was set for steel walls and ceiling and a concrete floor. The Initial Model geometric input cards are shown below.

```
HI/F   25.5500  25.5500  25.3000  30.8500  25.3000  20.6000  15.0500 10.00000 10.00000 15.05000  20.6000
WIDTH  1.75000  0.95000  3.04700  15.8530  5.25500  4.56600  6.03300  7.00800  9.66800  5.58300  6.58800
DEPTH  4.58000  0.78000  3.04700  15.8530  5.25500  4.56600  6.03300  7.00800  9.66800  5.58300  6.58800
HEIGH  2.80000  3.00000  5.55000  19.1500  5.55000  4.70000  5.55000  5.05000  5.05000  5.55000  4.70000
CEILI FIRECEIL YTONG100 PROMASIL STEEL    CONCR100 CONCR100 CONCR100 CONCR100 CONCR100 CONCR100 CONCR100
WALLS YTONG250 YTONG100 YTONG100 STEEL    CONCR100 CONCR100 CONCR100 CONCR100 CONCR100 CONCR100 CONCR100
```

```
FLOOR FIRE_FLR FIRE_FLR CONCR100 CONCR100 CONCR100 CONCR100 CONCR100 CONCR100 CONCR100 CONCR100 CONCR100
HVENT  1  2  1 0.95000  2.80000  0.00000  0.00000  0.00000  0.00000
CVENT  1  2  1 1.00000  1.00000  1.00000  1.00000  1.00000  1.00000  1.00000  1.00000  1.00000  1.00000  1.00000
1.00000  1.00000  1.00000  1.00000  1.00000  1.00000  1.00000  1.00000
HVENT  2  3  1 0.95000  3.00000  0.00000  0.00000  0.00000  0.00000
CVENT  2  3  1 1.00000  1.00000  1.00000  1.00000  1.00000  1.00000  1.00000  1.00000  1.00000  1.00000  1.00000
1.00000  1.00000  1.00000  1.00000  1.00000  1.00000  1.00000  1.00000
HVENT  8  9  1 1.08000  3.25000  0.00000  0.00000  0.00000  0.00000
CVENT  8  9  1 1.00000  1.00000  1.00000  1.00000  1.00000  1.00000  1.00000  1.00000  1.00000  1.00000  1.00000
1.00000  1.00000  1.00000  1.00000  1.00000  1.00000  1.00000  1.00000
VVENT  4  3  4.81000  2
VVENT  4  5  4.54000  2
VVENT  5  6  4.54000  2
VVENT  6  7  4.54000  2
VVENT  7  8  4.54000  2
VVENT  3 11  4.81000  2
VVENT 11 10  4.81000  2
VVENT 10  9  4.81000  2
```

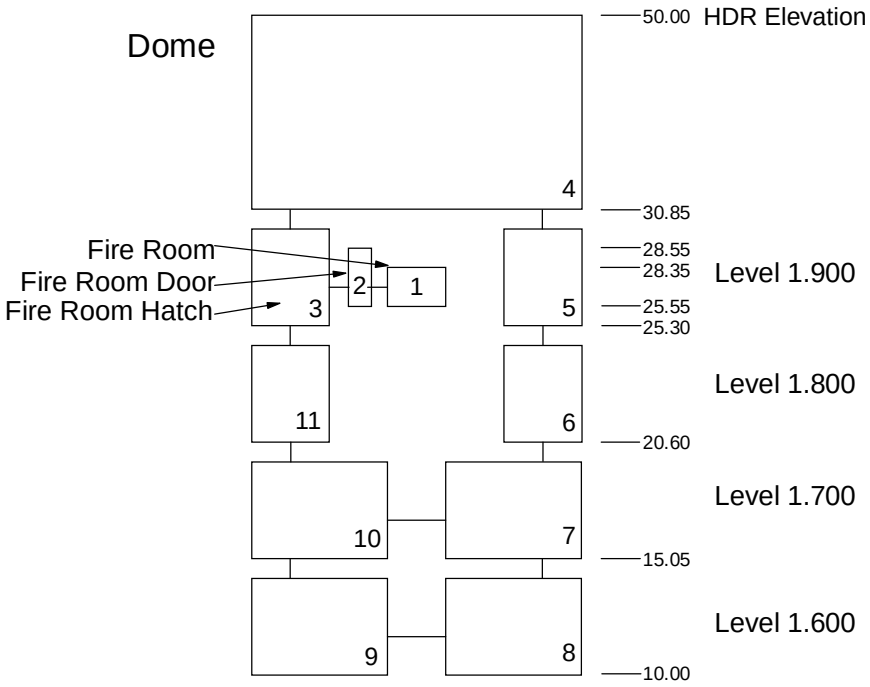

Figure 7.2: Initial Model Block Diagram

7.4.2 A Model

The A Model, schematically shown in Figure 7.3, is identical to the Initial Model with the exception of how the dome was treated. In the A Model the dome was subdivided into three compartments. The compartments were the spiral staircase side of the dome from the operating deck to the polar crane (one half of the cylindrical portion of the dome, the hemispherical top of the dome, and the second half of the lower dome. Flow connections between the compartments were set equal to the area of the surfaces in common between the compartments. Thus, three additional flow connections were specified along with the three new compartments. These were two vertical flow openings between the lower two nodes and the upper dome and one horizontal flow opening between the lower two nodes. The A Model geometric cards for the 13 volumes are shown below.

```
HI/F   25.5500  25.5500  25.3000  30.8500  40.0000  30.8500  25.3000  20.6000  15.0500 10.00000 10.00000 15.05000  20.6000
WIDTH  1.75000  0.95000  3.04700  12.3400  14.2400  12.3400  5.25500  4.56600  6.03300  7.00800  9.66800  5.58300  6.58800
DEPTH  4.58000  0.78000  3.04700  12.3400  14.2400  12.3400  5.25500  4.56600  6.03300  7.00800  9.66800  5.58300  6.58800
HEIGH  2.80000  3.00000  5.55000  9.1500   10.0000  9.15000  5.55000  4.70000  5.55000  5.05000  5.05000  5.55000  4.70000
CEILI FIRECEIL YTONG100 PROMASIL OFF      STEEL    OFF      CONCR100 CONCR100 CONCR100 CONCR100 CONCR100
WALLS YTONG250 YTONG100 YTONG100 STEEL    STEEL    STEEL    CONCR100 CONCR100 CONCR100 CONCR100 CONCR100
```

```
FLOOR FIRE_FLR FIRE_FLR CONCR100 CONCR100 OFF      CONCR100 CONCR100 CONCR100 CONCR100 CONCR100 CONCR100
HVENT  1  2  1 0.95000  2.80000  0.00000  0.00000  0.00000  0.00000
CVENT  1  2  1 1.00000  1.00000  1.00000  1.00000  1.00000  1.00000  1.00000  1.00000  1.00000  1.00000
1.00000  1.00000  1.00000  1.00000  1.00000  1.00000  1.00000  1.00000
HVENT  2  3  1 0.95000  3.00000  0.00000  0.00000  0.00000  0.00000
CVENT  2  3  1 1.00000  1.00000  1.00000  1.00000  1.00000  1.00000  1.00000  1.00000  1.00000  1.00000
1.00000  1.00000  1.00000  1.00000  1.00000  1.00000  1.00000  1.00000
HVENT  4  6  1 12.3400  9.15000  0.00000  0.00000  0.00000  0.00000
CVENT  4  6  1 1.00000  1.00000  1.00000  1.00000  1.00000  1.00000  1.00000  1.00000  1.00000  1.00000
1.00000  1.00000  1.00000  1.00000  1.00000  1.00000  1.00000  1.00000
HVENT 10 11  1 1.08000  3.25000  0.00000  0.00000  0.00000  0.00000
CVENT 10 11  1 1.00000  1.00000  1.00000  1.00000  1.00000  1.00000  1.00000  1.00000  1.00000  1.00000
1.00000  1.00000  1.00000  1.00000  1.00000  1.00000  1.00000  1.00000
VVENT  3  4  4.81000  2
VVENT  4  5  152.150  2
VVENT  5  6  152.150  2
VVENT  6  7  4.54000  2
VVENT  7  8  4.54000  2
VVENT  8  9  4.54000  2
VVENT  9 10  4.54000  2
VVENT  3 13  4.81000  2
VVENT 13 12  4.81000  2
VVENT 12 11  4.81000  2
```

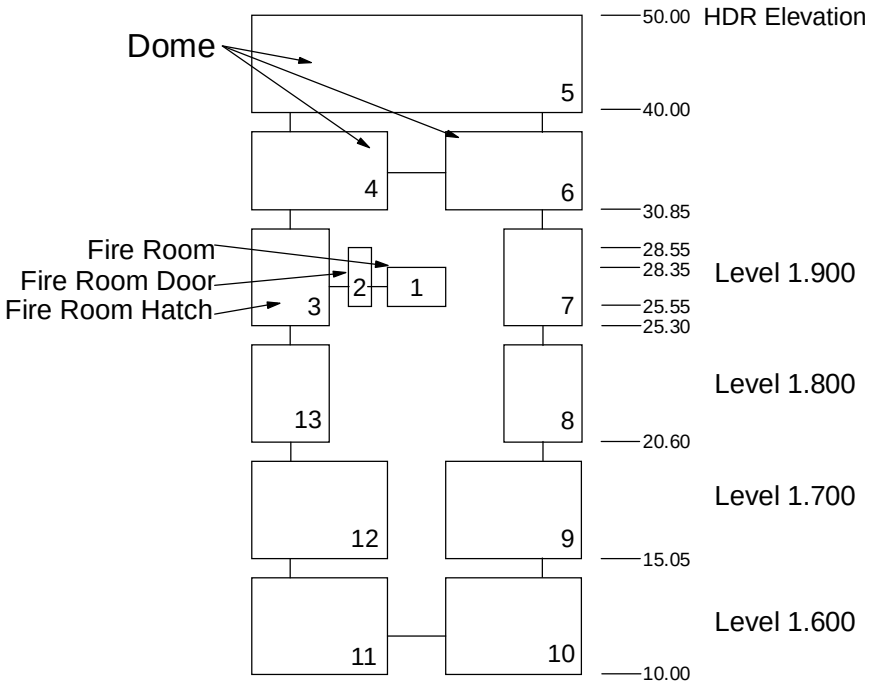

Figure 7.3: A Model Block Diagram

7.4.3 B Model

The B Model, schematically shown in Figure 7.4, is identical to the A Model with the exception of the vent connections specified in the dome. In the actual test, the flow induced by the fire rose from the maintenance hatch by the fire room straight up to the upper dome and from there circulated back down to the lower dome and the main staircase side. As a result of the flow connection between the two lower dome compartments in the A Model, CFAST shunted much of the mass flow directly to the main staircase side of the dome without going through the upper dome contrary to experimental evidence. To prevent this, the B Model removed this vent connection. Figure 7.4 contains a block diagram of the B Model geometry. The B Model geometric input cards for the 13 volumes are shown below.

```
HI/F   25.5500  25.5500  25.3000  30.8500  40.0000  30.8500  25.3000  20.6000  15.0500 10.00000 10.00000 15.05000  20.6000
WIDTH  1.75000  0.95000  3.04700  12.3400  14.2400  12.3400  5.25500  4.56600  6.03300  7.00800  9.66800  5.58300  6.58800
DEPTH  4.58000  0.78000  3.04700  12.3400  14.2400  12.3400  5.25500  4.56600  6.03300  7.00800  9.66800  5.58300  6.58800
```

```
HEIGH  2.80000  3.00000  5.55000  9.1500   10.0000  9.15000  5.55000  4.70000  5.55000  5.05000  5.05000  5.55000  4.70000
CEILI FIRECEIL YTONG100 PROMASIL OFF      STEEL    OFF      CONCR100 CONCR100 CONCR100 CONCR100 CONCR100 CONCR100 CONCR100
WALLS YTONG250 DOORWALL YTONG100 STEEL    STEEL    STEEL    CONCR100 CONCR100 CONCR100 CONCR100 CONCR100 CONCR100 CONCR100
FLOOR FIRE_FLR FIRE_FLR CONCR100 CONCR100 OFF      CONCR100 CONCR100 CONCR100 CONCR100 CONCR100 CONCR100 CONCR100 CONCR100
HVENT  1  2  1 0.95000  2.80000  0.00000  0.00000  0.00000  0.00000
CVENT  1  2  1 1.00000  1.00000  1.00000  1.00000  1.00000  1.00000  1.00000  1.00000  1.00000  1.00000  1.00000  1.00000
HVENT  2  3  1 0.95000  3.00000  0.00000  0.00000  0.00000  0.00000
CVENT  2  3  1 1.00000  1.00000  1.00000  1.00000  1.00000  1.00000  1.00000  1.00000  1.00000  1.00000  1.00000  1.00000
HVENT 10 11  1 1.08000  3.25000  0.00000  0.00000  0.00000  0.00000
CVENT 10 11  1 1.00000  1.00000  1.00000  1.00000  1.00000  1.00000  1.00000  1.00000  1.00000  1.00000  1.00000  1.00000
VVENT  3  4  4.81000  2
VVENT  4  5  152.150  2
VVENT  5  6  152.150  2
VVENT  6  7  4.54000  2
VVENT  7  8  4.54000  2
VVENT  8  9  4.54000  2
VVENT  9 10  4.54000  2
VVENT  3 13  4.81000  2
VVENT 13 12  4.81000  2
VVENT 12 11  4.81000  2
```

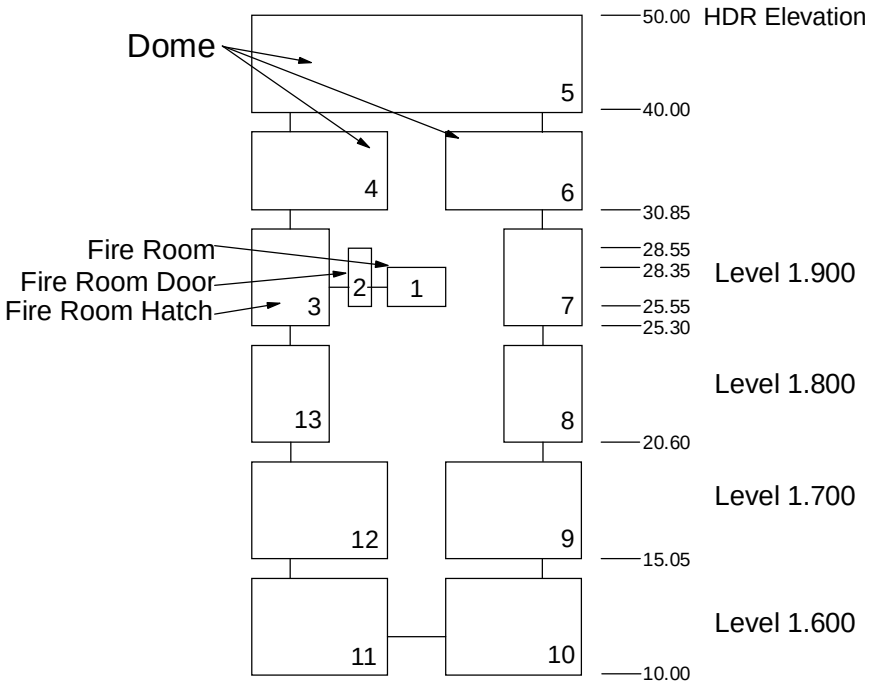

Figure 7.4: B Model Block Diagram

8 CFAST RESULTS AND COMPARISONS WITH HDR DATA

8.1 Introduction

This section compares the CFAST predictions using the three models described in Section 7 with measured data from the actual tests for two of the four oil pool fire tests, T52.11 and T52.14. Instrument descriptions and locations can be found in Section 3 of this report. The text and figures that follow will compare predictions of fire power, fuel availability, and nodalization of the dome on CFAST's predictive capabilities. In each of the figures that follow, the HDR sensor is identified by its instrument number and its axial position in terms of the HDR containment coordinate system.

As this section discusses model comparisons with data, it is important to define what the authors consider a good versus a poor comparison. CFAST, a zone model, is designed to be a quickly executed engineering tool with a relatively small learning curve for the potential user. Therefore, CFAST cannot be expected to make exact or near exact predictions to the locally measured data especially given the complexity of the HDR facility. However, it can be expected that CFAST should be able to reproduce the same regional and transient trends as seen in the data, predict with reasonable accuracy the significant phenomena of the experiments, and not introduce significant, non-existing phenomena.

In the following subsections, 8.2 and 8.3, the comparisons between computational results and data will be documented for the experiments T52.11 and T52.14, respectively.

8.2 Comparisons Between CFAST Predictions and T52.11 Data

8.2.1 Temperatures

All of the following graphical comparisons for the temperatures will be presented in the same format. CFAST results for upper layer quantities will be designated with the symbol 'U' and for lower layer quantities with the symbol 'L'. The initial, single-volume dome model of CFAST will use a solid line, the three-node dome model with a horizontal flow connection (model A) will use a dashed line, and the three-node dome model without a horizontal flow connection (model B) will use a dash-dot-dot line.

Figure 8.1 documents the comparisons of the three CFAST model results with measured temperatures in the fire room. As can be clearly seen, all three models results in about the same upper and lower layer temperatures. Minimal differences between the models are noticeable only in somewhat lower peak temperatures of the lower layer at 4 minutes for models A and B, with model A resulting in the lowest peak temperature. This small feedback is propagated by CFAST through the whole flow loop, affecting the lower layer, and is consistent with expectations. CFAST and the three models developed and utilized do not allow any feedback from the dome nodalization to propagate through to the upper layer of the fire room.

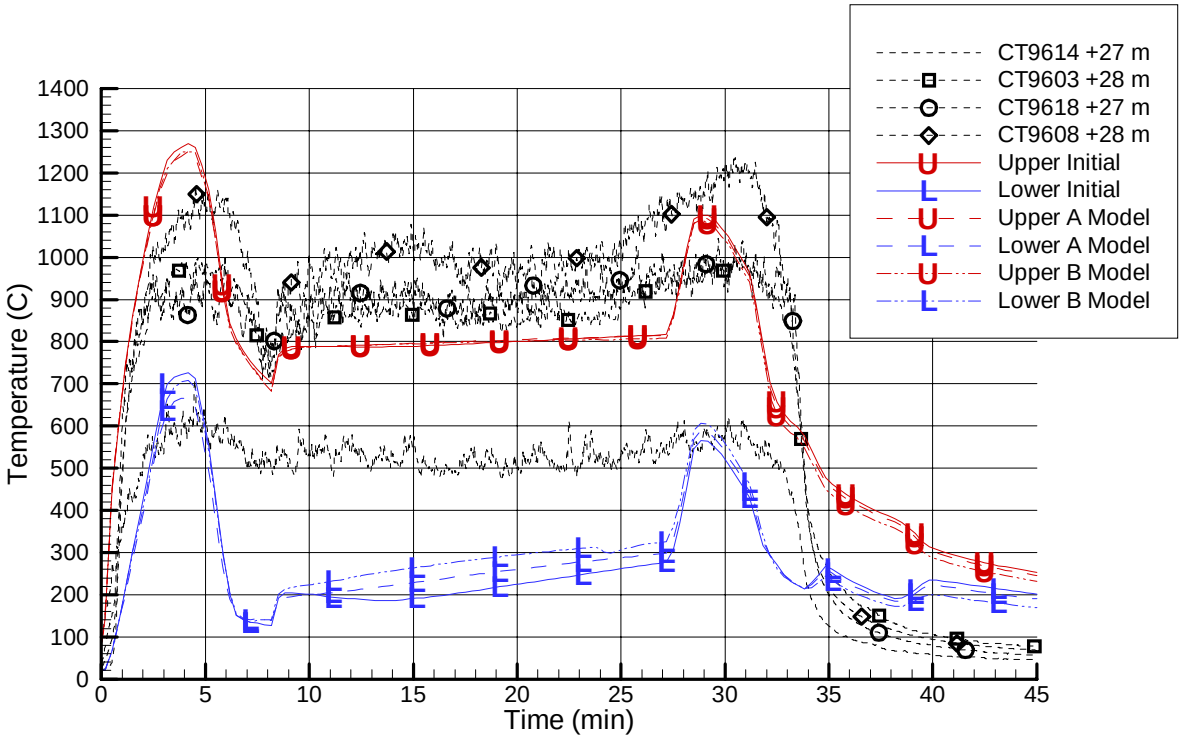

Figure 8.1: T52.11 Fire Room Temperatures

The agreement between all predictions and the measured data in the upper layer is excellent. Especially the initial temperature during the first 5 minutes is predicted very well. After 7 minutes into the fire the predicted upper gas layer temperature constitutes the lower bound of the measured data, which range from 50 to 250 °C higher during the remainder of the fire. The peak fire room temperature is over-predicted by all three models by approximately 140 °C with models A and B predicting slightly lower values. The time of the peak temperature is predicted by CFAST to be at 4 minutes whereas the test data shows it at 5 minutes; however, this is not unreasonable.

A complete analysis of the CFAST lower layer predictions is not possible due to the absence of instrumentation at lower elevations in the fire room. Sensor CT9614 at +27 m in elevation lies near the fire room doorway, and thus, is the best available sensor for which to make comparisons to. In the first 5.5 minutes of the fire the CFAST predictions for each model lie on top of CT9614. Given the fast growth and magnitude of the fire, it would not be unreasonable to expect that the lower layer would approach the conditions seen in regions of the upper portion of the fire room. After the peak of the fire, the predicted temperature decreases rapidly by 600 °C to 120 °C while CT9614 stays constant at 530 °C for the rest of the fire. After the peak of the fire one would expect cooler air to penetrate into the fire room lower layer and thus CT9614 should represent an upper bound, which it does. All predictions show a slow temperature rise from 8 min to 27 minutes which is not seen in the measured data. CFAST also predicts a large rise in lower layer temperature during the end phase of the fire which is not seen in the data for CT9614.

We also see that during the fire both the A Model and the B Model predict higher lower layer temperatures than the Initial Model with the B Model predicting the highest temperatures.

At the end of the fire, during the cooldown phase, CFAST does not predict the slope of the temperature decrease as steep as the data indicates. However, this may result from errors in the specified burn up curve. Furthermore, the CFAST predicted temperatures converge to a post-fire level approximately 150 °C above the measured temperatures with the B Model having the least over-prediction. CFAST also shows a slight oscillation in temperature of the lower layer between 33 minutes and 40 minutes which lacks any physical driving force in terms of the burn up curve during this time period. Lastly, it is worth mentioning that CFAST does an excellent job in predicting the post-fire thermal stratification in the fire room. Both the measured data and the CFAST predictions indicate a temperature spread of approximately 50 °C at the end of the rapid cooldown phase.

The following major conclusions can be drawn regarding CFAST model results:

1. There is excellent agreement with data in all major aspects of the fire dynamics and evolution in the fire room.
2. Results are nearly independent upon the dome nodalization.
3. The maximum temperature in the fire room is conservatively predicted.
4. The initial temperature rise is in perfect agreement with the measured data.
5. The predicted lower gas layer temperature response is good albeit somewhat too slow, with respect to initial temperature gradient.
6. The maximum lower layer temperature is predicted extremely well given the ambiguity in the identification of the lower gas layer conditions for this test.

Figure 8.2 summarizes the comparisons for the next upstream zone, the doorway. This was instrumented quite well and offers a unique opportunity for comparison. The following conclusions can be drawn for the CFAST predictions from the comparisons with the data as well as amongst the predictions:

1. The general agreement with the data is good, at times excellent.
2. The predictions are nearly independent upon the dome nodalization; some changes are noticeable in the lower gas layer temperatures.
3. The CFAST predictions for the upper layer are bounded by the measured data though it would appear that CFAST is somewhat under-predicting the temperature.
4. The initial upper-gas layer temperature rise after fire onset is in very good agreement with the data; deviations develop beyond 1.5 min into the transient.
5. The predicted trend is in excellent agreement with the data trend
6. The predicted lower layer temperatures are under-predicted by 30 to 50 °C with the B Model having the best agreement with the measurement.
7. There is no ambiguity associated with the identification of the gas layers in the doorway.
8. After good initial agreement, measured and predicted cooldown transients of both layers differ significantly. The predicted temperature of the lower layer increases

during the cooldown while the measured one increases. Again the B model shows the best agreement.

9. Measured and predicted thermal stratifications agree well, though with different temperature levels.

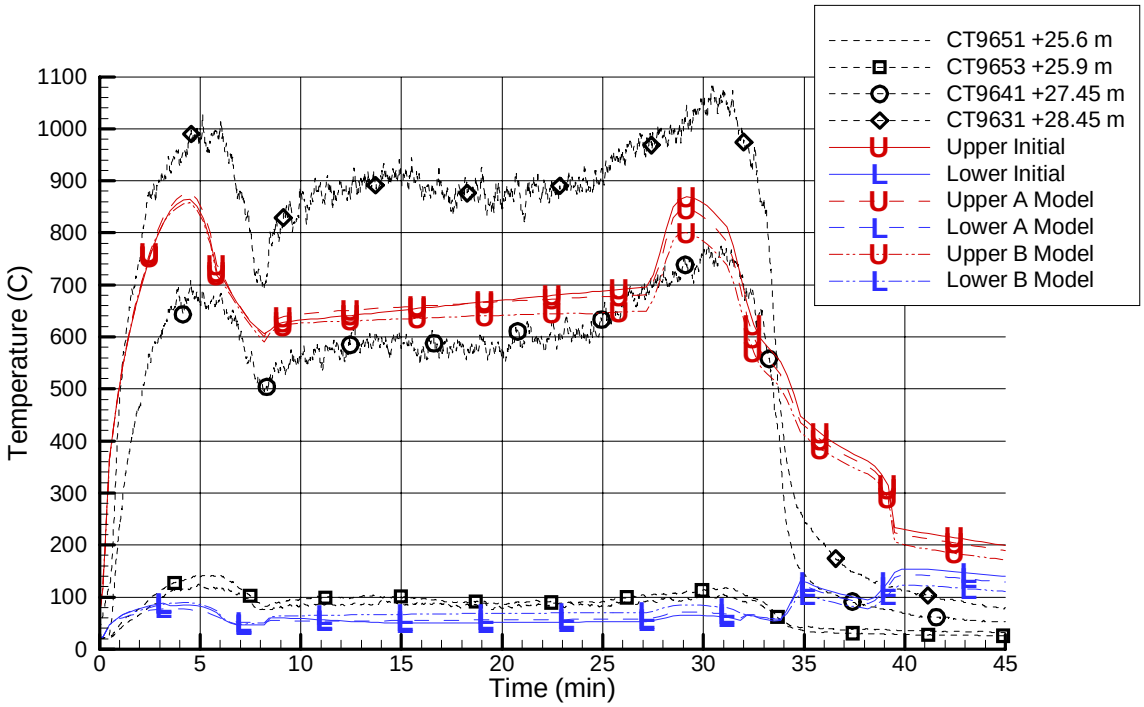

Figure 8.2: T52.11 Doorway Temperatures

Figure 8.3 summarizes the comparisons in the zone downstream of the doorway in the maintenance hatch to the dome. This is an extremely important zone, both with respect to the experiment as well as model chosen, because it provides the coupling between the fire room/doorway region with the dome and the rest of the containment. In fact, its importance becomes quite obvious by comparing the measured temperatures, which decrease from the upper doorway at 1100 °C, see Figure 8.2, down to 300°C maximum at the hatch entering the dome at the operating deck level. This tremendous reduction in temperature of the exiting fire plume is achieved by the very effective mixing/entrainment processes in this zone. It is clear that the processes in this coupling zone, and thus the capability of any code to simulate those, dominate the plume characteristics and evolution in all downstream nodes.

The two effects contributing to the mixing/entrainment processes in this zone are as follows:

1. Entrainment/mixing from the zone below by lifting much cooler containment atmosphere from lower elevations into this mixing region by virtue of a jet pump effect.
2. Entrainment/mixing by countercurrent downflow of cooler containment dome atmosphere due to continuity requirements and the fact that the fire plume does not occupy the complete flow area of the maintenance hatch. In fact, the fire plume is

asymmetrically placed towards the corner of the hatch closest to the fire room doorway. This results from the relative locations of the fire room doorway and the maintenance hatch along with the tapered ceiling of the region below the hatch.

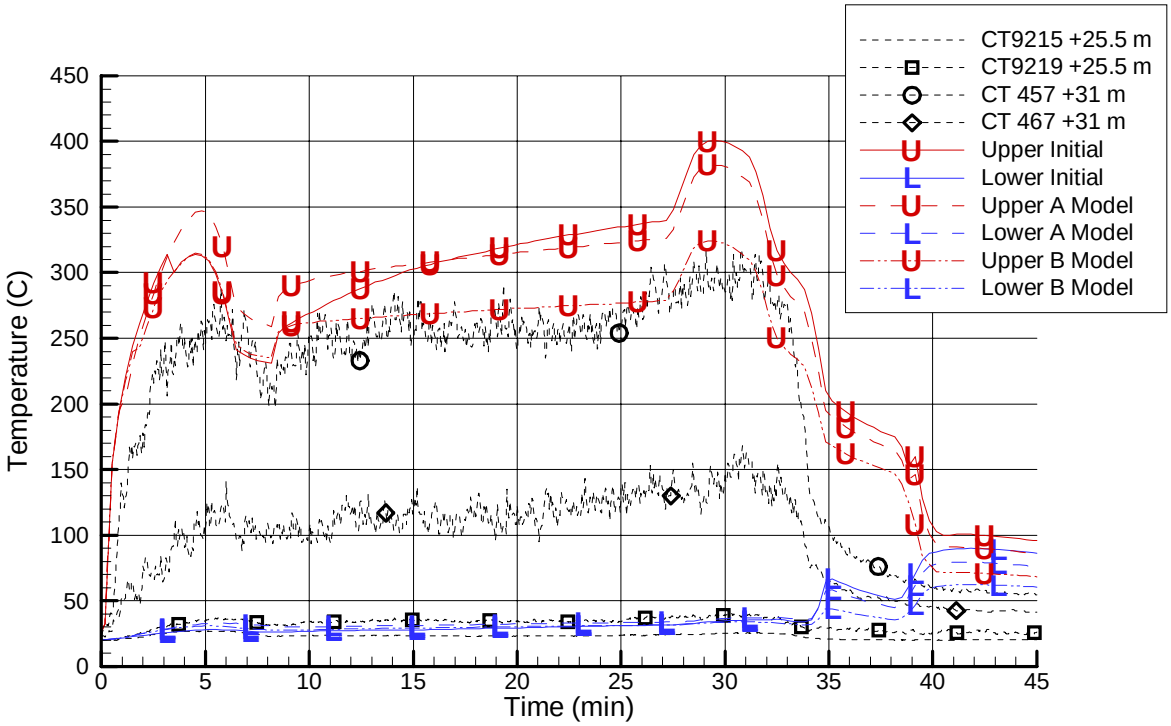

Figure 8.3: T52.11 Level 1.900 Hatch Region Temperatures

The following conclusions can be drawn for the CFAST model predictions in comparison with the data:

1. Since sensors CT457 and CT467 lie near the hot spot and near the edge of the plume respectively, they represent bounding values for the plume temperature. The hot layer of this region should be close to the hot spot temperature which represents a region little cooled by entrainment. CFAST predictions for all models exceed this upper bound by over 50 °C at the peak of the fire at 5 minutes.
2. All model predictions reduce the computed temperatures by more than a factor of 2 as compared to the doorway upper gas layer temperature, e.g. the massive cooling in this zone is simulated by CFAST, but the data indicate a temperature drop by a factor of 3. This means that CFAST does not predict as much entrainment and mixing as experimentally observed.
3. Aside from the noted differences in the level of temperatures, all CFAST models predict the temperature transient evolution very well, except during the initial fire phase, which in CFAST is dominated by the fire room dynamics, while the data clearly show slow mixing characteristics.
4. As this coupling zone is so close to the dome, the predicted upper gas layer temperatures are affected by the details of the dome nodalization in the 2 different

CFAST models. In fact, maximum predicted temperatures as well as the temperature evolutions at later times are affected. Allowing for 3 nodes in the dome and coupling between the lower nodes (A Model) tends to lower the predicted temperatures 25 °C during the steady-state portion, as more circulation is allowed for in the dome; the initial temperature peak though increases by 25 °C.

5. B Model without a horizontal flow connection decreases the temperature prediction during the steady-state portion to lie just above CT 457.
6. All CFAST-model predictions for the lower gas layer temperature are in excellent agreement with the data.
7. The predicted post-fire temperatures at 45 minutes are 75 °C to high compared to measured temperatures. The thermal stratification prediction is somewhat smaller than the measured stratification, 40 °C compared to 50 °C.
8. The measured lower layer temperatures show a slight decrease, whereas the CFAST predictions show a stepwise increase of 50 °C after the end of the fire. The CFAST predictions here are obviously controlled by the predicted fire room doorway temperature, whereas the measurement is controlled by the overall cooldown in the global circulation loop.

Figure 8.4 compares all 3 CFAST model predictions with data measured at different positions in the dome, ranging from +31 m, operating deck level, to +47.55 m, high in the hemispherical portion of the dome. These sensors are from the vertical rake formed by the center of the measurement grids combined with a few additional measurement locations. The data indicates that these sensor locations lie closer to the plume periphery than to the plume centerline. Note that for the A Model and B Model that the CT 486 sensor is not applicable to the dome node plotted as for those models the node upper elevation is +40 m.

The following conclusions can be drawn:

1. The three models of the dome used for the CFAST simulations result in quite different predictions for the upper gas layer temperature
2. With the exception of some minor time wise changes, all 3 models predict about the same lower gas layer temperature with differences within 5 °C.
3. As anticipated, the initial single-node dome representation results in the highest predicted upper gas layer temperature compared to those resulting from the A Model and the B Model. This is especially true during the early stage of the fire, up until 8 minutes, while at the later stages, times greater than 20 minutes, the prediction converges at a level between the results for the A Model and B Model.
4. The initial single-node dome model predicts an upper gas layer temperature, which approximately bounds the exit temperature of the plume at the level of the operating deck (+31 m), during the first 8 minutes of the fire. However, since the CFAST prediction represents an average for the entire dome's upper layer, it is clear that this is actually a substantial over-prediction. Thereafter, this CFAST model lies amidst the measured values in the dome for a more reasonable prediction.
5. The CFAST predicted upper layer temperatures for the A Model, with the flow connection, lies within the measured data in the upper region of the node. It also has

the closest match to the cooldown in both trend and magnitude. However, given that the sensors lie on the plume periphery, it is not certain as to whether or not the CFAST prediction is in this case an accurate representation of conditions overall in this region. It can only be said that they are not unreasonable.

6. The CFAST predicted upper layer temperatures for the B Model, without the flow connection, lies above the measured data in the upper region of the node. As such it may represent a slight over-prediction of the temperature in this region of the dome as compared to the A Model, but again firm conclusions can not be drawn due to the few measurement locations available for comparison.
7. The lower gas layer temperatures for all models show little change during the fire. This is not physically correct as some form of recirculation must have occurred in the dome due to continuity reasons (to feed the entrainment of the plume). CFAST, however, lacks the physical models to generate this sort of mass exchange.
8. Perplexingly, the lower layer temperature for the Initial Model exceeds that of the upper layer at the end of the cooldown phase.

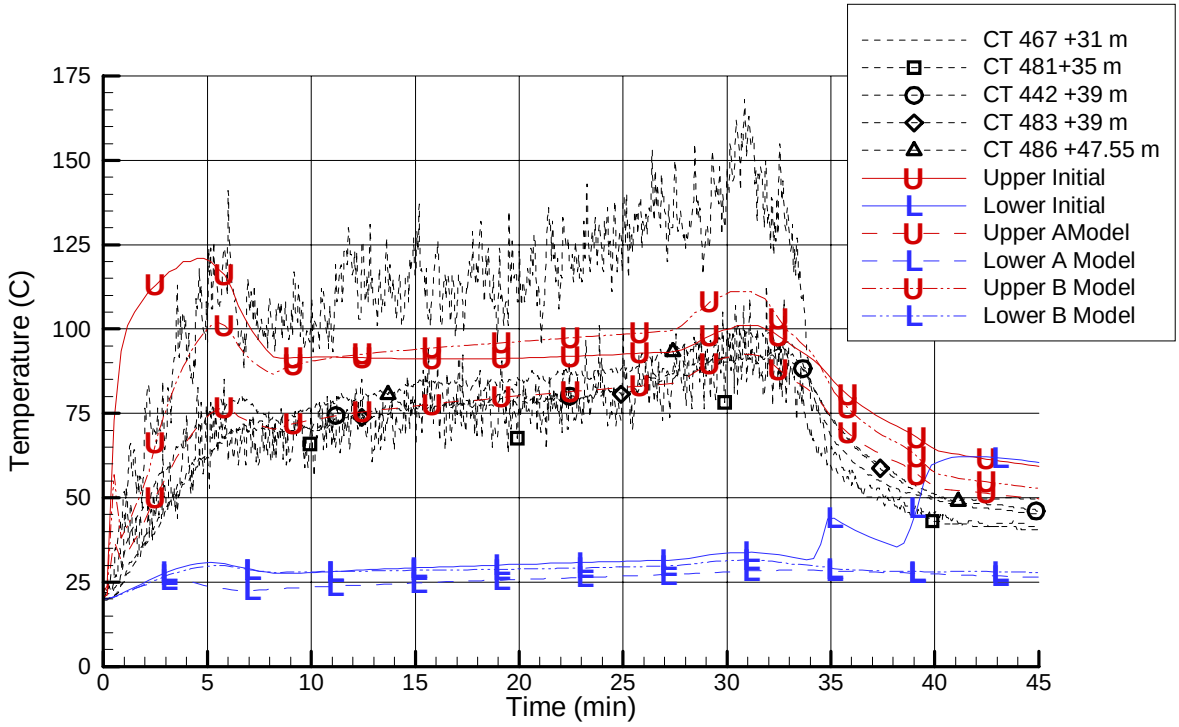

Figure 8.4: T52.11 Dome Temperatures Over Fire Room Hatch

Figure 8.5 compares data with predictions from the A Model and the B Model for zone 5, the uppermost dome region. The region represents the hemispherical portion of the dome from +40 m to + 50 m. The upper layer temperature from the Initial Model is included for comparative purposes only. The following conclusions can be drawn from Figure 8.5.

1. The upper layer temperature predicted by the A Model constitutes the lower bound of the measured data by under-predicting the measured temperatures by 10-15 °C.

2. The upper layer temperature computed by the B Model over-predicts the temperature in the dome at the peak of the fire by 10 °C, but afterwards perfectly matches the measured temperatures even during the post-fire phase.
3. For both the A Model and the B Model the lower layer temperature is not a meaningful quantity for comparison as the layer height for both models was zero.
4. When compared to the upper layer temperature of the initial model, the benefit of subdividing the dome is clearly seen.

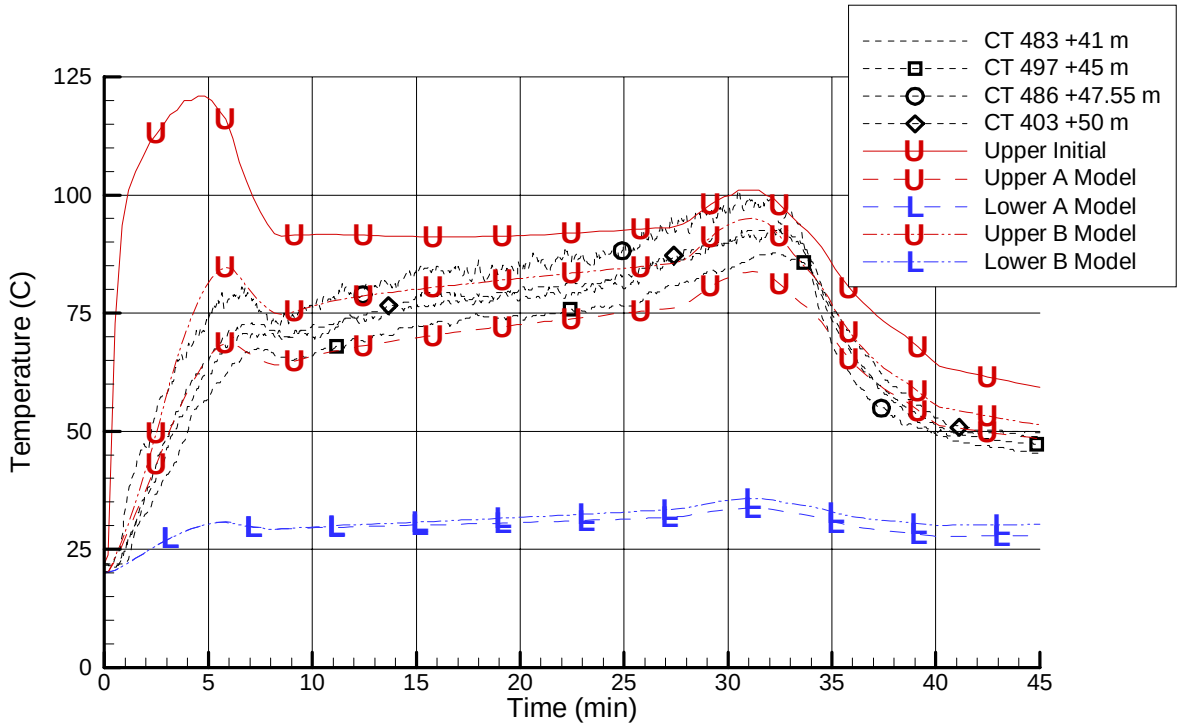

Figure 8.5: T52.11 Upper (Hemispherical) Dome Temperatures

Figure 8.6 presents the comparisons between the data with the predictions from models A and B for zone 6, the main staircase-side node in the dome from elevations +30.85 m to +40 m. The layer temperatures from the Initial Model's dome node are included for illustrative purposes only. The following conclusions can be drawn from this figure:

1. The A Model prediction for the upper layer over-predicts the data from sensor CT 488 at 37 m by about 10-30 °C. The long-term temperature gradient is matched very well. The CFAST result constitutes the upper bound for the measured temperatures in this zone, as the flow connection between the two lower dome nodes allows for flow of containment atmosphere from the spiral staircase side to bypass the cooling effect of the upper dome.
2. For the fire growth phase the B Model over-predicts slightly the data of sensor CT488 at 37 m. Beyond 9 minutes the B Model lies within the measured data until the cool down phase as it should. During the cooldown phase the B model over-predicts the average measured temperature by 5-10 °C.

3. Also, the B Model for the lower layer temperature is in very good agreement with the measured temperatures, CT419 and CT487 at +30.85 m and +31 m, respectively during the first 5 minutes. Since the layer height during the first few minutes is over +31 m, CFAST is making a superb prediction for this quantity.
4. On this side of the main staircase the CFAST upper gas layer is indeed the hotter zone as the warm gas from the spiral staircase is flowing downwards from the upper dome region toward the exit at the operating deck.
5. As with Figure 8.5, after the initial growth of the fire the predicted layer height for both models becomes so low as to make comparisons of the lower layer predictions meaningless.

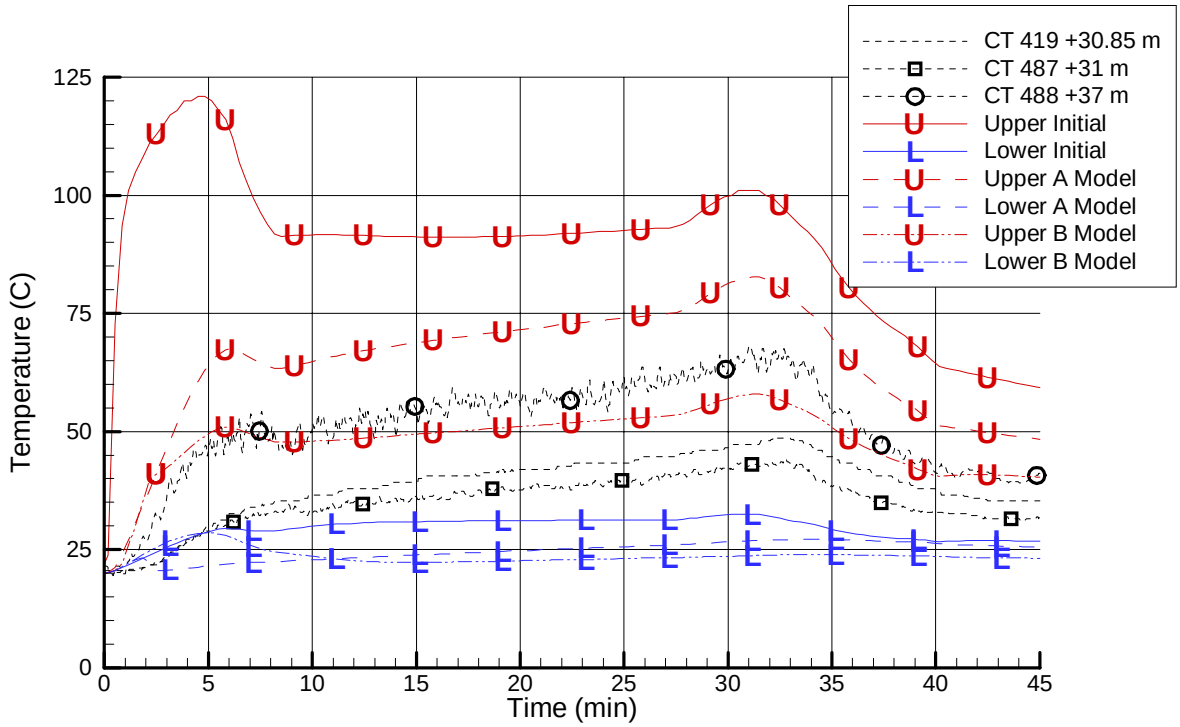

Figure 8.6: T52.11 Main Staircase Dome Temperatures

In summarizing the comparisons between data and CFAST predictions in the dome by comparing Figures 8.4 through 8.6 it becomes obvious that all three models have their individual advantages and disadvantages. The initial model has the advantage of simplicity, but does not perform well for the entire dome region. The A Model preserves the correct flow connections physically present in the dome, but results in an unphysical flow field. In total, the B Model was the best performer. All three provide the CFAST user a full spectrum of tools to cover all major fire aspects in the large-sized dome in the realm of model code capabilities. Judged from that perspective the CFAST results can be termed excellent. Although the 3-node discretization of the dome together with the no-flow/flow options between the 2 bottom zones achieved all major anticipated objectives, it can be speculated that the use of additional nodes may result in even better agreement with the locally measured temperatures.

Figure 8.7 compares the measured temperatures in node 7 (node 5 for the Initial Model) with the predictions of all three CFAST models. This is the node just below the operating deck level, equivalent to node 3 on the opposite, spiral staircase side, however, without the fire input. The sensor locations correspond to just above the operating deck hatch on the main staircase side to just above the hatch to the 1.800 level. The following conclusions are drawn from this figure:

1. All three CFAST models result in about the same lower layer temperature histories; small deviations amount to not more than 1 °C.
2. A Model and B Model results for the upper layer temperatures are superior compared with the initial, single-node dome model.
3. The model B predicted upper layer temperature is 2 °C above the temperature measured by sensor CT419 at +30.85 m for the duration of the fire, while model A results in an upper bound which is about 10 °C higher than the data. However, since CT419 lies above the region of interest, both models are over predicting the upper layer temperature.
4. All models under-predict the measured lower layer temperature at +25 m by about 5 °C beyond 7 minutes.

It is obvious from these comparisons that the 3-node models for the dome provide better agreements with the data than the Initial Model, single-node for the dome, for this uppermost node in the downward flow shaft. The B Model which forces the circulation through a longer loop, i.e. through the upper dome rather than across the operating deck as in the A Model, has the best match with the measured data. However, there is still not a large enough temperature drop indicating that either not enough heat is being removed to structures, or not enough entrainment is being calculated, or a combination thereof.

Figure 8.8 compares the measured temperatures with the three CFAST models in the lowest node, the 1.600 level, of the downward flow shaft. It is apparent that the down flow of warm gas induced by the fire exit on the opposite side is an extremely stringent test of the zone model capabilities. In fact, this flow situation is being thought as falling outside the realm of the standard fire simulation which tends not induce such large recirculatory flows. The two sensors shown are CT7703 and CT6601 which lie in the maintenance shaft near the mid-elevation of their respective levels.

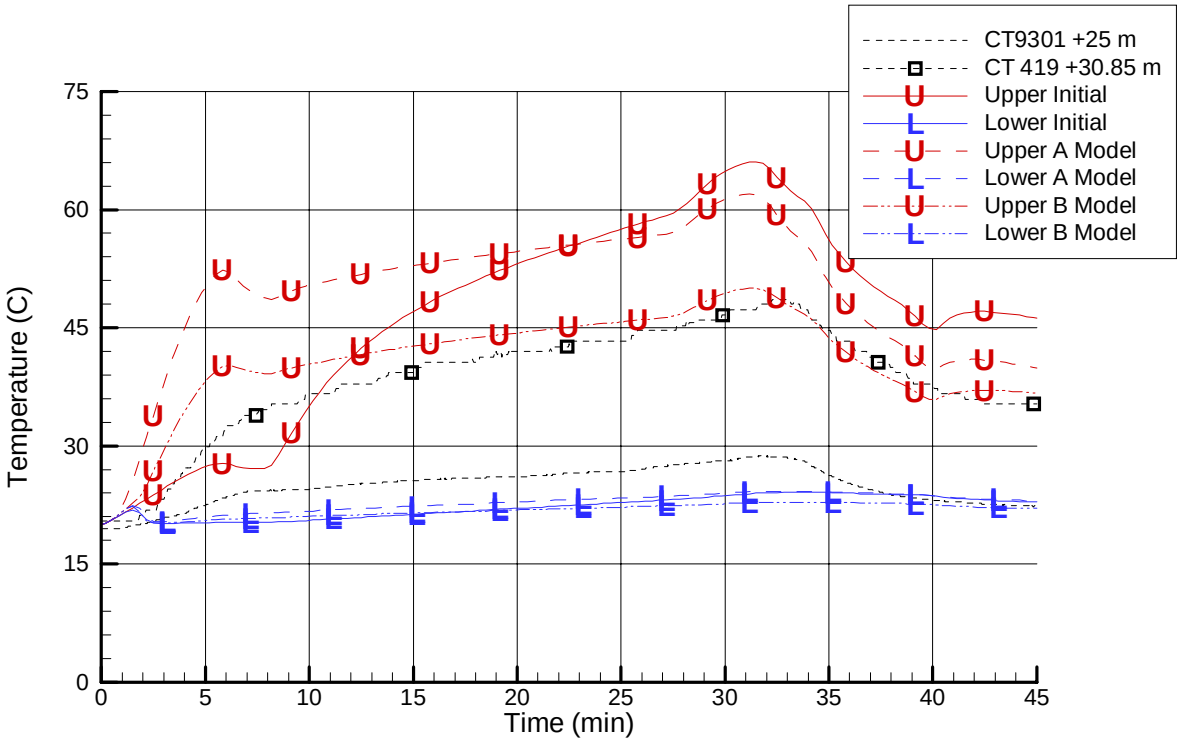

Figure 8.7: T52.11 1.900 Level Temperatures (Main Staircase)

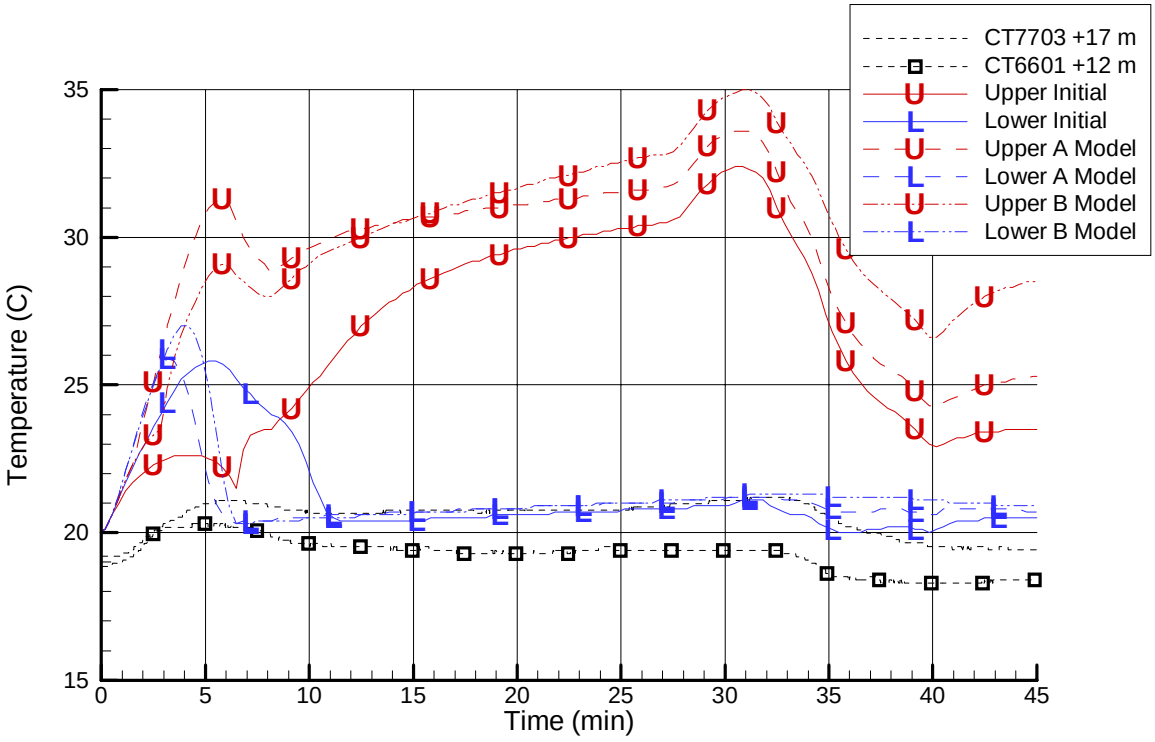

Figure 8.8: T52.11 1.600 Level Temperatures (Main Staircase)

With this background, the following conclusions can be drawn from the comparisons depicted in Figure 8.8:

1. All models produced more or less crossover of upper and lower layer temperatures during the early stages of the fire. This crossover occurs 13 minutes for the initial model, well past the peak of the fire, and at 6 and 7 minutes for A and B respectively.
2. If corrected for the initial offset in initial conditions, all three lower layer predictions match well the data of CT6601 past 12 minutes into the transient.
3. The measured temperature, CT6601, at 12 m indicates a temperature rise by 1.5 °C at 5 minutes while the models predict lower layer temperature rises of about 7 °C.
4. All models predict temperatures of 10 to 12 °C over those measured by CT7703 on the 1.700 level further bolstering the summary conclusions from Figure 8.9. The B Model results in the highest over prediction and the Initial Model the lowest which is counter to the situation shown in Figure 8.8 in which the B Model had the lowest over prediction and the Initial Model the highest. This would seem to indicate that the B Model has a significant drop in entrainment down the shaft as compared to the other models.
5. Notwithstanding the outcome of the final assessment, the CFAST results for the lower layer can be judged to be excellent, given the complexity of the simulation task.

Figure 8.9 shows the comparisons between the measured and CFAST-predicted temperatures for the lowest node in the opposite upward flow section of the flow loop on the spiral staircase side of the facility. This node is connected to the one discussed in Figure 8.8 by means of a horizontal flow connection that simulates the curved hallway connecting the two sides of the HDR facility on the 1.600 level. The following conclusions can be drawn:

1. All models result in a crossover of upper and lower layer temperatures. This occurs late in the transient for the Initial Model at 13 minutes, at 6 minutes for A Model, and at 7 min for B Model.
2. The A and B Model predictions for the lower layer temperature come closest to the measured data starting at 15 minutes. If corrected for the initial offset, the agreements would be nearly perfect.
3. The comparison between the model results shown in the previous figure, Figure 8.8, with those shown in this figure, Figure 8.9, indicates small but distinct changes along the flow path between the two nodes in the form of a cooldown of the upper layer and a heatup of the lower gas layer.

Finally, Figure 8.10 presents the comparisons between measured and CFAST-predicted temperatures in the spiral staircase maintenance hatch on the 1.800 level, below the fire compartments.

The following conclusions can be drawn from this figure:

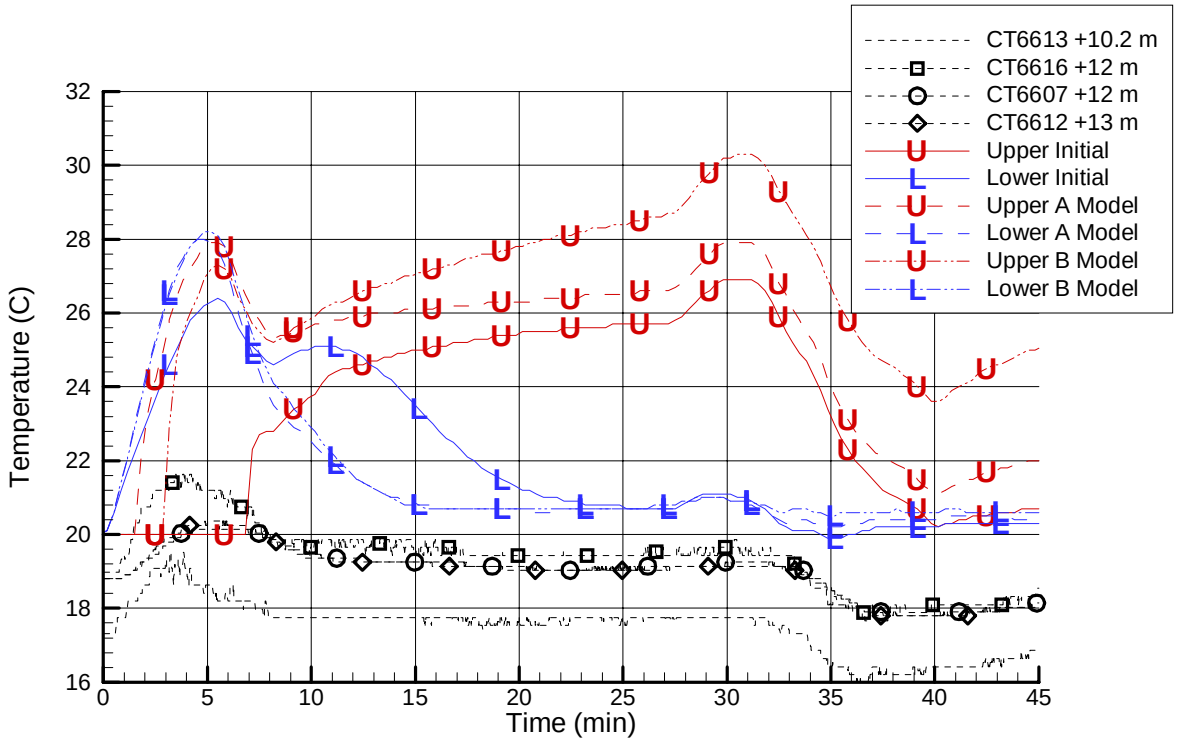

Figure 8.9: T52.11 1.600 Level Temperatures (Spiral Staircase)

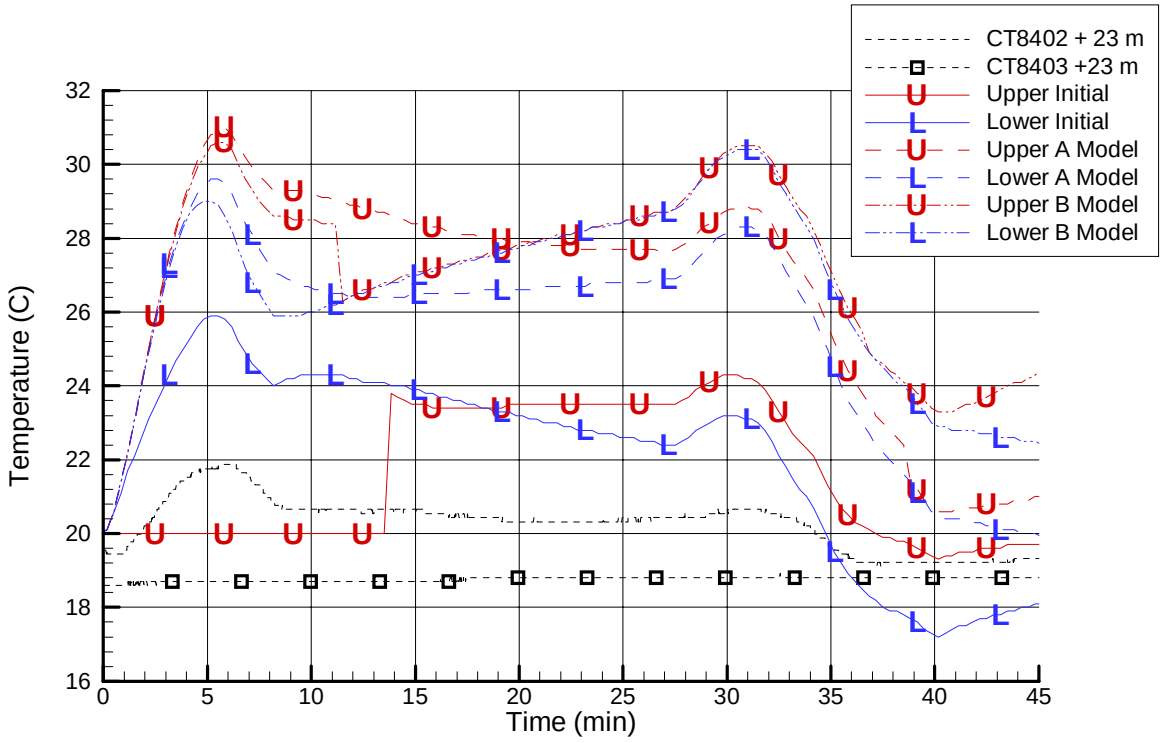

Figure 8.10: T52.11 1.800 Level Temperatures (Spiral Staircase)

1. The measured temperature shows a slightly more pronounced increase by 2 °C during the initial fire phase as seen in the zones discussed above.
2. A Model and B Model results largely over-predict by 6-10 °C.
3. The prediction from the initial, single-zone model fairs best in comparison with the data; although it features a crossover of upper and lower layers at 9 minutes, which is not observed in the other two models. In the case of the initial model the deviations between data and prediction are very small, ranging from 2-4 °C, whereas A Model and B Model generate results that differ by 6-10 °C.
4. From 13 minutes on, B Model predicts the same temperature for lower and upper layers; this is not observed in the other models' results.

This figure concludes the presentation of comparisons between measured and predicted temperatures along the whole flow loop in the HDR-containment for experiment T52.11. A similar set of figures is presented in subsection 8.3 for experiment T52.14 featuring a much higher fire power.

8.2.2 Velocities

This section presents comparisons of CFAST predicted velocities with those measured at various locations in the HDR facility. CFAST actually outputs mass flow rates whereas the HDR measured velocities. To make comparisons possible, CFAST mass flow predictions were converted to velocities by using the real gas law, the appropriate layer temperatures and heights, the CFAST mass flow rate prediction, and the geometry of the flow area. This results in an average velocity for a given flow area.

Figures 8.11 and 8.12 present comparisons between measured and CFAST-predicted velocities. Both figures display measured velocities judged as being representative for upper and lower layer movements. It is understood that the velocity is a continuously varying quantity over the height of the fire path, and in fact, selecting velocities measured at different elevations would result in other comparisons.

Figure 8.11 shows the comparisons between CFAST-predicted velocities between the fire room and doorway zone for all three models. The following conclusions can be drawn:

1. The quality of the predicted velocities of all 3 models does not depend upon the nodalization in the dome, in fact, only very minor changes can be identified.
2. All model results show a very good agreement between measured and predicted velocities of both upper and lower layers.
3. The predicted temporal velocity gradient of the upper layer agrees very well with the measured one during the first 7 minutes.
4. The initial insurge of cold atmosphere in the lower gas layer is over predicted during the first 5 min. of the fire.

5. The predicted upper layer velocites fall well within the spread of the measured velocities, while the predictions for the lower layer velocities consititute an upper bound for the measured ones over the experimental fire phase.
6. The post-fire velocity behavior of both layers is very well predicted by CFAST with the lower layer approaching stagnation faster than the upper layer which still flows out even after the fire actually stopped.

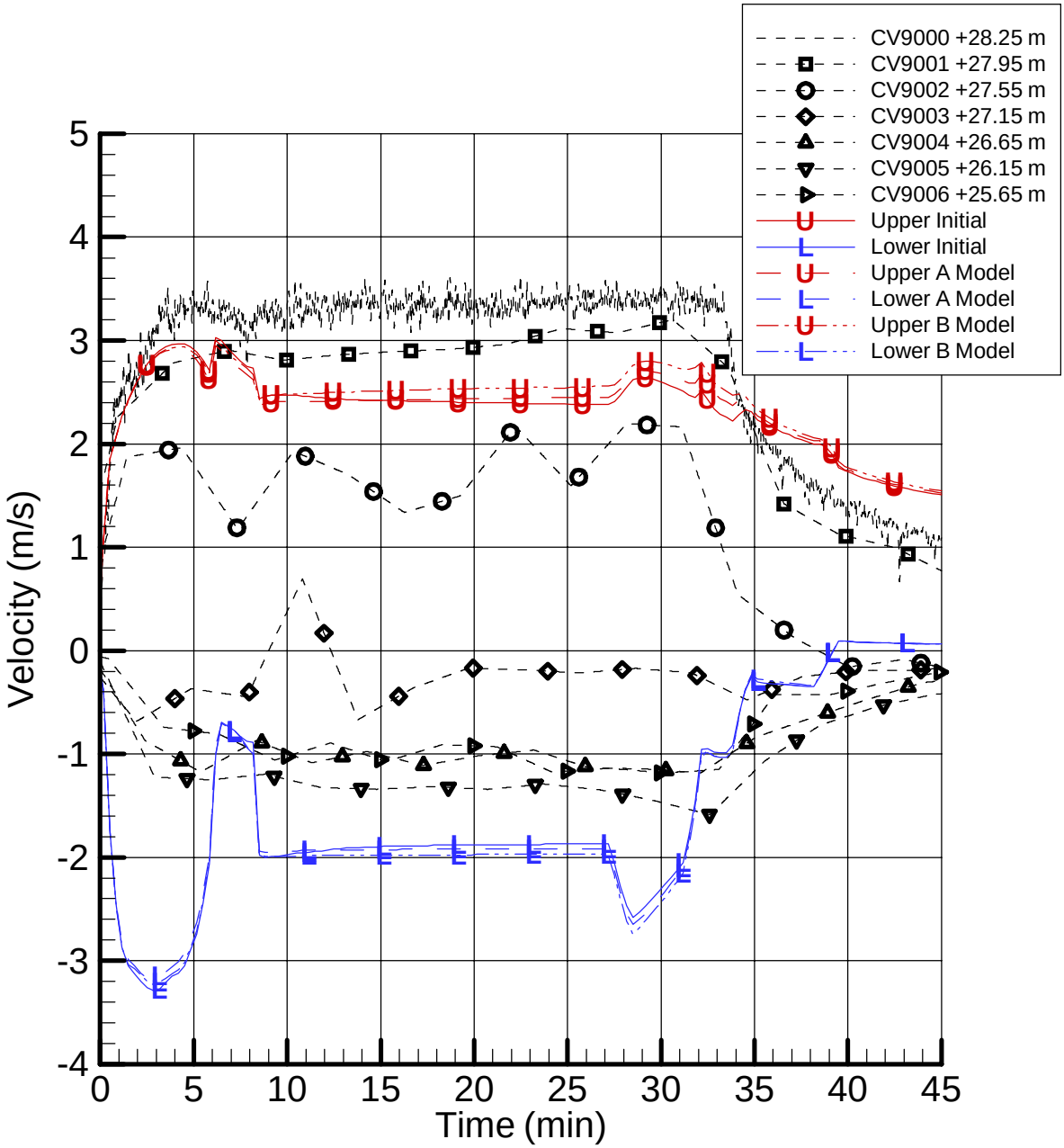

Figure 8.11: T52.11 Fire Room to Doorway Velocities

The overall comparisons reveal a partial success with the excellent predictive quality of the upper layer, but poorer predictive quality of the lower layer.

Figure 8.12 shows the comparisons of velocities between the doorway zone and maintenance hatch/spiral staircase zone below the operating deck. The conclusions from this figure are the same as for Figure 8.11 with the additional positive observation that in fact the agreements between data and predicted velocities are even better here. In fact, the agreement is outstanding in the realm of zone modeling. The following details emerge from the comparisons:

1. All three models generate the same results for the lower layer; results which are in excellent agreement with the lower layer velocities.
2. While the Initial Model sees no change in the predictive quality of the upper layer, the A and B models no longer predict average upper layer velocities that lie within the measured data.
3. At 45 minutes, the predicted difference between the upper and lower layer velocities is the same as that from the measured data.

As with Figure 8.11, Figure 8.12 shows again a partial success for CFAST, only this time for the lower layer rather than the upper layer.

Figure 8.13 compares numerous measured velocities with CFAST-predicted velocities at the exit of the maintenance hatch/spiral staircase into the dome at the level of the operating deck for all 3 models. The measured velocities are taken from the two-dimensional velocity sensor grid, grid # 2, located in the maintenance hatch, 15 cm above the operating deck. They reflect the asymmetric plume position at that level and the fact that the fire plume did not occupy the full cross-sectional opening. On the other hand, the CFAST-prediction as shown assumes that the fire plume fully occupies the cross-section. This explains why all 3 model predictions show systematically lower than measured velocities by a factor of two to four, which is also the factor difference in plume area between CFAST and the measured data. To illustrate this, in addition to the CFAST predictions, the B Model is shown scaled by a factor of three. Other conclusions from this figure are:

1. The B Model prediction comes closest to the data; it fairs best in terms of level and temporal trends.
2. The predicted velocity is only one-half to one-third of the measured lowest and highest velocities, respectively.
3. The initial temporal velocity gradient at that exit level is predicted very well in comparison with the data. The data show higher initial velocities at the start of the experiment.
4. The observed skewed velocity profile cannot be predicted by the zone model approach.
5. At the opening and with the asymmetric plume, a substantial downflow of cooler dome atmosphere was measured along the outer zones of the two-dimensional measurement grid.
6. If CFAST results are "corrected" for the actual flow area used by the plume, it can be seen that CFAST correctly predicts the mass flow rate.

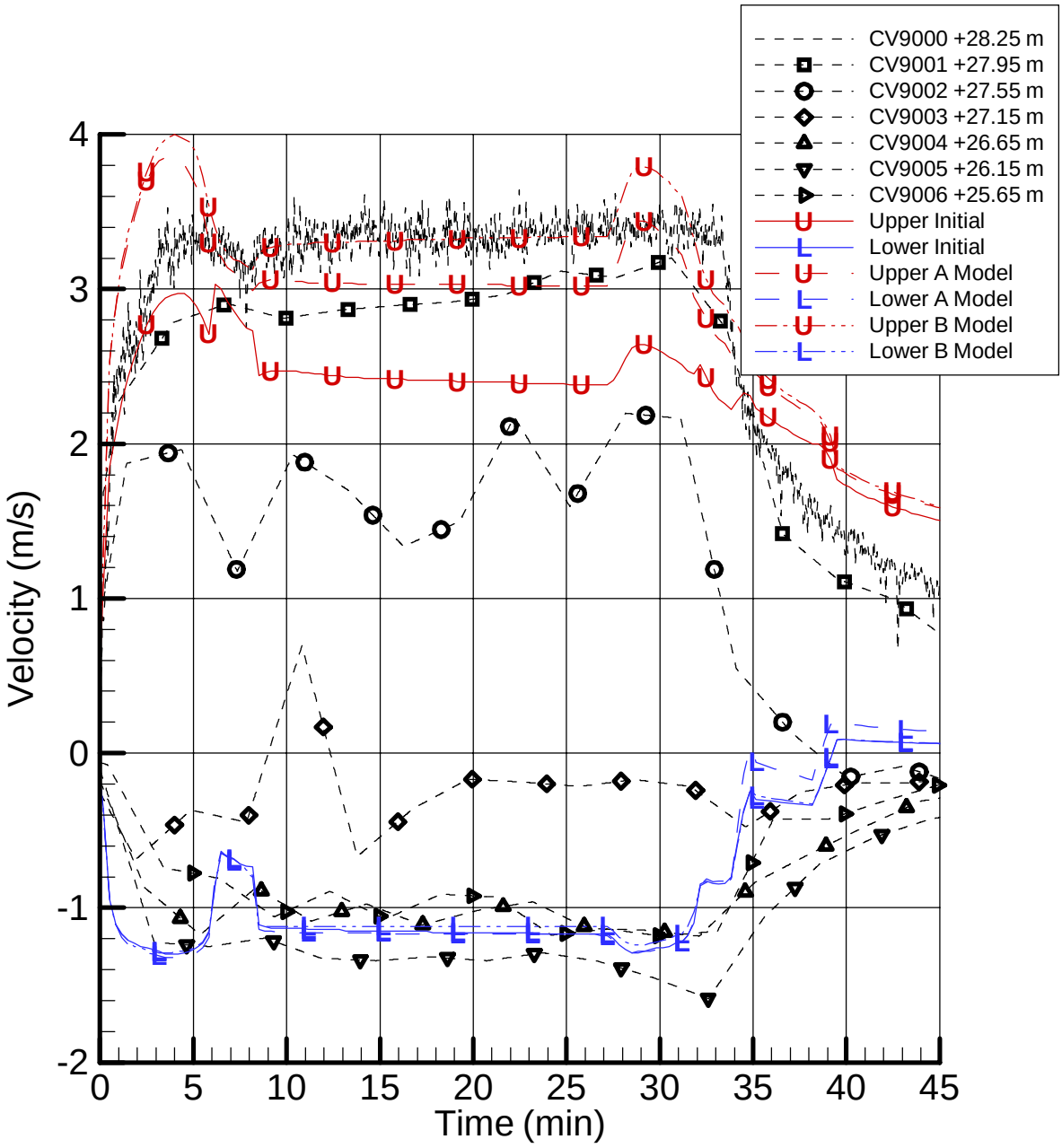

Figure 8.12: T52.11 Doorway to Hatch Area Velocities

In summary of the comparisons shown in Figure 8.13, CFAST is unable to cope with the details of the asymmetric geometry and resulting asymmetric flow conditions. Naturally, knowledge of the actual fraction of the cross-section area occupied by the plume can be fed back into the CFAST results to improve the velocity prediction at that position. However, such adjustments can only be performed if prior knowledge of the experiment is had beforehand. This exact adjustment was examined as part of the CFAST simulations performed in [38].

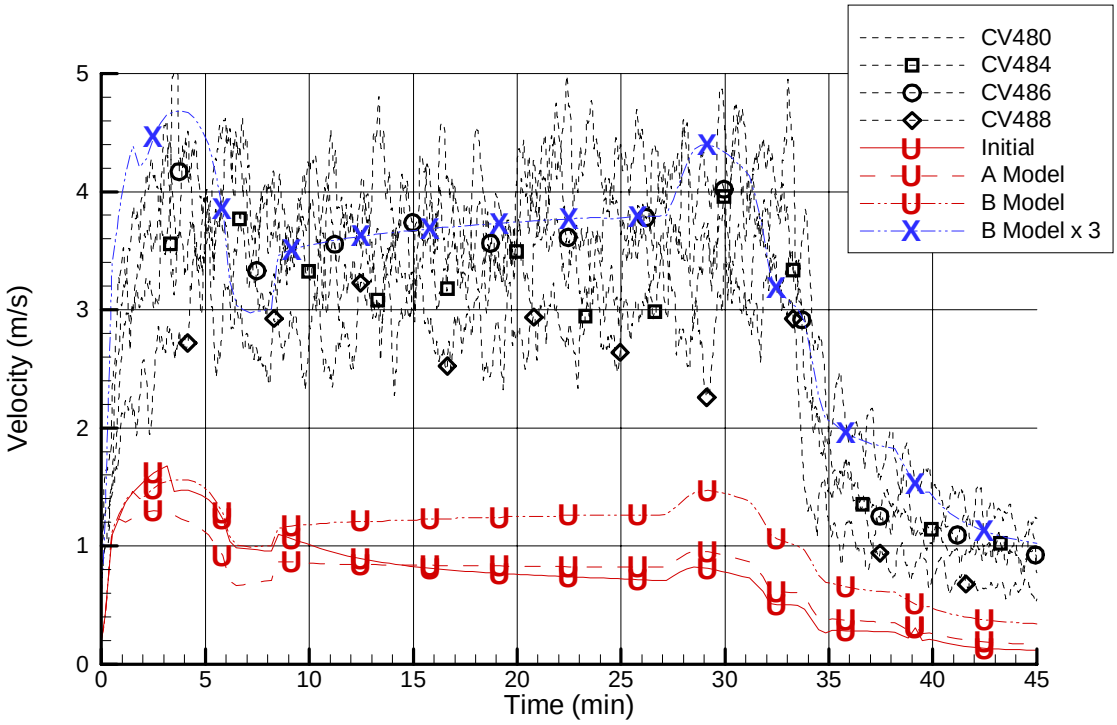

Figure 8.13: T52.11 Hatch to Dome Velocities (Spiral Staircase)

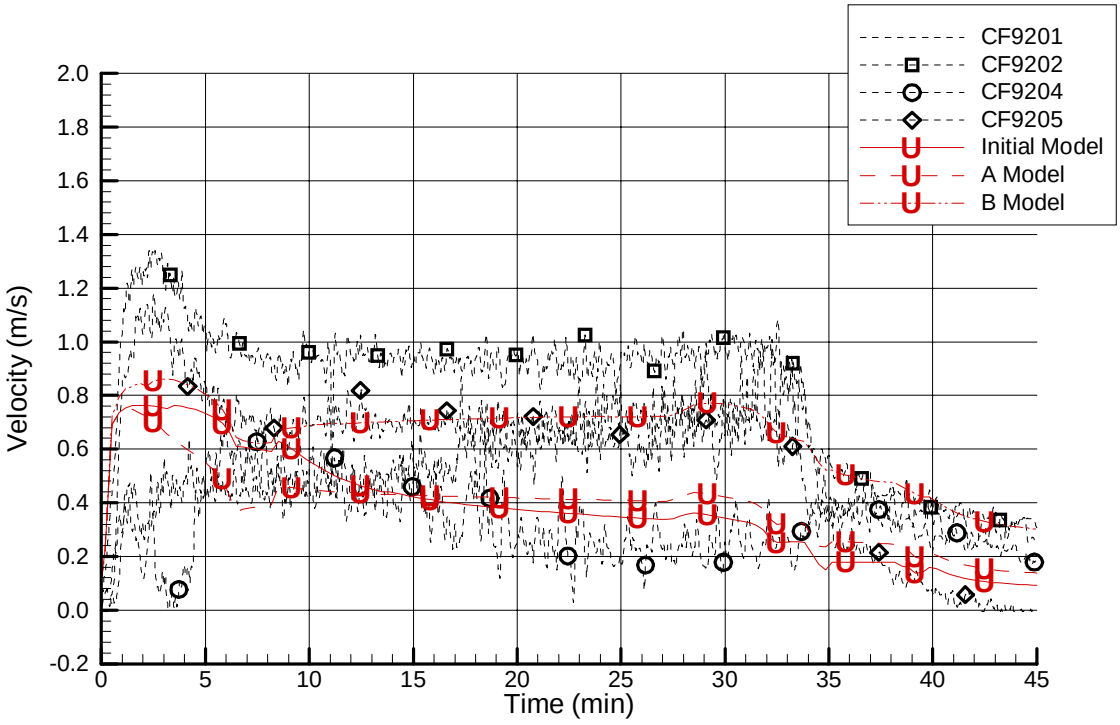

Figure 8.14: T52.11 1.800 to 1.900 Velocities (Spiral Staircase)

Figure 8.14 displays the comparisons between numerous velocities in measurement grid #3 at 25.5 m, at the maintenance hatch in the floor of the 1.900 level, and CFAST predictions for all three models. This position describes the upward flow induced in the spiral staircase side of the HDR facility. The following conclusions can be drawn from this figure:

1. The experimental data show a skew toward the inside, closer to containment centerline, surface of the maintenance hatch, e.g. the right hand side of Figure 3.16. This is somewhat surprising as the fire room doorway is located closer to the left-hand side of the hatch. The velocity sensor positioned in the middle of the right-hand side, CF9202, measures the highest velocity, while the other sensors measure lower velocities. The centerline velocity, CF9205, is the highest of the remaining curves and the top edge velocity, CF9204 is the lowest.
2. The three CFAST models result in distinctly different velocity predictions.
3. The overall best agreement is achieved by the velocity obtained by the B Model which shows a remarkable agreement with the average of the displayed velocity sensors. This agreement is maintained throughout the fire and the cooldown period of the test.
4. The A Model shows the lowest predicted velocity during the first 10 minutes of the fire, generally following the trend shown by CT9204, the lowest sensor value.
5. The Initial Model shows similar behavior to the B Model during the initial fire growth phase but deviates substantially starting at 10 minutes. After the deviation the Initial Model then shows similar behavior to the A Model though with a lower predicted velocity.
6. In general, each of the three models predicts an upward velocity that lies amidst the measured data.
7. The trend displayed by each of the three models also agrees well with the measured data.

To summarize the comparisons of Figure 8.14, it is obvious that the CFAST predicted velocities display a remarkable quality in comparison with the data. This holds for gradients, transient trends, and overall magnitude and is the more outstanding as this cross section is at the end of the whole flow loop.

8.2.3 Gas Concentrations

The transient development of gas concentrations such as oxygen, carbon monoxide, and carbon dioxide in the fire room and subsequent propagation into other containment subcompartments are important to know for planning proper and safe emergency and intervention strategies by fire departments and other emergency crews. The development and propagation of combustion product gases and aerosols is yet another characteristic signature of a fire scenario. Therefore, additional efforts were expended by the HDR facility in installing CO_2 sensors around the whole flow loop in the HDR containment in addition to a suite of gas concentration sensors in the upper doorway of the fire room. The following figures show the comparisons between CFAST predictions and measured data for all three input models.

Figures 8.15 through 8.17 display comparisons for O_2, CO_2, and CO in the fire room doorway, respectively. When viewing the figures it should be noted that all of the sensors lie at the very top of the doorway, whereas the CFAST values are average values for the entire layer. The following conclusions are drawn from the three figures:

1. All three models result in an excellent agreement with the measured oxygen depletion in the upper layer, Figure 8.15. Some deviations exist in the form of time delays and can be seen during the initial and final phases of the fire.
2. The models do not predict the time delay in oxygen consumption and transport as well as the rather fast refill of oxygen rich atmosphere once the fire ceased.
3. Each of the three models agree well with each other for both upper and lower layer oxygen concentrations.
4. The above observations also hold for the CO_2 and CO concentrations as displayed in Figures 8.16 and 8.17.
5. CFAST underpredicts the carbon dioxide concentration throughout all fire phases by about 2 to 2.5 v/o.
6. CFAST predicted initial temporal gradient is in excellent agreement with the data; however, the code does not account for the one minute time delay.
7. The predicted upper layer CO_2 concentrations show unphysical strong fluctuations during the post-fire phase, during which the B Model predicts a physically unrealistic , high, concentration of 11 v/o.
8. The CFAST predictions of all three models agree very well with the high-positioned carbon monoxide concentration sensor in the fire room doorway over the first 25 minutes; thereafter, the sensor trends into negative values.
9. As for CO_2, also the predicted CO concentrations in the upper layer show erratic and fluctuating behavior.

The overall conclusion is that CFAST shows an excellent predictive capability within the realm of a zone model. Post-fire deviations as described above have been noticed in previous HDR fire simulations with CFAST.

Figure 8.18 shows and compares the predictions for CO_2 from all three models in comparison with measured data in the dome. In order to properly relate the computational results to the data, measurements at different positions are displayed in the individual graphs and for the A Model and B Model the first dome node on the spiral staircase side of the facility is displayed. The following conclusions are drawn from the figure:

1. The predicted CO_2 concentration in the upper layer of the Initial Model is substantially higher than all measured values in the dome, no matter what position.
2. The single-node dome model is conservatively bounding.
3. The predicted CO_2 concentration of the A Model enhances mixing and results in predictions that best represent the average CO_2 concentration in that region of the dome.
4. The predicted CO_2 concentrations do not decrease during the post-fire phase as the data show.

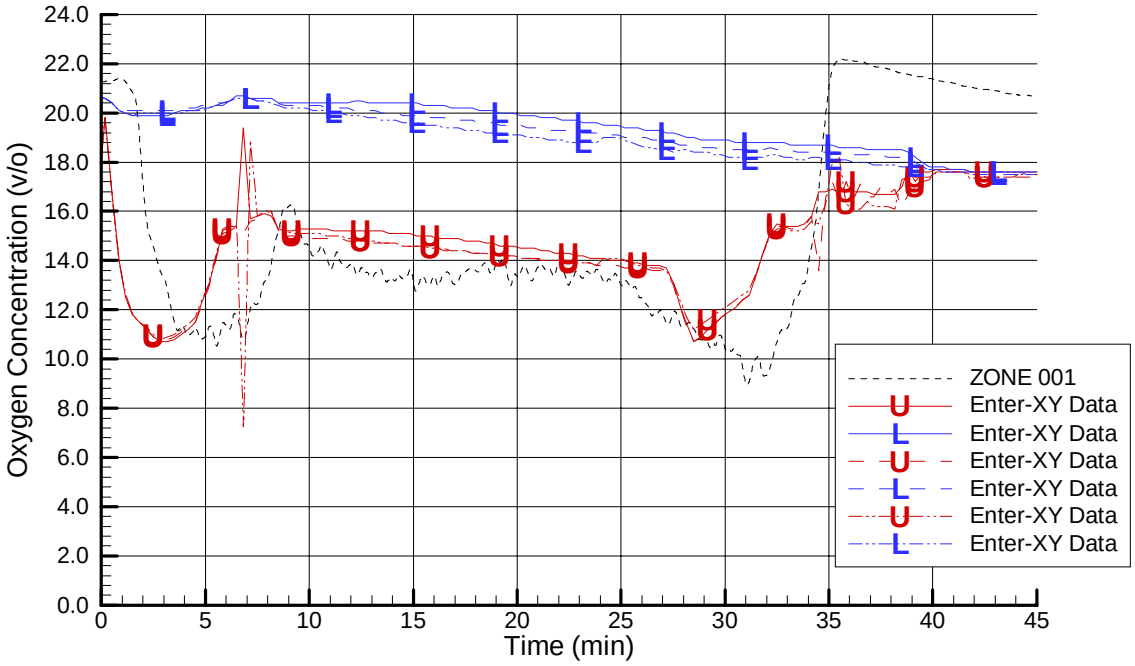

Figure 8.15: T52.11 Doorway Upper O_2 Concentration

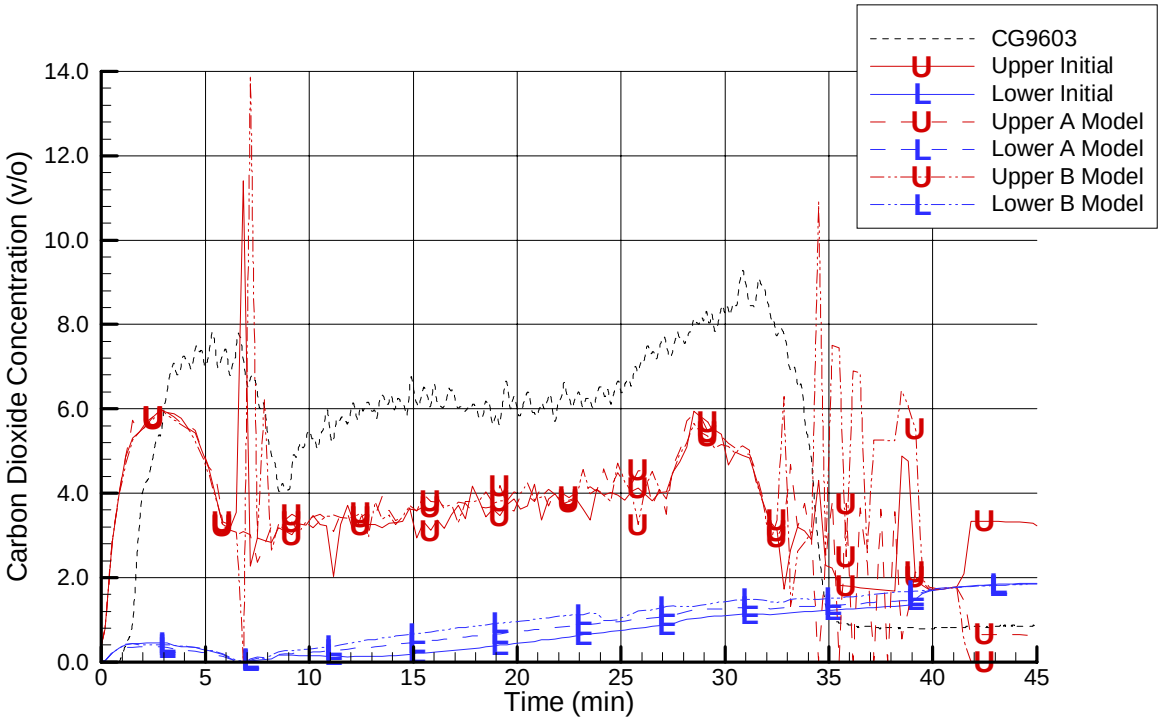

Figure 8.16: T52.11 Doorway Upper CO_2 Concentration

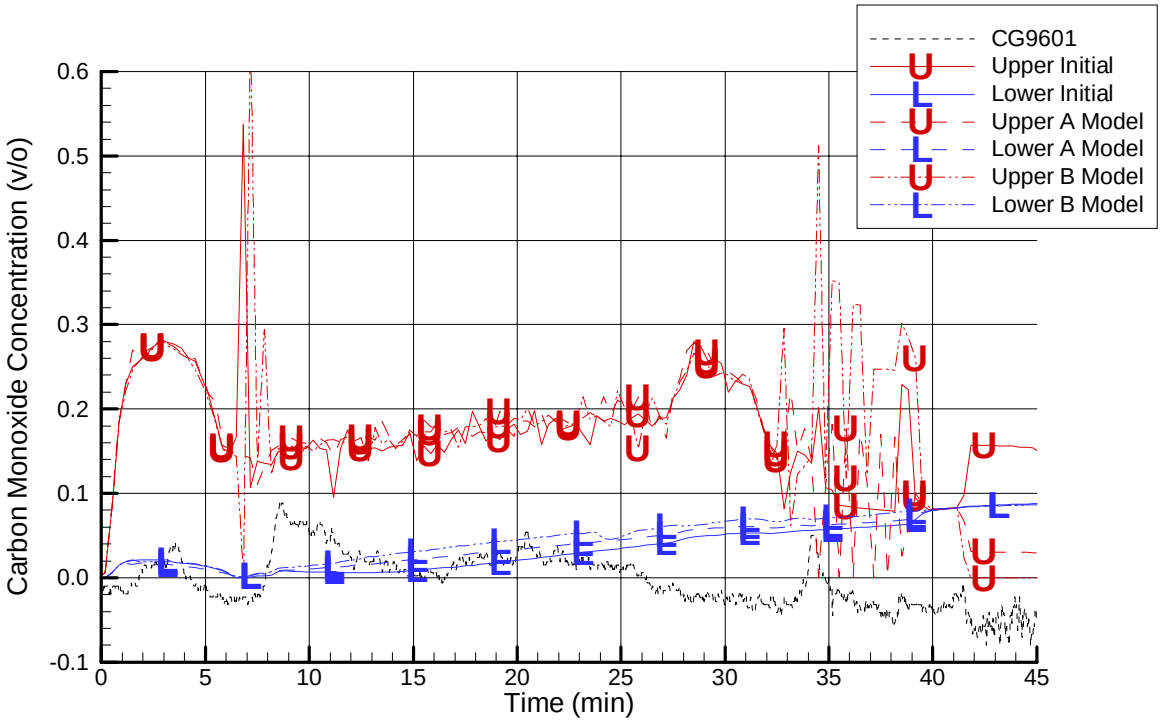

Figure 8.17: T52.11 Doorway Upper CO Concentration

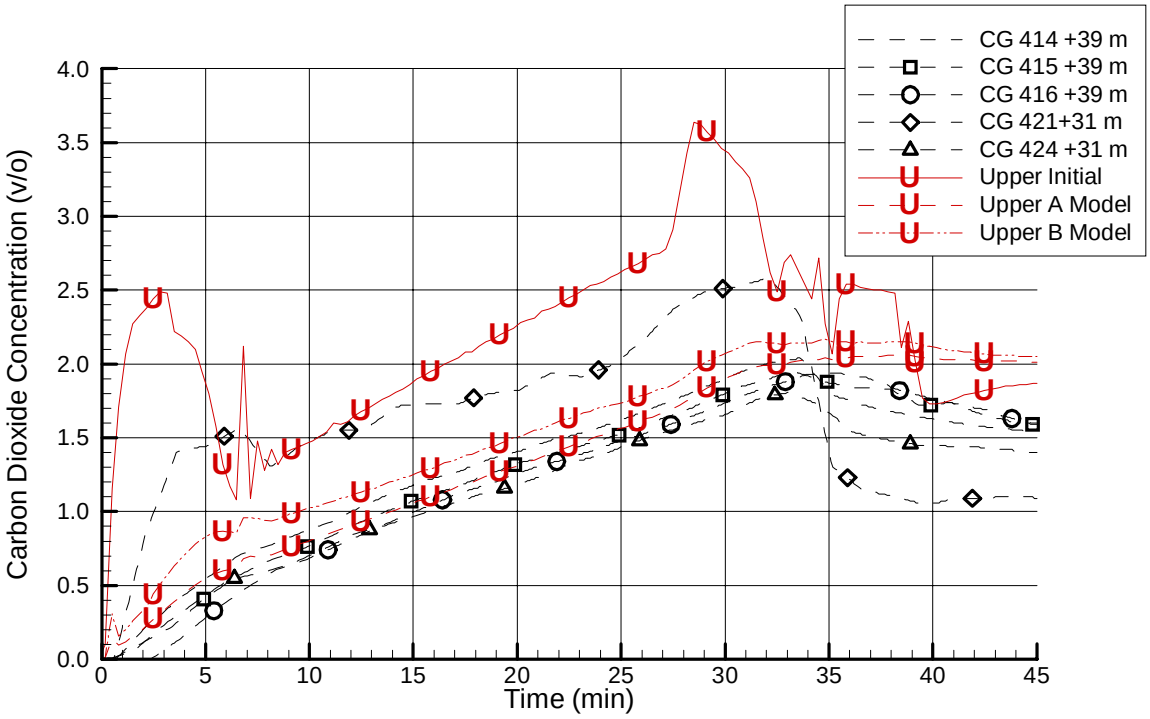

Figure 8.18: T52.11 Dome CO_2 Concentration

5. The predicted CO_2 concentration of the B Model, without vent, reduces mixing and thus results in a higher, yet still reasonable, CO_2 concentration than the A Model.

Figure 8.19 compares CFAST predictions for the downward flow entering the main staircase maintenance shaft vs. a sensor located at the shaft entrance. From this figure the following is concluded:

1. All three models lack the 5 minute time delay seen in the measured data.
2. As would be expected, the Initial Model results in an overly conservative value for the CO_2 concentration at the entrance to the downward flow portion of the loop.
3. The A Model, which allows direct communication between the two sides of the containment, is an improvement over the Initial Model, but still results in a slight over prediction.
4. The B Model, perfectly predicts the CO_2 concentration after the first 10 minutes of the fire and before the cooldown.
5. Neither the A Model nor the B Model show a reduction in CO_2 concentration after the end of the fire.

This figure clearly demonstrates the advantage of subdividing the dome as the three-dome-node models perform extremely well for this quantity.

Figures 8.20 through 8.22 depict the comparisons between predicted and measured CO_2 concentrations at three distinct points around the remainder of the global circulation loop for all three models. The graphs show, respectively, the main staircase maintenance shaft on the 1.900 level, the main staircase maintenance shaft on the 1.600 level at the bottom of the flow loop, and the spiral staircase maintenance shaft on the 1.700 level. The following conclusions are drawn from these figures:

1. All three models do display a decrease in CO_2 concentration around the circulation loop; though no model predicts a large enough decrease.
2. The comparisons with the predictions at the uppermost node show rather good agreement with the measurement for the A Model and B Model, while the Initial Model predicts a substantially larger delay than measured.
3. Starting at 20 minutes the predictions of all three models are conservative.
4. The predicted CO_2 concentrations of all three models slightly increase further even after the fire stopped, while the data shows a slight decrease.
5. At the lowest node in the spiral staircase shaft, the Initial Model shows the best agreement with the data during the first 15 minutes into the fire. Thereafter, all predictions are conservative up to a factor of 2 at 45 minutes.
6. At the spiral staircase node, only the Initial Model and the B Model give meaningful results, although greatly overpredicted, for the first 37 minutes.
7. The A Model at the spiral staircase node stays zero for the 36 minutes and then abruptly jumps to 1.6 v/o.

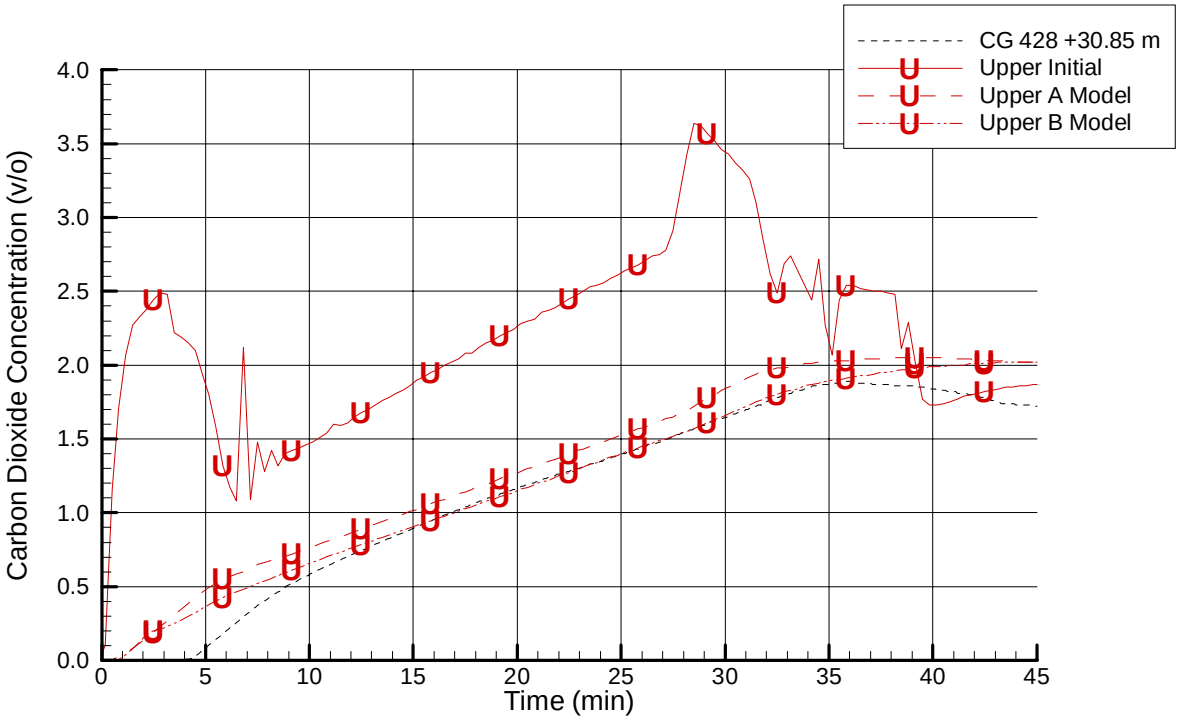

Figure 8.19: T52.11 Dome CO_2 Concentration (Main Staircase)

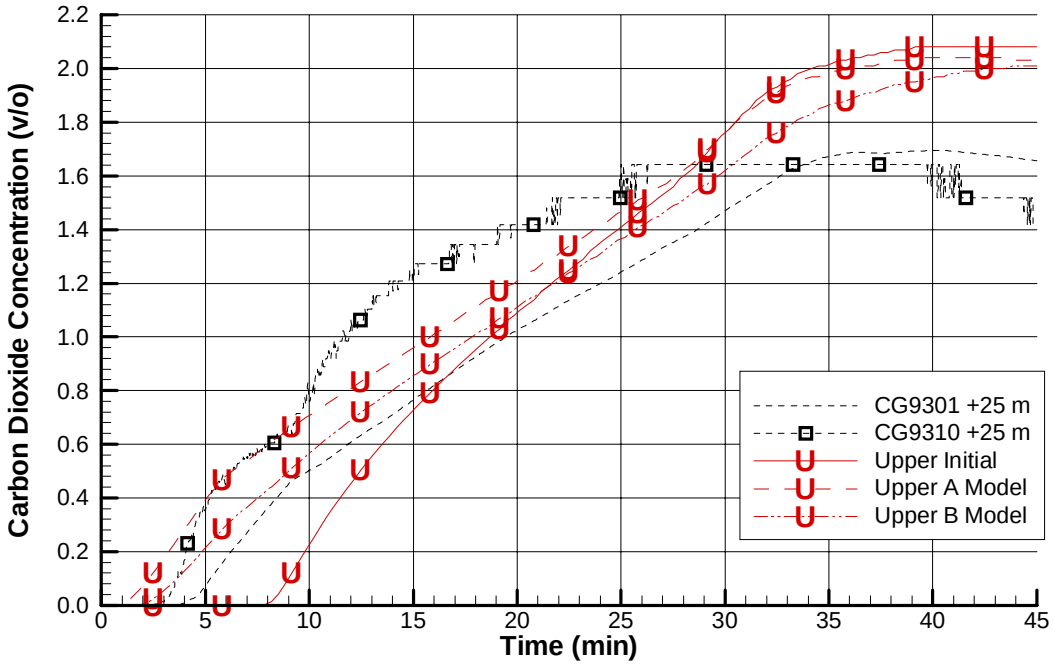

Figure 8.20: T52.11 1.900 Level CO_2 Concentration (Main Staircase)

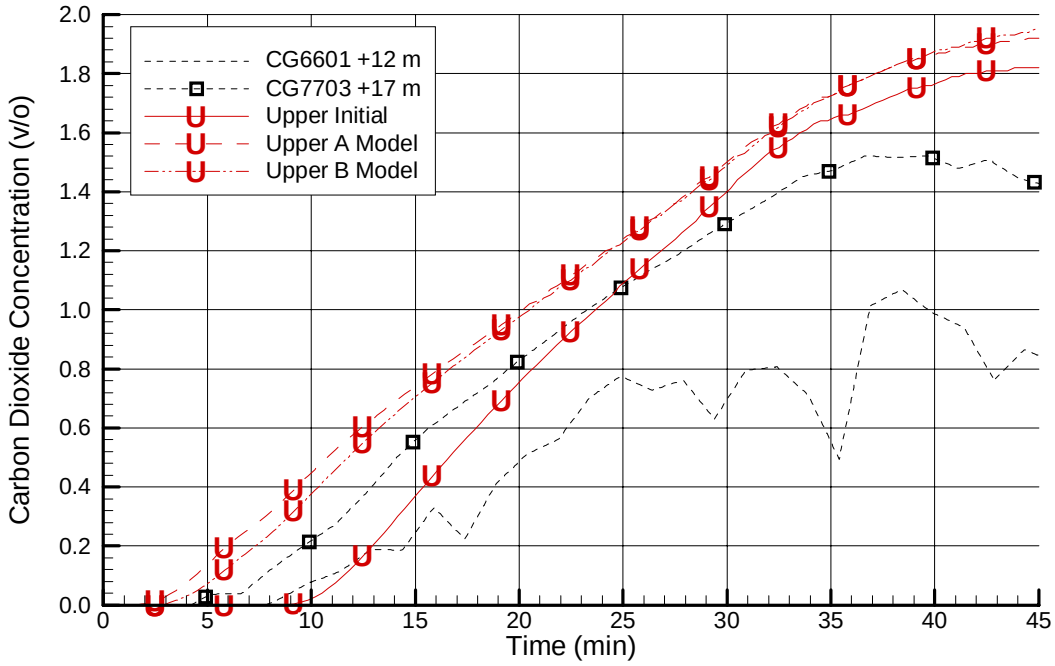

Figure 8.21: T52.11 1.600 Level CO_2 Concentration (Main Staircase)

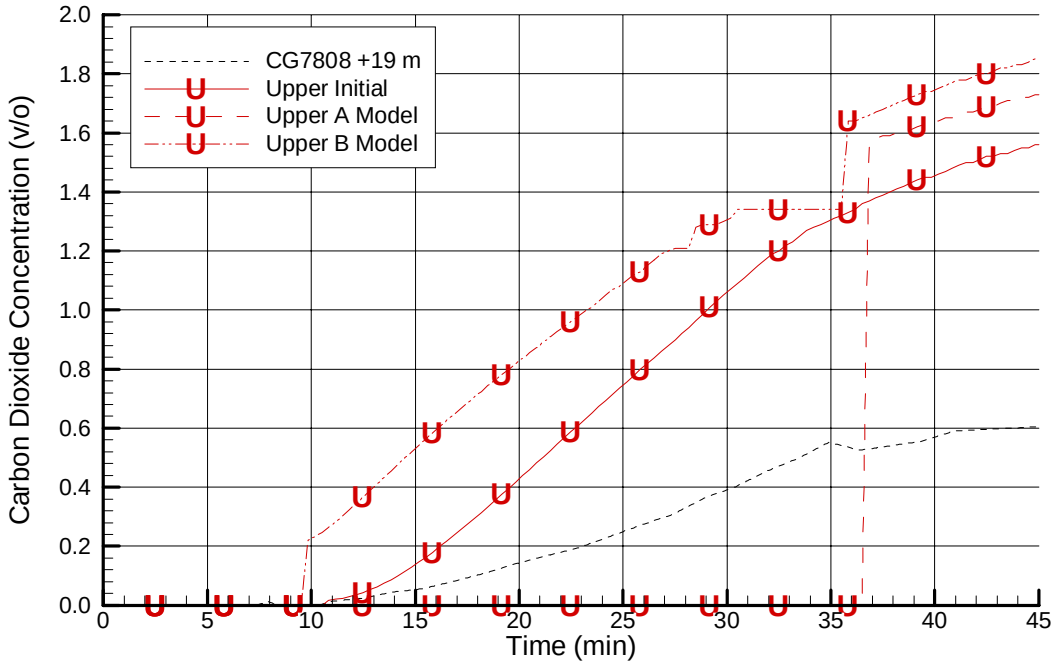

Figure 8.22: T52.11 1.700 Level CO_2 Concentration (Spiral Staircase)

In summary, although the CFAST CO_2 predictions are by no means perfect, they are conservative in comparison with the data and they do with minor exceptions show the correct trends seen in the data.

8.3 Comparisons Between CFAST Predictions and T52.14 Data

From the test details given in Section 4, Tables 4.1 and 4.2, it is clear that T52.14 comprised a fire of much higher power than T52.11. It is certainly interesting to see from a code validation point of view how CFAST predictions compare with data under these circumstances. Therefore, a small set of figures will be presented in the remainder of this section in order to make inferences regarding CFAST's predictive capabilities for this higher powered fire as compared to its capabilities seen for T52.11. A more complete discussion of these results along with the results for some additional models is available in [38].

The first figure of this subsection, Figure 8.23, shows the pyrolysis function that was input to CFAST. The CFAST curve was obtained by making fitting a piecewise linear curve to an HDR provided curve that was used in an earlier. international simulation effort for the T52.14 test [40].

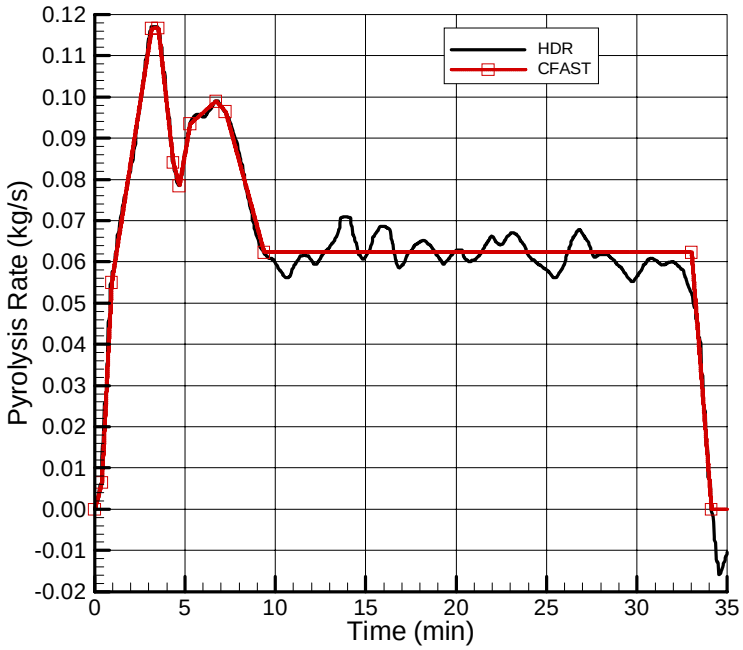

Figure 8.23: CFAST Pyrolysis Rate for T52.14

The second figure, Figure 8.24, shows the comparison between CFAST predicted values for the fire room upper layer temperature and data from the fire room. As with the T52.11 simulations, the predictions from model to model differed only slightly in the fire room. However, unlike the T52.11 results, the temperatures are greatly overpredicted by CFAST. CFAST does not perform as well with this much larger fire.

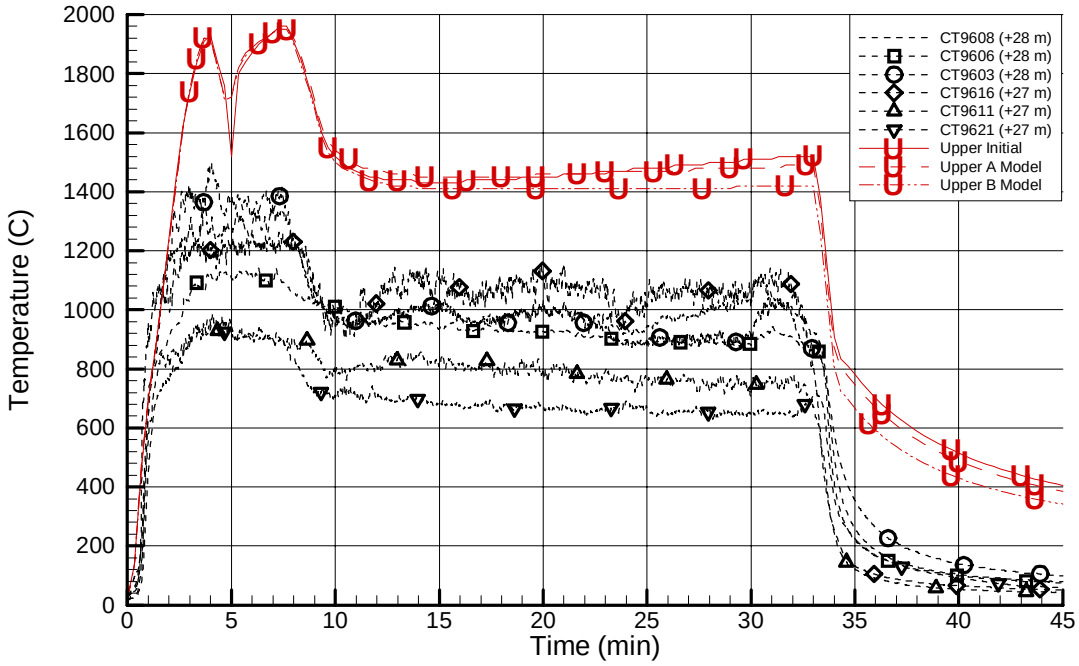

Figure 8.24: T52.14 Fire Room Upper Layer Temperature

The third figure, Figure 8.25, compares data with predictions for the upper region of the dome, same as for Figure 8.5. Given the large overprediction in temperature seen in the fire room, one might expect that CFAST would also be overpredicting in this location. However, this is not the case. In fact, the results of the three models in comparison with each other and with the data is almost identical to the observations made for Figure 8.5. In actuality both the Initial Model and the B Model perform slightly better for T52.14 than for T52.11 as the overprediction by the Initial Model is smaller and the B Model does not overpredict the peak temperature.

The final temperature figure for T52.14, Figure 8.26, is comparable to Figure 8.9 and shows CFAST computed temperatures and the HDR data for the region by the spiral staircase and the 1.600 Level, the start of the upward flow portion of the circulation loop. As with Figure 8.26, the same observations that were made for the equivalent T52.11 figure apply here. However, unlike Figure 8.25, the quality of the predictions is slightly worse for T52.14 as the upper layer temperatures are overpredicted by 2-4 °C more than in T52.11.

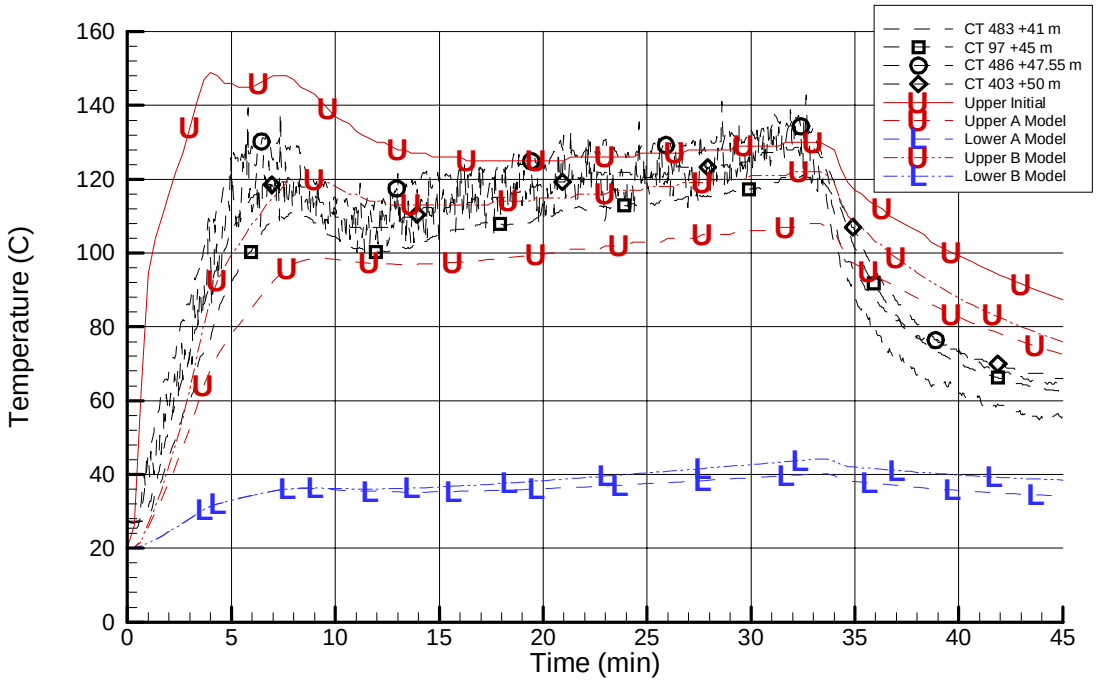

Figure 8.25: T52.14 Upper (Hemispherical) Dome Temperatures

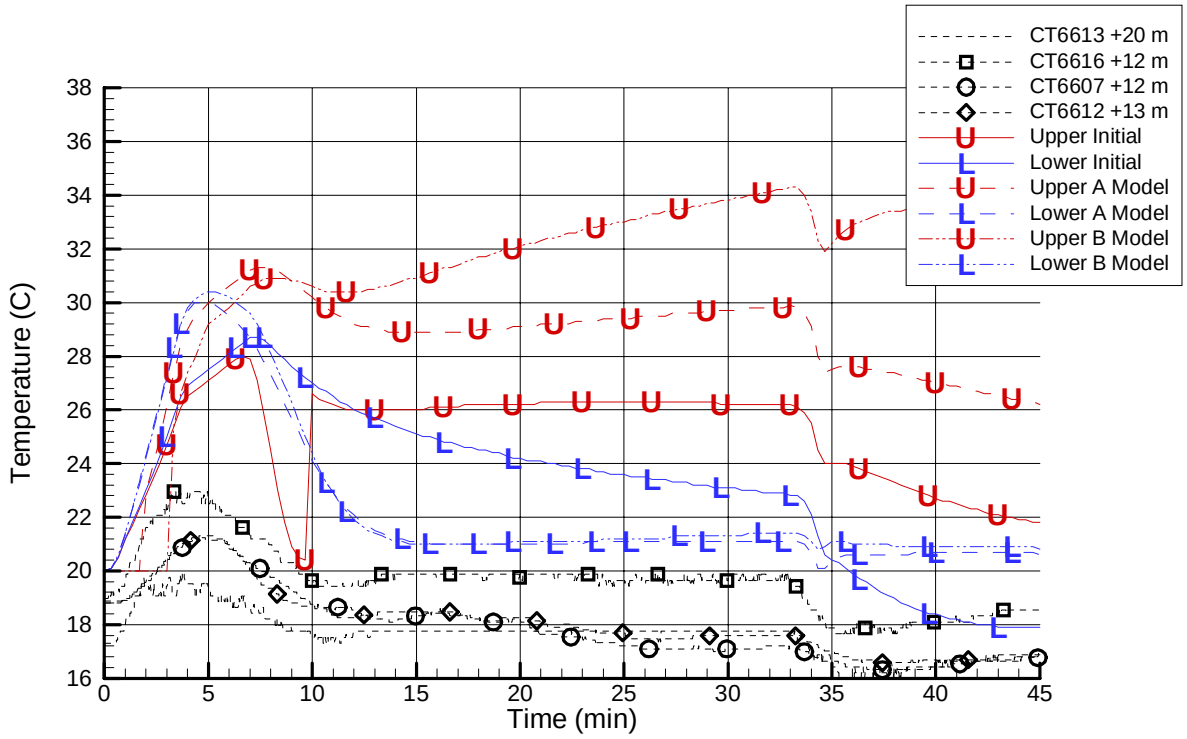

Figure 8.26: T52.14 1.600 Level Temperatures (Spiral Staircase)

Figure 8.27 below shows the predicted and measured velocities in the fire room doorway. In this figure it is observed that both upper and lower layer velocities are predicted very well whereas the T52.11 models only made such predictions for the upper layer. Unlike the T52.11 predictions, all of the T52.14 models do not accurately capture the post-fire velocities. The models all show slightly positive, almost 0 m/s velocities in the doorway while the data shows upper velocities near 1 m/s and lower velocities near -0.5 m/s after the fire.

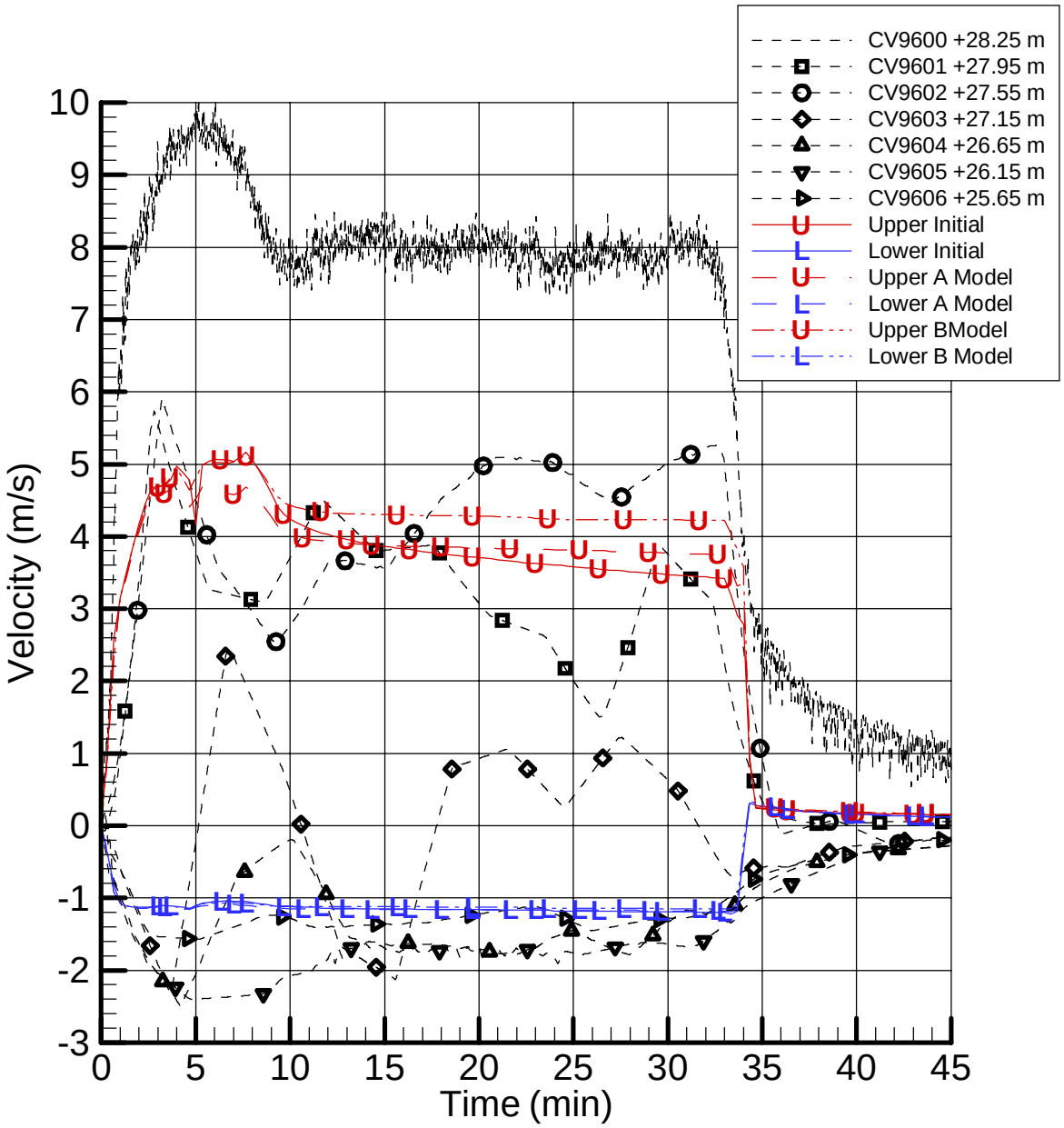

Figure 8.27: T52.14 Fire Room to Doorway Velocities

The second, and final, velocity figure for T52.14, Figure 8.28, compares the data with CFAST predictions for the gasses entering the fire level from the 1.800 level at sensor grid 3. As with the T52.11 results, the three T52.14 models show distinctly different predictions. However, the predictive quality during the peak of the fire is poorer for T52.14 than it is for T52.14. During the steady-state oil addition and during the cooldown, the Initial Model and the B Model predict within the range of the measured data, whereas the A Model is somewhat overpredicting the mass flow in the hatch.

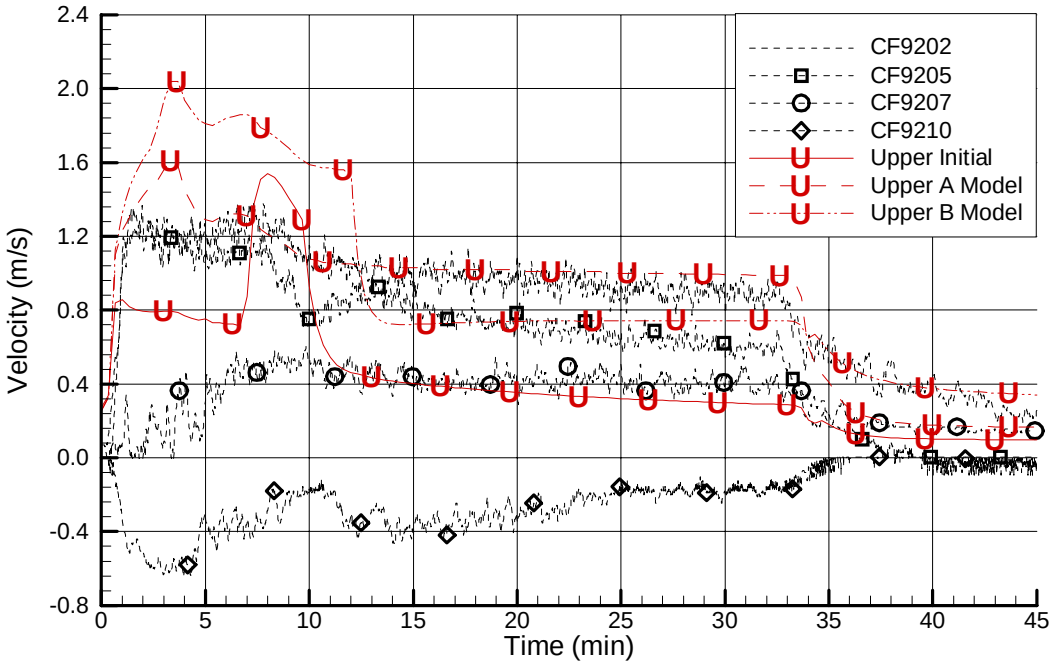

Figure 8.28: T52.14 1.800 to 1.900 Velocities (Spiral Staircase)

The next pair of figures, Figures 8.29 and 8.30, display the CFAST predicted O_2 and CO_2 concentrations, respectively, in the upper doorway along with the corresponding data for the T52.14 test. In figure 8.29, CFAST makes very poor predictions of the oxygen concentration in the doorway. Whereas the data predicts close to 0 v/o, CFAST predicts > 6 v/o throughout the fire. Furthermore, the data show a rapid decrease to near 0 v/o where the concentration remains until the end of the fire while CFAST predicts a time-varying concentration that follows the pyrolysis rate. CFAST also displays a non-physical, oscillatory behavior at the end of the fire during the start of the cooldown phase. Oscillations of almost 10 v/o in concentration are predicted. CFAST does not fare any better in Figure 8.30 showing the CO_2 concentration. CFAST predicted concentration during the steady-state oil addition is a gradual increase from 6 v/o to 8 v/o whereas the data indicates a plateau of 12 v/o. Also the same oscillatory behavior is seen at the end of the fire with near 10 v/o oscillations.

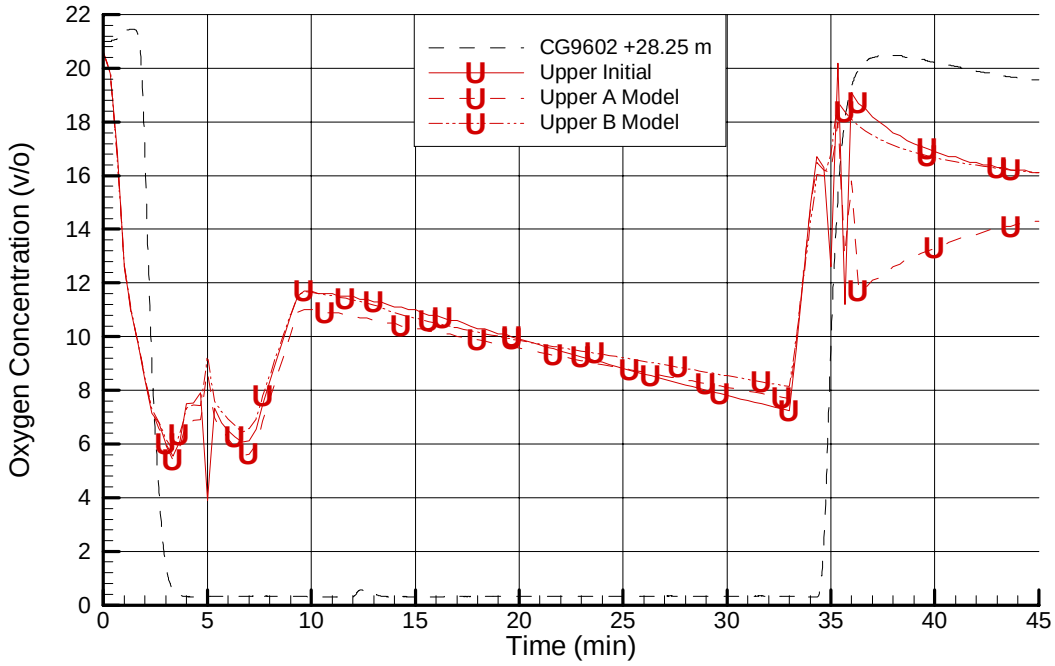

Figure 8.29: T52.14 Doorway Upper O_2 Concentration

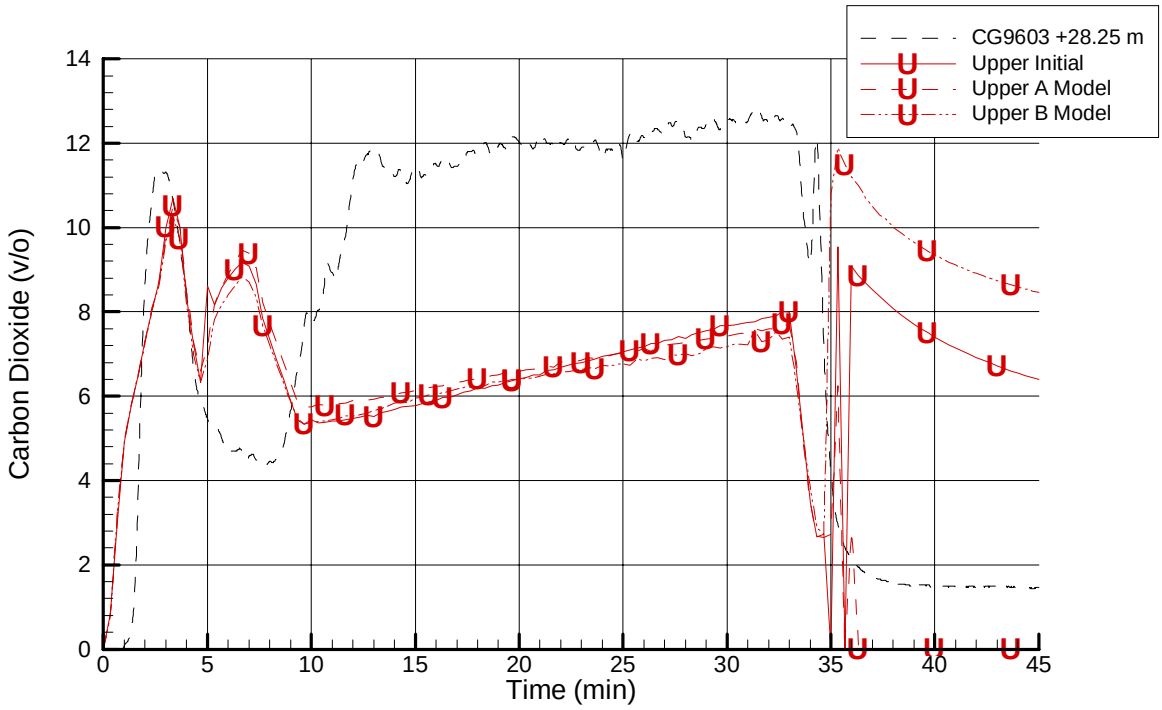

Figure 8.30: T52.14 Doorway Upper CO_2 Concentration

The final T52.14 figure, Figure 8.31, compares CFAST predictions for the CO_2 concentration on the main staircase side of the 1.600 level, the bottom of the downward portion of the global circulation loop, with data. For the first 20 minutes of the fire the A and B Models' predictions lie just above the data for CG7703. Since this sensor lies just above the region of interest, these two models are overpredicting the concentration as they did in T52.11. The Initial Model for the first twenty minutes lies between the two data curves indicating a good prediction. Beyond twenty minutes all three models diverge away from the data, and at the end of the fire none of the models show a gradual decrease in concentration during the cooldown. The predictive quality for this quantity is essentially the same as it was for T52.11.

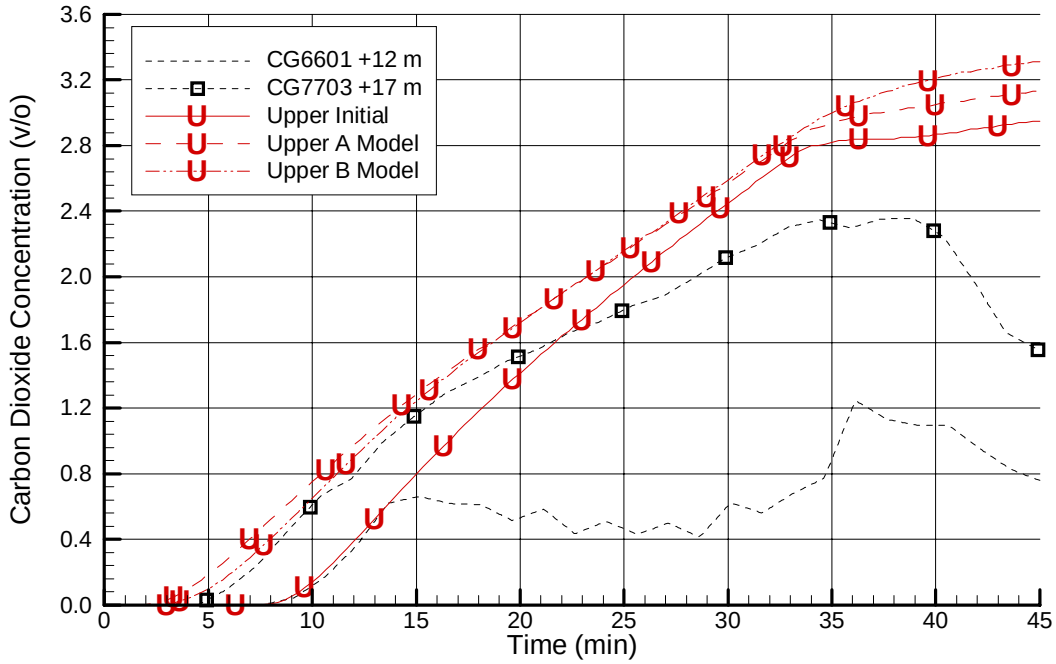

Figure 8.31: T52.14 1.600 Level CO_2 Concentration (Main Staircase)

The figures for CFAST's T52.14 predictions indicate that the higher power results in a degraded predictive quality near the fire, but little change in the far-field. Near-field temperature and gas concentration predictions were poor for T52.14 whereas they were adequate for T52.11. However, velocities were still predicted well. Far-field temperatures, velocities, and gas concentration predictions were almost as accurate for T52.14 as they were for T52.11 with T52.14 predictions being slightly worse than for T52.11. The large fire and extreme underventilated conditions cause CFAST difficulties in the near-field.

9 CFAST OBSERVATIONS AND COMMENTS

This section documents the general usability impressions the authors had while using CFAST for simulating the HDR T52 oil pool fire experiments. The first part addresses the accomplishments by and with CFAST over the spectrum of experiments covered during this validation effort. The second part covers differences and deviations in comparison with the data, behavior during code execution, performance of the implemented models, comments about the documentation, and comments about the capabilities and limitations of pre- and post-processors. The comments are made with respect to performance-based trends by regulatory bodies as they impose requirements in terms of quality. The chapter closes with suggestions for continued validation. A more complete discussion of both CFAST's capabilities and its weaknesses can be found in [38].

9.1 Accomplishments with CFAST

The following accomplishments were achieved with CFAST during the validation efforts using the oil pool fire experiments T52.11 and T52.14. The accomplishments listed in the following refer to the predictions made by the B model which was determined to be the best overall of the three models used in terms of performance:

- Unlike the T51 test series in which a small opening to the outside was required to initialize the pressure solver, CFAST was able to simulate the T52 tests in the HDR containment modeled as a completely enclosed structure throughout the test.

- The advantage of creating the appropriate subdivision and vent connections for an otherwise undivided dome was clearly demonstrated in the great improvements seen in the predictive quality.

- In the near field, temperature and gas concentrations were very well predicted for the T52.11 experiment. Mass flows were well predicted by CFAST for both the T52.11 and the T52.14 experiments.

- Temperatures, gas concentrations and mass flows are well predicted for the dome for both the T52.11 and T52.14 experiments. Given the poor vertical flow predictions observed while modeling the T51 test series, this was both surprising and encouraging in terms of future use of CFAST for performance-based reviews.

- In the far-field, gas concentrations are well predicted during the fire with even the time delay for CO_2 arrival being predicted correctly. As temperatures in the far-field are invariably low, it is phenomena such as inhalation toxicity that become dominant in terms of a performance-based analysis. The ability to correctly predict concentration and arrival times is critical, and for this particular scenario, CFAST is performing reasonably well.

- In general the basic trends seen in the data during the four phase of the fire (initial growth, decay from peak pyrolysis, quasi steady-state during fuel addition, and cooldown) are predicted by CFAST, sometimes with more or less deviations compared to the data.

The overall enhancement of CFAST's predictive quality in the case of the T52 experiments as compared to those previously analyzed is judged result from the arrangement of the fire room whose door is directly connected to a major flow path, while all previous experiments featured a long, horizontal hallway connecting the fire room with the vertical shaft over a substantial distance. The assessments of CFAST for both fundamental arrangements on behalf of the HDR experiments have resulted in major insights as accomplishments of this project.

9.2 Observed Limitations with CFAST

While CFAST did perform surprisingly well for the T52 test series, a number of deficiencies related to the code were observed. This subsection will briefly discuss those observations.

- Near-field temperatures and gas concentrations were poorly predicted by CFAST for the T52.14 experiment. As this test was highly underventilated in comparison to the T52.11 test, this would indicate that CFAST is not able to adequately cope with these extreme conditions of high fire power and low oxygen concentration.

- Gas concentration predictions for both T52.11 and T52.14 display oscillatory behavior during periods of rapid change in fire power (e.g. during the initial growth and during the cooldown). The oscillations are indicative of numerical instabilities in the species transport routines.

- Far-field temperatures were not well predicted with CFAST overpredicting the temperatures for both T52.11 and T52.14. While the safety significance is negligible due to the low temperatures involved it indicates that CFAST is not transferring and storing sufficient heat in the surface structures present in the fire compartments and the dome.

- The post-fire behavior of the far-field gas concentrations does not match the data, indicating that CFAST is not correctly capturing the more subtle post-fire transport processes driven by diffusion and very low-speed convective processes.

- CFAST cannot cope with asymmetries introduced by the specific geometric arrangement used in the T52 tests.

- While the ability to convert the binary output file into a comma-delimited, ASCII file is a great improvement over the prior ASCII report form, it is still cumbersome. For a large structure, such as the HDR facility, the number of compartments and hence the number of spreadsheet columns is such that current spreadsheet programs are unable to import the entire file. This necessitates a tedious process of file editing by the user in order to import the file.

- The DOS based interface that CFAST uses is cumbersome and does not allow for advanced features such as "cut and paste" from other applications. Furthermore, having to resort to using a virtual DOS machine results in increased execution times and increases the risk of system instabilities when trying to simultaneously use other applications.

9.3 Suggestions for Further Development and Validation

The work documented in this report and the prior volumes of this report series, [33], [34] and [37], as well as the primary author's dissertation [38] identified a number of areas in which CFAST could use further development and refinement. Some suggestions follow to improve CFAST. These suggestions are especially important in light of current interest in the desire to use CFAST for performance-based fire safety analyses.

- Migrate the code away from a DOS environment to a pure Windows environment. This will accrue a number of usability benefits, as a Windows program operations such as cut and paste will be available. Furthermore the look and feel of the program will be identical to other Windows software resulting in an immediate sense of familiarity. Lastly, as Windows program the code can make use of the Windows built-in, helpfile applets to aid the user when creating an input file. Lastly, Microsoft has stated that it wishes to remove support for DOS applications from future versions of Windows. While this may not happen in the very near future, it should be prepared for. In this context it is interesting to note that the Office of Information Technology (OIT) at the University of Maryland recently announced it will close all of its help desks and support for DOS and Windows 3.X.

- Examine the code's numerics for gas concentration calculations. The oscillations seen in the code indicate either a timestep problem or use of single precision math where double-precision is called for.

- Add correlations which account for asymmetries in the fire room and flow through vents.

- Develop an improved combustion model. First, in its current implementation it is entirely up to the user to specify the combustion products. That is the quality of output is highly dependent on quantities that the user cannot know ahead of time for a blind computation. Second, prior work has shown that CFAST is not capable of correctly tracking combustion products if an oxygen containing fuel is specified.

- Add additional heat transfer correlations to expand the code's usability over a wider spectrum of forced, natural convection, and mixed convection regimes.

- Create another document to be distributed with CFAST that discusses how to approach modeling of large structures or odd-sized rooms such as atrium, shafts, or very long hallways.

- Further improvements are needed in the determination of mass flows between compartments, especially far-field vertical flows.

- Further benchmarking of the code for fires in complex structures, especially one's with operating ventilation systems is needed.

10 REFERENCES

1. Schall, M. and Valencia, L. *Data Compilation of the HDR Containment for Input Data Processing for Pre-Test Calculations* (English Translation of PHDR Working Report 3.143/79). Project HDR Nuclear Center. Karlsruhe, Germany. PHDR Working Report 3.279/82. Jan. 1982.
2. Müller, K. and Dobbernack, R. *Evaluation of Fire Behavior in Compartment Networks in a Closed Containment, Design Report, Test Group BRA-E, Exploratory Experiments T51.1* (In German). Project HDR Nuclear Center. Karsruhe, Germany. PHDR Working Report 5.025/84. Dec. 1984.
3. Tenhumberg. *Evaluation of Fire Behavior in Compartment Networks inc a Closed Containment, Data Report, Test Group BRA-E, Experiments T51.11-T51.15, Test Period 01/24 - 02/01/1985* (In German). Project HDR Nuclear Center. Karlsruhe, Germany. PHDR Working Report 5.43/85. Feb. 1985.
4. *Supplemental Data Report, Test Group BRA-E, Experiments T51.11-T51.15* (In German). Project HDR Nuclear Center. Karlsruhe, Germany. PHDR Working Report 5.038/85. April 1985.
5. Tenhumberg. *Evaluation of Fire Behavior in Compartment Networks in a Closed Containment, Data Report, Test Group BRA-E, Experiments T51.16-T51.19, Test Period 06/25 - 07/01/85* (In German). Project HDR Nuclear Center. Karlsruhe, Germany. PHDR Working Report 5.055/85. July 1985.
6. Müller, K., Wegener, H. and Dobbernack, R. *Evaluation of Fire Behavior in a Compartment Network in a Closed Containment, Supplemental Design Report, Test Group BRA, Experiments T51.2.* Project HDR Nuclear Center. Karlsruhe, Germany. PHDR Working Report 5.069/86. June 1986.
7. Grimm, R. *Evaluation of Fire Behavior in a Compartment Network in a Closed Containment, Supplemental Design Report, Test Group BRA, Test Group T51.21-T51.24* (In German). Project HDR Nuclear Center. Karlsruhe, Germany. PHDR Working Report 5.078/86. May 1986.
8. *Evaluation of Fire Behavior in a Compartment Network in a Closed Containment, Quick Look Report, Test Group BRA, Experiments T51.11-T51.19* (In German). Project HDR Nuclear Center. Karlsruhe, Germany. PHDR Working Report 61-85. June 1986.
9. Rautenberg, J., Dobbernack, R., Müller, K., and Volk, R. *Evaluation of Fire Behavior in a Compartment Network in a Closed Containment, Final Evaluation Report, Test Group BRA, Experiments T51.1; T51.2* (In German). Project HDR Nuclear Center. Karlsruhe, Germany. PHDR Working Report 82-91. March 1991.
10. Nowlen, S.P. *A Summary of the Fire Testing Program at the German HDR Test Facility.* Sandia National Laboratories. NUREG/CR-6173. Nov. 1995.
11. Müller, K. and Valencia, L. *Experiments with Hydrocarbon Fire in the Dome Region of the HDR Under Natural Ventilation Conditions, Design Report, Test Group BRA, Experiments T52.1/T52.2* (In German). Project HDR Nuclear Center. Karlsruhe, Germany. PHDR Working Report 5.075/86. Feb. 1987.
12. Bader and Jansen. *Experiments with Hydrocarbon Fire in the Dome Region of the HDR Under Natural Ventilation Conditions, Supplemental Data Report, Test Group BRA,*

Experiments T52.1-4 (In German). Project HDR Nuclear Center. Karlsruhe, Germany. PHDR Working Report 5.115/87. June 1987.

13. Rautenberg, J., Müller, K., Volk, R., Max, U., and Dobbernack, R. *Experiments with Hydrocarbon Fire in the Dome Region of the HDR Under Natural Ventilation Conditions, Final Evaluation Report, Test Group BRA, Experiments T52.1-14* (In German). Project HDR Nuclear Center. Karlsruhe, Germany. PHDR Working Report 89-90. March 1991.
14. Müller, K., et al. *Evaluation of the Behavior of Compartment Networks During a Large Hydrocarbon Fire in a Closed Containment, Design Report, Test Group: Large Hydrocarbon Fire, Experiments E41.1-5* (In German). Project HDR Nuclear Center. Karlsruhe, Germany. PHDR Working Report 40.002/88. Oct. 1988.
15. Wenzel, H., Grimm, L. and Löhr, L. *Evaluation of the Behavior of Compartment Networks During a Large Hydrocarbon Fire in a Closed Containment, Data Report, Experiments E41.1-4* (In German). Project HDR Nuclear Center. Karlsruhe, Germany. PHDR Working Report 40.008/89. Dec. 1989.
16. Jansen and Bader. *Evaluation of the Behavior of Compartment Networks During a Large Hydrocarbon Fire in a Closed Containment, Supplemental Data Report, Experiments E41.1-4* (In German). Project HDR Nuclear Center. Karlsruhe, Germany. PHDR Working Report 40.002/88. Feb. 1989.
17. Rautenberg, J., Dobbernack, R., Müller, K., and Volk, R. *Evaluation of the Behavior of Compartment Networks During a Large Hydrocarbon Fire in a Closed Containment, Final Evaluation Report, Experiments E41.1-4* (In German). Project HDR Nuclear Center. Karlsruhe, Germany. PHDR Technical Report 103-92. Dec. 1992.
18. Müller, K. and Volk, R. *Behavior of Oil Fires in a Closed Subsystem With Ventilation Connected and Variable Door Opening, Design Report, Experiments E41.5-10* (In German). Project HDR Nuclear Center. Karlsruhe, Germany. PHDR Working Report 40.024/90. Aug. 1990.
19. Wenzel, H., Grimm, L. and Löhr, L. *Behavior of Oil Fires in a Closed Subsystem With Ventilation Connected and Variable Door Opening, Data Report, Experiments E41.5-10* (In German). Project HDR Nuclear Center. Karlsruhe, Germany. PHDR Working Report 40.026/90. Vol. 1 and 2.
20. Max, U., Müller, K., et al. *Behavior of Oil Fires in a Closed Subsystem With Ventilation Connected and Variable Door Opening, Quick Look Report, Experiments E41.5-10* (In German). Project HDR Nuclear Center. Karlsruhe, Germany. PHDR Technical Report 122-93. 1993.
21. Müller, K., Wegener H., and Löhr, L. *Cable Fire in an Enclosed Multi-Compartment Arrangement in the Containment, Design Report, Experiments E42* (In German). Project HDR Nuclear Center. Karlsruhe, Germany. PHDR Working Report 40.03/91. Feb. 1992.
22. Wenzel, H. and Löhr, L. *Cable Fire in an Enclosed Multi-Compartment Arrangement in the Containment, Data Report, Experiments E42, Time Period 01/21-02/18/92* (In German). Project HDR Nuclear Center. Karlsruhe, Germany. PHDR Working Report 40.042/91. Aug. 1992.
23. Rautenberg, J., Max U., Müller, K., and Hans, J. *Cable Fire in an Enclosed Multi-Compartment Arrangement in the Containment, Final Evaluation Report, Experiments E42* (In German). Project HDR Nuclear Center. Karlsruhe, Germany. PHDR Technical Report 123-94. April 1994.

24. Karwat, H., Müller, K., and Max, U. C*EC Standard Problem: Prediction of Effects Caused by a Cable Fire Experiment Within the HDR Containment, Task Specification.* Feb. 1992. (Revision July 1992.)
25. Karwat, H., Müller, K., and Max, U. C*EC Standard Problem: Prediction of Effects Caused by a Cable Fire Experiment Within the HDR Containment, Final Comparison Report.* EUR 15648 EN. Aug. 1993.
26. Green, J. Notebook for Development of E11.4 CONTAIN Model for the HDR Hydrogen Mixing Test. Dept. of Materials and Nuclear Engineering. University of Maryland. College Park, MD. 1992.
27. Holzbauer, H. *Blind Post-Test Predictions of HDR-H_2-Distribution Experiments E11.2 and E11.4 Using FATHOMS* (In German).Batelle Institute e.v. Frankfurt/Main, FRG. Final Report BIEV R67238-1. Dec. 1990.
28. Holzbauer, H. *Parametric Open Post-Test Predictions and Analysis of the HDR-H_2-Distribution Experiment E11.2 and E11.4 with the Computer Code GOTHIC* (In German). Batelle Institute e.v. Frankfurt/Main, FRG. Final Report BIEV R67706-1. August 1990.
29. Portier, R., Reneke, P., Jones, W., and Peacock, R. *User's Guide for CFAST Version 1.6*. Building and Fire Research Laboratory, NIST. Gaithersburg, MD. NISTIR 4985. Dec. 1992.
30. Peacock, R., et al. *CFAST, the Consolidated Model of Fire Growth and Smoke Transport.* Building and Fire Research Laboratory, NIST. Gaithersburg, Maryland. NIST Technical Note 1299. Feb. 1993.
31. George, T. et. al. *GOTHIC Containment Analysis Package Technical Manual, Version 3.4.* Numerical Applications Inc. for EPRI. RP3408-1. July, 1991.
32. McGrattan, K., Baum, H., and Rehm, R. *Buoyant Convection of a Thermally Expandable Fluid in a 3D Enclosure.* Building and Fire Research Laboratory, NIST. Gaithersburg, MD. June, 1997.
33. Floyd, J., Wolf, L., and Krawiec, J. *HDR Fire Test Data and Accompanying Conclusions from Present Code Capabilities, Volume 1: Test Series Description for T51 Gas Fire Test Series.* Final Report NIST Contract 60NANB6D0127. NIST GCR 97-727. NIST. Gaithersburg, MD. 1997.
34. Floyd, J., Wolf, L., and Krawiec, J. *HDR Fire Test Data and Accompanying Conclusions from Present Code Capabilities, Volume 2: CFAST Validation for HDR T51 Gas Fire Test Series.* Final Report NIST Contract 60NANB6D0127. NIST GCR 97-731. NIST. Gaithersburg, MD. 1997.
35. Rockett, J. *HDR Reactor Containment Fire Modeling with BR12.* Fire Technology Laboratory. Technical Research Centre of Finland (VTT). VTT Publication 113. 1992.
36. *FLUENT User's Guide, Release 4.4.* Fluent Incorporated. Lebanon, NH. 1996.
37. Floyd, J., Wolf, L., and Krawiec, J. *HDR Fire Test Data and Accompanying Conclusions from Present Code Capabilities, Volume 3:Test Series Description for T51 Wood Crib Fire Test Series.* Final Report NIST Contract 60NANB6D0127. NIST GCR 99-778. NIST. Gaithersburg, MD. 1999.
38. Floyd, J. *Evaluation of the Predictive Capabilities of Current Computational Methods for Fire Simulation Using the HDR T51 and T52 Tests with a Focus on Performance Based Codes.* Ph.D. Dissertation. University of Maryland. College Park, MD. May, 2000.

39. Travis, J., et al. *GASFLOW: A Computational Fluid Dynamics Code for Gases, Aerosols, and Combustion*. LA-13357. LANL. Los Alamos, NM. Oct., 1998.
40. Travis, J.., et al. "GASFLOW: A Computational Model to Analyze Combustion Events in Nuclear Containment and Facility Buildings." P*roceedings of 3rd International Seminar on Fire Safety of Nuclear Power Plants*. Müller, K. editor. HDR Nuclear Center. Karlsruhe, Germany. 1993. pp 211-262.

APPENDIX A: INPUT FILES

This section gives the CFAST input files for the case documented in Chapter 8.

A.1 T52.11 Input Cases

A.1.1 Initial Model (Single Node Dome)

```
VERSN    3T52-11 Dome to Level 1.6
#VERSN 3 T52-11 Dome to Level 1.6
TIMES   3600     20     20     00      0
THRMF T51MAT.DF
DUMPR T5211JF3.HIS
TAMB  293.150        101300. 0.000000
EAMB  293.150        101300. 0.000000
HI/F   25.5500  25.5500  25.3000  30.8500  25.3000  20.6000  15.0500 10.00000 10.00000 15.05000  20.6000
WIDTH  1.75000  0.95000  3.04700  15.8530  5.25500  4.56600  6.03300  7.00800  9.66800  5.58300  6.58800
DEPTH  4.58000  0.78000  3.04700  15.8530  5.25500  4.56600  6.03300  7.00800  9.66800  5.58300  6.58800
HEIGH  2.80000  3.00000  5.55000  19.1500  5.55000  4.70000  5.55000  5.05000  5.05000  5.55000  4.70000
CEILI FIRECEIL YTONG100 PROMASIL STEEL    CONCR100 CONCR100 CONCR100 CONCR100 CONCR100 CONCR100 CONCR100
WALLS YTONG250 YTONG100 YTONG100 STEEL    CONCR100 CONCR100 CONCR100 CONCR100 CONCR100 CONCR100 CONCR100
FLOOR FIRE_FLR FIRE_FLR CONCR100 CONCR100 CONCR100 CONCR100 CONCR100 CONCR100 CONCR100 CONCR100 CONCR100
HVENT  1  2  1 0.95000  2.80000  0.00000  0.00000  0.00000  0.00000
CVENT  1  2  1 1.00000  1.00000  1.00000  1.00000  1.00000  1.00000  1.00000  1.00000  1.00000  1.00000  1.00000
1.00000  1.00000  1.00000  1.00000  1.00000  1.00000  1.00000  1.00000
HVENT  2  3  1 0.95000  3.00000  0.00000  0.00000  0.00000  0.00000
CVENT  2  3  1 1.00000  1.00000  1.00000  1.00000  1.00000  1.00000  1.00000  1.00000  1.00000  1.00000  1.00000
1.00000  1.00000  1.00000  1.00000  1.00000  1.00000  1.00000  1.00000
HVENT  8  9  1 1.08000  3.25000  0.00000  0.00000  0.00000  0.00000
CVENT  8  9  1 1.00000  1.00000  1.00000  1.00000  1.00000  1.00000  1.00000  1.00000  1.00000  1.00000  1.00000
1.00000  1.00000  1.00000  1.00000  1.00000  1.00000  1.00000  1.00000
VVENT  4  3  4.81000  2
VVENT  4  5  4.54000  2
VVENT  5  6  4.54000  2
VVENT  6  7  4.54000  2
VVENT  7  8  4.54000  2
VVENT  3 11  4.81000  2
VVENT 11 10  4.81000  2
VVENT 10  9  4.81000  2
CHEMI 170.000  20.000  0.000  4.250E+007  293.000  349.000 0.200
LFBO 1
LFBT 2
CJET OFF
FPOS   0.875  2.290  0.000
FTIME    30.00     70.00    103.60    190.00    220.00    292.00    340.00    400.00    520.00    526.00   1660.00   1732.00
1900.00   1960.00   2050.00   2110.00   2320.00   2392.00   3600.00
FHIGH  0.00000   0.00000   0.25000   0.25000   0.25000   0.25000   0.25000   0.25000   0.25000   0.25000   0.25000   0.25000
0.25000   0.25000   0.25000   0.25000   0.25000   0.25000   0.25000   0.25000
FAREA  0.00000   0.00000   1.00000   1.00000   1.00000   1.00000   1.00000   1.00000   1.00000   1.00000   1.00000   1.00000
1.00000   1.00000   1.00000   1.00000   1.00000   1.00000   1.00000   1.00000
FMASS  0.00000   0.00000   0.04000   0.05700   0.06800   0.06800   0.06400   0.05200   0.02500   0.02500   0.03600   0.03600
0.05700   0.04000   0.01800   0.01800   0.00500   0.00500   0.00000   0.00000
FQDOT  0.00000   0.00000  1700000.  2422500.  2890000.  2890000.  2720000.  2210000.  1062500.  1062500.  1530000.  1530000.
2422500.  1700000.   765000.   765000.   212500.   212500.   0.00000   0.00000
HCR    0.00000   0.00000   0.15294   0.15294   0.15294   0.15294   0.15294   0.15294   0.15294   0.15294   0.15294   0.15294
0.15294   0.15294   0.15294   0.15294   0.15924   0.15924   0.15924   0.15924
O2     0.00000   0.00000   0.00000   0.00000   0.00000   0.00000   0.00000   0.00000   0.00000   0.00000   0.00000   0.00000
0.00000   0.00000   0.00000   0.00000   0.00000   0.00000   0.00000   0.00000
OD     0.00000   0.00000   0.03000   0.03000   0.03000   0.03000   0.03000   0.03000   0.03000   0.03000   0.03000   0.03000
0.03000   0.03000   0.03000   0.03000   0.03000   0.03000   0.03000   0.03000
CO     0.00000   0.00000   0.03000   0.03000   0.03000   0.03000   0.03000   0.03000   0.03000   0.03000   0.03000   0.03000
0.03000   0.03000   0.03000   0.03000   0.03000   0.03000   0.03000   0.03000
```

A.1.2 A Model (3 Node Dome With Vent Connection)

```
VERSN    3T52-11 Dome to Level 1.6
#VERSN 3 T52-11 Dome to Level 1.6
#WITH VENT CONNECTION BETWEEN NODE #4 AND #6
TIMES   3600     20     20     00      0
THRMF T51MAT.DF
DUMPR T5211ka3.HIS
TAMB  293.150        101300. 0.000000
EAMB  293.150        101300. 0.000000
HI/F   25.5500  25.5500  25.3000  30.8500  40.0000  30.8500  25.3000  20.6000  15.0500 10.00000 10.00000 15.05000  20.6000
WIDTH  1.75000  0.95000  3.04700  12.3400  14.2400  12.3400  5.25500  4.56600  6.03300  7.00800  9.66800  5.58300  6.58800
DEPTH  4.58000  0.78000  3.04700  12.3400  14.2400  12.3400  5.25500  4.56600  6.03300  7.00800  9.66800  5.58300  6.58800
HEIGH  2.80000  3.00000  5.55000  9.1500   10.0000  9.15000  5.55000  4.70000  5.55000  5.05000  5.05000  5.55000  4.70000
CEILI FIRECEIL YTONG100 PROMASIL OFF      STEEL    OFF      CONCR100 CONCR100 CONCR100 CONCR100 CONCR100
WALLS YTONG250 YTONG100 YTONG100 STEEL    STEEL    STEEL    CONCR100 CONCR100 CONCR100 CONCR100 CONCR100
FLOOR FIRE_FLR FIRE_FLR CONCR100 CONCR100 OFF      CONCR100 CONCR100 CONCR100 CONCR100 CONCR100 CONCR100
HVENT  1  2  1 0.95000  2.80000  0.00000  0.00000  0.00000  0.00000  0.00000
CVENT  1  2  1 1.00000  1.00000  1.00000  1.00000  1.00000  1.00000  1.00000  1.00000  1.00000  1.00000  1.00000  1.00000
1.00000  1.00000  1.00000  1.00000  1.00000  1.00000  1.00000  1.00000
HVENT  2  3  1 0.95000  3.00000  0.00000  0.00000  0.00000  0.00000  0.00000
CVENT  2  3  1 1.00000  1.00000  1.00000  1.00000  1.00000  1.00000  1.00000  1.00000  1.00000  1.00000  1.00000  1.00000
1.00000  1.00000  1.00000  1.00000  1.00000  1.00000  1.00000  1.00000
HVENT  4  6  1 12.3400  9.15000  0.00000  0.00000  0.00000  0.00000
CVENT  4  6  1 1.00000  1.00000  1.00000  1.00000  1.00000  1.00000  1.00000  1.00000  1.00000  1.00000  1.00000  1.00000
1.00000  1.00000  1.00000  1.00000  1.00000  1.00000  1.00000  1.00000
HVENT 10 11  1 1.08000  3.25000  0.00000  0.00000  0.00000  0.00000
CVENT 10 11  1 1.00000  1.00000  1.00000  1.00000  1.00000  1.00000  1.00000  1.00000  1.00000  1.00000  1.00000  1.00000
1.00000  1.00000  1.00000  1.00000  1.00000  1.00000  1.00000  1.00000
VVENT  3  4  4.81000  2
VVENT  4  5  152.150  2
VVENT  5  6  152.150  2
VVENT  6  7  4.54000  2
VVENT  7  8  4.54000  2
VVENT  8  9  4.54000  2
VVENT  9 10  4.54000  2
VVENT  3 13  4.81000  2
VVENT 13 12  4.81000  2
VVENT 12 11  4.81000  2
CHEMI 170.000  20.000  0.000  4.250E+007  293.000  349.000 0.200
LFBO 1
LFBT 2
CJET OFF
FPOS   0.875  2.290  0.000
FTIME    30.00     70.00    103.60    190.00    220.00    292.00    340.00    400.00    520.00    526.00   1660.00   1732.00
1900.00   1960.00   2050.00   2110.00   2320.00   2392.00   3600.00
FHIGH  0.00000   0.00000   0.25000   0.25000   0.25000   0.25000   0.25000   0.25000   0.25000   0.25000   0.25000   0.25000
0.25000   0.25000   0.25000   0.25000   0.25000   0.25000   0.25000   0.25000
FAREA  0.00000   0.00000   1.00000   1.00000   1.00000   1.00000   1.00000   1.00000   1.00000   1.00000   1.00000   1.00000
1.00000   1.00000   1.00000   1.00000   1.00000   1.00000   1.00000   1.00000
FMASS  0.00000   0.00000   0.04000   0.05700   0.06800   0.06800   0.06400   0.05200   0.02500   0.02500   0.03600   0.03600
0.05700   0.04000   0.01800   0.01800   0.00500   0.00500   0.00000   0.00000
FQDOT  0.00000   0.00000  1700000.  2422500.  2890000.  2890000.  2720000.  2210000.  1062500.  1062500.  1530000.  1530000.
2422500.  1700000.   765000.   765000.   212500.   212500.   0.00000   0.00000
HCR    0.00000   0.00000   0.15294   0.15294   0.15294   0.15294   0.15294   0.15294   0.15294   0.15294   0.15294   0.15294
0.15294   0.15294   0.15294   0.15294   0.15924   0.15924   0.15924   0.15924
O2     0.00000   0.00000   0.00000   0.00000   0.00000   0.00000   0.00000   0.00000   0.00000   0.00000   0.00000   0.00000
0.00000   0.00000   0.00000   0.00000   0.00000   0.00000   0.00000   0.00000
OD     0.00000   0.00000   0.03000   0.03000   0.03000   0.03000   0.03000   0.03000   0.03000   0.03000   0.03000   0.03000
0.03000   0.03000   0.03000   0.03000   0.03000   0.03000   0.03000   0.03000
CO     0.00000   0.00000   0.03000   0.03000   0.03000   0.03000   0.03000   0.03000   0.03000   0.03000   0.03000   0.03000
0.03000   0.03000   0.03000   0.03000   0.03000   0.03000   0.03000   0.03000
```

A.1.3 B Model (3 Node Dome Without Vent Connection)

```
VERSN    3T52-11 Dome to Level 1.6
#VERSN 3 T52-11 Dome to Level 1.6
#WITHOUT VENT CONNECTION BETWEEN NODE #4 AND #6
TIMES   3600     20     20     00      0
THRMF T51MAT.DF
DUMPR T5211kb3.HIS
TAMB  293.150        101300. 0.000000
EAMB  293.150        101300. 0.000000
HI/F   25.5500  25.5500  25.3000  30.8500  40.0000  30.8500  25.3000  20.6000  15.0500 10.00000 10.00000 15.05000  20.6000
WIDTH  1.75000  0.95000  3.04700  12.3400  14.2400  12.3400  5.25500  4.56600  6.03300  7.00800  9.66800  5.58300  6.58800
DEPTH  4.58000  0.78000  3.04700  12.3400  14.2400  12.3400  5.25500  4.56600  6.03300  7.00800  9.66800  5.58300  6.58800
HEIGH  2.80000  3.00000  5.55000  9.1500   10.0000  9.15000  5.55000  4.70000  5.55000  5.05000  5.05000  5.55000  4.70000
CEILI FIRECEIL YTONG100 PROMASIL OFF      STEEL    OFF      CONCR100 CONCR100 CONCR100 CONCR100 CONCR100 CONCR100 CONCR100
WALLS YTONG250 YTONG100 YTONG100 STEEL    STEEL    STEEL    CONCR100 CONCR100 CONCR100 CONCR100 CONCR100 CONCR100 CONCR100
FLOOR FIRE_FLR FIRE_FLR CONCR100 CONCR100 OFF      CONCR100 CONCR100 CONCR100 CONCR100 CONCR100 CONCR100 CONCR100 CONCR100
HVENT  1  2  1 0.95000  2.80000  0.00000  0.00000  0.00000  0.00000
CVENT  1  2  1 1.00000  1.00000  1.00000  1.00000  1.00000  1.00000  1.00000  1.00000  1.00000  1.00000  1.00000  1.00000
1.00000  1.00000  1.00000  1.00000  1.00000  1.00000  1.00000  1.00000
HVENT  2  3  1 0.95000  3.00000  0.00000  0.00000  0.00000  0.00000
CVENT  2  3  1 1.00000  1.00000  1.00000  1.00000  1.00000  1.00000  1.00000  1.00000  1.00000  1.00000  1.00000  1.00000
1.00000  1.00000  1.00000  1.00000  1.00000  1.00000  1.00000  1.00000
HVENT 10 11  1 1.08000  3.25000  0.00000  0.00000  0.00000  0.00000
CVENT 10 11  1 1.00000  1.00000  1.00000  1.00000  1.00000  1.00000  1.00000  1.00000  1.00000  1.00000  1.00000  1.00000
1.00000  1.00000  1.00000  1.00000  1.00000  1.00000  1.00000  1.00000
VVENT  3  4  4.81000  2
VVENT  4  5  152.150  2
VVENT  5  6  152.150  2
VVENT  6  7  4.54000  2
VVENT  7  8  4.54000  2
VVENT  8  9  4.54000  2
VVENT  9 10  4.54000  2
VVENT  3 13  4.81000  2
VVENT 13 12  4.81000  2
VVENT 12 11  4.81000  2
CHEMI 170.000  20.000  0.000  4.250E+007  293.000  349.000 0.200
LFBO 1
LFBT 2
CJET OFF
FPOS   0.875  2.290  0.000
FTIME    30.00     70.00    103.60    190.00    220.00    292.00    340.00    400.00    520.00    526.00   1660.00   1732.00
1900.00   1960.00   2050.00   2110.00   2320.00   2392.00   3600.00
FHIGH  0.00000   0.00000   0.25000   0.25000   0.25000   0.25000   0.25000   0.25000   0.25000   0.25000   0.25000   0.25000
0.25000   0.25000   0.25000   0.25000   0.25000   0.25000   0.25000   0.25000
FAREA  0.00000   0.00000   1.00000   1.00000   1.00000   1.00000   1.00000   1.00000   1.00000   1.00000   1.00000   1.00000
1.00000   1.00000   1.00000   1.00000   1.00000   1.00000   1.00000   1.00000
FMASS  0.00000   0.00000   0.04000   0.05700   0.06800   0.06800   0.06400   0.05200   0.02500   0.02500   0.03600   0.03600
0.05700   0.04000   0.01800   0.01800   0.00500   0.00500   0.00000   0.00000
FQDOT  0.00000   0.00000  1700000.  2422500.  2890000.  2890000.  2720000.  2210000.  1062500.  1062500.  1530000.  1530000.
2422500.  1700000.   765000.   765000.   212500.   212500.   0.00000   0.00000
HCR    0.00000   0.00000   0.15294   0.15294   0.15294   0.15294   0.15294   0.15294   0.15294   0.15294   0.15294   0.15294
0.15294   0.15294   0.15294   0.15294   0.15924   0.15924   0.15924   0.15924
O2     0.00000   0.00000   0.00000   0.00000   0.00000   0.00000   0.00000   0.00000   0.00000   0.00000   0.00000   0.00000
0.00000   0.00000   0.00000   0.00000   0.00000   0.00000   0.00000   0.00000
OD     0.00000   0.00000   0.03000   0.03000   0.03000   0.03000   0.03000   0.03000   0.03000   0.03000   0.03000   0.03000
0.03000   0.03000   0.03000   0.03000   0.03000   0.03000   0.03000   0.03000
CO     0.00000   0.00000   0.03000   0.03000   0.03000   0.03000   0.03000   0.03000   0.03000   0.03000   0.03000   0.03000
0.03000   0.03000   0.03000   0.03000   0.03000   0.03000   0.03000   0.03000
```

A.2 T52.14 Input Cases

A.2.1 Initial Model (Single Node Dome)

```
VERSN    3T52-14 Dome to Level 1.6
#VERSN 3 T52-14 Dome to Level 1.6
TIMES   3600     20     20     00      0
THRMF T51MAT.DF
DUMPR T5214JF2.HIS
TAMB  293.150        101300. 0.000000
EAMB  293.150        101300. 0.000000
HI/F   25.5500  25.5500  25.3000  30.8500  25.3000  20.6000  15.0500 10.00000 10.00000 15.05000  20.6000
WIDTH  1.75000  0.95000  3.04700  15.8530  5.25500  4.56600  6.03300  7.00800  9.66800  5.58300  6.58800
DEPTH  4.58000  0.78000  3.04700  15.8530  5.25500  4.56600  6.03300  7.00800  9.66800  5.58300  6.58800
HEIGH  2.80000  3.00000  5.55000  19.1500  5.55000  4.70000  5.55000  5.05000  5.05000  5.55000  4.70000
CEILI FIRECEIL YTONG100 PROMASIL STEEL    CONCR100 CONCR100 CONCR100 CONCR100 CONCR100 CONCR100 CONCR100
WALLS YTONG250 YTONG100 YTONG100 STEEL    CONCR100 CONCR100 CONCR100 CONCR100 CONCR100 CONCR100 CONCR100
FLOOR FIRE_FLR FIRE_FLR CONCR100 CONCR100 CONCR100 CONCR100 CONCR100 CONCR100 CONCR100 CONCR100 CONCR100
HVENT  1  2  1 0.95000  2.80000  0.00000  0.00000  0.00000  0.00000
CVENT  1  2  1 1.00000  1.00000  1.00000  1.00000  1.00000  1.00000  1.00000  1.00000  1.00000  1.00000  1.00000
1.00000  1.00000  1.00000
HVENT  2  3  1 0.95000  3.00000  0.00000  0.00000  0.00000  0.00000
CVENT  2  3  1 1.00000  1.00000  1.00000  1.00000  1.00000  1.00000  1.00000  1.00000  1.00000  1.00000  1.00000
1.00000  1.00000  1.00000
HVENT  8  9  1 1.08000  3.25000  0.00000  0.00000  0.00000  0.00000
CVENT  8  9  1 1.00000  1.00000  1.00000  1.00000  1.00000  1.00000  1.00000  1.00000  1.00000  1.00000  1.00000
1.00000  1.00000  1.00000
VVENT  4  3  4.81000  2
VVENT  4  5  4.54000  2
VVENT  5  6  4.54000  2
VVENT  6  7  4.54000  2
VVENT  7  8  4.54000  2
VVENT  3 11  4.81000  2
VVENT 11 10  4.81000  2
VVENT 10  9  4.81000  2
CHEMI 170.000  20.000  0.000  4.250E+007  293.000  349.000 0.200
LFBO 1
LFBT 2
CJET OFF
FPOS   0.875  2.290  0.000
FTIME    23.26     55.97    188.47    210.41    260.14    280.71    316.20    402.16    433.58    561.71   1980.00   2045.96
3600.00
FHIGH  0.00000   0.25000   0.25000   0.25000   0.25000   0.25000   0.25000   0.25000   0.25000   0.25000   0.25000   0.25000
0.25000   0.25000
FAREA  0.00000   2.00000   2.00000   2.00000   2.00000   2.00000   2.00000   2.00000   2.00000   2.00000   2.00000   2.00000
2.00000   2.00000
FMASS  0.00000   0.00650   0.05496   0.11658   0.11672   0.08412   0.07847   0.09346   0.09899   0.09646   0.06231   0.06231
0.00000   0.00000
FQDOT  0.00000   276420.  2335799.  4954688.  4960710.  3574934.  3335078.  3971822.  4207007.  4099349.  2648267.  2648268.
0.00000   0.00000
HCR    0.00000   0.00000   0.15294   0.15294   0.15294   0.15294   0.15294   0.15294   0.15294   0.15294   0.15294   0.15294
0.15294   0.15294
O2     0.00000   0.00000   0.00000   0.00000   0.00000   0.00000   0.00000   0.00000   0.00000   0.00000   0.00000   0.00000
0.00000   0.00000
OD     0.00000   0.00000   0.03000   0.03000   0.03000   0.03000   0.03000   0.03000   0.03000   0.03000   0.03000   0.03000
0.03000   0.03000
CO     0.00000   0.00000   0.03000   0.03000   0.03000   0.03000   0.03000   0.03000   0.03000   0.03000   0.03000   0.03000
0.03000   0.03000
#GRAPHICS ON
DEVICE 1
WINDOW    0.    0.    0. 1279. 1023. 4095.
```

A.2.2 A Model (3 Node Dome With Vent Connection)

```
VERSN    3T52-14 Dome to Level 1.6
#VERSN 3 T52-14 Dome to Level 1.6
#WITH VENT CONNECTION BETWEEN NODE #4 AND #6
TIMES   3600     20     20     00      0
THRMF T51MAT.DF
DUMPR T5214ka2.HIS
TAMB  293.150        101300. 0.000000
EAMB  293.150        101300. 0.000000
HI/F   25.5500  25.5500  25.3000  30.8500  40.0000  30.8500  25.3000  20.6000  15.0500 10.00000 10.00000 15.05000  20.6000
WIDTH  1.75000  0.95000  3.04700  12.3400  14.2400  12.3400  5.25500  4.56600  6.03300  7.00800  9.66800  5.58300  6.58800
DEPTH  4.58000  0.78000  3.04700  12.3400  14.2400  12.3400  5.25500  4.56600  6.03300  7.00800  9.66800  5.58300  6.58800
HEIGH  2.80000  3.00000  5.55000  9.1500   10.0000  9.15000  5.55000  4.70000  5.55000  5.05000  5.05000  5.55000  4.70000
CEILI FIRECEIL YTONG100 PROMASIL OFF      STEEL    OFF      CONCR100 CONCR100 CONCR100 CONCR100 CONCR100
WALLS YTONG250 YTONG100 YTONG100 STEEL    STEEL    STEEL    CONCR100 CONCR100 CONCR100 CONCR100 CONCR100
FLOOR FIRE_FLR FIRE_FLR CONCR100 CONCR100 OFF      CONCR100 CONCR100 CONCR100 CONCR100 CONCR100 CONCR100
HVENT  1  2  1 0.95000  2.80000  0.00000  0.00000  0.00000  0.00000
CVENT  1  2  1 1.00000  1.00000  1.00000  1.00000  1.00000  1.00000  1.00000  1.00000  1.00000  1.00000  1.00000
HVENT  2  3  1 0.95000  3.00000  0.00000  0.00000  0.00000  0.00000
CVENT  2  3  1 1.00000  1.00000  1.00000  1.00000  1.00000  1.00000  1.00000  1.00000  1.00000  1.00000  1.00000
HVENT  4  6  1 12.3400  9.15000  0.00000  0.00000  0.00000  0.00000
CVENT  4  6  1 1.00000  1.00000  1.00000  1.00000  1.00000  1.00000  1.00000  1.00000  1.00000  1.00000  1.00000
HVENT 10 11  1 1.08000  3.25000  0.00000  0.00000  0.00000  0.00000
CVENT 10 11  1 1.00000  1.00000  1.00000  1.00000  1.00000  1.00000  1.00000  1.00000  1.00000  1.00000  1.00000
VVENT  3  4  4.81000  2
VVENT  4  5  152.150  2
VVENT  5  6  152.150  2
VVENT  6  7  4.54000  2
VVENT  7  8  4.54000  2
VVENT  8  9  4.54000  2
VVENT  9 10  4.54000  2
VVENT  3 13  4.81000  2
VVENT 13 12  4.81000  2
VVENT 12 11  4.81000  2
CHEMI 170.000  20.000  0.000  4.250E+007  293.000  349.000 0.200
LFBO 1
LFBT 2
CJET OFF
FPOS   0.875  2.290  0.000
FTIME    23.26     55.97    188.47    210.41    260.14    280.71    316.20    402.16    433.58    561.71   1980.00   2045.96
3600.00
FHIGH  0.00000   0.25000   0.25000   0.25000   0.25000   0.25000   0.25000   0.25000   0.25000   0.25000   0.25000   0.25000
0.25000   0.25000
FAREA  0.00000   2.00000   2.00000   2.00000   2.00000   2.00000   2.00000   2.00000   2.00000   2.00000   2.00000   2.00000
2.00000   2.00000
FMASS  0.00000   0.00650   0.05496   0.11658   0.11672   0.08412   0.07847   0.09346   0.09899   0.09646   0.06231   0.06231
0.00000   0.00000
FQDOT  0.00000   276420.  2335799.  4954688.  4960710.  3574934.  3335078.  3971822.  4207007.  4099349.  2648267.  2648268.
0.00000   0.00000
HCR    0.00000   0.00000   0.15294   0.15294   0.15294   0.15294   0.15294   0.15294   0.15294   0.15294   0.15294   0.15294
0.15294   0.15294
O2     0.00000   0.00000   0.00000   0.00000   0.00000   0.00000   0.00000   0.00000   0.00000   0.00000   0.00000   0.00000
0.00000   0.00000
OD     0.00000   0.00000   0.03000   0.03000   0.03000   0.03000   0.03000   0.03000   0.03000   0.03000   0.03000   0.03000
0.03000   0.03000
CO     0.00000   0.00000   0.03000   0.03000   0.03000   0.03000   0.03000   0.03000   0.03000   0.03000   0.03000   0.03000
0.03000   0.03000
#GRAPHICS ON
DEVICE 1
WINDOW    0.    0.    0. 1279. 1023. 4095.
```

A.2.3 B Model (3 Node Dome Without Vent Connection)

```
VERSN    3T52-14 Dome to Level 1.6
#VERSN 3 T52-14 Dome to Level 1.6
#WITHOUT VENT CONNECTION BETWEEN NODE #4 AND #6
TIMES   3600     20     20     00      0
THRMF T51MAT.DF
DUMPR T5214kb2.HIS
TAMB  293.150        101300. 0.000000
EAMB  293.150        101300. 0.000000
HI/F   25.5500  25.5500  25.3000  30.8500  40.0000  30.8500  25.3000  20.6000  15.0500 10.00000 10.00000 15.05000  20.6000
WIDTH  1.75000  0.95000  3.04700  12.3400  14.2400  12.3400  5.25500  4.56600  6.03300  7.00800  9.66800  5.58300  6.58800
DEPTH  4.58000  0.78000  3.04700  12.3400  14.2400  12.3400  5.25500  4.56600  6.03300  7.00800  9.66800  5.58300  6.58800
HEIGH  2.80000  3.00000  5.55000  9.1500   10.0000  9.15000  5.55000  4.70000  5.55000  5.05000  5.05000  5.55000  4.70000
CEILI FIRECEIL YTONG100 PROMASIL OFF      STEEL    OFF      CONCR100 CONCR100 CONCR100 CONCR100 CONCR100 CONCR100 CONCR100
WALLS YTONG250 DOORWALL YTONG100 STEEL    STEEL    STEEL    CONCR100 CONCR100 CONCR100 CONCR100 CONCR100 CONCR100 CONCR100
FLOOR FIRE_FLR FIRE_FLR CONCR100 CONCR100 OFF      CONCR100 CONCR100 CONCR100 CONCR100 CONCR100 CONCR100 CONCR100 CONCR100
HVENT  1  2  1 0.95000  2.80000  0.00000  0.00000  0.00000  0.00000
CVENT  1  2  1 1.00000  1.00000  1.00000  1.00000  1.00000  1.00000  1.00000  1.00000  1.00000  1.00000  1.00000  1.00000
HVENT  2  3  1 0.95000  3.00000  0.00000  0.00000  0.00000  0.00000
CVENT  2  3  1 1.00000  1.00000  1.00000  1.00000  1.00000  1.00000  1.00000  1.00000  1.00000  1.00000  1.00000  1.00000
HVENT 10 11  1 1.08000  3.25000  0.00000  0.00000  0.00000  0.00000
CVENT 10 11  1 1.00000  1.00000  1.00000  1.00000  1.00000  1.00000  1.00000  1.00000  1.00000  1.00000  1.00000  1.00000
VVENT  3  4  4.81000  2
VVENT  4  5  152.150  2
VVENT  5  6  152.150  2
VVENT  6  7  4.54000  2
VVENT  7  8  4.54000  2
VVENT  8  9  4.54000  2
VVENT  9 10  4.54000  2
VVENT  3 13  4.81000  2
VVENT 13 12  4.81000  2
VVENT 12 11  4.81000  2
CHEMI 170.000  20.000  0.000  4.250E+007  293.000  349.000 0.200
LFBO 1
LFBT 2
CJET OFF
FPOS   0.875  2.290  0.000
FTIME    23.26     55.97    188.47    210.41    260.14    280.71    316.20    402.16    433.58    561.71   1980.00   2045.96
3600.00
FHIGH  0.00000   0.25000   0.25000   0.25000   0.25000   0.25000   0.25000   0.25000   0.25000   0.25000   0.25000   0.25000
0.25000   0.25000
FAREA  0.00000   2.00000   2.00000   2.00000   2.00000   2.00000   2.00000   2.00000   2.00000   2.00000   2.00000   2.00000
2.00000   2.00000
FMASS  0.00000   0.00650   0.05496   0.11658   0.11672   0.08412   0.07847   0.09346   0.09899   0.09646   0.06231   0.06231
0.00000   0.00000
FQDOT  0.00000   276420.  2335799.  4954688.  4960710.  3574934.  3335078.  3971822.  4207007.  4099349.  2648267.  2648268.
0.00000   0.00000
HCR    0.00000   0.00000   0.15294   0.15294   0.15294   0.15294   0.15294   0.15294   0.15294   0.15294   0.15294   0.15294
0.15294   0.15294
O2     0.00000   0.00000   0.00000   0.00000   0.00000   0.00000   0.00000   0.00000   0.00000   0.00000   0.00000   0.00000
0.00000   0.00000
OD     0.00000   0.00000   0.03000   0.03000   0.03000   0.03000   0.03000   0.03000   0.03000   0.03000   0.03000   0.03000
0.03000   0.03000
CO     0.00000   0.00000   0.03000   0.03000   0.03000   0.03000   0.03000   0.03000   0.03000   0.03000   0.03000   0.03000
0.03000   0.03000
#GRAPHICS ON
DEVICE 1
WINDOW    0.    0.    0. 1279. 1023. 4095.
```

NIST-114
(REV. 11-94)
ADMAN 4.09

U.S. DEPARTMENT OF COMMERCE
NATIONAL INSTITUTE OF STANDARDS AND TECHNOLOGY

(ERB USE ONLY)
ERB CONTROL NUMBER | DIVISION

PUBLICATION REPORT NUMBER | CATEGORY CODE
NIST GCR 01-809

PUBLICATION DATE | NUMBER PRINTED PAGES
December 2000

MANUSCRIPT REVIEW AND APPROVAL

INSTRUCTIONS: ATTACH ORIGINAL OF THIS FORM TO ONE (1) COPY OF MANUSCRIPT AND SEND TO THE SECRETARY, APPROPRIATE EDITORIAL REVIEW BOARD.

TITLE AND SUBTITLE (CITE IN FULL) Evaluation of the HDR Fire Test Data and Accompanying Computational Activities with Conclusions from Present Code Capabilities. Volume 4: Test Series Description and CFAST Validation for HDR T52 Oil Pool Fire Test Series

CONTRACT OR GRANT NUMBER
60NANB6D0127

TYPE OF REPORT AND/OR PERIOD COVERED
June 2000

AUTHOR(S) (LAST NAME, FIRST INITIAL, SECOND INITIAL)
Floyd, J., Wolf, L., Rauch, B., Mun, K.

PERFORMING ORGANIZATION (CHECK (X) ONE BLOCK)
- [ ] NIST/GAITHERSBURG
- [ ] NIST/BOULDER
- [ ] JILA/BOULDER

LABORATORY AND DIVISION NAMES (FIRST NIST AUTHOR ONLY)

SPONSORING ORGANIZATION NAME AND COMPLETE ADDRESS (STREET, CITY, STATE, ZIP)
U.S. Department of Commerce
National Institute of Standards and Technology, Gaithersburg, MD 20899-8640

PROPOSED FOR NIST PUBLICATION

- [ ] JOURNAL OF RESEARCH (NIST JRES)
- [ ] J. PHYS. & CHEM. REF. DATA (JPCRD)
- [ ] HANDBOOK (NIST HB)
- [ ] SPECIAL PUBLICATION (NIST SP)
- [ ] TECHNICAL NOTE (NIST TN)
- [ ] MONOGRAPH (NIST MN)
- [ ] NATL. STD. REF. DATA SERIES (NIST NSRDS)
- [ ] FEDERAL INF. PROCESS. STDS. (NIST FIPS)
- [ ] LIST OF PUBLICATIONS (NIST LP)
- [ ] NIST INTERAGENCY/INTERNAL REPORT (NISTIR)
- [ ] LETTER CIRCULAR
- [ ] BUILDING SCIENCE SERIES
- [ ] PRODUCT STANDARDS
- [x] OTHER NIST GCR

PROPOSED FOR NON-NIST PUBLICATION (CITE FULLY) [ ] U.S. [ ] FOREIGN

PUBLISHING MEDIUM
- [x] PAPER
- [ ] CD-ROM
- [ ] DISKETTE (SPECIFY)
- [ ] OTHER (SPECIFY)

SUPPLEMENTARY NOTES

ABSTRACT (A 2000-CHARACTER OR LESS FACTUAL SUMMARY OF MOST SIGNIFICANT INFORMATION. IF DOCUMENT INCLUDES A SIGNIFICANT BIBLIOGRAPHY OR LITERATURE SURVEY, CITE IT HERE. SPELL OUT ACRONYMS ON FIRST REFERENCE.) (CONTINUE ON SEPARATE PAGE, IF NECESSARY.)

The HDR (Heiss-Dampf Reaktor) facility, shown in Figure 1.1, was the containment building for a decommissioned, experimental reactor in Germany. The building, while smaller in volume than a typical US containment building, contained many features which made it valuable for use in a containment research program. Many of these features also make it extremely valuable as a generic source of test data for industrial facilities. The building was a cylinder approximately 20 m in diameter by 50 m in height topped by a 10 m radius hemispherical dome for a total facility height of 60 m. Internally the building was divided into eight levels with each level further subdivided into smaller compartments. For a typical HDR test approximately 60-70 compartments were available. Compartments were connected by a variety of flow paths which included doorways, pipe runs, cable trays, hatches, and staircases. Three fixed and two adjustable vertical channels were provided for in the form of an elevator shaft, two staircases, and two sets of equipment hatches running the axial length of the building which could be opened or closed to change the available vertical flow path at each level. Much of the original equipment from the nuclear steam supply system was still present in the facility including the reactor vessel, primary and secondary piping, pumps, electrical connections, and ventilation and exhaust systems. The total free volume of the facility was 11,000 m^3 of which the dome contained 4,800 m^3 above the operating deck. The HDR containment, its compartments, and internal structural materials, vent flow openings and other pertinent data are documented in [1].

KEY WORDS (MAXIMUM OF 9; 28 CHARACTERS AND SPACES EACH; SEPARATE WITH SEMICOLONS; ALPHABETIC ORDER; CAPITALIZE ONLY PROPER NAMES)
codes; evaluation; fire tests; pool fires; test data; validation

AVAILABILITY
- [x] UNLIMITED
- [ ] FOR OFFICIAL DISTRIBUTION - DO NOT RELEASE TO NTIS
- [ ] ORDER FROM SUPERINTENDENT OF DOCUMENTS, U.S. GPO, WASHINGTON, DC 20402
- [x] ORDER FROM NTIS, SPRINGFIELD, VA 22161

ELECTRONIC INFORMS

NOTE TO AUTHOR(S): IF YOU DO NOT WISH THIS MANUSCRIPT ANNOUNCED BEFORE PUBLICATION, PLEASE CHECK HERE. [ ]